THE ROLE OF SOLVENT IN THE SYNTHESIS OF MESOPOROUS $M_2P_2O_7$ (M: Co(II), Ni(II), AND Mn(II)) AND $Mn_{2-x}M_xP_2O_7$ (M: Co(II) AND Ni(II)) THIN FILMS AND THEIR OXYGEN EVOLUTION REACTION PERFORMANCE

A THESIS SUBMITTED TO

THE GRADUATE SCHOOL OF ENGINEERING AND SCIENCE

OF

BILKENT UNIVERSITY

IN PARTIAL FULFILLMENT OF THE REQUIREMENTS

FOR

THE DEGREE OF MASTER OF SCIENCE

IN

CHEMISTRY

By

Gözde Ceran

September 2025

THE ROLE OF SOLVENT IN THE SYNTHESIS OF MESOPOROUS $M_2P_2O_7$ (M: Co(II), Ni(II), AND Mn(II)) AND $Mn_{2-x}M_xP_2O_7$ (M: Co(II) AND Ni(II)) THIN FILMS AND THEIR OXYGEN EVOLUTION REACTION PERFORMANCE

By Gözde Ceran

September, 2025

We certify that we have read this thesis and that in our opinion it is fully adequate, in scope and in quality, as a thesis for the degree of Master of Science.

_____

Ömer Dağ (Advisor)

_____

Ferdi Karadaş

_____

Emre Büküşoğlu

Approved for the Graduate School of Engineering and Science:

_____

Orhan Arıkan

Director of the Graduate School

ABSTRACT

The Role of Solvent In The Synthesis of Mesoporous $M_2P_2O_7$ (M: Co(II), Ni(II), And Mn(II)) And $Mn_{2-x}M_xP_2O_7$ (M: Co(II) And Ni(II)) Thin Films And Their Oxygen Evolution Reaction Performance

Gözde Ceran

Master of Science, Chemistry

Advisor: Prof. Ömer Dağ

September, 2025

Mesoporous transition metal pyrophosphates ($M_2P_2O_7$) have attracted considerable attention due to their diverse structural features and wide range of potential applications in catalysis, ion exchange, and energy storage. This study presents a novel synthesis route for high surface area and porous $M_2P_2O_7$ materials, focusing on the influence of solvent selection on their structural and electrochemical properties. $Co_2P_2O_7$, $Ni_2P_2O_7$, $Mn_2P_2O_7$, and binary metal pyrophosphates have been synthesized via a molten salt-assisted self-assembly (MASA) method using pyrophosphoric acid (PPA, $H_4P_2O_7$), salt $[Mn(H_2O)_4](NO_3)_2$, $[Co(H_2O)_6](NO_3)_2$, and $[Ni(H_2O)_6](NO_3)_2$), surfactant (pluronic, P123), and solvents (ethanol, butanol, and methanol). Sol-gel process takes place both in ethanol and butanol, while methanol-based solutions remained cloudy. After centrifugation, the solution, supernatant, and precipitate parts are coated onto substrates to form lyotropic liquid crystalline (LLC) mesophases, followed by calcination at different temperatures to obtain mesoporous metal pyrophosphates.

Structural evolution was monitored by small-angle XRD and ATR-FTIR techniques. Aging of the supernatants at room temperature produce semi-solid mesostructures via polymerization between metal species and PPA. Calcination between 300 and 700 ºC yields highly porous $M_2P_2O_7$ materials with BET surface areas of 145, 410, and 83 m^2/g for Co(II), Ni(II) and Mn(II) pyrophosphates, respectively. XRD analysis shows that $Ni_2P_2O_7$ crystallizes at 700ºC, regardless of the solvent, while the $Co_2P_2O_7$ and $Mn_2P_2O_7$ samples crystallize at lower temperatures. Supernatant-derived samples mainly form $M_3(PO_4)_2$, metal oxides, and some

undefined impurities. High crystallization temperatures results in the pores collapse and surface area loss.

Electrodes are fabricated on FTO and graphite rod (GR) substrates; between these two electrodes, the GR coated electrodes have a better electrochemical stability. Electrochemical measurements (cyclic voltammetry (CV), multi-step chronoamperometry (MCA), and multi-step chronopotentiometry (MCP)) were performed in 1 M KOH using a three-electrode system. Post electrochemical analysis reveales that $M_2P_2O_7$ transforms into metal hydroxide in alkaline media. To evaluate the intrinsic activity, CVs were also conducted in a neutralized electrolyte (2.4 M KOH + 0.6 M $H_4P_2O_7$) solution, where the metal hydroxides exhibite superior OER performance. The $Mn_2P_2O_7$ electrodes are unstable due to disproportionation of Mn(VI) to MnO_4^- and MnO_2 during OER. To improve performance, $Mn_{2-x}M_xP_2O_7$ (M=Co(II), Ni(II); x=0.05,0,10, 0,25) binary electrodes are also fabricated, exhibiting higher surface areas and better OER activity. Notably, ethanol- derived MnNi25% (with 25% Ni(II)) and butanol-derived MnCo10% (10% Co(II)) precipitates, calcined at 300ºC, display high surface areas of 202 and 144 m^2/g, respectively. These electrodes display high stability in OER and have overpotentials of 280-300 mV at 1 mA/cm^2 current density.

Keywords: Mesoporous metal pyrophosphates, lyotropic liquid crystalline (LLC) mesophases, molten-salt assisted self-assembly, sol-gel synthesis, metal hydroxides, oxygen evolution reaction (OER)

ÖZET

Mezo-gözenekli $M_2P_2O_7$ (M: Co(II), Ni(II), And Mn(II)) ve $Mn_{2-x}M_xP_2O_7$ (M: Co(II) And Ni(II)) İnce Filmlerinin Sentezinde Çözücünün Rolü ve Oksijen Evrim Reaksiyonu Performansları

Gözde Ceran

Yüksek Lisans, Kimya

Tez Danışmanı: Prof. Ömer Dağ

Eylül, 2025

Mezogözenekli geçiş metali pirofosfatlar ($M_2P_2O_7$), çeşitli yapısal özellikleri ve kataliz, iyon değişimi ile enerji depolama gibi geniş uygulama alanları nedeniyle büyük ilgi görmektedir. Bu çalışmada, yüksek yüzey alanına ve gözenekliliğe sahip $M_2P_2O_7$ malzemelerinin sentezi için yeni bir yöntem sunulmakta; farklı çözücülerin yapısal ve elektrokimyasal özellikler üzerindeki etkisi incelenmektedir. $Co_2P_2O_7$, $Ni_2P_2O_7$, $Mn_2P_2O_7$ ve ikili pirofosfatlar; pirofosforik asit (PPA, $H_4P_2O_7$), tuz $[Mn(H_2O)_4](NO_3)_2$, $[Co(H_2O)_6](NO_3)_2$, ve $[Ni(H_2O)_6](NO_3)_2$), yüzey aktif madde (pluronik P123), ve çözücüler (etanol, bütil alkol, metanol) kullanılarak eriyik tuz yardımlı kendiliğinden oluşma (EYKO) yöntemiyle sentezlenmiştir. Etanol ve bütil alkol sistemlerinde sol-jel oluşumu gözlemlenmiş, metanol çözeltileri ise bulanık kalmıştır. Santrifüjleme sonrası elde edilen çözelti, süpernatant ve çökelti fazları çeşitli yöntemlerle yüzeylere kaplanarak liyotropik sıvı kristal (LSK) arafazları oluşturulmuş, ardından farklı sıcaklıklarda kalsine edilmiştir.

Yapısal gelişim, küçük açılı XRD ve ATR-FTIR teknikleriyle izlenmiştir. Süpernatan fazlarının oda sıcaklığında bekletilmesi, metaller ve PPA arasında gerçekleşen hızlı polimerizasyon sayesinde yarı katı arayapılar oluşmasına neden olmuştur. 300-700 ºC aralığında yapılan kalsinasyon işlemi, sırasıyla Co(II), Ni(II) ve Mn(II) pirofosfatlar için 145,

410, and 83 m^2/g BET yüzey alanına sahip yüksek gözeneklilikte $M_2P_2O_7$ malzemeleri üretmiştir. XRD analizleri, $Ni_2P_2O_7$'nin çözücüden bağımsız olarak 700ºC'de kristallendiğini; $Co_2P_2O_7$ ve $Mn_2P_2O_7$'nin ise daha düşük sıcaklıklarda kristallendiğini göstermiştir. Süpernatan fazlarının kalsinasyonu $M_3(PO_4)_2$, metal oksitler ve tanımlanamayan çeşitli safsızlıklar vermiştir. Yüksek kristallenme sıcaklıkları gözenek yapısının çökmesine ve yüzey alanının düşmesine neden olmuştur.

FTO ve grafit çubuk (GÇ) yüzeylerine kaplanan elektrotlar arasında, GÇ destekli olanlar daha iyi elektrokimyasal stabilite göstermiştir. 1 M KOH ortamında yapılan elektrokimyasal ölçümler (CV, MCA, MCP) sonrası yapılan analizler, $M_2P_2O_7$'nin bazik ortamda ilgili metal hidroksitlere dönüştüğünü ortaya koymuştur. Gerçek katalitik aktivitenin değerlendirilmesi için 2.4 M KOH + 0.6 M $H_4P_2O_7$ içeren nötralize bir elektrolit ortamında da CV testleri yapılmış ve metal hidroksitlerin OER performansının daha üstün olduğu gösterilmiştir. $Mn_2P_2O_7$ elektrotları, MnO_4^- oluşumuna yol açan bozunma nedeniyle kararsız davranmıştır. Bu sorunu aşmak ve performansı artırmak amacıyla $Mn_{2-x}M_xP_2O_7$ (M=Co(II), Ni(II); x=0.05,0,10, 0,25) ikili sistemleri geliştirilmiş; bu sistemler hem yüzey alanı hem de OER aktivitesinde artış sağlamıştır. Özellikle, 300ºC'de kalsine edilen ethanol kaynaklı MnNi25% (Ni(II)'nin 25% olduğu) ve bütanol kaynaklı MnCo10% (Co(II)'nin 10% olduğu) çökeltileri sırasıyla 202 ve 144 m^2/g yüzey alanlarına sahip olmuş, bu elektrotlar yüksek OGR stabilitesi göstermiş ve 0.28-0.30 Mv/dec aşırı potantiyel değerleriyle öne çıkmıştır.

Anahtar Kelimeler: Mezogözenekli metal pirofosfatlar, liyotropik sıvı kristal (LSK) arafazlar, eriyik tuz yardımlı kendiliğinden oluşma yöntemi, sol-jel sentezi, metal hidroksitler, oksijen evrim reaksiyonu (OER)

To my family…

Acknowledgment

First and foremost, I would like to express my gratitude to my advisor, Prof. Ömer Dağ, for his invaluable guidance, inspiring mentorship, and constant support throughout this journey. His profound knowledge, scientific perspective, and patient encouragement have not only shaped the direction of this research but also played a key role in my growth as a researcher. I feel fortunate to have worked under his supervision.

I would also like to thank TÜBİTAK for financial support during my undergraduate and graduate studies, provided under project number 222Z040.

I am sincerely grateful to my thesis committee members: Asst. Prof. Ferdi Karadaş and Assoc. Prof. Emre Büküşoğlu for their insightful feedback and constructive criticism to enhancing the quality of this thesis.

I would like to extend my heartfelt thanks to Işıl Ulu, who was my supervisor during a part of this thesis. She patiently taught me everything I needed to know in the laboratory and supported me with great care and kindness. I am also very thankful to Irmak Karakaya Durukan, who guided me through the electrochemical analyses and was always generous with her time, support, and knowledge.

My sincere thanks also go to my former colleagues; Assel Amirzhanova, Hamid Ali Raza, Najeeb Ullah, Pamir Göksu, and Elifnur Adalı, as well as our current team members Muratcan Ös, Başak Nur Koçak, and İsmail Yılmaz, for their inspiring, supportive and often joyful conversations that created a warm and motivating work environment.

I am deeply thankful to my mother Şahver Ceran, my father Mustafa Ceran, and my sister Cemre Ceran for their endless love, encouragement, and unwavering belief in me. Their constant support has been my greatest source of strength throughout this journey, and I am truly grateful to have them by my side.

Last but certainly not least, I want to thank my dearest and beloved boyfriend, Furkan Cırdı, whose endless encouragement, calming presence and boundless patience and love made a real difference. His support uplifted me during challenging times and inspired me to keep moving forward, and for that, I am forever grateful.

Table of Contents

Chapter 1 1
1. Introduction 1
1.1. Mesoporous Materials 1
1.1.1. Hard-Templating Method 2
1.1.2. Soft-Templating Method 3
1.1.3. Molten Salt Assisted Sef-Assembly (MASA) Method 4
1.1.4. Sol-gel Synthesis 5
1.1.4.1. The Effect of Solvent on Sol-gel Synthesis 7
1.2. Lyotropic Liquid Crystalline Mesophases (LLC) 7
1.3. Transition Metal Pyrophosphates 8
1.4. Metal Hydroxides 9
1.5. Electrochemistry Background 10
1.5.1. Cyclic Voltammetry 10
1.5.2. Chronoamperometry 10
1.5.3. Chronopotentiometry 11
Chapter 2 12
2. Experimental Section 12
2.1. Materials 12
2.2. Preparation of M(II):Acid:P123 Solutions 12
2.3. Preparation of M(II):Acid:P123 Mesophases 14
2.4. Synthesis of Mesoporous Metal Pyrophosphates 15
2.5. Preparation of Electrodes 16
2.6. Instrumentation 17
2.6.1. Polarized Optical Microscope (POM) 17
2.6.2. X-Ray Diffraction (XRD) Patterns 17
2.6.3. Attenuated Total Reflection Fourier-Transform Infrared (ATR-FTIR) Spectroscopy 17
2.6.4. Fourier-Transform Infrared (FTIR) Spectroscopy 17
2.6.5. Scanning Electron Microscope (SEM) 18
2.6.6. Transmittance Electron Microscope (TEM) 18
2.6.7. N_2-Adsorption-Desorption Measurements 18
2.6.8. Electrochemical Characterization 18
Chapter 3 20

3. Results and Discussion 20
3.1. Synthesis and Characterization of Single Metal Pyrophosphates ($M_2P_2O_7$, M: Co(II), Ni(II), and Mn(II)) 20
3.1.1. Preparation and Characterization of Co(II):PPA:P123 Mesophases 20
3.1.1.1. Co(II):PPA:P123 Ethanol System 20
3.1.1.2. Co(II):PPA:P123 Butanol System 26
3.1.1.3. Co(II):PPA:P123 Methanol System 28
3.1.1.4. Solvent Comparison in the Cobalt System 29
3.1.2. Preparation and Characterization of Ni(II):PPA:P123 Mesophases 31
3.1.2.1. Ni(II):PPA:P123 Ethanol System 31
3.1.2.2. Ni(II):PPA:P123 Butanol System 33
3.1.2.3. Ni(II):PPA:P123 Methanol System 36
3.1.2.4. Solvent Comparison in the Nickel System 37
3.1.3. Preparation and Characterization of Mn(II):PPA:P123 Mesophases 38
3.1.3.1. Mn(II):PPA:P123 Ethanol System 38
3.1.3.2. Mn(II):PPA:P123 Butanol System 39
3.1.3.3. Mn(II):PPA:P123 Methanol System 41
3.1.3.4. Solvent Comparison in the Manganese System 42
3.1.4. Synthesis and Characterization of Mesoporous $Co_2P_2O_7$ 43
3.1.4.1. Ethanol System 43
3.1.4.2. Butanol System 48
3.1.4.3. Methanol System 51
3.1.4.4. Solvent Comparison of Mesoporous $Co_2P_2O_7$ 54
3.1.4.5. Electrochemical Characterization of Mesoporous $Co_2P_2O_7$ and Its Transformation to β-$Co(OH)_2$ 55
3.1.5. Synthesis and Characterization of Mesoporous $Ni_2P_2O_7$ 62
3.1.5.1. Mesoporous $Ni_2P_2O_7$ from Ethanol System 62
3.1.5.2. Mesoporous $Ni_2P_2O_7$ from Butanol System 66
3.1.5.3. Mesoporous $Ni_2P_2O_7$ from Methanol System 73
3.1.5.4. Solvent Comparison of Mesoporous $Ni_2P_2O_7$ 76
3.1.5.5. Electrochemical Characterization of Mesoporous $Ni_2P_2O_7$ and Its Transformation to β-$Ni(OH)_2$ 77
3.1.6. Synthesis and Characterization of Mesoporous $Mn_2P_2O_7$ 85
3.1.6.1. Mesoporous $Mn_2P_2O_7$ from Ethanol System 85
3.1.6.2. Mesoporous $Mn_2P_2O_7$ from Butanol System 88
3.1.6.3. Mesoporous $Mn_2P_2O_7$ from Methanol System 89
3.1.6.4. Solvent Comparison of Mesoporous $Mn_2P_2O_7$ 91
3.1.6.5. Electrochemical Characterization of Mesoporous $Mn_2P_2O_7$ and Its Transformation to β-$Mn(OH)_2$ 92
3.2. Synthesis and Characterization of Binary Metal Pyrophosphates ($M_{2-x}M'_xP_2O_7$, M= Mn, and M'= Ni(II) and Co(II)) 96
3.2.1. Ethanol Systems 97

3.2.1.1. Mesophases of the MnNi5-10-25% from Ethanol Systems 97
3.2.1.2. Mesoporous $Mn_{2-x}Ni_xP_2O_7$ from Ethanol MnNi5-10-25% Mixtures ... 98
3.2.1.3. Mesophases of the MnCo5-10-25% from Ethanol Systems 103
3.2.1.4. Mesoporous $Mn_{2-x}Co_xP_2O_7$ from Ethanol MnCo5-10-25% Mixtures 103
3.2.2. Butanol Systems 106
3.2.2.1. Mesophases of the MnNi5-10-25% from Butanol Systems 106
3.2.2.2. Mesoporous $Mn_{2-x}Ni_xP_2O_7$ from Butanol MnNi5-10-25% Mixtures . 107
3.2.2.3. Mesophases of the MnCo5-10-25% from Butanol Systems 110
3.2.2.4. Mesoporous $Mn_{2-x}Co_xP_2O_7$ from Butanol MnCo5-10-25% Mixtures 112
3.2.3. Methanol Systems 116
3.2.3.1. Mesophases of the MnNi5-10-25% from Methanol Systems 116
3.2.3.2. Mesoporous $Mn_{2-x}Ni_xP_2O_7$ from Methanol MnNi5-10-25% Mixtures 116
3.2.3.3. Mesophases of the MnCo5-10-25% from Methanol Systems 121
3.2.3.4. Mesoporous $Mn_{2-x}Co_xP_2O_7$ from Methanol MnCo5-10-25% Mixtures 122
3.3. Electrochemical Characterization of Mesoporous Binary Metal Pyrophosphates 123
3.3.1. Ethanol Systems 123
3.3.2. Butanol Systems 130
3.3.3. Methanol Systems 139
Chapter 4 143
4. Conclusion 143
Chapter 5 146
5. Future Recommendations 146
Bibliography 149

List of Figures

Figure 1.1: The schematic representation of hard-templating method. 2

Figure 1.2: The schematic representation of micelle formation. 3

Figure 1.3: The schematic representation of hard-templating method. 3

Figure 2.1: The drop-cast coating method. 15

Figure 2.2: The schematic representation of synthesis of mesoporous metal pyrophosphates. 15

Figure 2.3: Preparation of coated FTO electrodes. 16

Figure 2.4: Preparation of graphite rod (GR) electrodes..... 16

Figure 2.5: Schematic representation of electrochemical setup for the three-electrode system. 19

Figure 3.1: Small-angle XRD patterns of Co(II):Acid:P123 solutions with salt mole ratios of 10-100 in ethanol..... 21

Figure 3.2: Small-angle XRD patterns of Co(II):Acid:P123 solutions with salt mole ratios of 10-100 in ethanol after 1 week. 23

Figure 3.3: Small-angle XRD patterns of Co(II):Acid:P123 supernatant parts with salt mole ratios of 10-100 from ethanol system. 24

Figure 3.4: a), c), d) Time-dependent ATR-FTIR spectra of Co(II):PPA:P123 solution, supernatant, and precipitate parts from ethanol system, and b) pyrophosphate peak intensity to nitrate peak intensity ratio from the solution. 26

Figure 3.5: a) Photograph of the sol-gel formed in butanol system, b) small-angle XRD patterns of Co(II):Acid:P123 solution, supernatant and precipitate parts in butanol system. 27

Figure 3.6: Time-dependent ATR-FTIR spectra of Co(II):PPA:P123 a) solution, b) supernatant, and c) precipitate parts in butanol system..... 27

Figure 3.7: a) Photograph of the Co(II):PPA:P123 methanol solution and small-angle XRD patterns of Co(II):PPA:P123 b) solution, c) supernatant, and d) precipitate parts during methanol evaporation. 28

Figure 3.8: Time-dependent ATR-FTIR spectra of the (a) solution, (b) supernatant, and (c) precipitate parts in methanol system. 29

Figure 3.9: Photographs of the solutions of Co(II):PPA:P123 in a) butanol, b) ethanol, and c) methanol solvents..... 29

Figure 3.10: a) Sol-gel formation in Ni(II):PPA:P123 solution, b) time-dependent small-angle XRD patterns of the Ni(II):PPA:P123 (30-15PPA) ethanol (b) solution, (c) supernatant, and (d) precipitate parts. 32

Figure 3.11: Time-dependent ATR-FTIR spectra of Ni(II):PPA:P123 a) solution, b) supernatant, and c) precipitate parts in ethanol. 33

Figure 3.12: POM images of Ni(II):PPA:P123 (1:30:15) (a) solution, (b) supernatant, and (c) precipitate parts in ethanol after 5 hours aging. 33

Figure 3.13: a) Sol-gel formation in Ni(II):PPA:P123 solution, b) time-dependent small-angle XRD patterns of the Ni(II):Acid:P123 (30-15PPA) butanol solution, supernatant and precipitate parts. 34

Figure 3.14: Time-dependent ATR-FTIR spectra of Ni(II):Acid:P123 a) solution, b) supernatant, c) precipitate parts in butanol system, d) Gas phase FTIR spectra of $Ni_2P_2O_7$ solution at the beginning of the experiment (0 min) and after 1 day. 35

Figure 3.15: POM images of the Ni(II):PPA:P123 (30:15:1) a) solution, b) supernatant, and c) precipitate parts after 1 day aging. 36

Figure 3.16: a) Photograph of the clear 30:15PPA Ni(II) methanol solution and time-dependent small-angle XRD patterns of the b) solution, and c) supernatant parts..... 36

Figure 3.17: Time-dependent ATR-FTIR spectra of the Ni(II):PPA:P123 methanol system a) solution and b) supernatant samples..... 37

Figure 3.18: Photographs of the solutions of Ni(II):PPA:P123 in a) butanol, b) ethanol, and c) methanol solvents. 37

Figure 3.19: Time-dependent small-angle XRD patterns of the Mn(II):Acid:P123 (30-15PPA) ethanol a) solution, b) supernatant, and c) precipitate parts. 38

Figure 3.20: Time-dependent ATR-FTIR spectra of Mn(II):PPA:P123 (30-15PPA) ethanol a) solution, b) supernatant, and c) precipitate parts. 39

Figure 3.21: Time-dependent small-angle XRD patterns of the Mn(II):PPA:P123 samples in a) solution, b) supernatant, and c) precipitate parts. 40

Figure 3.22: Time-dependent ATR-FTIR spectra of Mn30-15PPA butanol a) solution, b) supernatant, and c) precipitate parts. 40

Figure 3.23: (a) Photograph of the methanol solution of Mn30-15PPA and the time-dependent small-angle XRD patterns of (b) solution, (c) supernatant, and (d) precipitate parts. 41

Figure 3.24: Time-dependent ATR-FTIR spectra of methanol a) solution, b) supernatant, and c) precipitate parts. 42

Figure 3.25: Photographs of the solutions of Mn(II):PPA:P123 in a) butanol, b) ethanol, and c) methanol solvents. 42

Figure 3.26: Photographs of the mesoporous $Co_2P_2O_7$ samples, obtained from Co30-15PPA ethanol solution, calcined at different temperatures..... 44

Figure 3.27: a) ATR-FTIR spectra and b) XRD patterns of the $Co_2P_2O_7$ samples, obtained from ethanol solution and calcined at indicated temperatures. 44

Figure 3.28: a) ATR-FTIR spectra and high angle XRD patterns of the b) $Co_3(PO_4)_2$ powders at different calcination temperatures, and c) $Co_3(PO_4)_2$ powder calcined at 600ºC together with reference $Co_3(PO_4)_2$ (red, ICDD – 00-013-0503). 45

Figure 3.29: a) SEM, b), and c) TEM images of the powder, obtained from supernatant part of ethanol solution, calcined at 500ºC. 45

Figure 3.30: a) ATR-FTIR spectra and b) high angle XRD patterns of the mesoporous $Co_2P_2O_7$ powders at different calcination temperatures with reference $Co_2P_2O_7$ (pink, ICDD – 00-013-0503)..... 46

Figure 3.31: a) N_2 (77 K) adsorption and desorption isotherms and b) pore-size distribution plots of the $Co_2P_2O_7$ samples, obtained from the precipitate part of the ethanol solution..... 46

Figure 3.32: a) SEM image of the $Co_2P_2O_7$ samples, calcined at a) 300ºC, b) 500ºC, and c) 700ºC. 47

Figure 3.33: The schematic representation of the change in the porosity upon further calcination of the $Co_2P_2O_7$ samples (blue spheres represent $Co_2P_2O_7$ particles/pore-wall and light gray spheres are the pores)..... 47

Figure 3.34: Photographs of the $Co_2P_2O_7$ samples, prepared from Co30-15PPA butanol solution and calcined at different temperatures..... 48

Figure 3.35: a) ATR-FTIR spectra and b) high-angle XRD patterns of the calcined samples of Co30-15PPA butanol solution part. 49

Figure 3.36: SEM images of the samples, prepared from Co30-15PPA butanol supernatant part, calcined at different calcination temperatures; a)300ºC, b)500ºC, and c)700ºC. 49

Figure 3.37: a) ATR-FTIR spectra and b) high-angle XRD patterns of the samples from calcined Co30-15PPA butanol precipitate part. 50

Figure 3.38: a) N_2 (77 K) adsorption-desorption isotherms, and b) BJH pore size distribution plots of the $Co_2P_2O_7$ samples, obtained from the precipitate part of the butanol solution..... 50

Figure 3.39: SEM images of the Co30-15PPA butanol precipitate, calcined at different temperatures; a) 300ºC b) 500ºC, and c) 700ºC. 51

Figure 3.40: Photographs of the $Co_2P_2O_7$ samples, obtained from Co30-15PPA methanol solution, calcined at different temperatures. 52

Figure 3.41: a) ATR-FTIR spectra and b) high-angle XRD patterns of calcined samples of the Co30-15PPA methanol solution..... 52

Figure 3.42: a) ATR-FTIR spectra and b) high-angle XRD patterns of calcined samples of the Co30-15PPA methanol solution..... 53

Figure 3.43: a) ATR-FTIR spectra and b) high-angle XRD patterns of the calcined samples of the Co30-15PPA methanol precipitate..... 53

Figure 3.44: SEM images of the Co30-15PPA methanol precipitate, calcined at a) 300ºC and b) 400ºC..... 54

Figure 3.45: The solutions of $Co_2P_2O_7$ in i) ethanol, ii) butanol, iii) methanol solvents a) poured into pyrex cup, and b) dried at 100ºC for one day..... 55

Figure 3.46: A selected group of CVs from 50 cycles in 1 M KOH electrolyte solution with a scan rate of 50 mV/s of the $Co_2P_2O_7$ (ethanol solution coated) FTO electodes..... 56

Figure 3.47: A selected group of CVs from 50 cycles in 1 M KOH electrolyte solution with a scan rate of 50 mV/s of the $Co_2P_2O_7$ (ethanol solution coated) FTO electrodes. 56

Figure 3.48: A selected group of CVs from 50 cycles in 1 M KOH electrolyte solution with a scan rate of 50 mV/s of the $Co_2P_2O_7$ (ethanol solution supernatant coated) FTO electrodes.. 57

Figure 3.49: a) Three cycle CVs of the electrode coated using Co30-15PPA ethanol supernatant and calcined at 600ºC, b) chronoamperometry experiment and Tafel slope, c) and d) chronopotentiometry experiment, and e) a schematic representation of the electrode during OER. 58

Figure 3.50: A selected group of CVs from 50 cycles in 1 M KOH electrolyte solution with a scan rate of 50 mV/s of the $Co_2P_2O_7$ from a) and b) butanol solution, c) and d) methanol solution and supernatant, coated FTO electrodes (calcined at 300ºC). 58

Figure 3.51: a) The ATR-FTIR spectra and b) high-angle XRD patterns of the $Co_2P_2O_7$ samples put into 1 M KOH solution, c) The unit cell structure of $Co(OH)_2$. 59

Figure 3.52: The SEM images of $Co(OH)_2$ sample obtained from the transformation of $Co_2P_2O_7$ sample aged in 3 M KOH solution. 60

Figure 3.53: a) A selected group of CVs from 100 cycles of the $Co_2P_2O_7$ coated FTO electrode with scan rate of 100 mV/s and in 0.05 M KOH electrolyte solution, b) CVs in the 0-1 V potential window, c) $Co_2P_2O_7$ coated GR electrode 5^{th} cycles of the CVs with consecutive addition of 0.5 ml of 1 M KOH solution, and d) current densities at 1.5 V at 5^{th} CVs each step as a function of volume of 1 M KOH added. 61

Figure 3.54: Photographs of the $Ni_2P_2O_7$ samples, obtained from Ni30-15PPA ethanol solution, calcined at different temperatures. 62

Figure 3.55: a) ATR-FTIR spectra and b) high-angle XRD patterns of the calcined samples of the Ni30-15PPA ethanol solution. 63

Figure 3.56: SEM images of Ni30-15PPA ethanol solution calcined at different calcination temperatures; a) 300ºC, b) 400ºC, c) 500ºC, d) 600ºC, and e) 700ºC. 64

Figure 3.57: a) N_2 (77 K) adsorption-desorption isotherm, and b) BJH pore size distribution plot of $Ni_2P_2O_7$ sample, obtained by calcination of the Ni30-15PPA ethanol solution at 300ºC. 64

Figure 3.58: a) Powder XRD patterns and b) ATR-FTIR spectra of the calcined/annealed ethanol precipitate. 65

Figure 3.59: a) N_2 (77 K) adsorption-desorption isotherms and b) BJH pore size dsitribution plots of the precipitate from ethanol system of Ni30-15PPA, calcined at indicated temperatures. 65

Figure 3.60: SEM images of the Ni30-15PPA ethanol precipitate, calcined at different calcination temperatures; a) 300ºC, b) 400ºC, c) 500ºC, d) 600ºC, and e) 700ºC. 66

Figure 3.61: Photographs of the $Ni_2P_2O_7$ samples, obtained from the Ni30-15PPA butanol solution, calcined at different temperatures. 66

Figure 3.62: a) ATR-FTIR spectra and b) high-angle XRD patterns of the Ni30-15PPA butanol solution, calcined at indicated temperatures. 67

Figure 3.63: a) N_2 (77 K) adsorption-desorption isotherms and b) BJH pore size distribution plots of the gel-phase from butanol system of Ni30-15PPA, calcined at indicated temperatures. 68

Figure 3.64: SEM images of the Ni30-15PPA samples, from butanol solution part calcined at a) 300ºC, b) 400ºC, c) 500ºC, d) 600ºC, and e) 700ºC. 69

Figure 3.65: a) N_2 (77 K) adsorption-desorption isotherm, and b) BJH pore size distribution plots of Ni30-15PPA butanol supernatant, calcined at 300ºC and 400ºC samples. 69

Figure 3.66: SEM images of the Ni30-15PPA samples, obtained from butanol supernatant, calcined at a), b) 300ºC and c), d) 400ºC. 70

Figure 3.67: a) ATR-FTIR spectra and b) high-angle XRD patterns of the Ni30-15PPA butanol precipitate, calcined samples. 71

Figure 3.68: a) and b) Normalized ATR-FTIR spectra of the calcined Ni30-15PPA of butanol precipitate and absorbance at 3224 cm^{-1} vs c) calcination temperature and d) BET surface area plots. 71

Figure 3.69: a) N_2 (77 K) adsorption-desorption isotherms and b) BJH pore size distribution plots of the calcined Ni30-15PPA of butanol precipitate. 72

Figure 3.70: SEM images of the Ni30-15PPA samples, obtained from butanol precipitate, calcined at a) 300ºC, b) 400ºC, c) 500ºC, d) 600ºC, and e) 700ºC. 72

Figure 3.71: Photographs of the $Ni_2P_2O_7$ samples, obtained from Ni30-15PPA methanol solution, calcined at different temperatures. 73

Figure 3.72: a) ATR-FTIR spectra and b) high-angle XRD patterns of the Ni30-15PPA methanol solution, calcined at indicated temperatures. 73

Figure 3.73: a) N_2 (77 K) adsorption-desorption isotherms and b) BJH pore size distribution plots of $Ni_2P_2O_7$, obtained from Ni30-15PPA methanol solution and calcined at different temperatures. 74

Figure 3.74: SEM images of the $Ni_2P_2O_7$ powders, prepared from the methanol solution and calcined at a) 300ºC, b) 400ºC, c) 500ºC, d) 600ºC, and e) 700ºC. 74

Figure 3.75: a) Photographs of the Ni30-15PPA methanol solution a) after centrifugation, and b) after 1 day aging, and c) high-angle XRD patterns of the precipitate, calcined at different temperatures. 75

Figure 3.76: a) N_2 (77 K) adsorption-desorption isotherm, and b) BJH pore size distribution plot of $Ni_2P_2O_7$ calcined at different temperatures obtained from Ni30-15PPA in methanol solution precipitate part. 75

Figure 3.77: SEM images of the samples, obtained from the Ni30-15PPA methanol precipitate after calcination at different temperatures; a) 300ºC, b) 400ºC, c) 500ºC, d) 600ºC, and e) 700ºC. 76

Figure 3.78: A selected group of CVs from 50 cycles in 1 M KOH electrolyte solution with a scan rate of 50 mV/s of the FTO $Ni_2P_2O_7$ electrodes coated from ethanol solution and calcined at a) 300, b) 400, c) 500, and d) 600ºC. 78

Figure 3.79: A selected group of CVs from 50 cycles in 1 M KOH electrolyte solution with a scan rate of 50 mV/s of the FTO $Ni_2P_2O_7$ electrodes, coated with butanol solution and calcined at a) 300, b) 400, c) 500, and d) 600ºC..... 78

Figure 3.80: A selected group of CVs from 50 cycles in 1 M KOH electrolyte solution with a scan rate of 50 mV/s of the FTO $Ni_2P_2O_7$ electrodes, coated with methanol solution, and calcined at a) 300, b) 400, c) 500, and d) 600ºC. 79

Figure 3.81: A selected group of CVs from 50 cycles in 1 M KOH electrolyte solution with a scan rate of 50 mV/s of the GR $Ni_2P_2O_7$ electrodes, coated from ethanol and calcined at a) 300, b) 400, c) 500, and d) 600ºC. 80

Figure 3.82: A selected group of CVs from 50 cycles in 1 M KOH electrolyte solution with a scan rate of 50 mV/s of the GR $Ni_2P_2O_7$ electrodes, coated with butanol solution and calcined at a) 300, b) 400, c) 500, and d) 600ºC..... 80

Figure 3.83: A selected group of CVs from 50 cycles in 1 M KOH electrolyte solution with a scan rate of 50 mV/s of the GR $Ni_2P_2O_7$ electrodes, coated from methanol and calcined at a) 300, b) 400, c) 500, and d) 600ºC..... 81

Figure 3.84: a) The chronoamperometry plot, indicating 44 mV/dec Tafel slope and b) chronopotentiometry plot of GR-$Ni_2P_2O_7$ electrode, prepared frombutanol and calcined at 300ºC. 81

Figure 3.85: a) The ATR-FTIR spectra and b) high-angle XRD patterns of the $Ni_2P_2O_7$ samples, kept in 1 M KOH solution for various durations, c)-d) SEM image and EDX spectrum of the $Ni_2P_2O_7$ samples, kept in 1 M KOH solution for 60 minutes and washed and dried, e)-f) N_2 adsorption-desorption isotherms and pore-size distribution plots of $Ni_2P_2O_7$ and $Ni(OH)_2$ powders. 83

Figure 3.86: a) 5^{th} CVs after addition of 0-15.5 ml of 1M KOH to neuralized (2.4M KOH + 0.6M $H_4P_2O_7$ solution) electrolite solution and b) plot of current density versus added KOH at 1.5 V. 84

Figure 3.87: The schematic representation of the surface of the electrode (Region I) 0-3.5 ml, (Region II) 4-7.5 ml, and (Region III) 8-15.5 ml addition of 1 M KOH to a neuralized (2.4 M KOH + 0.6 M $H_4P_2O_7$) solution. 85

Figure 3.88: Photographs of the $Mn_2P_2O_7$ samples, obtained from the Mn30-15PPA ethanol solution, calcined at different temperatures. 85

Figure 3.89: a) ATR-FTIR spectra and b) high-angle XRD patterns of the Mn30-15PPA ethanol solution after calcination. 86

Figure 3.90: a) ATR-FTIR spectra and b) high-angle XRD patterns of the calcined Mn30-15PPA ethanol precipitates. 86

Figure 3.91: a) N_2 (77 K) adsorption-desorption isotherm and b) BJH pore size distribution plot of the calcined (at 300ºC) Mn30-15PPA ethanol precipitate. 87

Figure 3.92: SEM images of the Mn30-15PPA of ethanol precipitate after calcination at a) 300ºC and b) 400ºC. 87

Figure 3.93: Photographs of the $Mn_2P_2O_7$ powders, obtained from the Mn30-15PPA butanol solution after calcination at indicated temperatures. 88

Figure 3.94: a) ATR-FTIR spectra and b) high-angle XRD patterns of the calcined Mn30-15PPA butanol solution. 88

Figure 3.95: a) ATR-FTIR spectra and b) high-angle XRD patterns of Mn30-15PPA butanol precipitate part calcined samples, c) N_2 (77 K) adsorption-desorption isotherm, and d) pore-size distribution plot of $Mn_2P_2O_7$ calcined at 300ºC obtained from Mn30-15PPA butanol precipitate part. 89

Figure 3.96: Photographs of the $Mn_2P_2O_7$ samples, obtained from the calcined Mn30-15PPA methanol solution. 90

Figure 3.97: a) ATR-FTIR spectra and b) high-angle XRD patterns of the calcined Mn30-15PPA methanol solution. 90

Figure 3.98: a) ATR-FTIR spectra and b) high-angle XRD patterns of the samples from calcined Mn30-15PPA methanol precipitate. 90

Figure 3.99: a) N_2 (77 K) adsorption-desorption isotherm, and b) BJH pore size distribution plot of the calcined Mn30-15PPA methanol solution (calcined at 300ºC) powder. 91

Figure 3.100: The solutions of $Mn_2P_2O_7$ in i) ethanol, ii) butanol, iii) methanol a) poured into pyrex cup, and b) dried at 100ºC for one day, c) the pore-size distributions of the Mn30-15PPA precipitate, calcined at 300ºC. 91

Figure 3.101: A selected group of CVs from 50 cycles in 1 M KOH electrolyte solution with a scan rate of 50 mV/s of the FTO $Mn_2P_2O_7$ electrodes, coated with ethanol solution and calcined at a) 300, b) 400, c) 500, and d) 600ºC. 93

Figure 3.102: : A selected group of CVs from 50 cycles in 1 M KOH electrolyte solution with a scan rate of 50 mV/s of the FTO $Mn_2P_2O_7$ electrodes, coated from butanol and calcined at a) 300, b) 400, c) 500, and d) 600ºC. 93

Figure 3.103: A selected group of CVs from 50 cycles in 1 M KOH electrolyte solution with a scan rate of 50 mV/s of the FTO $Mn_2P_2O_7$ electrodes, coated from methanol and calcined at a) 300, b) 400, c) 500, and d) 600ºC. 94

Figure 3.104: a) The ATR-FTIR spectra and b) high-angle XRD patterns of the $Mn_2P_2O_7$ samples, kept in 1 M KOH solution for durations, given in the spectra and patterns. 95

Figure 3.105: a) $Mn_2P_2O_7$ coated GR electrode, 5^{th} CVs with consecutive addition of 0.5 ml of 1 M KOH solution, b) same CVs, zoomed in, and c) current densities at 1.5 V at 5^{th} CVs at each step as a function of volume of 1 M KOH added. 96

Figure 3.106: Photographs of the a) MnNi5%, b) MnNi10%, and c) MnNi25% ethanol mixtures. 97

Figure 3.107: Small-angle XRD patterns of the (left to right) MnNi5% ethanol solution, supernatant, and precipitate. 97

Figure 3.108: Small-angle XRD patterns of the (left to right) MnNi10% ethanol solution, supernatant, and precipitate. 98

Figure 3.109: Small-angle XRD patterns of the MnNi25% ethanol solution and supernatant parts. 98

Figure 3.110: a), c), and d) ATR-FTIR spectra and b), d), and f) high-angle XRD patterns of the calcined MnNi5%, MnNi10%, and MnNi25% ethanol solutions. 99

Figure 3.111: SEM images of the MnNi25% ethanol solution, calcined at a) 300, b) 400, c) 500, d) 600, and e) 700ºC. 100

Figure 3.112: a), c), and d) ATR-FTIR spectra and b),d, and f) high-angle XRD patterns of calcined samples of the MnNi5%, MnNi10%, and MnNi25% ethanol precipitates. 100

Figure 3.113: a) N_2 (77 K) adsorption-desorption isotherms, and b) BJH pore size distribution plots of the calcined MnNi5%, MnNi10%, MnNi25%, and pure $Mn_2P_2O_7$ samples, from ethanol precipitate, calcined at 300ºC. 101

Figure 3.114: SEM images of the MnNi5% ethanol precipitate, calcined at a) 300, b) 400, c) 500, d) 600, and e) 700ºC. 102

Figure 3.115: SEM images of the MnNi10% precipitate (from ethanol solvent), calcined at a) 300, b) 400, c) 500, d) 600, and e) 700ºC. 102

Figure 3.116: SEM images of the calcined MnNi25% precipitate (from ethanol solvent) after calcination at a) 300, b) 400, and c) 500ºC. 103

Figure 3.117: Photographs of the a) MnCo5%, b) MnCo10%, and c) MnCo25% ethanol mixtures. 103

Figure 3.118: a), c), and d) ATR-FTIR spectra and b), d), and f) high-angle XRD patterns of the calcined MnCo5%, MnCo10%, and MnCo25% ethanol solutions. 104

Figure 3.119: a) N_2 (77 K) adsorption-desorption isotherms, and b) BJH pore size distribution plot of the MnCo25% from ethanol solution, calcined at 300ºC. 105

Figure 3.120: a), b), and d)) high-angle XRD patterns of the MnCo5%, MnCo10%, and MnCo25% samples and c) ATR-FTIR spectra of the MnCo25% samples, obtained from ethanol solution and calcined at various temperatures. 105

Figure 3.121: SEM images of the calcined MnCo25% precipitate (from ethanol solvent) after calcination at a) 300, b) 400, c) 500, d) 600, and e) 700ºC. 106

Figure 3.122: Photographs of the a) MnNi5%, b) MnNi10%, and c) MnNi25% butanol mixtures. 106

Figure 3.123: Small-angle XRD patterns of the (left to right) MnNi5% butanol solution, supernatant and precipitate parts. 107

Figure 3.124: Small-angle XRD patterns of the MnNi10% butanol solution and supernatant parts. 107

Figure 3.125: Small-angle XRD patterns of the MnNi25% butanol solution and supernatant parts. 107

Figure 3.126: a), c), and d) ATR-FTIR spectra and b), d), and f) high-angle XRD patterns of the calcined MnNi5%, MnNi10%, and MnNi25% butanol solutions. 108

Figure 3.127: a), c), and d) ATR-FTIR spectra and b),d, and f) high-angle XRD patterns of the calcined MnNi5%, MnNi10%, and MnNi25% butanol precipitate. 109

Figure 3.128: SEM images of the MnNi5% precipitate (from butanol) after calcination at a) 300, b) 400, c) 500, d) 600, and e) 700ºC. 110

Figure 3.129: SEM images of the MnNi10% precipitate (from butanol) after calcination at a) 300, b) 400, c) 500ºC. 110

Figure 3.130: Photographs of the a) MnCo5%, b) MnCo10%, and c) MnCo25% butanol mixtures. 110

Figure 3.131: Small-angle XRD patterns of the (left to right) MnCo5% solution, supernatant and precipitate parts of butanol system. 111

Figure 3.132: Small-angle XRD patterns of the (left to right) MnCo10% solution, supernatant and precipitate parts of butanol system. 111

Figure 3.133: Small-angle XRD patterns of the (left to right) MnCo25% solution, supernatant and precipitate parts of butanol system. 111

Figure 3.134: a), c), and d) ATR-FTIR spectra and b), d), and f) high-angle XRD patterns of the calcined MnCo5%, MnCo10%, and MnCo25% samples from butanol solutions. 112

Figure 3.135: SEM images of the MnCo5% from butanol solution, calcined at a) 300, b) 400, c) 600, and d) 700ºC. 113

Figure 3.136: SEM images of the MnCo25% from butanol solution, calcined at a) 300, b) 400, c) 500, d) 600 and e) 700ºC. 113

Figure 3.137: a), c), and d) ATR-FTIR spectra and b),d, and f) high-angle XRD patterns of the calcined MnCo5%, MnCo10%, and MnCo25% samples, from butanol precipitate. 114

Figure 3.138: a) N_2 (77 K) adsorption-desorption isotherms, and b) BJH pore size distribution plot of MnCo5%, MnCo10%, and pure $Mn_2P_2O_7$ butanol precipitate, calcined at 300ºC. 115

Figure 3.139: SEM images of the MnCo10% butanol precipitate, calcined at a) 300, b) 400, c) 500, d) 600, and e) 700ºC. 115

Figure 3.140: Photographs of the a) MnNi5%, b) MnNi10%, and c) MnNi25% mixtures in methanol. 116

Figure 3.141: Small-angle XRD patterns of the a) MnNi10% and b) MnNi25% butanol supernatants. 116

Figure 3.142: a), c), and d) ATR-FTIR spectra and b),d, and f) high-angle XRD patterns of the MnNi5%, MnNi10%, and MnNi25% methanol solution calcined samples. 117

Figure 3.143: a) (77 K) N_2 adsorption-desorption isotherms, and b) BJH pore size distribution plots of the MnNi10%, MnNi25% methanol solution, calcined at 300ºC. 118

Figure 3.144: SEM images of the MnNi5% methanol solution, calcined at a) 300, b) 400, c) 500, d) 600, and e) 700ºC. 118

Figure 3.145: a), c), and d) ATR-FTIR spectra and b),d, and f) high-angle XRD patterns of the MnNi5%, MnNi10%, and MnNi25% methanol precipitate, calcined samples. 119

Figure 3.146: SEM images of the MnNi5% precipitate (from methanol solvent), calcined at a) 400, b) 500, c) 600, and d) 700ºC..... 120

Figure 3.147: SEM images of the MnNi10% % precipitate (from methanol solvent), calcined at a) 300, b) 500, and c) 700ºC..... 120

Figure 3.148: SEM images of the MnNi25% % precipitate (from methanol solvent), calcined at a) 300, b) 500, and c) 700ºC..... 120

Figure 3.149: Photographs of the a) MnCo5%, b) MnCo10%, and c) MnCo25% mixtures in methanol..... 121

Figure 3.150: a) ATR-FTIR spectra and b) high-angle XRD patterns of the MnCo25% from methanol solution, calcined samples..... 121

Figure 3.151: a) and c) ATR-FTIR spectra, and b) and d) high-angle XRD patterns of MnCo5% and MnCo10% methanol precipitate, calcined samples..... 122

Figure 3.152: SEM images of the MnCo10% precipitate (from methanol solvent), calcined at a) 300, b) 400, c) 500, d) 600, and e) 700ºC. 123

Figure 3.153: SEM images of the MnCo10% methanol precipitate, calcined at a) 300, b) 400, c) 500, d) 600, and e) 700ºC..... 123

Figure 3.154: a),b),c) 50 CV cycles and d), e), f) multistep chronoamperometry plots with Tafel slopes of the MnNi5%-300ºC, MnNi10%-300ºC, and MnNi25%-300ºC coated GR electrodes. 124

Figure 3.155: Multi-step chronopotentiometry plots of the MnNi5%-300ºC, MnNi10%-300ºC, and MnNi25%-300ºC electrodes, from ethanol system. 125

Figure 3.156: A selected group of CVs from 50 cycles in 1 M KOH electrolyte solution with a scan rate of 50 mV/s of the MnCo5% electrode, calcined at different temperatures..... 126

Figure 3.157: a) Multistep chronoamperometry plots with their Tafel slopes and b) Multi-step chronopotentiometry plots of the MnCo5%-300ºC, MnCo5%-400ºC, MnCo5%-500ºC, and MnCo5%-600ºC electrodes, from ethanol system. 126

Figure 3.158: A selected group of CVs from 50 cycles in 1 M KOH electrolyte solution with a scan rate of 50 mV/s of the MnCo10% electrode, calcined at different temperatures..... 127

Figure 3.159: a) Multi-step chronoamperometry plots with Tafel slopes, b) multi-step chronopotentiometry plots of the MnCo10%-300ºC, MnCo10%-400ºC, MnCo10%-500ºC, and MnCo10%-600ºC electrodes, from ethanol system. 128

Figure 3.160: A selected group of CVs from 50 cycles in 1 M KOH electrolyte solution with a scan rate of 50 mV/s of the MnCo25%, calcined at different temperatures. 128

Figure 3.161: a) Multistep chronoamperometry plots with Tafel slopes and b) multi-step chronopotentiometry plots of the MnCo25%-300ºC, MnCo25%-400ºC, MnCo25%-500ºC, and MnCo25%-600ºC electrodes, from ethanol system. 129

Figure 3.162: Multi-step chronopotentiometry plots of the MnCoX% and MnNiX% electrodes with the least overpotentials in ethanol system. 130

Figure 3.163: A selected group of CVs from 50 cycles in 1 M KOH electrolyte solution with a scan rate of 50 mV/s of the MnNi5% electrodes, calcined at different temperatures. 130

Figure 3.164: a) Multistep chronoamperometry plots with Tafel slopes and b) multi-step chronopotentiometry plots of the MnNi5%-300ºC, MnNi5%-400ºC, MnNi5%-500ºC, and MnNi5%-600ºC electrodes in butanol system. 131

Figure 3.165: A selected group of CVs from 50 cycles in 1 M KOH electrolyte solution with a scan rate of 50 mV/s of the MnNi10% electrodes, calcined at different temperatures. 131

Figure 3.166: a) Multistep chronoamperometry plots with Tafel slopes and b) Multi-step chronopotentiometry plots of the MnNi10%-300ºC, MnNi10%-400ºC, MnNi10%-500ºC, and MnNi10%-600ºC electrodes, from butanol system. 132

Figure 3.167: A selected group of CVs from 50 cycles in 1 M KOH electrolyte solution with a scan rate of 50 mV/s of the MnNi25% electrodes, calcined at different temperatures. 133

Figure 3.168: a) Multistep chronoamperometry plots with Tafel slopes and b) Multi-step chronopotentiometry plots of the MnNi25%-300ºC, MnNi25%-400ºC, MnNi25%-500ºC, and MnNi25%-600ºC electrodes, from butanol system. 133

Figure 3.169: A selected group of CVs from 50 cycles in 1 M KOH electrolyte solution with a scan rate of 50 mV/s of the MnCo5% electrodes, calcined at different temperatures. 134

Figure 3.170: a) Multistep chronoamperometry plots with Tafel slopes and b) multi-step chronopotentiometry plots of the MnCo5%-300ºC, MnCo5%-400ºC, MnCo5%-500ºC, and MnCo5%-600ºC electrodes, from butanol system. 135

Figure 3.171: A selected group of CVs from 50 cycles in 1 M KOH electrolyte solution with a scan rate of 50 mV/s of the MnCo10% electrodes, calcined at different temperatures. 135

Figure 3.172: a) Multistep chronoamperometry plots with Tafel slopes and b) multi-step chronopotentiometry plots of MnCo10%-300ºC, MnCo10%-400ºC, MnCo10%-500ºC, and MnCo10%-600ºC electrodes in butanol system. 136

Figure 3.173: A selected group of CVs from 50 cycles in 1 M KOH electrolyte solution with a scan rate of 50 mV/s of the MnCo25% electrodes, calcined at different temperatures. 137

Figure 3.174: a) Multistep chronoamperometry plot with Tafel slopes and b) multi-step chronopotentiometry plots of MnCo10%-300ºC, MnCo10%-400ºC, MnCo10%-500ºC, and MnCo10%-600ºC electrodes in butanol system. 138

Figure 3.175: Multi-step chronopotentiometry plots of the MnCoX% and MnNiX% electrodes with the least overpotentials from the butanol system. 138

Figure 3.176: a),b),c) A selected group of CVs from 50 cycles in 1 M KOH electrolyte solution with a scan rate of 50 mV/s and d), e), f) multi-step chronoamperometry plots with Tafel slopes of the MnNi5%-300ºC, MnNi10%-300ºC, and MnNi25%-300ºC GR coated electrodes. 139

Figure 3.177: Multi-step chronopotentiometry plots of the MnNi5%-300ºC, MnNi10%-300ºC, and MnNi25%-300ºC electrodes from methanol system. 140

Figure 3.178: a),b),c) A selected group of CVs from 50 cycles in 1 M KOH electrolyte solution with a scan rate of 50 mV/s and d), e), f) multi-step chronoamperometry plots with Tafel slopes of the MnCo5%-300ºC, MnCo10%-300ºC, and MnCo25%-300ºC coated GR electrodes. .. 140

Figure 3.179: Multi-step chronopotentiometry plots of the MnCo5%-300ºC, MnCo10%-300ºC, and MnCo25%-300ºC electrodes. 141

Figure 3.180: Multi-step chronopotentiometry plots of the MnCoX% and MnNiX% electrodes with the least overpotentials, from the methanol system. 141

Figure 3.181: Multi-step chronopotentiometry plots of the electrodes with the least overpotentials from the ethanol, butanol, and methanol systems. 142

Figure 5.1: a) N_2 (77 K) adsorption and desorption isotherms and b) BJH pore-size distribution plots of the $Ni_2P_2O_7$ samples, obtained from three different alcohols. 147

Figure 5.2: High-angle XRD patterns of a) MnNi33%, b) MnNi50% ethanol solution calcined samples and c) N_2 (77 K) adsorption and desorption isotherms and b) BJH pore-size distribution plots of the MnNi33% and MnNi50% ethanol solution 300ºC calcined samples..... 148

List of Tables

Table 2.1: Amounts of ingredients used for given molar ratios of the $Ni_2P_2O_7$, $Co_2P_2O_7$, and $Mn_2P_2O_7$ solutions. 13

Table 3.1: The BET surface area, BJH pore width, and pore volume of the $Co_2P_2O_7$ samples, obtained from the precipitate part of the $Co_2P_2O_7$ ethanol solution. 47

Table 3.2: The BET surface area, BJH pore width, and pore volume values of the $Co_2P_2O_7$ calcined samples, obtained from the Co30-15PPA butanol precipitate. 51

Table 3.3: The BET surface area, BJH pore width, and pore volume values of the calcined $Co_2P_2O_7$ samples, obtained from the Co30-15PPA methanol precipitate. 54

Table 3.4: The BET surface area, BJH pore width, and pore volume values of the calcined $Ni_2P_2O_7$ samples, obtained from the Ni30-15PPA ethanol precipitate. 66

Table 3.5: The BET surface area, BJH pore width, and pore volume values of the calcined $Ni_2P_2O_7$ samples obtained from Ni30-15PPA butanol solution. 68

Table 3.6: The BET surface area, BJH pore width, and pore volume values of the $Ni_2P_2O_7$ samples obtained from Ni30-15PPA butanol supernatant calcined at 300ºC and 400ºC..... 70

Table 3.7: The BET surface area, BJH pore width, and pore volume values of the calcined $Ni_2P_2O_7$ samples, obtained from Ni30-15PPA butanol precipitate. 72

Table 3.8: The BET surface area, BJH pore width, and pore volume values of the calcined $Ni_2P_2O_7$ samples, obtained from Ni30-15PPA methanol supernatant. 74

Table 3.9: The BET surface area, BJH pore width, and pore volume values of the calcined $Ni_2P_2O_7$ samples, obtained from Ni30-15PPA methanol precipitate. 76

Table 3.10: The BET surface area, BJH pore width and pore volume values of the MnNi5%, MnNi10%, MnNi25%, and pure $Mn_2P_2O_7$ ethanol precipitates, calcined at 300ºC. 102

Table 3.11: The BET surface area, BJH pore width and pore volume values of MnCo5%, MnCo10%, and pure $Mn_2P_2O_7$ butanol precipitates, calcined at 300ºC. 115

Table 3.12: The BET surface area, BJH pore width and pore volume values of the MnCo5%, MnCo10%, and pure $Mn_2P_2O_7$ butanol precipitates, calcined at 300ºC. 118

List of Abbreviations

IUPAC: International Union of Pure and Applied Chemistry

LC: Liquid Crystal

LLC: Lyotropic Liquid Crystal

CMC: Critical Micelle Concentration

EISA: Evaporation Induced Self-Assembly

MASA: Molten Salt-Assisted Self-Assembly

MPP: Metal Pyrophosphates

PPA: Pyrophosphoric Acid

XRD: X-Ray Diffraction

POM: Polarized Optical Microscopy

SEM: Scanning Electron Microscopy

TEM: Transmission Electron Microscopy

EDX: Energy Dispersive X-Ray Spectroscopy

ATR-FTIR: Attenuated Total Reflection Fourier-Transform Infrared

BET: Brauner, Emmett, and Teller

BJH: Barrett, Joyner, and Halenda

RT: Room Temperature

ICDD: International Centre for Diffraction Data

OER: Oxygen Evolution Reaction

FTO: Fluorine doped Tin Oxide

GR: Graphite Rod

CV: Cyclic Voltammetry

Chapter 1

1. Introduction

1.1. Mesoporous Materials

The International Union of Pure and Applied Chemistry (IUPAC) classifies porous materials into three categories: microporous (pores with less than 2 nm in diameter), mesoporous (pores between 2 and 50 nm), and macroporous (pores greater than 50 nm) [1]. Over the past few decades, nanoscale porous materials have attracted considerable attention due to their extensive surface area, open structure, narrow pore-size distribution, high porosity and other advantageous properties [2]. These materials play a key role in drug delivery systems, energy storage and conversion, and catalysis [3][4][5].

The synthesis and characterization of mesoporous materials began in 1990, when Yanagisawa and his co-workers synthesized alkyltrimethlyammonium-kanemite complexes, which were then calcined to obtain complexes with pores 2-4 nm in diameter and a surface area of 900 m^2/g [6]. They reported that the chain length of the surfactant used is determining the pore size distribution.

Later, significant advances in this field were made by Kresge and his team, who synthesized mesoporous silica using a liquid-crystal templating mechanism. They studied mesoporous silicas and modified layered materials that were amorphous or paracrystalline, exhibiting a very broad pore-size distribution [7]. Altough pore size can be controlled by intercalation of layered

silicates using surfactants, the final product often mimics the layered nature of the precursor [6]. However, Kresge and his team synthesized mesoporous solids by the calcination of alumina silicate gels in the presence of surfactants, resulting in materials with regular arrays of uniform channels. They demostrated that the pore size distribution of mesoporous materials could be precisely controlled [8]. Subsequently, mesoporous silica has been employed as a template to synthesize other mesoporous materials through hard-templating method [9]. Non-siliceous materials have also been produced using the surfactant-templating approach without involving silica, a technique referred to as the soft-templating method.

1.1.1. Hard-Templating Method

Hard-templating method has been widely used for the synthesis of mesoporous materials. In the hard-templating, also known as 'nanocasting', rigid and porous templates, i.e. silica, carbon or assemblies of nanoparticles, are coated with the desired material, the precursor [9][10][11]. After calcination or treatment with acid or base, the template is removed to have the desired mesoporous structure. A schematic representation of the synthesis via the hard templating method is shown in Figure 1.1.

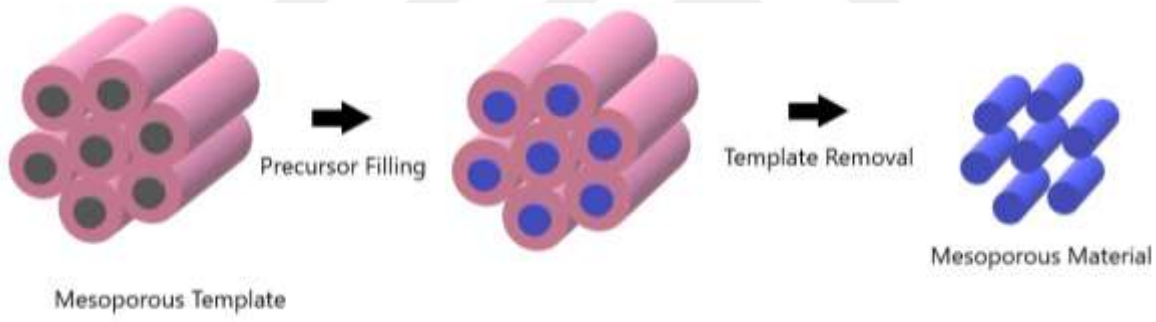


Figure 1.1: The schematic representation of hard-templating method.

Ryoo et al. introduced the hard template synthesis method and, in 1999, reported the synthesis of a mesoporous carbon with an average pore size of 3 nm, using cubic mesoporous silica as a template [12]. Since this breakthrough, the method has been used for the synthesis of a variety of mesoporous materials.

Altough hard templating is a highly effective approach for producing diverse mesoporous structures, it is difficult to apply for the synthesis of thin films or monoliths, which are essential for many practical applications. Furthermore, no side reactions should ocur between the template and the precursor; this requirement limits the applicability of the method to certain material systems [13]. In addition, the removal of the template often leads to the collapse of the pore structure, negatively impacting the material's performance [16].

1.1.2. Soft-Templating Method

Soft-templating method is extensively used for synthesizing various mesoporous materials, relying on lyotropic liquid crystalline (LLC) phases formed by surfactants. Due to hydrophobic and hydrophilic interactions, surfactant molecules tend to self-assemble into micelles, featuring a hydrophilic shell and a hyrdophobic core, see Figure 1.2. These micelles then organize into LLC structures.

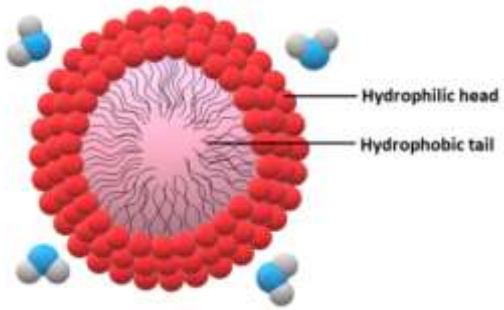


Figure 1.2: The schematic representation of micelle formation.

During this assembly process, a clear solution containing both inorganic precursors and surfactants is first prepared. As the volatile components evaporate, gelation occurs, leading to the formation of a mesophase. Finally, the surfactant is removed, typically through calcination or solvent extraction, resulting in the desired mesoporous structure [14][15]. Figure 1.3 shows a schematic representation of the soft-templating method.

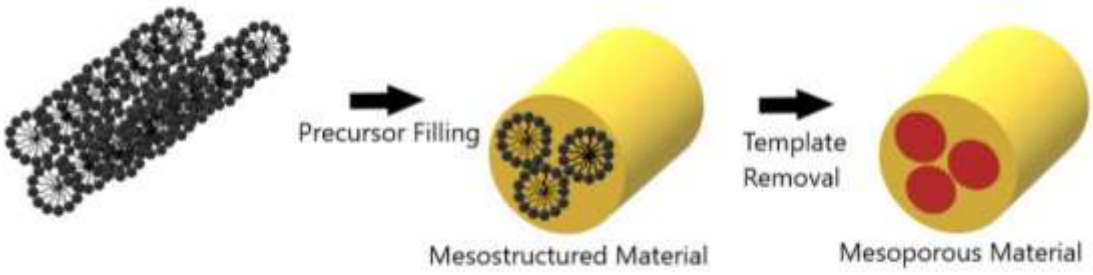


Figure 1.3: The schematic representation of hard-templating method.

Although the soft-templating method enables the synthesis of a wide variety of materials, achieving precise control over morphology and the producing of materials with high surface area is generally more straightforward using the hard-templating method. One of the challenges in soft-templating method is the rapid hydrolysis of the metal precursor during

synthesis, which is hard to control [16][17]. Furthermore, for the successful formation of a stable mesostructure, the precursor must be capable of polymerizing and generating a framework with sufficient mechanical strength to prevent pore collapse during template removal [16].

A widely used soft-templating technique for the preparation of mesoporous materials and thin films is evaporation-induced self assembly (EISA), first reported by by Brinker [18] and Ozin [19]. This technique involves the self-assembly of molecules driven by the evaporation of a volatile solvent, enabling the formation of patterned structures in sub-45-nm range [20]. To avoid exceeding the critical micelle concentration, low concentrations of inorganic precursors and block polymers are dissolved in a volatile solvent, followed by deposition. In the EISA process, surfactant molecules serve as templates and play a crucial role. These surfactants are typically classified as i) ionic surfactants, which contain charged ionic groups, and ii) nonionic surfactants, which have neutral hydrophilic head and hydrophobic tails. This method has been successfully employed to synthesize mesoporous materials such alumina, titania, mixed metal oxides, metal phosphates, and metal pyrophosphates [21].

1.1.3. Molten Salt Assisted Self-Assembly (MASA) Method

In 2011, Dag group introduced a novel synthesis technique, known as molten salt-assisted self-assembly (MASA), for the preparation of various mesoporous materials. In this method, a metal salt, solvent, and surfactant are used, with the metal salt acting as a secondary solvent during the assembly process. Due to the soft confinement effect (SCE), the metal salt does not crystallize, even at low temperatures within the hydrophilic domains of the mesophase. This stability arises from the interaction between the molten salt and the charged hydrophilic-hydrophobic interface of surfactant domains.

During the assembly process, the precursor solution is typically spin-coated or drop-cast coated onto a glass substrate to form a LLC mesophase. The sample is then subjected to high-temperature treatment to remove the surfactants, resulting in the formation of mesoporous thin-film materials.

The MASA method was first applied to the synthesis of Zinc Oxide (ZnO) and Cadmium Oxide (CdO)-coated silica thin films, where it was demonstrated that a significant amount of metal salts could be confined within the surfactant domains and silica walls [22]. Subsequently, the method has been extended to the synthesis of various mesoporous materials, including metal

titanates (Zn_2TiO_4, $CdTiO_3$, $CoTiO_3$, $MnTiO_3$, and $Li_4Ti_5O_{12}$) [23][24][25][26], metal lithiates ($LiCoO_2$, $LiMn_2O_4$, $LiMn_{2-x}O_{4-x}$) [14][22][24], metal cobaltites ($MnCo_2O_4$, $ZnCo_2O_4$, and $NiCo_2O_4$) [25], metal oxides such as NiO [26], and lithium metal phosphates with high surface area and diverse applications [27].

The MASA method differs fundamentally from the EISA approach. While EISA relies on solvent evaporation and forms mesostructured solids rapidly, often limiting its compatibility with metal alkoxides due to premature hydrolysis and condensation, MASA enables the formation of a stable LLC mesophase at higher salt-to-surfactant concentrations. This allows for a more controlled gel aging process prior to thermal treatment, accommodating a broader range of metal precursors, including those unsuitable for EISA. Furthermore, MASA offers tunable control over film thickness through adjustment of the initial solution concentration and is compatible with multiple deposition techniques such as spin-coating, dip-coating, drop-casting, and spray coating.

1.1.4. Sol-gel Synthesis

There are a variety of solid-state methods available for synthesizing target materials; however, these approached often make it difficult to control particle size and morphology [35]. As alternatives to solid-state chemistry, techniques such as coprecipitation, hydrothermal and solvothermal processing and sol-gel chemistry have emerged [36]. Among these, sol-gel chemistry is particularly attractive due to its ability to offer control over particle size and morphology, shorther synthesis times, and lower processing temperatures [35]. Nevertheless, it does not ensure homogeneity throughout the precursor solution. Therefore, controlling phase segregation is essential to achieving uniformity in the final material.

Interest in sol-gel processing of inorganic ceramics and glasses dates back to the mid-1800s, when Ebelman [37][38] and Graham [39] investigated the acid-catalyzed hydrolysis of tetraethyl orthosilicate (TEOS) to form silica gels. They observed that the resulting material was a glass-like form of SiO_2, from which fibers, optical lenses, and composites could be fabricated. However, due to the extremely long drying times, often taking over a year to avoid cracking, the method initially lacked technological relevance [40].

From the late 1800s to the 1920s, gels attracted significant attention due to the discovery of Liesegang Rings, with prominent scientists like Ostwalds [41] and Lord Rayleigh [42] exploring the periodic precipitation and crystal growth phenomena within gels. Although this period yielded extensive descriptive studies, the physico-chemical mechanisms behind these phenomena remained poorly understood.

In the 1950s and 1960s, Roy and colleagues advanced the sol-gel methods to synthesize chemically homogeneous ceramic oxides (i.e. Al, Si, Ti, Zr) that were difficult to produce via traditional techniques [43][44][45]. Around the same time, Iler's work on silica chemistry led to the commercial development of colloidal silica (i.e. Du Pont's Ludox) [46]. Additionally, Stöber *et al.* improved the sol-gel processing by introducing ammonia as a catalyst, enabling better control over particle size and moprholody [47].

Overbeek [48][49] and Sugimoto [50] demonstrated that rapid nucleation followed by controlled particle growth without supersaturation can produce monodispersed colloidal oxide particles. Building on this foundation, Metijevic and his collaborators developed a wide range of colloidal powders with precise size and morphology. These included various oxides, hydroxides, carbonates, sulfides, metals, composites, and coated particles [51]-[54]. The scope of sol-gel processing was later extended to fissile materials enabling the formation of rigid gel spheres of UO_2 and UO_2-PuO_2 through spray techniques [55]. In addition, both glass and polycrystalline ceramic fibers, such as TiO_2-SiO_2, ZrO_2-SiO_2, Al_2O_3, and others, have been successfully fabricated using sol-gel methods [56][57].

Sol-gel monoliths can be synthesized using three main approaches: (i) gelation of colloidal solutions, (ii) hydrolysis and polycondensation of precursors followed by supercritical drying, and (iii) aging and drying under ambient conditions [40]. A sol is defined as a liquid dispersion of colloidal particles sized 1-100 nm, which can form a rigid gel network with submicron pores and long polymer chains [58].

The sol-gel process is governed by several critical parameters, including pH, solvent, temperature, agitation, time, and catalysts. Among these, pH plays a particularly influential role, as it significantly affects the structures and final properties of the material [59]. Solvents assist in maintaining nanoparticles in dispersion and facilitate the polycondensation reactions [60]. Proper agitation is necessary to ensure uniform mixing, disrupt localized gelation domains, and promote homogeneity throughout the system [61]. Gelation time is also essential; if the process is rushed, complete and uniform gel network may not form. Temperature accelerates reaction kinetics and reduces the gelation time, which can otherwise take weeks [62]. Lastly, catalysts, both acidic and basic, also affect the rate of reactions, each of affecting the gelation process differently [63].

Sol-gel derived materials offer several advantages, including high purity, low processing temperatures, and cost-effectiveness compared to other synthesis techniques [58]. This technique facilitates the straightforward formation of metal oxide nanoparticles and enables simpler and more versatile coating processes. Key benefits include low-cost production,

high compositional control, and the ability to create amorphous layers and metal oxide nanoparticles [64].

Altough the sol-gel synthesis has been known and studied for decades, and offers many advantages over the other alternative methods, it is mostly used for the synthesis of metal oxides. In this study, the sol-gel synthesis is employed for the synthesis of mesoporous metal pyrophosphates ($M_2P_2O_7$, M: Co(II), Ni(II), and Mn(II)) and mesoporous binary metal pyrophosphates ($Mn_{2-x}M_xP_2O_7$, M: Co(II) and Ni(II)).

1.1.4.1. The Effect of Solvent on Sol-gel Synthesis

This study focuses on the effect of solvent in sol-gel synthesis, which will be discussed in more detail in this section. Altough parameters like pH, temperature, and catalyst have not yet been systematically studied, literature provides insights into how solvents influence the extent of condensation of the polymeric network.

In 1986, Artaki et al. showed that highly polar protic solvents slow condensation by deactivating nucleophiles and stabilizing reactants, increasing activation energy [90]. Dipolar aprotic solvents slow the reaction less, while non-polar aprotic solvents are most efficient.

In 2012, Shokuhfar et al. investigated the effect of dilution on the film thickness, prosity, refractive index, and surface morphologies of nanostructured silica thin film [91]. They reported that with increasing dilution, the porosity and light transmittance increased.

A very recent study by Mitran et al. in 2023 about the effect of solvents, water, ethanol, methanol, and butanol, on the sol-gel synthesis of mesoporous $CoAl_2O_4$, its structural and catalytic properties in 1,4-butanediol lactonization to γ-butyrolactone [92]. In this study, water and ethanol led to better catalytic performance due to balanced hydrolysis-condensation rates and more controlled Co/Al incorporation, while methanol and butanol caused aluminum enrichment and lower Co^{3+}/Co^{2+} ratios, likely due to differences in solvent polarity, protic character, and metal-solvent interactions. These factors influenced the structural formation, oxygen vacancy concentration, and overall activity of $CoAl_2O_4$.

1.2. Lyotropic Liquid Crystalline Mesophases (LLC)

Liquid crystals (LC) are the fourth phases of matter with properties between solids and liquids. They flow like liquids but possess a degree of molecular ordering characteristic of solids, forming unique mesostructures/mesophases [28]. The liquid crystalline phase was first

discovered in 1888 by Reinitzer [29], and was later described as a thermodynamically stable liquid crystalline state by Lehmann [30].

LC phases have been divided into two subgroups i) thermotropic and ii) lyotropic liquid crystals. Thermotropic liquid-crystalline materials undergo reversible phase transitions at specific and well-defined temperatures. The thermotropic mesophases are divided into two groups based on molecular shape; i) calamitic liquid crystals, composed of rod-shaped molecules, ii) discotic or columnar liquid crystals, made up of disk-shaped molecules [28]. However, lyotropic liquid crystals form in solutions of amphiphilic molecules. Micelles, shown in Figure 1.2, are formed by amphiphilic molecules due to solubility difference between their hydrophobic and hydrophilic parts in a specific solvent. When the micelle concentration or, in this case the surfactant concentration, reaches the critical micelle concentration (CMC), micelles begin to form. At higher concentrations, these micelles self-assemble into lyotropic liquid crystalline (LLC) mesophases such as lamellar, hexagonal, or cubic structures.

The first reported use of LLC mesophases as templates for the synthesis of ordered mesoporous silicates was by Kresge et al. in 1992 [8]. This was followed in 1995 by Attard et al., who utilized non-ionic surfactants ($C_{12}EO_8$ and $C_{16}EO_8$) to fabricate mesoporous silica monoliths and thin films. In 2001, Dag et al. introduced molten salts as a second component in the mesophase and demonstrated liquid crystalline behaviour using a non-ionic surfactant (10-lauryl ether) in combination with transition metal salts such as Co(II), Ni(II), Zn(II), and Cd(II) at various mole ratios [31]. Our reasearch group has also investigated the influence of different anions on LLC phases formed from surfactant-metal salt systems as well as the behaviour of larger surfactants, such as Pluronics [32]-[34].

1.3. Transition Metal Pyrophosphates

Metal pyrophosphates have recently gained attention due to their excellent redox properties, natural abundance, eco-friendliness, low synthesis cost, and suitability for supercapacitor (SC) applications. Their layered morphology, high conductivity, and good reversibility make them ideal for Faradaic reactions [65].

Wei at al. introduced hexagonal Na-doped $Ni_2P_2O_7$ tablets with a high BET surface area of 190.5 m^2/g and 2-4 nm mesopores, enhancing ion/electron accessibility [66]. Sankar et al. developed binder free $Ni_2P_2O_7$ nanorods, which are 60-135 nm in diameter, 22-28 micrometer in length, directly grown on Ni foam, promoting efficient electrolyte diffusion [67]. Zhou et al. synthesized porous $Ni_2P_2O_7$ nanowires with 2-4 nm interlinked mesopores via a solvothermal method [68].

In 2020, Matheswaran et al. synthesized Ni-Co pyrophosphates at varying temperatures, forming nano-grass structures that retained morphology even after 1000 cycles [69]. Zhang et al. created $Co_2P_2O_7$ with rose-like concentric rings by adjusting calcination temperature, indicating high crystallinity and enhanced electrochemical performance [70].

H. Liu et al. developed a unique round, ring-shaped cobalt manganese pyrophosphate $(Co_{0.55}Mn_{0.45})_2P_2O_7$ using a simple one-step microwave method [71]. The material featured a honey-comb like porous structure, offering abundant electroactive sites. It was coated with nitrogen-doped graphene (NG), enhancing its performance. This structure delivered a high specific capcity of 236.21 mAh/g at 1 A/g and maintained 86.7% capacity after 10,000 cycles in a three-electrode setup.

More recently, A. Padhy et al. introduced partially graphitized carbon cobalt pyrophosphate (GC-CPP), which showed enhanced crystallinity, a larger surface area, and more active sites. GC-CPP demonstrated superior oxygen evolution reaction (OER) performance in alkaline media, requiring 165 mV overpotential to reach 10 mA/cm^2 with a low Tafel slope of 41 mV/dec [72]. As a supercapacitor electrode, GC-CPP exhibitied a high specific capacitance of 900 F/g, with an energy density of 31.25 Wh/kg and power density of 21 kW/kg. It also maintained 89% capacitance after 10,000 cycles and 98% coulombic efficiency, indicating excellent stability and reversibility.

R. BoopathiRaja et al. synthesized bare $Mn_2P_2O_7$ and $Mn_2P_2O_7$@PPy composite electrodes using hydrothermal and chemical polymerization methods [73]. The composite showed a nano-flake and sunflower-like heterostructure with a large surface area, 93 m^2/g, and small pore size, 11 nm, enhancing its electrochemical performance. In a three-electrode setup, it delivered a high specific capacitance of 658 F/g at 1 A/g with 99.1% retention after 10,000 cycles.

Most reports suggest that during electrochemical testing, $M_2P_2O_7$ electrodes undergo stepwise oxidation to $M_2P_2O_7(OH)_2$ (M^{3+}) and then to $M_2P_2O_7(O)_2$ (M^{4+}). However, this proposed mechanism is incorrect and misleading, as demonstrated by Ulu et al. [81] , and our findings. In reality, pyrophosphate-based electrodes are highly unstable in alkaline media and readily convert into metal hydroxides. This transformation is often overlooked due to the use of additives in electrode fabrication, which complicates post-electrochemical measurement analysis.

1.4. Metal Hydroxides

Transition metal hydroxides, particularly those of nickel and cobalt, are widely studied as supercapacitor electrodes due to their fast and reversible redox reactions, as well as high

specific capacitance. Their layered structures, especially in the α-phase, offer large interlayer spacing, about 8.0 Å for α-$Ni(OH)_2$ and 4.6 Å for the β-phase, which facilitates ion transport [74][75]. The α-phase includes interlayer water molecules and shows superior electrochemical performance, including promising potential for oxygen evolution reaction, OER [76]. However, it is thermodynamically unstable in alkaline media and tends to irreversibly convert into the more stable β-phase.

To optimize electrochemical performance and structural stability, various synthesis methods such as chemical precipitation, hydrothermal synthesis, and electrodeposition have been used to produce diverse morphologies like nanowires, nanoflakes and flowerlike structures [77]-[79].

1.5. Electrochemistry Background

To analyze an electrode's performance and stability in water splitting, very well-known techniques, cyclic voltammetry (CV), chronoamperometry (CA), Tafel slope analysis, and chronopotentiometry (CP) measurements are performed.

1.5.1. Cyclic Voltammetry

Cyclic voltammetry is a widely used and effective technique for analyzing redox-active species. In this method, the potential is swept linearly between two values, typically from negative to positive, and the resulting current is recorded to produce a voltammogram. A reference electrode, such as silver/silver chloride (Ag/AgCl) is used to maintain stable potential at the working electrode, which is coated with the active material.

As the potential becomes more positive, oxidation occurs, resulting in anodic current; during the reverse sweep, reduction leads to cathodic current. The voltages at which these peaks occur are referred to as anodic and cathodic peak potentials, and they provide insight into the redox behavior and reversibility of the system.

1.5.2. Chronoamperometry

In this technique, the current is measured with respect to time while keeping the potential constant. It is used to analyze the concepts related with diffusion processes and kinetics of chemical and electrochemical reactions. It is used mostly for Tafel slope analysis which provides information about the rate-determining step in the electrochemical process and likely the mechanism [80]. Low Tafel slope indicates less overpotential required for the reaction to occur. The Tafel equation is given as:

$$\eta = a + b\log j$$

In Eqn 1., b is the Tafel slope (mV/dec), a is a constant value, j is current density (mA/cm^2).

1.5.3. Chronopotentiometry

In this technique, the potential is measured with respect to time while keeping the current applied constant. It is an extremely useful technique for the calculation of overpotentials which is the difference between the theoretical OER potential and the actual potential required for the reaction to occur at specific current density. By using the Nernst equation, values of the overpotentials can be calculated at a specific pH value. In this work, electrochemical measurements are carried out in 1 M KOH electrolyte solution, having a pH value of 13.6.

$$2H_2O(l) + O_2(g) + 4H^+ + 4e^- \quad E^0 = 1.229\,V\ vs\ NHE$$

$$E = E^0 - \frac{RT}{nF} log P_{O_2}[H^+]^4$$

$$E = E^0 - \frac{0.0592}{4} log_{10} P_{O_2}[H^+]^4$$

At Ph= 13.6, [H^+]= 10^{-14} M and P_{O_2}= 1 atm, when these values are put into the above given equation, the minimum required voltage for this reaction can be found as 0.40 V. The overpotentials in this work will be calculated by subtracting this value from the measured value.

Chapter 2

2. Experimental Section

2.1. Materials

Pyrophosphoric acid (PPA, ≥94%), manganese(II) nitrate tetrahydrate ($[Mn(H_2O)_4](NO_3)_2$, 97%), cobalt (II) nitrate hexahydrate ($[Co(H_2O)_6](NO_3)_2$, 98%), nickel (II) nitrate hexahydrate ($Ni(H_2O)_6](NO_3)_2$, 99,9%), Poly(ethylene glycol)-block-poly(propylene glycol)-block-poly(ethylene glycol) (PEO-PPO-PEO), Pluronic P-123, (MW~ 5800 g/mol, 99,9%) were purchased from the Sigma-Aldrich.

Absolute ethanol (99.9%), methanol (99.9%), and 1-butanol (≥99.0%) are purchased from ISOLAB.

2.2. Preparation of M(II):Acid:P123 Solutions

Cloudy solutions of $[M(OH_2)_6](NO_3)_2$ salts (where M is Mn(II), Co(II), and Ni(II), acid, pyrophosphoric acid ($H_4P_2O_7$, PPA), and surfactant (P123) were prepared in 10 ml of ethanol, methanol, and butanol solvents. For cobalt system, the mole ratio of the salts/P123 and PPA/P123 are varied from 10 to 100 with an increment of 10, but for the others, 1:30:15 mole ratio was used, see Table 2.1.

Table 2.1: Amounts of ingredients used for given molar ratios of the $Ni_2P_2O_7$, $Co_2P_2O_7$, and $Mn_2P_2O_7$ solutions.

Co(II) solutions;

Mole ratio / Ingredients	**P123**	**$[Co(H_2O)_6](NO_3)_2$**	**$H_4P_2O_7$ (PPA)**	**Solvent**
1:10:5	1.000 g	0.506 g	0.155 g	10 g
1:20:10	1.000 g	1.012 g	0.310 g	10 g
1:30:15	1.000 g	1.518 g	0.465 g	10 g
1:40:20	1.000 g	2.024 g	0.620 g	10 g
1:50:25	1.000 g	2.530 g	0.775 g	10 g
1:60:30	1.000 g	3.036 g	0.929 g	10 g
1:70:35	1.000 g	3.542 g	1.085 g	10 g
1:80:40	1.000 g	4.048 g	1.240 g	10 g
1:90:45	1.000 g	4.554 g	1.393 g	10 g
1:100:50	1.000 g	5.060 g	1.550 g	10 g

Ni(II) solution;

Mole ratio / Ingredients	**P123**	**$[Ni(H_2O)_6](NO_3)_2$**	**$H_4P_2O_7$ (PPA)**	**Solvent**
1:30:15	1.000 g	1.490 g	0.460 g	10 g

Mn(II) solution;

Mole ratio / Ingredients	**P123**	**$[Mn(H_2O)_4](NO_3)_2$**	**$H_4P_2O_7$ (PPA)**	**Solvent**
1:30:15	1.000 g	1.295 g	0.457 g	10 g

Mn(II)/Co(II) solutions;

Metal Compositions/ Ingredients	**P123**	**$[Mn(H_2O)_4](NO_3)_2$**	**$[Co(H_2O)_6](NO_3)_2$**	**$H_4P_2O_7$ (PPA)**	**Solvent**
MnCo5%	1.000 g	1.230 g	0.105 g	0.457 g	10 g
MnCo10%	1.000 g	1.1655 g	0.211 g	0.457 g	10 g
MnCo25%	1.000 g	0.972 g	0.527 g	0.457 g	10 g

Mn(II)/Ni(II) solutions;

Metal Compositions/ Ingredients	**P123**	**$[Mn(H_2O)_4](NO_3)_2$**	**$[Ni(H_2O)_6](NO_3)_2$**	**$H_4P_2O_7$ (PPA)**	**Solvent**
MnNi5%	1.000 g	1.230 g	0.105 g	0.457 g	10 g
MnNi10%	1.000 g	1.1655 g	0.211 g	0.457 g	10 g
MnNi25%	1.000 g	0.972 g	0.527 g	0.457 g	10 g

Half of the liquified surfactant (at 80ºC) and the salt in 5 g of alcohol in a 20 ml vial and the other half of the surfactant is added to the other 20 ml vial, in which pyrophosphoric acid is dissolved. After these ingredients are dissolved, the second vial is poured into the first one very slowly. As most of the solutions are cloudy, by centrifugation process (6000 rpm for 15 minutes), the supernatant and precipitate are separated. And characterizaiton is performed using the solution, supernatant, and precipitate parts.

2.3. Preparation of M(II):Acid:P123 Mesophases

The solution and supernatant parts are coated over micrsocopic slides via drop-cast coating method. A few drops of the solution are placed on a microscope slide, and spread to achieve a homogeneous and thin distribution on the glass slide. Then, it is left in a vertical position until no more liquid drips from it, see Figure 2.1. However, the gel-like solid was spread onto the microscope slide either by squeezing and pulling between two glass slides or by using spatula. These drop-casted slides of the solution, supernatant, and precipitate parts are used for characterization. The slides of supernatant part is also used for calcination process.

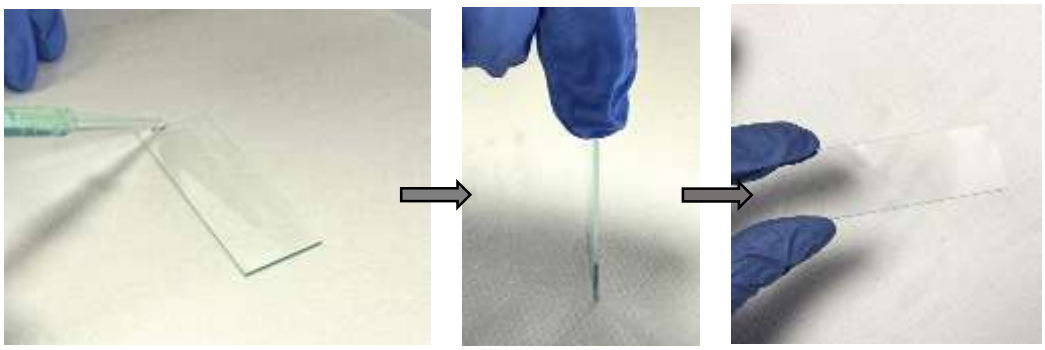


Figure 2.1: The drop-cast coating method.

2.4. Synthesis of Mesoporous Metal Pyrophosphates

For the solution part, it is directly poured onto pyrex petri-dish and put into 100 ºC oven for 1 day to remove the solvent then it is scrapped from the pyrex as a powder and put into combustion bath or ceramic cuvette for calcination at 300, 400, 500, 600, and 700 ºC to obtain mesoporous metal pyrophosphates. For the supernatant part, drop casted slides are directly calcined at 300 ºC in a preheated oven for 1 hour to remove the surfactant and produce metal pyrophosphates and then annealed at higher temperatures as in the solution part. For the precipitate, after the centrifugation, the gel-like solid collected at the bottom of the centrifuge tube is kept in 100 ºC oven for 1 day and it is then collected, ground in a mortar and calcined at 300 ºC in a pre-heated oven for 1 hour and annealed at higher temperatures. Annealing time is the same for solution, supernatant, and precipitate parts 1 hour for each calcination temperature. Figure 2.2 shows a schematic representation of above samples.

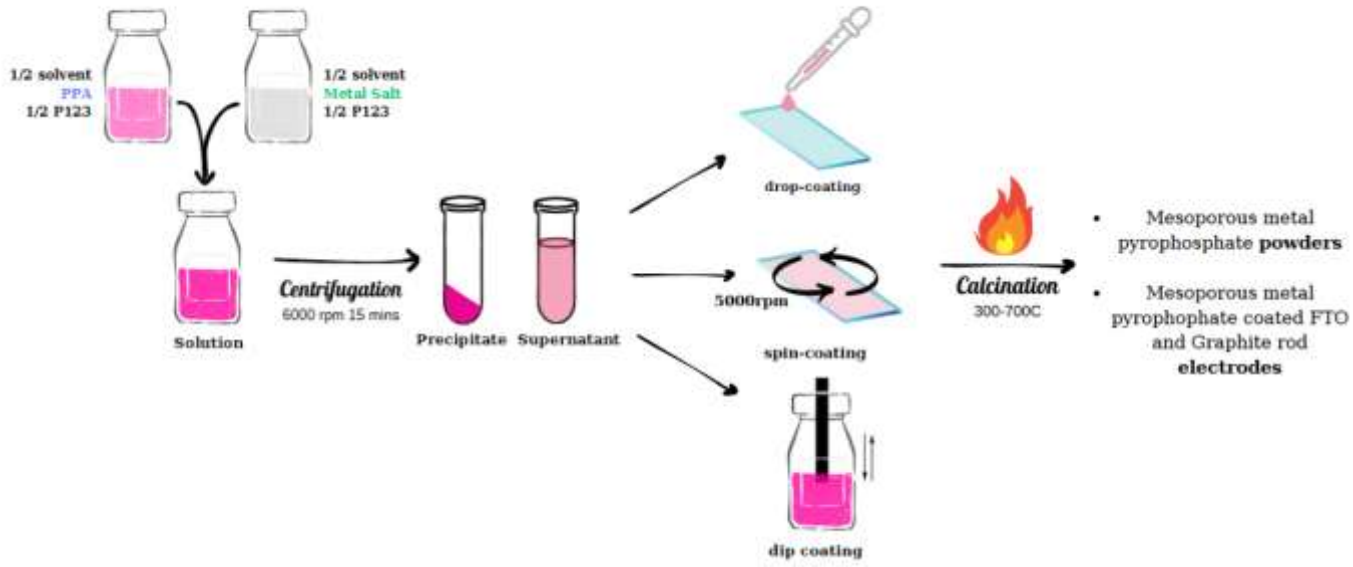


Figure 2.2: The schematic representation of synthesis of mesoporous metal pyrophosphates.

2.5. Preparation of Electrodes

The electrodes for the electrochemical measurements are fabricated by using two different substrates and two different methods: spin coating over fluorine-doped tin oxide (FTO) and dip coating over a pure graphite rod. For the coating of 2x1 cm^2 FTO substrate, after half of the electrode surface, 1 cm^2 is covered by the tape, the rest is spin coated with the solution or supernatant parts usually at 5000 rpm (see Figure 2.3). For the pure graphite rod substrate, 15 mm graphite rods are cut into 3 mm pieces and put into sonicator for almost 1.5 minutes to clean them. Afterwards they are kept in 80 ºC oven for 1 night to get rid of the ethanol. After diluting the solution and supernatant parts, pure graphite rod with 3 mm diameter is dip coated with a pulling speed of 1.45 mm/s to obtain a 1 cm^2 area coated sample (see Figure 2.4). As dip-coating method gives thicker films over the substrate, 5x diluted solutions and supernatant parts are used. Then the electrodes are calcined directly in a preheated oven at different calcination temperatures (300, 400, 500, 600, and 700 º) for 1 hour.

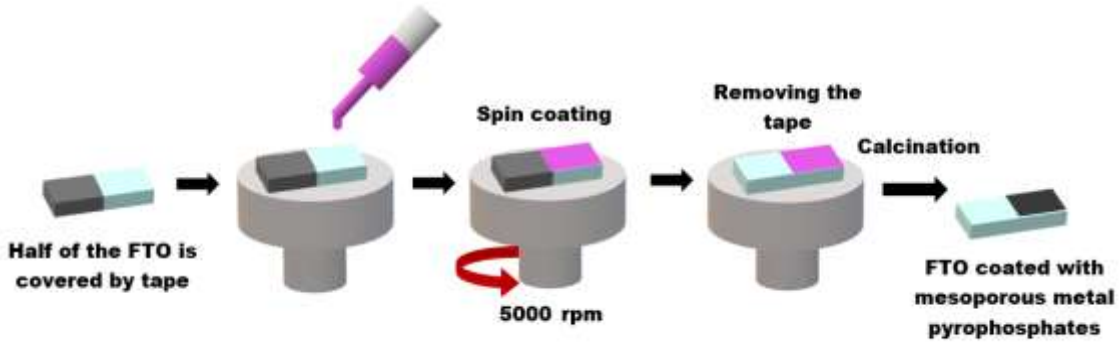


Figure 2.3: Preparation of coated FTO electrodes.

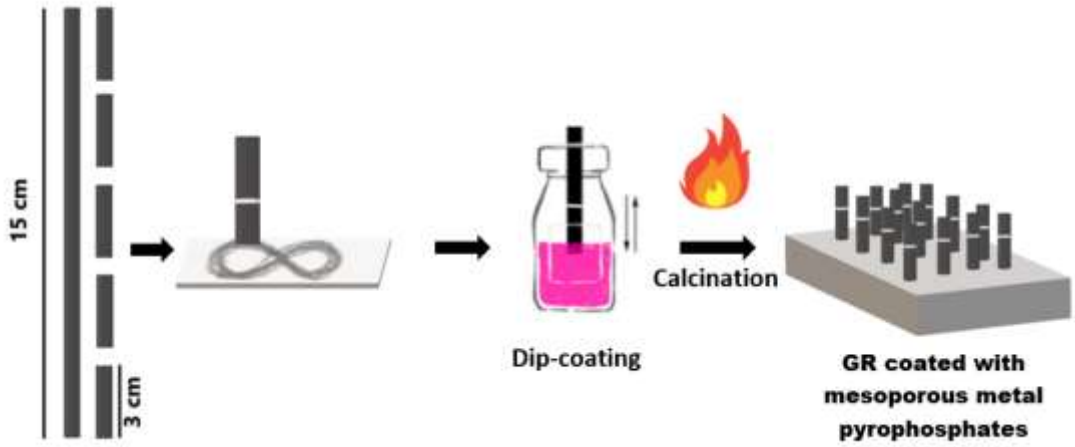


Figure 2.4: Preparation of graphite rod (GR) electrodes.

2.6. Instrumentation

2.6.1. Polarized Optical Microscope (POM)

POM images of the drop-cast coated solution, supernatant and precipitate parts on microscope slides are recorded using ZEISS Axio Scope A1 polarizing optical microscope in transmittance mode using 5X, 10X, 20X, and 50X magnifications between the crossed polarizers to observe the mesophase formation. The hexagonal mesophase is anisotropic and birefriengent and displays a fan-texture but, the cubic phase is isotropic and appears dark between the crossed polarizers.

2.6.2. X-Ray Diffraction (XRD) Patterns

The small-angle (1-5º, 2θ) XRD measurements of the solutions and supernatant parts that are coated by drop-cast method on microscope slides are carried using a Rigaku Miniflex Diffractometer equipped with a CuK_α (λ =1.5405 Å) X-rays source that is operating at 30 kV/ 15 mA and a Scintillator NaI (T1) detector with a Be window. The scan speed was 0.5º/min and the step size was 0.01. For the wide-angle XRD (10-80º, 2θ) measurements of the powders that are packed on a sample holder are carried either using Rigaku Miniflex (with scan speed of 0.5º/min and the scan size of 0.01) or a PANanlytical Multipurpose X-ray diffractometer, equipped with a CuK_α (λ= 1.5405 Å) X-ray source, operating at 45 kV/40mA.

2.6.3. Attenuated Total Reflection Fourier-Transform Infrared (ATR-FTIR) Spectroscopy

ATR-FTIR spectra of the solution, supernatant, and precipitate parts before calcination and after calcination are recorded using a Bruker Alpha Platinum ATR-FTIR spectrometer with a Digi Tect TM DLATGS detector. The spectra are collected for 64 scans in the 400-4000 cm^{-1} range with a resolution of 4 cm^{-1}. For the liquids (solution and supernatant parts) few drops are put on the ATR-FTIR crystal and for the gel-like precipitate and powders, they are put directly on top of the ATR-FTIR crystal to follow the gel formation.

2.6.4. Fourier-Transform Infrared (FTIR) Spectroscopy

For some samples, especially for the powders, a Bruker Tensor 27 model FTIR spectrometer with a Digi Tect TM DLATGS detector was used. The spectra were collected as it was with ATR-FTIR.

2.6.5. Scanning Electron Microscope (SEM)

SEM images of the powders were collected using an FEI Quanta 200 FEG at an operating voltage of 15 kV and spot size of 3 nm under a high vacuum (about 10^{-6} Torr). The powders are put on carbon tape that is attached to the aluminum sample holder. For the EDAX spectra of the samples are collected at 15 kV with a spot size of 3 nm.

2.6.6. Transmittance Electron Microscope (TEM)

TEM images of powder samples were collected by using an FEI Technai G2 F30 at an operating voltage of 200 kV. To collect high-quality images, the spin-coated samples were used. The thin films are scrapped, after calcination, from the microscope slide, ground in a mortar using absolute ethanol, and dispersed using a sonicator for 30 min. Finally, a few drops of the dispersed solution are put on a TEM grid (holey carbon film on a 200-mesh copper grid) and heated under a powerful light for drying.

2.6.7. N_2-Adsorption-Desorption Measurements

The N_2-adsorption-desorption (77.4 K) isotherms are collected using a Micromeritics Tristar 3000 automated gas adsorption analyzer, P/P_0 from 0.02 to 0.99 over 5-minute intervals. Before the measurements, the sample tubes, used for the analysis, are cleaned by keeping them overnight in an aqua-regia, followed by washing with water and ethanol and dried for 30 minutes. After drying, the tube's weight is recorded after evaquating it under vacuum for almost 1 hour. Then, 75 mg powder samples are put in above tube and dehydrated under a 20 mTorr vacuum at 200ºC for 2 hours. After the dehydration process, the weight of the tube with sample is also recorded and the tube with sample is placed on the instrument with an isothermal jacket to keep the temperature stable since the measurement was carried out in liquid nitrogen.

2.6.8. Electrochemical Characterization

All electrochemical studies were carried out using a three-electrode cell, shown in Figure 2.5, a Pt wire as a counter electrode, Ag/AgCl (3.5 M KCl) electrode as a reference electrode, and either graphite rod or FTO coated with the samples as the working electrode in a polypropylene cell with 1 M KOH electrolyte solution. The electrochemical measurements are carried using a Gamry instrument (potentiostat-IFC5000-07565). The measured potentials are corrected and reported as the normal hydrogen electrode (NHE). Cyclic voltammetry (CV) measurements of the coated FTO electrodes were recorded in the potential range of -0.5 to 2.0 V (vs. Ag/AgCl) at a scan rate of 50 mV/s. Similarly, CV curves for the coated GR electrodes

were recorded within a potential window of -0.5 to 1.5 V (vs. Ag/AgCl) at the same scan rate. To evaluate the Tafel slopes of these electrodes, multi-step chronoamperometry experiments were conducted in the potential range of 0.5 to 0.8 V, with each voltage step held for 300 seconds to allow the current to reach a steady state. Subsequently, multi-step chronopotentiometry measurements were performed to assess the overpotential at current densities of 1, 10, 20, 30, 40, 50, 60, 70, 80, 90, and 100 mA. Each current step was applied for 60 minutes to examine the long-term stability of the electrodes.

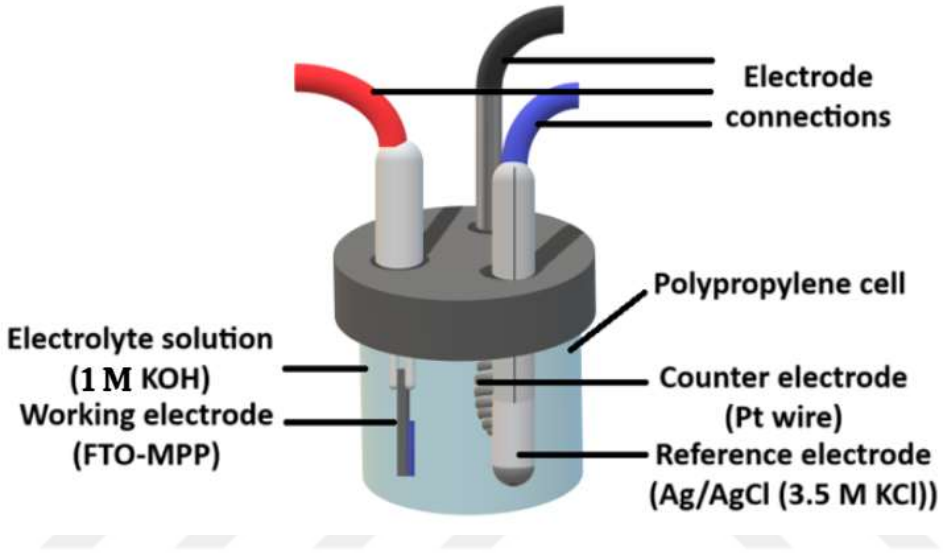


Figure 2.5: Schematic representation of the electrochemical setup for the three-electrode system.

Chapter 3

3. Results and Discussion

3.1. Synthesis and Characterization of Single Metal Pyrophosphates ($M_2P_2O_7$, M: Co(II), Ni(II), and Mn(II))

3.1.1. Preparation and Characterization of Co(II):PPA:P123 Mesophases

The solutions of Co(II):Acid:P123 are prepared as described in the experimental section in Table 2.1 in ethanol, methanol, and 1-butanol solvents. The ratios of the gradients are determined to maintain the stoichiometric balance (2:1, Co(II):PPA). The PPA is added at half the amount of the salt/P123 mole ratio and varied from 10 to 100 with 10 increments to investigate the mesophase formation and its stability.

3.1.1.1. Co(II):PPA:P123 Ethanol System

Since the solutions are either cloudy or gel, centrifugation at 6000 rpm for 15 minutes is necessary to separate the precipitate and the supernatant. Afterwards, the solution and supernatant parts are separately drop-casted onto microscope slides to obtain the mesophases/mesostructured semi-solid phase by evaporating the excess solvent under ambient laboratory conditions. The samples are denoted as X-YPPA (where X is the salt/P123 and Y is acid/P123 mole ratios and PPA stands for pyrophosphoric acid). The resulting mesophases are then characterized by small-angle XRD, ranging from 1 to 5º, 2θ, to analyze their stability during aging at room temperature (RT) for 5 hours or 1 day. Figure 3.1 shows the XRD patterns of all ratios of the Co(II):Acid:P123 mesophases prepared in ethanol solvent and aged at RT. During this process, excess water and ethanol evaporate under the ambient conditions

throughout the aging process, leading to the formation of a gel phase. The diffraction lines at small angles prove that the mesophases have an ordered mesostructure.

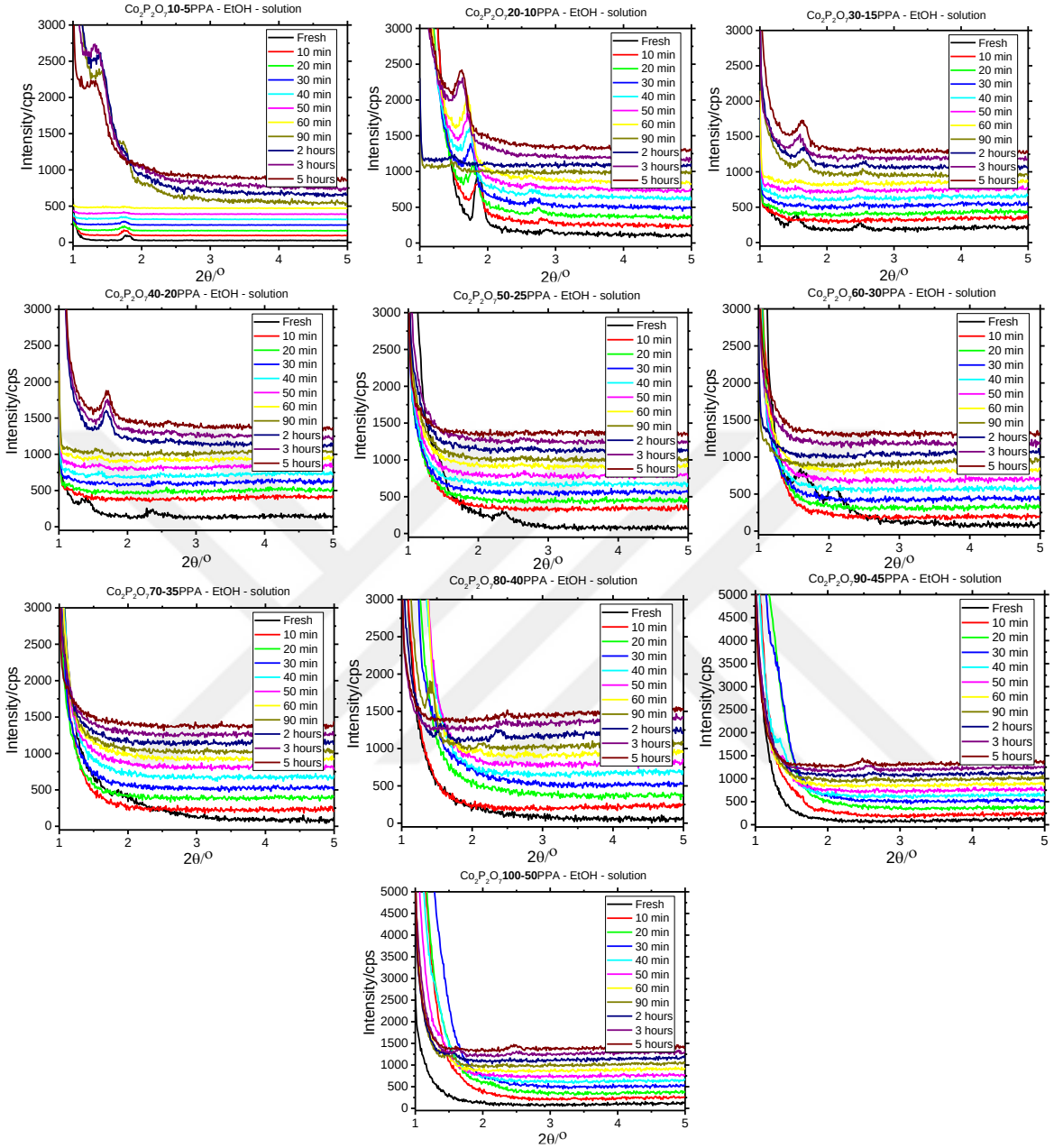


Figure 3.1: Small-angle XRD patterns of Co(II):PPA:P123 solutions with salt mole ratios of 10-100 in ethanol.

Minor changes in the diffraction patterns during gelation suggest that the water evaporation rate varies depending on the solution concentration and solvent. Diffraction plane with the highest d-spacing is likely below 1º, 2θ, which could not be measured using our XRD set-up. Therefore, the observed diffraction lines likely correspond to higher-order (hkl) planes of the mesophases with smaller d-spacings.

In the small-angle XRD patterns of the samples, obtained from Co(II) ethanol solutions with mole ratios ranging from 10 to 100, the first diffraction line is probably below 1°, 2θ, as previously mentioned. In the pattern of the 10-5PPA sample, the first diffraction line is obviously below 1° and the second line at 1.79°, 2θ. The second diffraction line appears after 90 minutes of aging (see Figure 3.1). Two diffraction lines, at 1.25° and 1.75°, 2θ, are observed upon aging the solution. Indexing the pattern provides a unit cell parameter *a* of 153.4 Å. The structure is 2D hexagonal, which is one of the common phase of the LLC phases. Therefore, the most intense line, due to (100) plane of the 2D hexagonal phase, must have a d-spacing of 132.8 Å and the corresponding 2θ of 0.66° that cannot be measured in our diffractometer. In the pattern of 20-10PPA sample, there are two diffraction lines at 1.87° and 1.61°, 2θ, and after 5 hours, the one line disappears and only the line at 1.61°, 2θ, becomes the dominant one in the pattern (see Figure 3.1(b)). In the pattern of 30-15PPA sample, there are two diffraction lines, observed at 1.54° and 2.49°, 2θ (see Figure 3.1(c)). The 40-20PPA sample has two lines at 1.38° and 2.35°, 2θ, in the first measurement, but after 2 hours, a new diffraction line appears at 1.71°, 2θ (see Figure 3.1(d)). The samples 50-25PPA and 60-30PPA diffracts two lines at 1.38° and 2.35°, and 1.60° and 2.10°, 2θ, respectively. They display two diffraction lines but, these lines disappear with further aging (see Figure 3.1(d and e)). There are two diffraction lines that appear after 90 minutes at 1.41° and 2.16°, and 1.63° and 2.43°, 2θ, respectively, in the patterns of the 80-40PPA and 100-50PPA samples. The changes, in the diffraction patterns, are due to changes in the structure/order in the mesophase. The general trend is that with increasing the salt concentration one may assume the unit cell will expand to accomodate increased ingredient concentration (salt and acid). However, this may not be true due to change in the number of surfactant molecules in the micelle domains. It is likely that the micelle domains are rich with surfactant at low concentrations but, decreases with increasing ingredient concentration. It means that the same amount of surfactant may form more micelle domains to accomodate high salt and acid concentrations. In the literature, it is a known phenomena that the number of surfactant per micelle varies in different media or concentration of the species in the media. The number of surfactant per micelle is known as aggregation number that is a flexible number and senses the media [82].

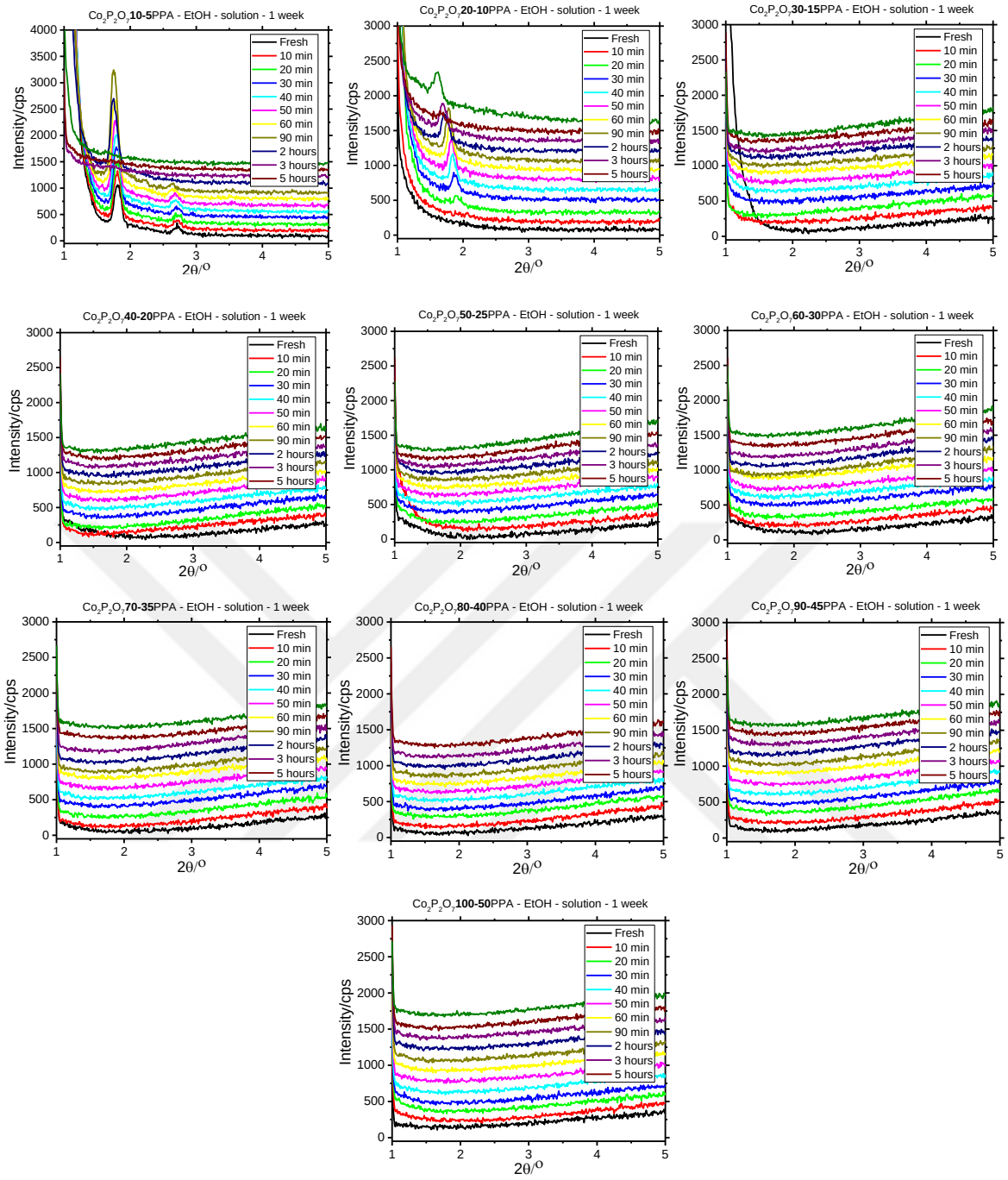


Figure 3.2: Small-angle XRD patterns of Co(II):PPA:P123 solutions with salt mole ratios of 10-100 in ethanol after 1 week.

To assess the stability and the formation of ordered mesophases, the samples were prepared and aged for 1 week prior to small-angle XRD measurements. As shown in Figure 3.2, an ordered mesophase formation is observed only in the 10-5PPA and 20-10PPA samples, the other mole ratios are disordered. In the 10-5PPA mole ratio, two diffraction lines appear at 1.81 and 2.71^{o}, which gradually shift to 1.75 and 2.64^{o}, 2θ, within 90 minutes and then disappear. In the 20-10PPA sample, a diffraction line coming up after 20 minutes at 1.92^{o} and it shifts to 1.62^{o}, 2θ, after one day-aging.

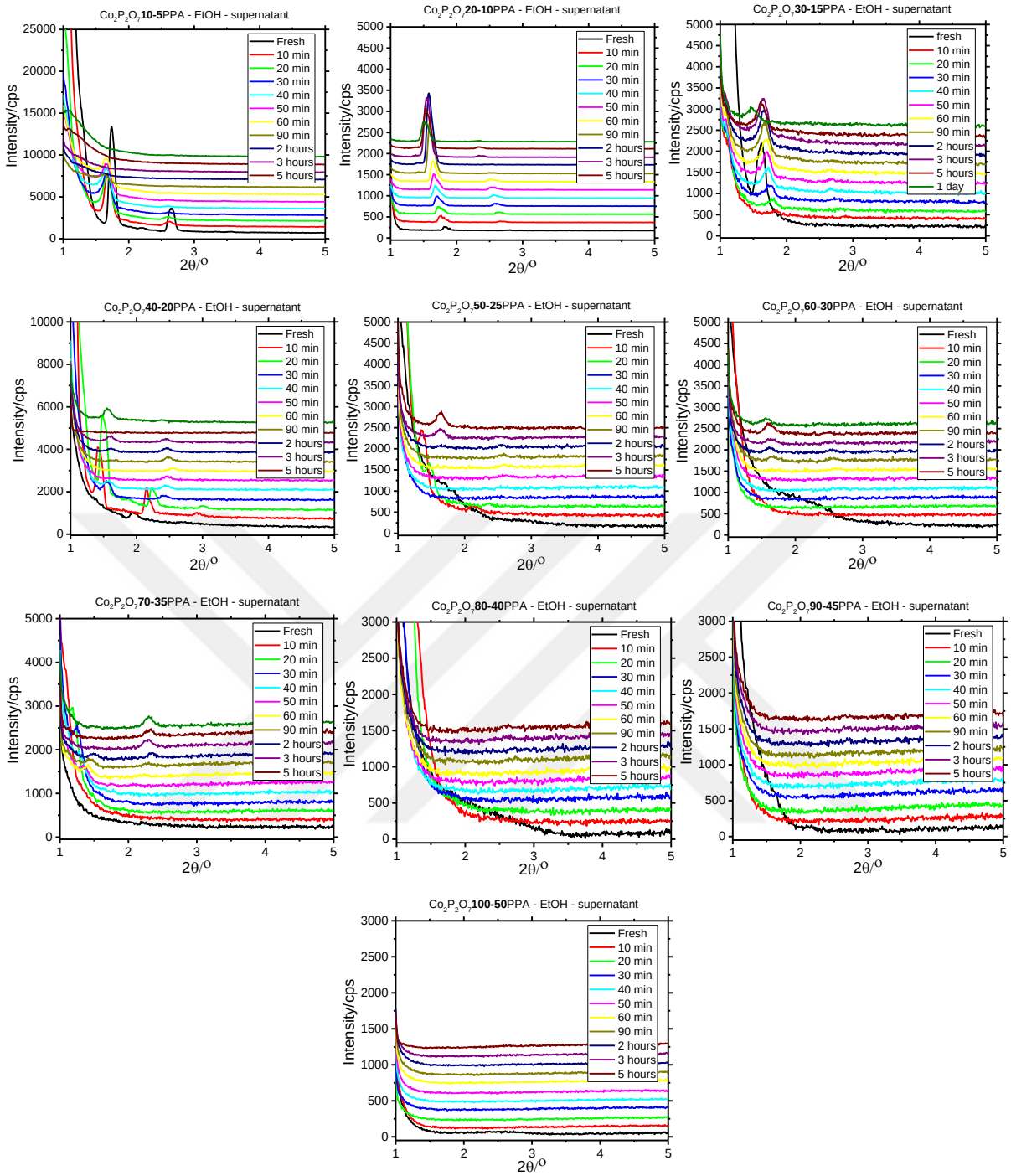


Figure 3.3: *S*mall-angle XRD patterns of Co(II):PPA:P123 supernatant parts with salt mole ratios of 10-90 from ethanol system.

The supernatant part of each 10-100 mole ratios are also drop-cast coated on microscope slides and time dependent small-angle XRD patterns were collected to check the order of the mesophases. In the 10-5PPA sample, two diffraction lines are observed at 1.75 2.65°, 2θ. Only one diffraction line is observed at 1.09°, 2θ, after one day-aging. In the XRD pattern of 20-10PPA sample, the two week lines are observed at 1.85 and 2.80°, 2θ, and after one day-aging, these lines shift to 1.52 and 2.32°, 2θ, respectively. In the pattern of 30-15PPA sample, there

seems only one diffraction line that is observed at 1.62º in the first measurement, shifts to 1.86º in the 2nd measurement, and finally shifts to 1.46º, 2θ, after one day-aging. Moreover, the XRD pattern of 40-20PPA sample display only one diffraction line at 1.96º in the first measurement, but in 10 and 20 minutes three diffraction lines are observed at 1.43, 2,16, and 2.93, and at 1.49, 2.26, and 3º, 2θ, respectively. But in further aging (30 minutes), two lines remain at 1.58 and 2.42º, 2θ. The samples of 50-25PPA and 60-30PPA behaves similary. Clearly, the supernatants contain less Co(II), PPA, and P123 species because some ingredients precipitate and separated out. Therefore, the XRD patterns mimic the low ingredient mesophases as discussed previously. However, above Co80-40PPA clear solutions form disordered mesophases.

The aging process is further analysed using ATR-FTIR spectroscopy using only 30:15:1 ratio samples. The sol-gel solution, precipitate and supernatant parts after the centrifugation process were placed onto the ATR crystal immediately after preparation, and time-dependent ATR-FTIR spectra were measured. Note that as the solvent evaporates, change in the solution concentration leads to a variation in the refractive index that affectes the ATR-FTIR intensities. To overcome this effect, the spectra are normalized using a signal of a non-volatile specie to compare the spectra with each other. Since the amount of surfactant remaines constant during the evaporation process, the normalization was performed based on the surfactant peaks around, 2800-3000cm^{-1} region.

Figure 3.4 a), c) and d) presents the time-dependent ATR-FTIR spectra of the cobalt pyrophosphate solution, supernatant and precipitate parts in ethanol. The peaks around 850-1200 cm^{-1} are due to the pyrophosphate species, the peaks at around 3300-3600 cm^{-1} range originate from the stretching modes of water, and the peaks at around 1290-1450 cm^{-1} are due to the nitrate species. Figure 3.4 b) shows the change in the pyrophosphate peak intensity-to-nitrate peak intensity ratio over time. The trend in the plot is a clear indication of the evaporation of water as well as nitrates as either nitric acid or its decomposition products. Increase of the pyrophosphate to nitrate intensity ratio indicates the progression of a polymerization reaction between Co(II) ions and PPA, see chemical equation 1.

$$\mathbf{2}Co(NO_3)_2 + H_4P_2O_7 + nH_2O \rightarrow Co_2H_xP_2O_7(NO_3)_x.nH_2O(s) + (4-x)HNO_3(g) \quad \textbf{Eqn. 1}$$

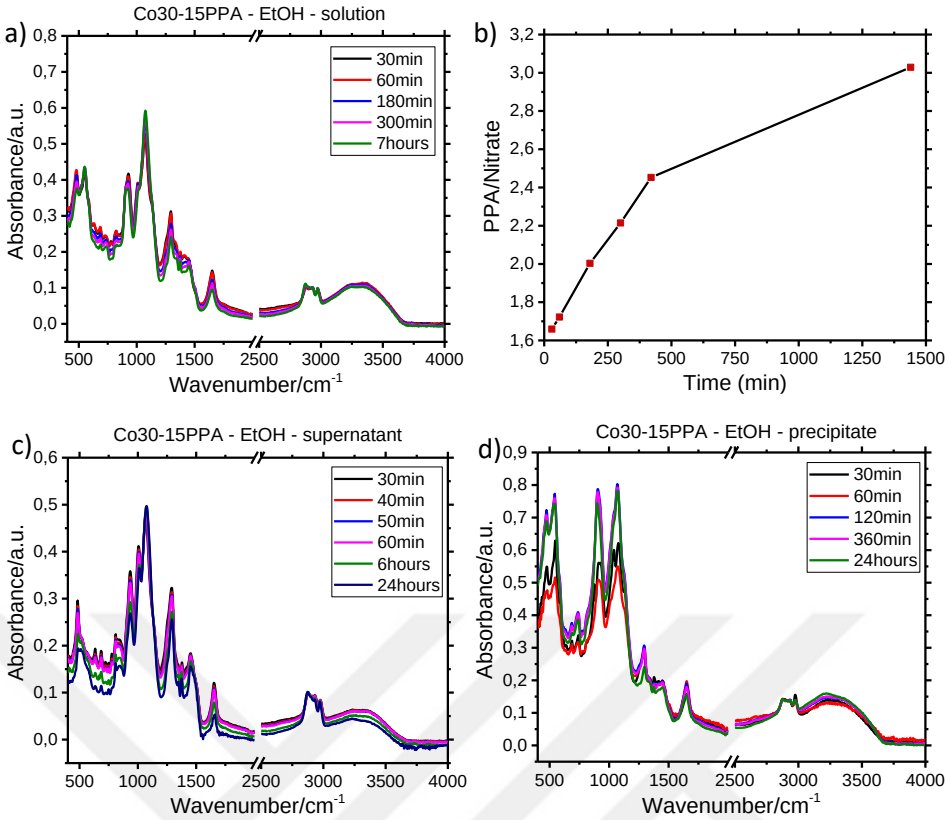


Figure 3.4: a), c), d) Time-dependent ATR-FTIR spectra of the Co(II):PPA:P123 solution, supernatant, and precipitate parts from ethanol system, and b) Pyrophosphate peak intensity to nitrate peak intensity ratio from the solution part.

3.1.1.2. Co(II):PPA:P123 Butanol System

Butanol solution of 30:15:1 Co(II):PPA:P123 ratio is also prepared and analyzed using XRD technique. As the solvent is changed to butanol, the sol-gel process occurs faster, but the gel-phase breaks into a solution, when it is shaken or stirred. Figure 3.5(a) shows a photograph of this mixture, showing the transformation of the solution to a gel-phase. The microscope slide is drop-cast coated with solution part but, because of the sol-gel formation the coating is very thick. The solution is centrifuged to separate the supernatant and the precipitate parts. The small-angle XRD patterns of these three parts are shown in Figure 3.5(b) Once again, only in the supernatant part, there is an ordered mesophase formation.

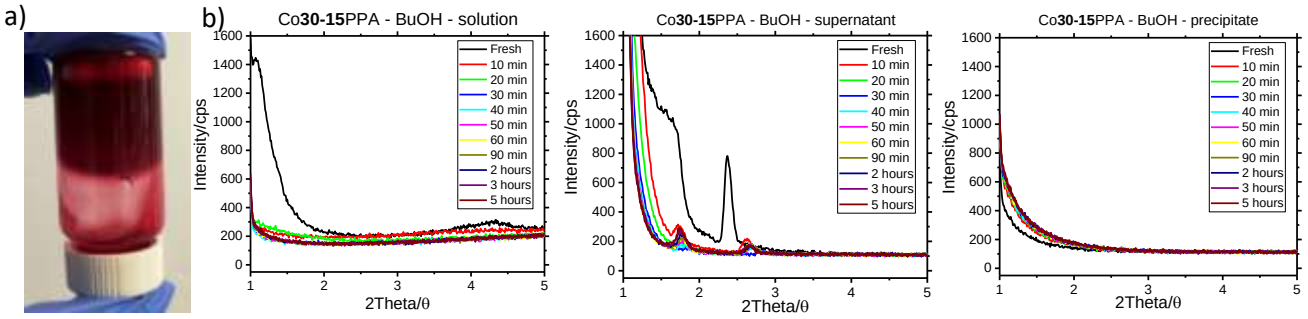


Figure 3.5: a) Photograph of the sol-gel formed in butanol system, b) small-angle XRD patterns of Co(II):PPA:P123 solution, supernatant and precipitate parts in butanol system.

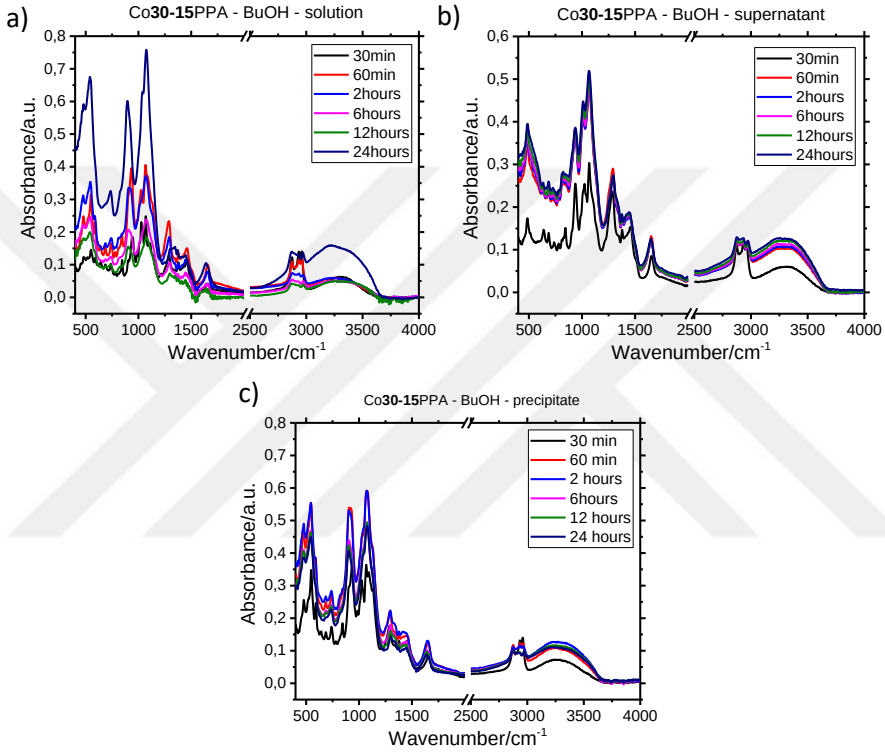


Figure 3.6: Time-dependent ATR-FTIR spectra of the Co(II):PPA:P123 a) solution, b) supernatant, and c) precipitate parts in butanol system.

Figure 3.6 displays the ATR-FTIR spectral changes during aging of above three samples (namely solution, supernatant and precipitate). The spectra of the Co(II):PPA butanol solution display clear differences between the solution and supernatant parts in the pyrophosphate and nitrate regions. In solution and precipitate parts, there are only two main peaks in the pyrophosphate region which belong to the asymmetric and symmetric stretching modes of the phosphate groups. However, in supernatant part, there are more peaks in the pyrophosphate region with more intense nitrate peaks. It means that the supernatant part produce different pyrophosphate species and more nitrate in the semi-solid structure that form with complete butanol evaporation. It is clear in the spectra of the solution part, there is a very fast polymerization reaction in which the nitrate and water species are removed from the sample.

Therefore X and Y in the semi-solid structure is significantly reduced in the precipitate and solution phases.

3.1.1.3. Co(II):PPA:P123 Methanol System

Methanol solution of the 30:15:1 Co(II):PPA:P123 composition is also prepared and analyzed in the solution phase during methanol evaporation. Methanol solution is very different from the butanol and ethanol solutions, because it becomes cloudy in a short time after mixing the solutions. There is a gel formation and the amount of precipitate collected is much less. The small-angle XRD patterns show that there is an ordered mesophase formation only in the supernatant part.

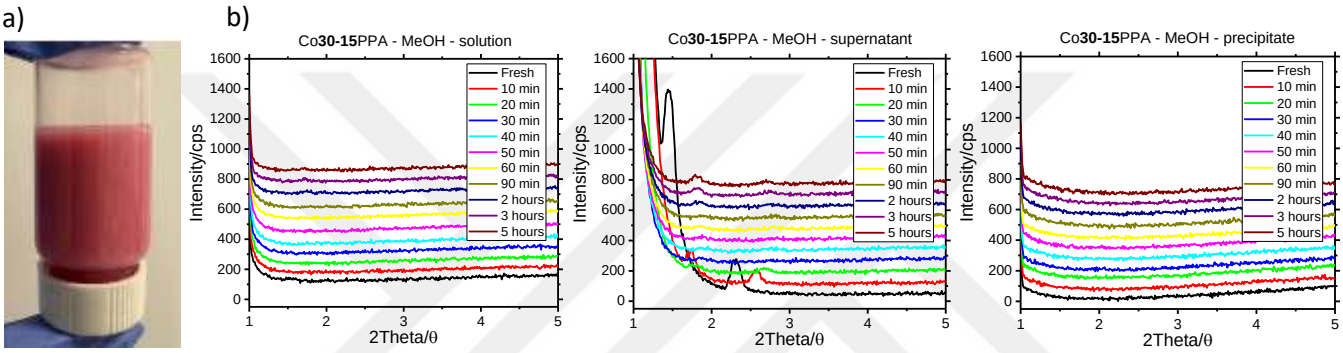


Figure 3.7: a) Photograph of the Co(II):PPA:P123 methanol solution and small-angle XRD patterns of the Co(II):PPA:P123 b) solution, c) supernatant, and d) precipitate parts during methanol evaporation.

The samples, drop-cast coated on the microscope slides, are thinner than the solution parts of the butanol and ethanol solutions because there is no gelation. Also, the coated samples dry very quickly and turn into pale pink even before the measurements started. In the supernatant part, there are very intense diffraction lines at 1.46 and 2.31º, 2θ. Until 40 minutes, the diffraction lines gradually shift to higher angles, to 1.90 and 2.80º, 2θ, respectively. Afterwards, these two diffraction lines shift towards smaller angles and reach to 1.82º and 2.72º, respectively, after 1 day-aging.

The ATR-FTIR spectra of the methanol solution, supernatant, and precipitate parts show decomposition of the nitrate species and display an increase in the absorbance of the pyrophosphate species, indicating the extend of the polymerization reaction in Equation 1. Also, as time passes, there are cracks on the samples over the ATR diamond, therefore the samples were pressed to enhance the signals. In the precipitate, as it dries very quickly after 5 minutes, the sample must be pressed to collect decent spectra.

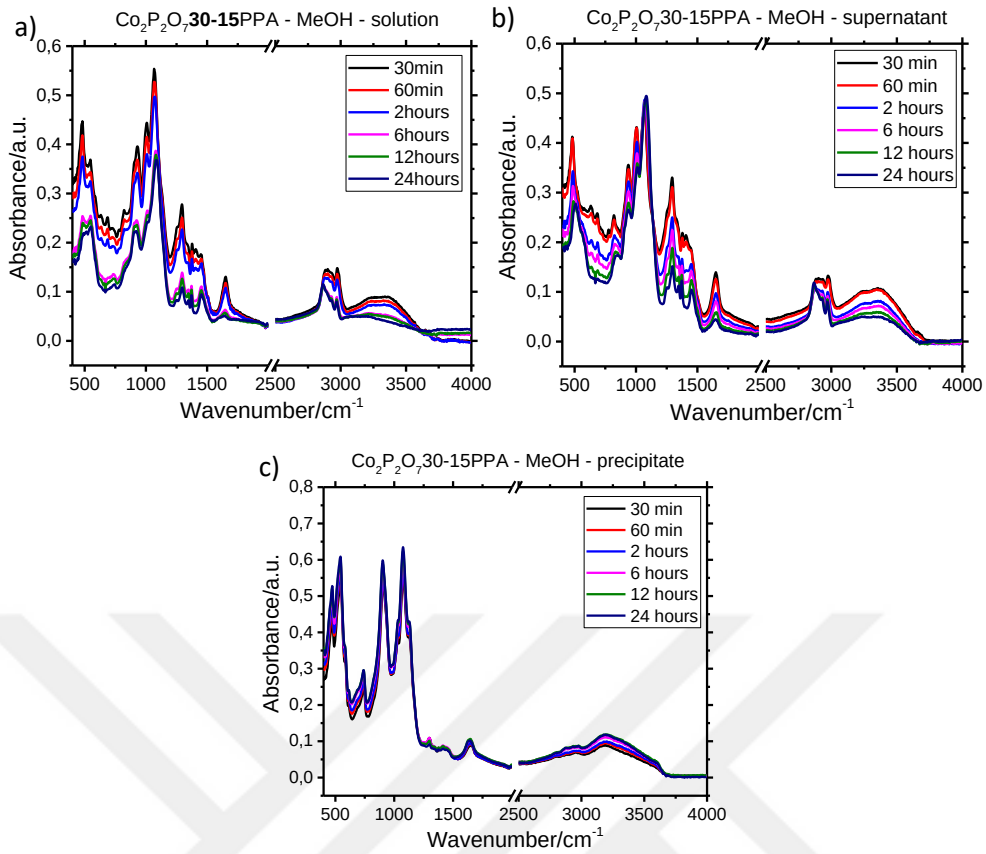


Figure 3.8: Time-dependent ATR-FTIR spectra of the a) solution, b) supernatant, and c) precipitate parts in Co(II):PPA:P123 methanol system.

3.1.1.4. Solvent Comparison in the Cobalt System

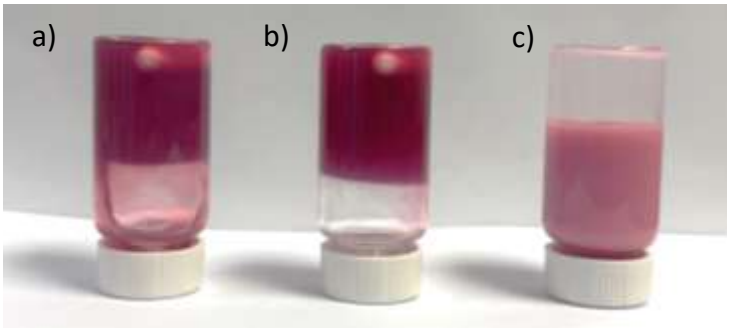


Figure 3.9: Photographs of the solutions of Co(II):PPA:P123 in a) butanol, b) ethanol, and c) methanol solvents.

Major difference among the above solvent system is the colors of the solutions. In butanol and ethanol, the color of the solution/gel is darker pink than that of in methanol, which is likely related to the particle size of the aggregated semi-solid $Co_2H_xP_2O_7(NO_3)_x \cdot yH_2O$ species. In the ethanol and butanol solvents, there is a sol-gel formation. The gelation is very fast in butanol while it takes one or two minutes to form in ethanol. Because, butanol acts as a co-surfactant and enhances micelle formation, which increases the aggregation of the $Co_2H_xP_2O_7(NO_3)_x \cdot yH_2O$ particles. Butanol solution is very hard to homogeneously mix the acid

and the metal salt solutions since the mixture undegoes a fast gelation. In order to slow down the sol to gel formation, the amount of butanol solvent can be increased. However, in ethanol, the solution is clear for some-time when the two solutions are mixed. However, in few minutes, it starts to become cloudy and then complete gelation is observed. However, the sol-gel process occurs in the ethanol systems like in the butanol solution. Therefore, working with ethanol may be better choice because it provides some kind of control over the particle size, homogeneity, morphology, surface area, etc.

A very critical and important chemical phenomena, solubility, should be considered here as well. Unfortunately, there are no K_{sp} values for the $Co_2H_xP_2O_7(NO_3)_x \cdot yH_2O$ particles (as well as $Co_2P_2O_7$ particles) in the literature. However, the $[Co(OH_2)_6](NO_3)_2$ salt disolves very quickly in ethanol and methanol solvents but, it takes 5-10 minutes to dissolve in butanol while PPA and P123 dissolve very quickly in these solvents. Higher solubility of the metal salt may result in a smaller particle size. Moreover, the nucleation and growth also play a role and their rate may be different in these solvents as well. If the nucleation of the particles is faster than their growth, very small and many particles will form in the solution. However, if the nucleation is a slower process, compared to growth, one may observe larger particles and precipitation.

Also, the effect of the acidity of the solvents should be considered. Among these solvents, water is more acidic than the others. Note that a clear solution is obtained in water and remains stable for weeks. Methanol is the second acidic solvent. In methanol, again, there is a cloudy solution formation but as the solution age for more than a day a white colored precipitate forms at the bottom of the vial. Ethanol is less acidic compared to methanol but, more acidic than butanol. Even tough there is a sol-gel formation in ethanol it forms more slowly compared to butanol solution. It is likely that the solvent acidity/basicity has some effect on the particle formation through dissociation of PPA to its anions ($H_3P_2O_7^-$, $H_2P_2O_7^{2-}$, etc.) and also the solvent-particle interaction determines the behaviour of these solutions. Note also that the dissociation constants of PPA are also unkown in these solvents. These constants needs to be evaluated to fully understand above observations.

In methanol, there is an ordered mesophase/mesostructured semi-solid formation and it can be used in the thin-film synthesis and related applications. However, butanol and ethanol systems are good to employ for sol-gel processes that also produce mesostructured semi-solids with high surface area and applicable for large scale production of powder samples (see later).

3.1.2. Preparation and Characterization of Ni(II):PPA:P123 Mesophases

The solutions of Ni(II):Acid:P123 are prepared as described in the experimental section and the compositions are listed in Table 1.2 in ethanol, methanol, butanol solvents. The 30-15PPA mole ratio is chosen for the investigation. A sol-gel formation is observed in the nickel pyrophosphate solutions in both buthanol and ethanol but, the solution is cloudy in methanol. The sol-gel formation is faster in butanol than ethanol. In butanol solvent, even after one or two shakes it was very hard to remove the stirrer from the gel. However, in ethanol case, the solution can be shaken one or two times, then it is kept undisturbed to obtain the gel-phase within one minute-less stable gel-phase is observed. However, as time passes, the gel becomes more stable and again the stirr bar is hard to remove from the gel. In methanol solvent, the solution is cloudy and a white precipitate forms at the bottom of the vial after 1 day aging the solution. Even though the sample is centrifuged at 6000 rpm for 15 minutes, the amount of the precipitate collected is very small.

3.1.2.1. Ni(II):PPA:P123 Ethanol System

Immediately after the two solutions are combined, there is a gelation (see Figure 3.2.1(a). It is not so stable and undergoes precipitation when the solution is stirred or shaken. And it is hard to keep the gel stable and to drop-coat it on a microscope slide for further analysis. Also, as the collected precipitate is gel-like, it is also hard to coat on a microscope slide as a thin layer. A very small amount of precipitate is taken and put in between of two microscope slides and then one of them is slide over the other to coat it as even as possible as a thin layer. Figure 3.10(b) shows that small-angle XRD patterns of the samples, obtained from solution, supernatant and precipitate parts. The patterns show that only in supernatant part, there is an ordered mesophase formation. However, it can be because of the thickness of the solution and precipitate parts on the microscope slide.

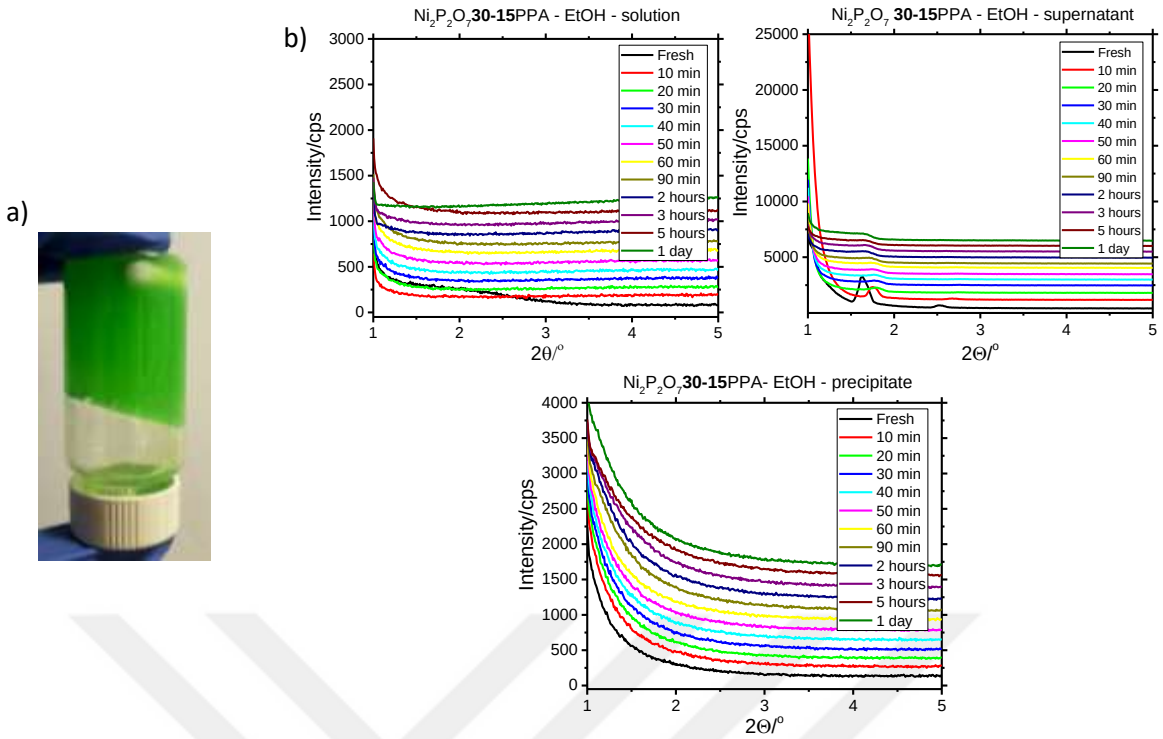


Figure 3.10: a) Sol-gel formation in Ni(II):PPA:P123 solution, b) time-dependent small-angle XRD patterns of the Ni(II):PPA:P123 (30-15PPA) ethanol (b) solution, (c) supernatant, and (d) precipitate parts.

The small-angle XRD patterns display lines due to an ordered mesophase, formed from the supernatant part. Two diffraction lines are observed at 1.64 and 2.54º, 2θ, that shift to higher angles with aging (to 1.74 and 2.72º, respectively). However, the gels which are obtained from the solution and precipitate parts have no diffraction lines in their small-angle XRD patterns (see Figure 3.10(b and d)). It means that the gels, obtained from solution and precipitate, are disordered.

$$2Ni(NO_3)_2{\cdot}6H_2O + H_4P_2O_7 \rightarrow Ni_2H_xP_2O_7(NO_3)_x{\cdot}nH_2O(s) + HNO_3(g) \quad \textbf{Eqn. 2}$$

The time-dependent ATR-FTIR experiments show that the removal of the solvents in the samples takes 30 minutes. After 30 minutes, the phosphate peaks become obvious and the amount of nitrate species drop during this time. When the metal center, cobalt, is changed to nickel, no big change occurs in the ATR-FTIR spectra. The nitrate decomposition is very clear in the ATR-FTIR spectra of solution and supernatant parts, indicating extend of the polymerization reaction, Eqn. 2. Moreover, in the precipitate part, most of the nitrates are removed from the mesophase, no big difference is observed even after 24 hours of aging, see Figure 3.11(c).

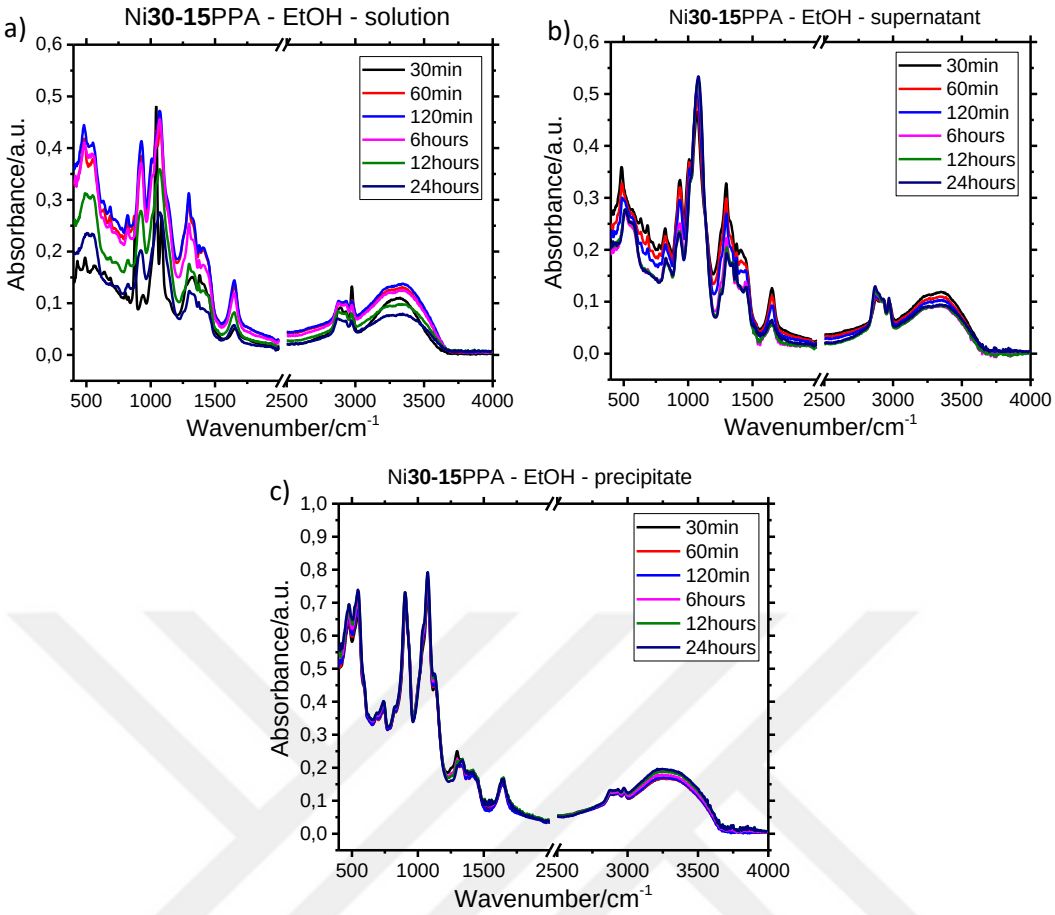


Figure 3.11: Time-dependent ATR-FTIR spectra of Ni(II):PPA:P123 a) solution, b) supernatant, and c) precipitate parts in ethanol.

Figure 3.12 displays POM images of the samples, obtained from solution, supernatant, and precipitate. The cracks, observed in the images are due to stress, caused by drying the gels. But, in all cases the samples can be coated over microscope slide to obtain thick (monolith) and thin films.

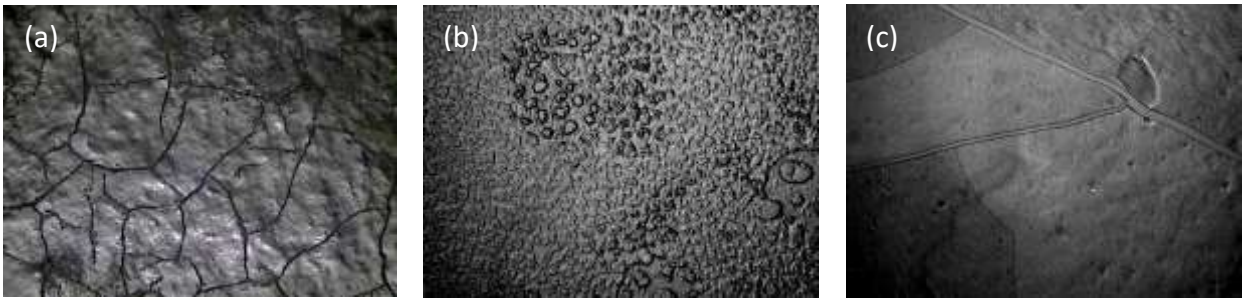


Figure 3.12: POM images of Ni(II):PPA:P123 (1:30:15) (a) solution, (b) supernatant, and (c) precipitate parts in ethanol after 5 hours aging.

3.1.2.2. Ni(II):PPA:P123 Butanol System

Upon combining the acid and salt solutions, the vial is shaken very gently to form a gel, which is more stable than the gel formed in ethanol. Again, it is hard to use this gel sample,

because when it is coated on a substrate to characterize, the structure is disturbed. When the solution is coated on a microscope slide for the small-angle XRD measurement, the dropped solution also forms a gel and the sample on the microscope slide becomes very thick. Figure 3.13(b) displays the small-angle XRD patterns of the samples, obtained from solution, supernatant, and precipitate parts.

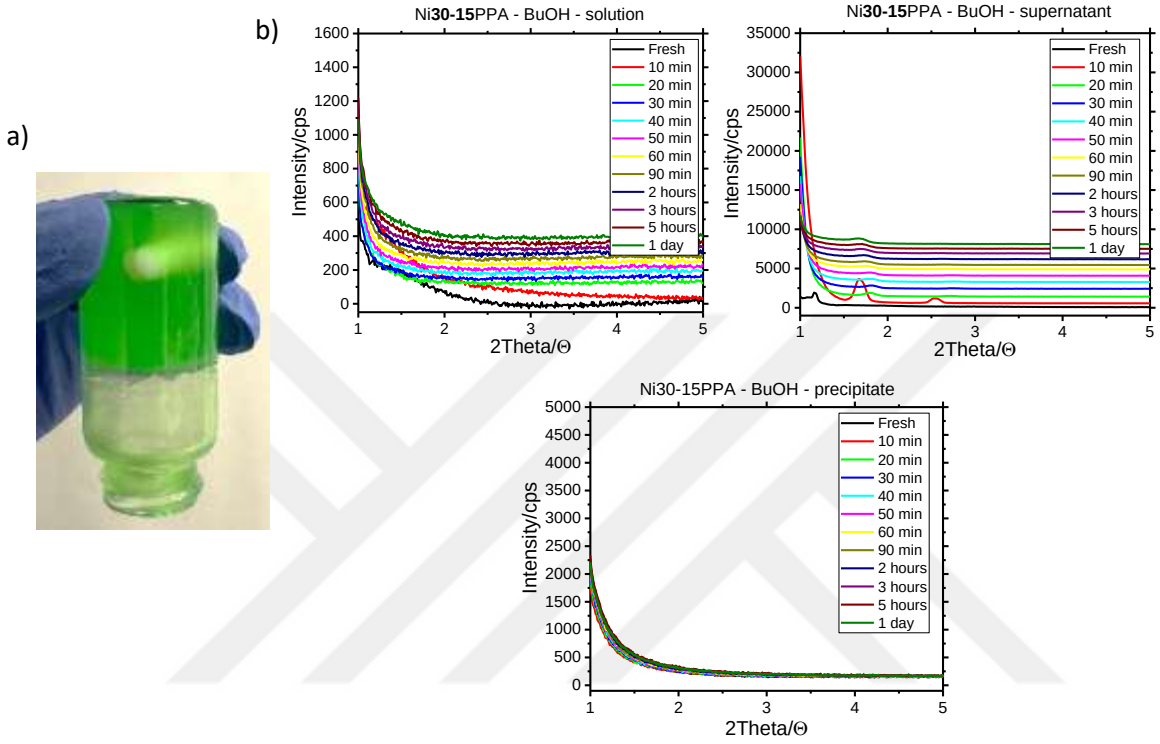


Figure 3.13: a) Sol-gel formation in Ni(II):PPA:P123 solution, b) time-dependent small-angle XRD patterns of the Ni(II):PPA:P123 (30-15PPA) butanol solution, supernatant and precipitate parts.

The small-angle diffraction patterns show that the mesophase, obtained from the supernatant part, is an ordered mesophase/ mesostructured semi-solid. The patterns display two diffraction lines at 1.09 and 1.17º, 2θ, in the freshly coated sample, but in 10 minutes, the pattern changes and two new lines at 1.69 and 2.54º, 2θ, corresponding to 52.2 and 34.8 Å d-spacing, respectively, are observed. These lines correspond to (200) and (300) planes of a cubic phase and accords well with the POM image (see Figure 3.15(b)). However, after 1 day aging, only one diffraction line remains at 1.69º, 2θ, showing a phase or order change with aging due to further polymerization of nickel and pyrophosphate ions as the buthanol evaporates. However, in the XRD patterns of the samples, coated from the solution and precipitate parts, there is no diffraction line in the small-angles, indicating a disordered structure, but these samples are still mesostructured, as evidenced from the N_2 adsorption-desorption measurements of their calcined samples (see later).

The ATR-FTIR spectra of the samples, see Figure 3.14, obtained from 30-15PPA butanol solution and supernatant parts are different compared to Co(II) samples in both pyrophosphate and nitrate regions. The nitrate region is significantly more intense indicating the extend of polymerization is low in both solution and supernatant parts. However, in the precipitate part, the nitrate peaks lose their intensity, indicating more polymerization reaction and precipitation.

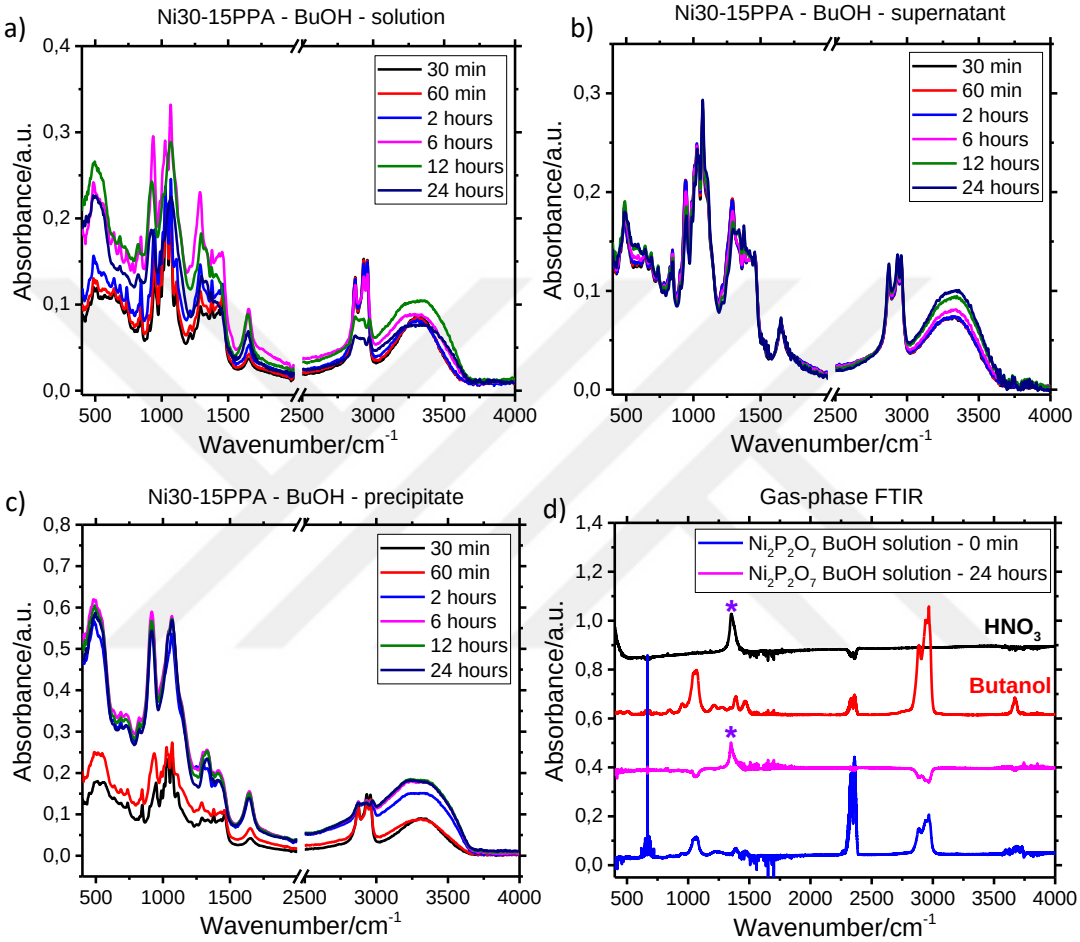


Figure 3.14: Time-dependent ATR-FTIR spectra of Ni(II):PPA:P123 a) solution, b) supernatant, c) precipitate parts in butanol system, d) Gas phase FTIR spectra of $Ni_2P_2O_7$ solution at the beginning of the experiment (0 min) and after 1 day.

To evaluate the products of the polymerization reaction, gas-phase FTIR spectra were also collected. Figure 3.14(d) displays the gas-phase FTIR spectra of nitric acid, butanol, and the gas-phase of above solution. First, a drop of butanol solvent is placed in gas-cell and the FTIR spectra are collected for 1 day. Then, the gas cell was cleaned and one drop of HNO_3 solution was placed and again, the FTIR spectra were collected for 1 day (black spectrum). After these spectra are collected, the solutions in two vials were mixed in the gas-cell and time-dependent FTIR spectra were collected. After 24 hours, the nitric acid and gas-phase of the

solution display a peak at 1450 cm^{-1} due to nitrate decomposition species and consistent with the suggested reaction in Eqn. 2.

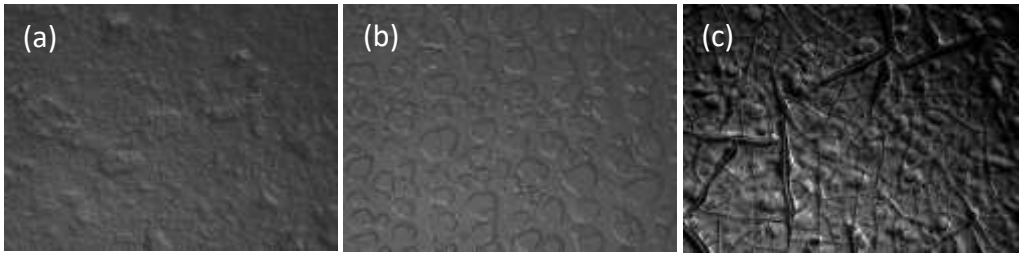


Figure 3.15: POM images of the Ni(II):PPA:P123 (30:15:1) a) solution, b) supernatant, and c) precipitate parts after 1 day aging.

POM images of the three samples are shown in Figure 3.15. The supernatant produces a smooth film over the glass slide but, both solution and precipitate form thicker films with particle like species. The images are dark between the crossed polarizer, indicating an isotropic structure (either cubic or disordered) and consistent with the small-angle XRD patterns.

3.1.2.3. Ni(II):PPA:P123 Methanol System

The Ni(II):PPA:P123 methanol solution behaves very differently than the other solvents, because the methanol solution is clear and no sol-gel formation is observed, see Figure 3.16(a). Color of the precipitate after aging and/or after the precipitation is white and the amount of the precipitate is very small. The solution is clear, as the supernatant part. The coated supernatant samples display diffraction lines in the small-angle XRD patterns, indicating that there is an ordered and stable mesophase formation. The diffraction line is observed at 1.83º that shifts to 1.71º, 2θ, after 1 day aging. The first diffraction line is at 1.91º and it shifts to 1.67º, 2θ, after 1 day aging the supernatant part.

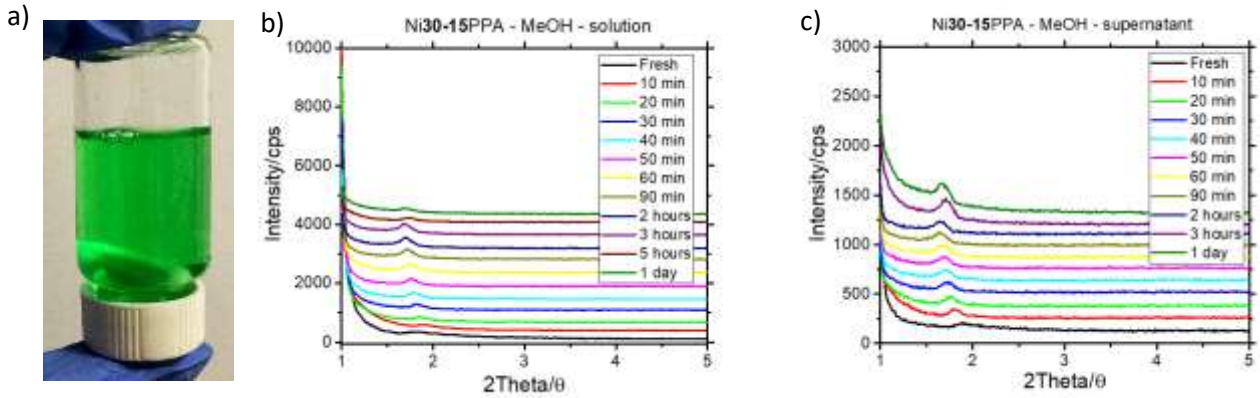


Figure 3.16: a) Photograph of the clear Ni30:15PPA methanol solution and time-dependent small-angle XRD patterns of the b) solution, and c) supernatant parts.

The time dependent ATR-FTIR spectra of the Ni(II):PPA:P123 methanol system both solution and supernatant samples are given in Figure 3.17. The spectra are very similar. Since the precipitate is very small amount, removing the precipitate does not alter the solution composition. Also, the decrease in the nitrate peaks as time passes is very clear in these spectra, again supporting the provided reaction in Eq. 2.

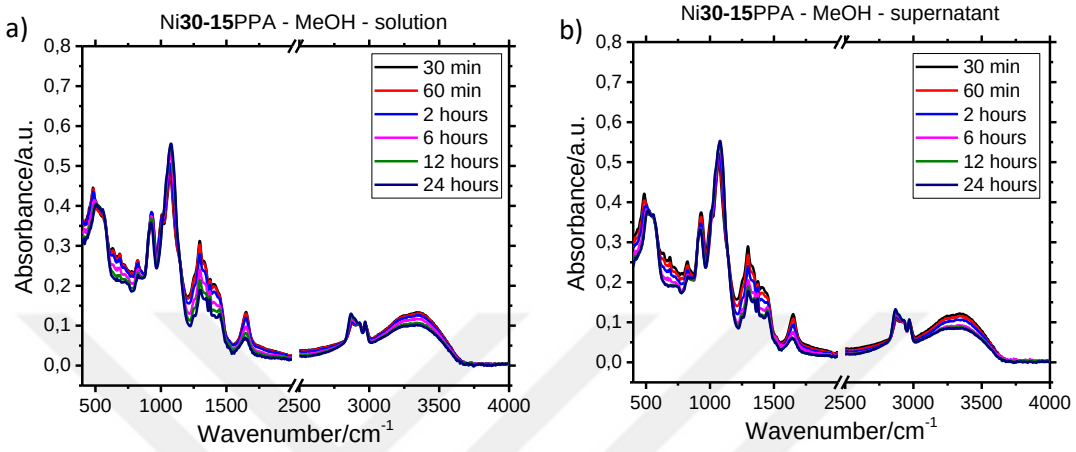


Figure 3.17: Time-dependent ATR-FTIR spectra of the Ni(II):PPA:P123 methanol system a) solution and b) supernatant samples.

3.1.2.4. Solvent Comparison in the Nickel System

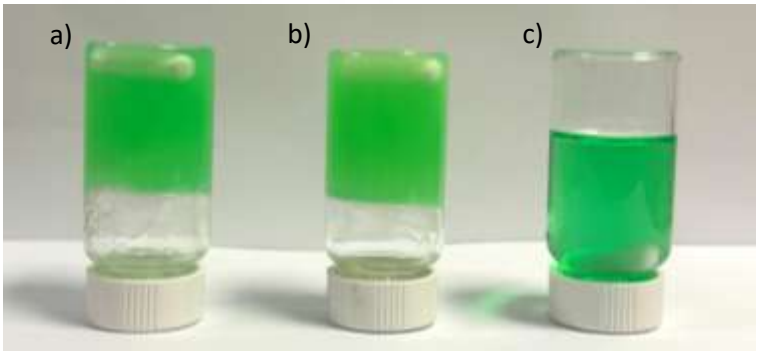


Figure 3.18: Photographs of the solutions of Ni(II):PPA:P123 in a) butanol, b) ethanol, and c) methanol solvents.

This section compares the effect of all solvents on the nickel solutions. In ethanol and butanol solvents, a sol-gel process is effective, see Figure 3.18. The process is very fast in butanol but, it takes one or two minutes in ethanol solvent. Origin is as it is discussed in the cobalt system (see Section: 3.1.1.4.)

Since butanol may act as a co-surfactant, it is important to test alcohols with longer carbon chains that may work better in the sol-gel synthesis [93]. Therefore, hexanol and 1-propanol were also tested as the solvents. In hexanol, the sol-gel formation is very fast as it is

in butanol. However, when the solvent is changed to 1-propanol, the sol-gel formation takes much longer time like in ethanol.

In methanol, there is an ordered mesophase/mesostructured semi-solid formation and it can be used in the thin-film synthesis and related applications. However, the butanol and ethanol systems can be used to synthesize large-scale powder samples with high surface area (see later).

3.1.3. Preparation and Characterization of Mn(II):PPA:P123 Mesophases

The Mn30:15PPA solutions are prepared as mentioned in Experimental Section, Table 1.1. After mixing the acid and salt solutions, in ethanol, butanol and methanol solvents the solutions become cloudy. In butanol and methanol solutions, the color changes immediately after mixing the solutions. There is a very unstable sol-gel formation in ethanol and butanol solvent but there is no gelation in methanol solutions.

3.1.3.1. Mn(II):PPA:P123 Ethanol System

The ethanol solution is a cloudy and pale pink, characteristic for octahedral Mn(II) species. Since there is an unstable sol-gel formation, a centrifugation process is applied to separate the precipitate and characterized in all three parts. There are no diffraction lines in the samples of solution and precipitate parts in the small-angle XRD patterns but, the supernatant part display a diffraction line at 1.88º, 2θ, after 50 minutes aging. This diffraction line shifts to 1.72º, 2θ, after 1 day of aging, indicating the formation of an ordered mesophase, see Figure 3.19.

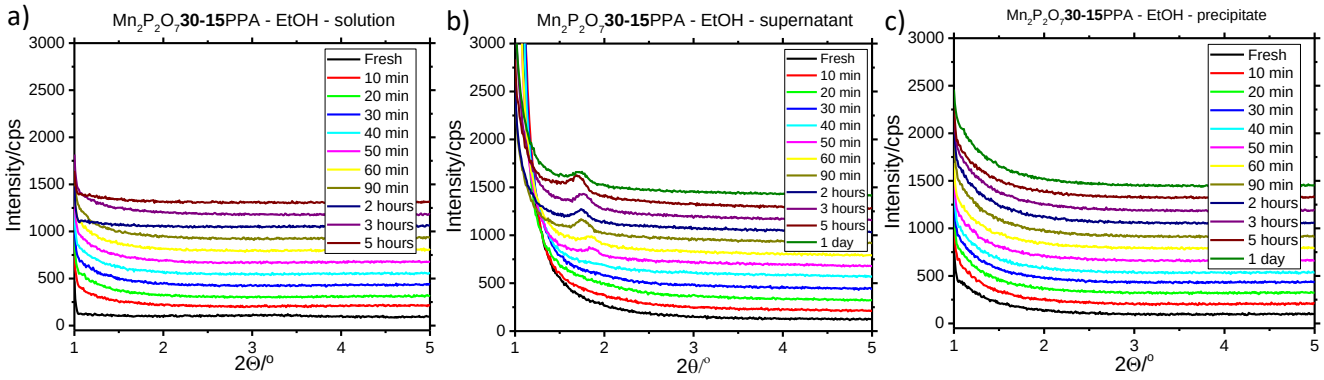


Figure 3.19: Time-dependent small-angle XRD patterns of the Mn(II):PPA:P123 (30-15PPA) ethanol a) solution, b) supernatant, and c) precipitate parts.

Figure 3.20 presents the time-dependent ATR-FTIR spectra of the manganese solution, supernatant and precipitate parts in ethanol. There is a clear indication of the evaporation of water as well as nitrates as either nitric acid or its decomposition products. Increasing the

intensity ratio of the pyrophosphate to nitrate species also indicates the progression of a polymerization reaction in Eqn. 3.

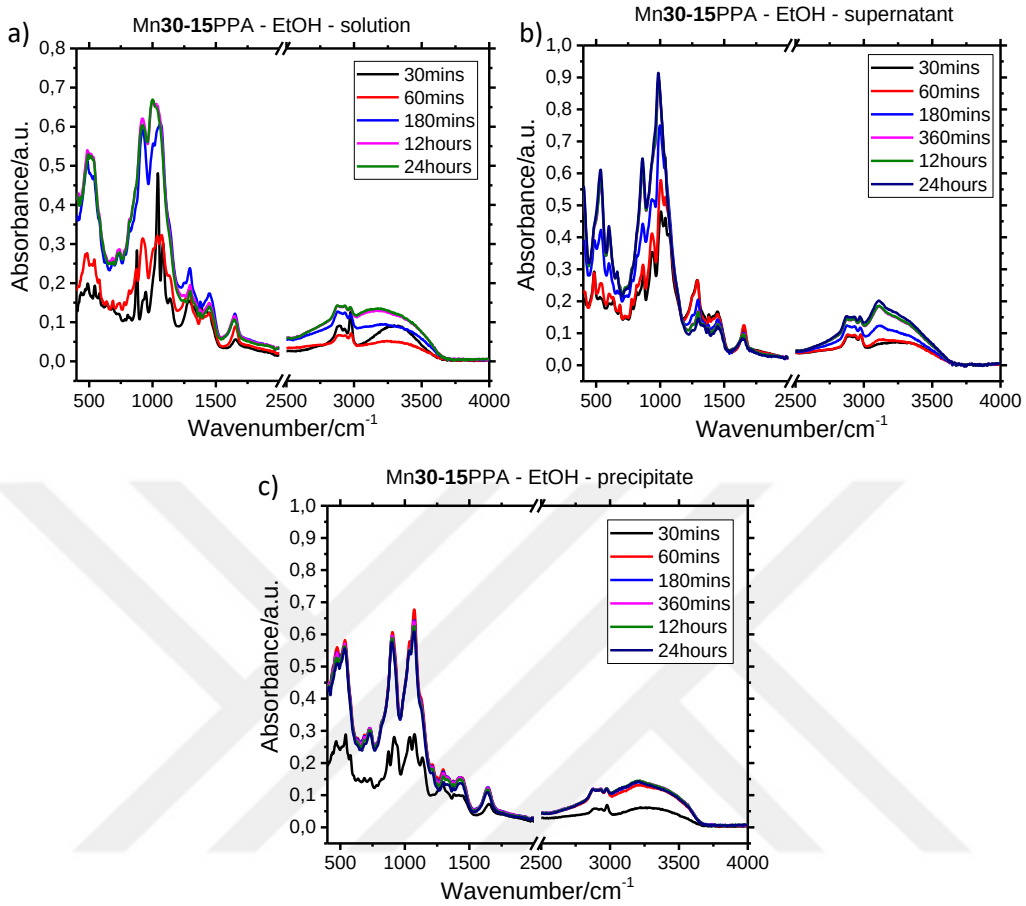


Figure 3.20: Time-dependent ATR-FTIR spectra of Mn(II):PPA:P123 (30-15PPA) ethanol a) solution, b) supernatant, and c) precipitate parts.

There is also a clear difference in the phosphate region. While the phosphate region is very similar in solution and precipitate parts, two almost the same absorbance signals, in supernatant region the absorbance difference between the asymmetric and symmetric stretchings in phosphates changes which is an indication of another phase or other species' formation.

$$\mathbf{2Mn(NO_3)_2 + H_4P_2O_7 + nH_2O \rightarrow Mn_2H_xP_2O_7(NO_3)_x.nH_2O(s) + (4-x)HNO_3(g)} \quad \textbf{Eqn. 3}$$

3.1.3.2. Mn(II):PPA:P123 Butanol System

Manganese pyrophosphate solution, prepared in butanol solvent, also undergoes a sol-gel process. However, the gel-phase is less stable compared to both cobalt and nickel systems.

While in both solution and precipitate parts there is no ordered mesophase formation, in the supernatant part, an ordered mesophase forms, see Figure 3.21.

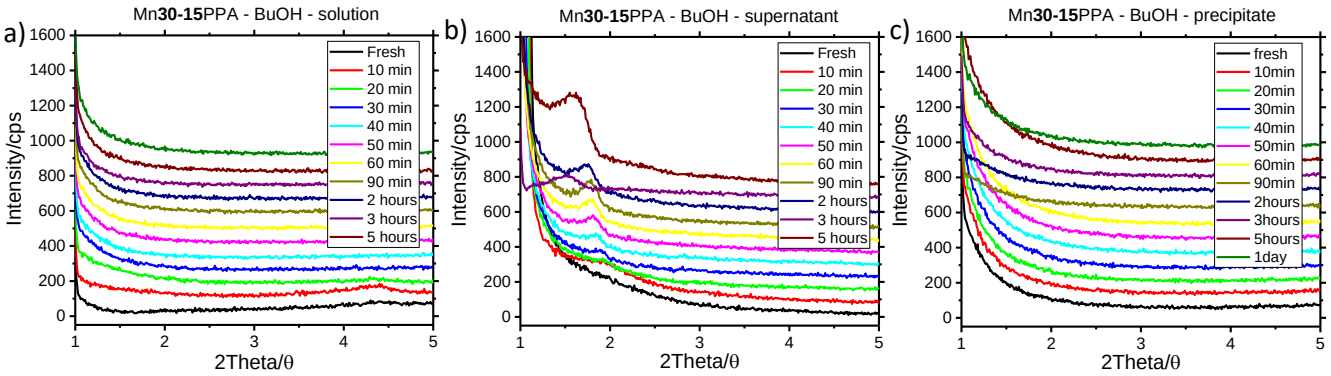


Figure 3.21: Time-dependent small-angle XRD patterns of the Mn(II):PPA:P123 samples in a) solution, b) supernatant, and c) precipitate parts.

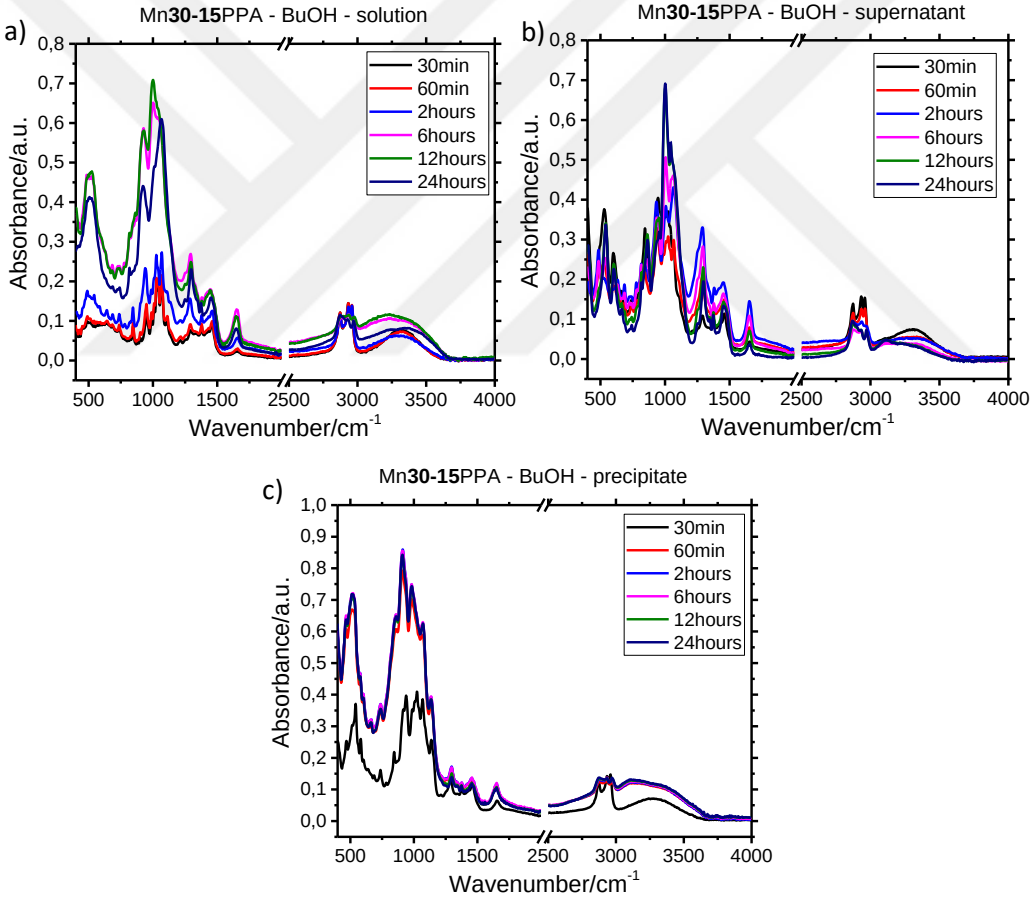


Figure 3.22: Time-dependent ATR-FTIR spectra of Mn30-15PPA, butanol a) solution, b) supernatant, and c) precipitate parts.

ATR-FTIR spectra of the manganese pyrophosphate butanol solution, shown in Figure 3.22, is different than that of in ethanol solution. There are more than two signals in the pyrophosphate region. However, the extend of the polymerization reaction is less in the supernatant but more in the precipitate.

3.1.3.3. Mn(II):PPA:P123 Methanol System

Manganese pyrophosphate solution, prepared in methanol, does not undergo a sol-gel process. The color of the solution is pale pink but, it turns into brownish color as it is aged. Therefore, the characterization was carried only using the freshly prepared pale pink colored solution.

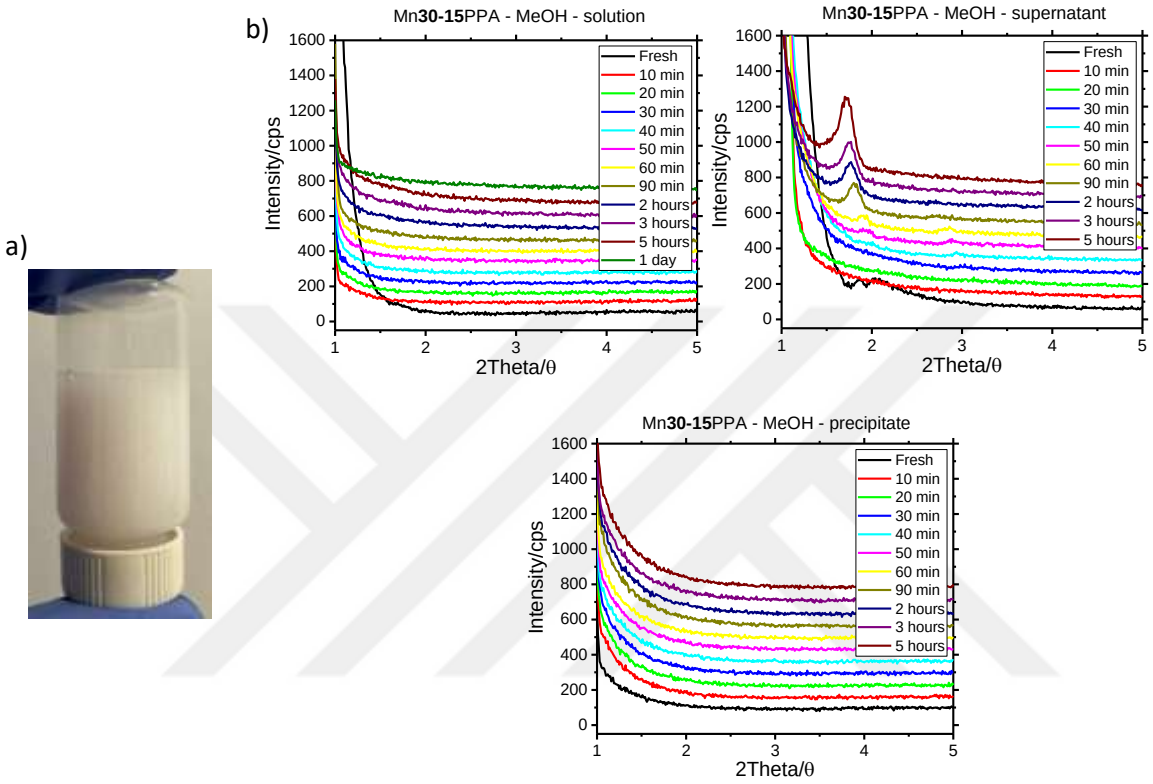


Figure 3.23: a) Photograph of the methanol solution of Mn30-15PPA and b) time-dependent small-angle XRD patterns of solution, supernatant, and precipitate parts.

The time-dependent small-angle XRD patterns of the solution, supernatant, and precipitate parts, are given in Figure 3.23. The patterns show that there is an ordered mesophase formation only in the supernatant part. Tthe diffraction lines appear after 40 minutes at 2.0 and 2.94º , 2θ, then it shifts to 1.71º, 2θ, where the second line disappears.

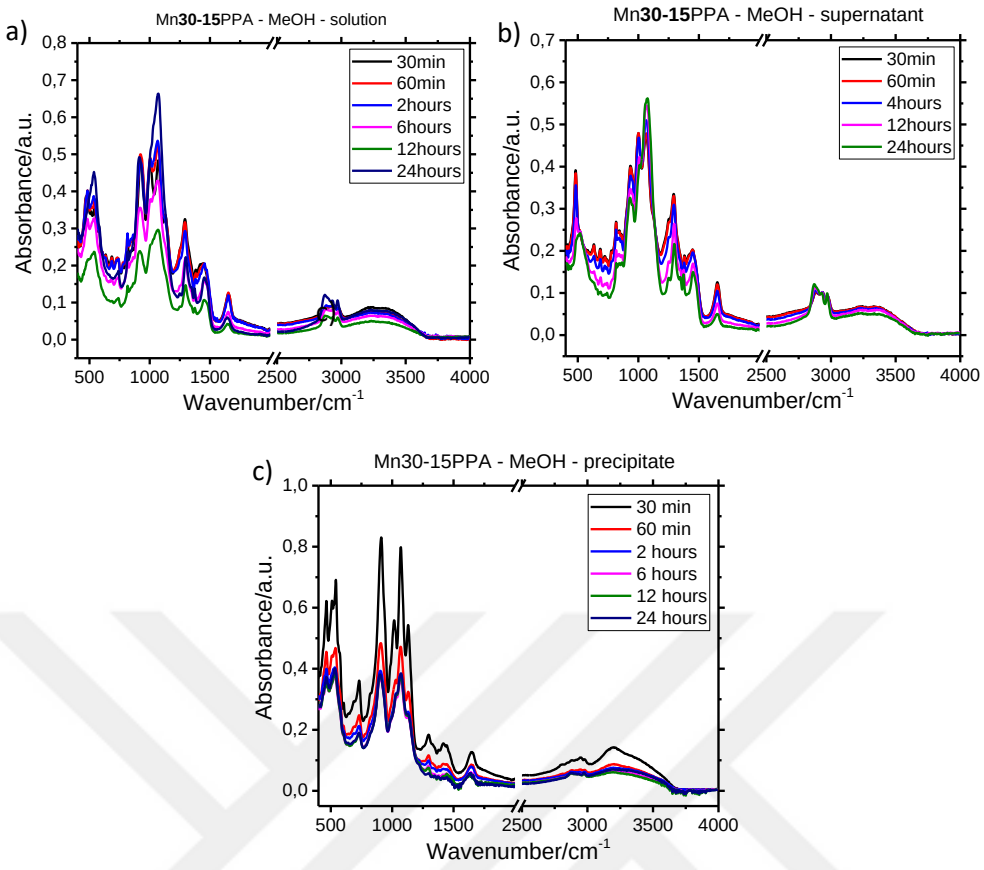


Figure 3.24: Time-dependent ATR-FTIR spectra of the methanol a) solution, b) supernatant, and c) precipitate parts.

Figure 3.24 displays the time-dependent ATR-FTIR spectra of the solution, supernatant, and precipitate parts. The spectra show that the polymerization reaction is more than supernatant and solution. However, the precipitate displays very weak nitrate peaks that eventually almost disappear in the spectra with aging.

3.1.3.4. Solvent Comparison in the Manganese System

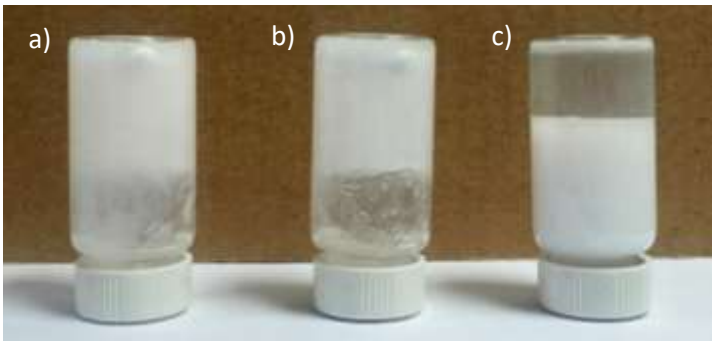


Figure 3.25: Photographs of the solutions of the Mn(II):PPA:P123 in a) butanol, b) ethanol, and c) methanol solvents.

Figure 3.25 displays the photos of the three solutions. If the solvent is butanol, there is a quick sol-gel formation. In ethanol, the gel formation takes one or two minutes similar to the other salt systems. The methanol solution stays solution, no sol-gel formation occurs. However, compared to other metals, cobalt and nickel, the sol-gel formation with manganese salt is much less stable. The colors of these solutions turn to pale pink color with aging for five to ten minutes and it goes to light brown color as they are further aged, namely one or two days.

Amount of the precipitate, collected after the centrifugation, is more in butanol and least in the methanol solution. Also, in the supernatant part, there is an ordered mesophase formation in each of these solvent systems but, in the solution and precipitate parts, there is no ordered structure, as the small-angle XRD patterns suggest. However, it should be noted that coating the gels on microscope slides, as a thin sample, is very difficult. Therefore, the thickness of these samples, solution and precipitate parts, may hinder the ordered mesophase formation.

In each of these solutions, the nitrates are very quickly decomposing out from the samples. It is hard to see the amount of the nitrates in these samples because the solvents are dominating the spectra at least first 30 minutes of aging. Controlling the sol-gel process may provide a control on the nucleation and growth and the particle size/pore-wall thickness. If the nucleation step is faster than the growth, the gelation step may yield highly porous and high-surface-area materials (see latter).

3.1.4. Synthesis and Characterization of Mesoporous $Co_2P_2O_7$

3.1.4.1. Ethanol System

The Co(II):PPA:P123 sol-gel solution is directly poured into a pyrex petri dish in order not to disturb the gel-phase and kept in oven at 100ºC for 1 day. The sample is completely dried and the powder collected is first ground in a mortar, then it is put into a combustion crucible and calcined at 300ºC to remove the surfactant to obtain mesoporous $Co_2P_2O_7$ powders. This sample is then further annealed up to 700ºC and characterized at each calcination step by several techniques. The first observation for these calcined samples is their colors. At 100ºC, the color of the powder is pink but, it turnes into black colored powder at higher calcination temperatures, see Figure 3.26.

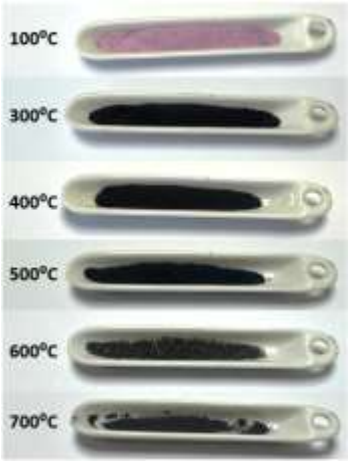


Figure 3.26: Photographs of the mesoporous $Co_2P_2O_7$ samples, obtained from Co30-15PPA ethanol solution, calcined at different temperatures.

The XRD patterns of the $Co_2P_2O_7$ samples, calcined at different temperatures, are given in Figure 3.27(b). The powders are amorphous up to 600ºC and becomes crystalline over 600ºC. All the diffraction lines can be indexed to ICDD-00-013-0503 card of the α-$Co_2P_2O_7$ in the ICDD bank. In the ATR-FTIR spectra of the calcined samples, see Figure 3.27(a), the peaks at high frequency region (1050-1200 cm^{-1}) correspond to pyrophosphate groups. The peaks at around 750-930 cm^{-1} result from the symmetric and asymmetric modes of the bridged P-O-P group and the peaks around 500-600 cm^{-1} result from the bending modes of the pyrophosphates and also Co-O sretching modes [83]. As the sample crystallizes above 600ºC, the pyrophosphate peaks become much better resolved and sharper and consistent with the XRD data.

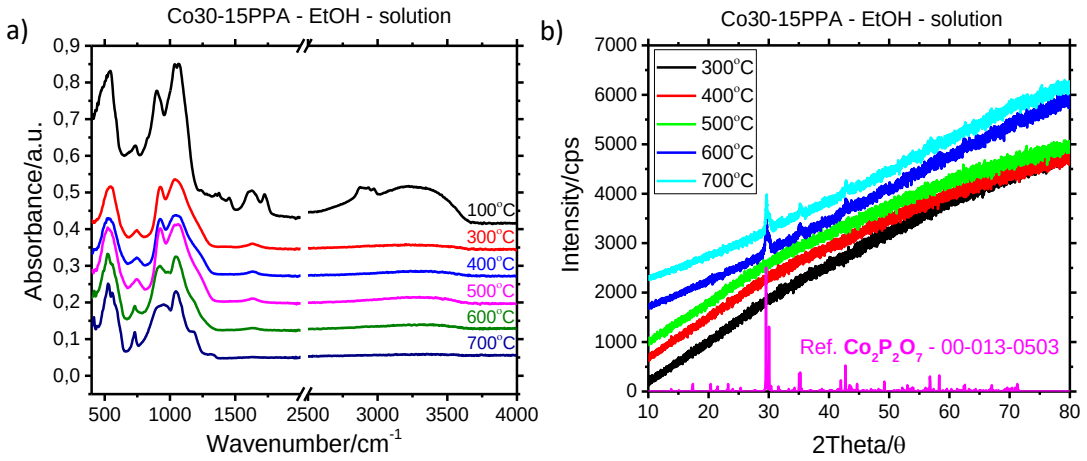


Figure 3.27: a) ATR-FTIR spectra and b) XRD patterns of the $Co_2P_2O_7$ samples, obtained from ethanol solution and calcined at indicated temperatures.

The supernatant part is also drop-cast coated on microscope slides and calcined at 300ºC in a pre-heated oven for 1 hour. Then, the samples are scrapped from the glass surface and

collected in combustion crucibles to calcine further at higher temperatures. Figure 3.28 displays the ATR-FTIR spectra and high-angle XRD patterns of the powders. The sample is amorphous up to 600ºC. It becomes crystalline at 600ºC and gives diffraction lines that match with $Co_3(PO_4)_2$ crystal rather than $Co_2P_2O_7$. SEM and TEM images are shown in Figure 3.29. The images display disordered mesopores throughout the particles.

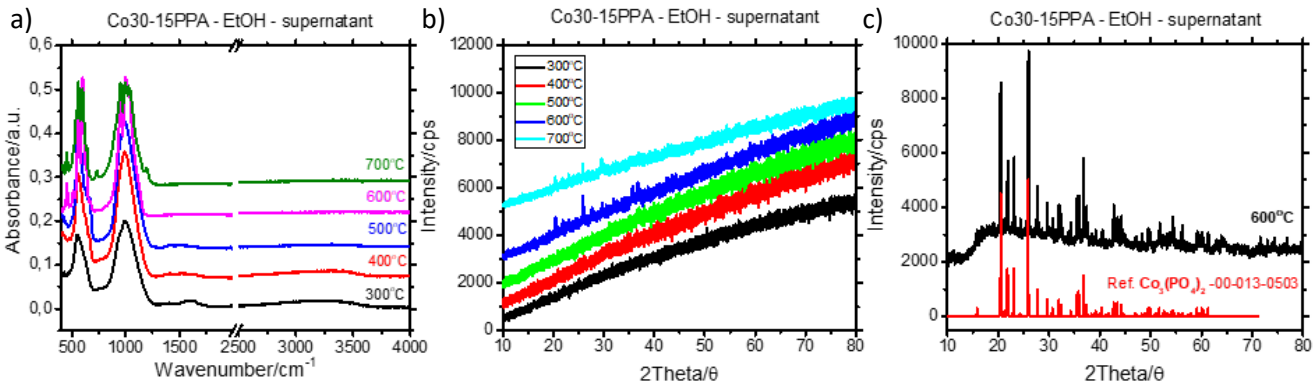


Figure 3.28: a) ATR-FTIR spectra and high angle XRD patterns of the b) $Co_3(PO_4)_2$ powders at different calcination temperatures, and c) $Co_3(PO_4)_2$ powder calcined at 600ºC together with reference $Co_3(PO_4)_2$ (red, ICDD – 00-013-0503).

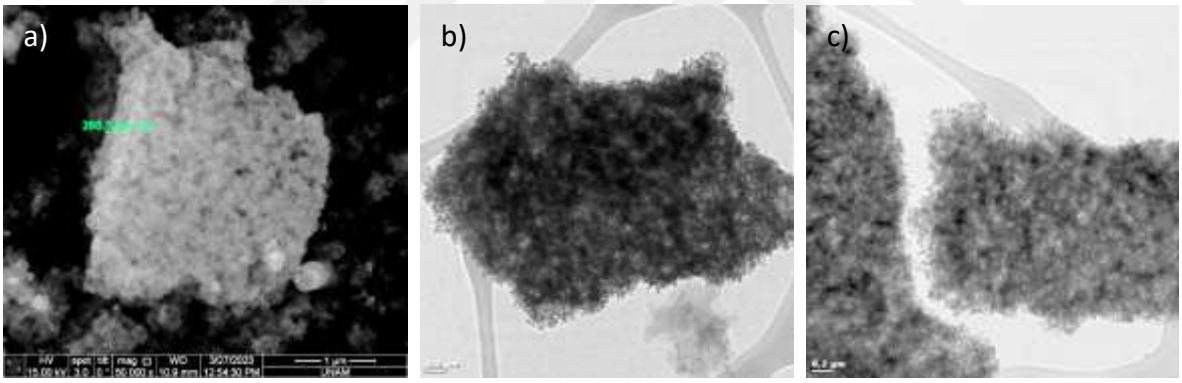


Figure 3.29: a) SEM, b), and c) TEM images of the powder, obtained from supernatant part of ethanol solution, calcined at 500ºC.

After the supernatant part is removed from the centrifuge tube, the tube with the precipitate is put into an oven at 100ºC for 1 day to remove the solvent. Next day, the dried powder is first ground in a mortar, then the powder is put into combustion crucible and calcined at different temperatures (300-700ºC). Calcination of the precipitate part also produces mesoporous $Co_2P_2O_7$ similar to the solution phase. Figure 3.30 displays their ATR-FTIR specra and XRD patterns. The spectra and patterns are very similar to those of the samples, obtained from the solution phase (compare Figures 3.27 and Figure 3.30)

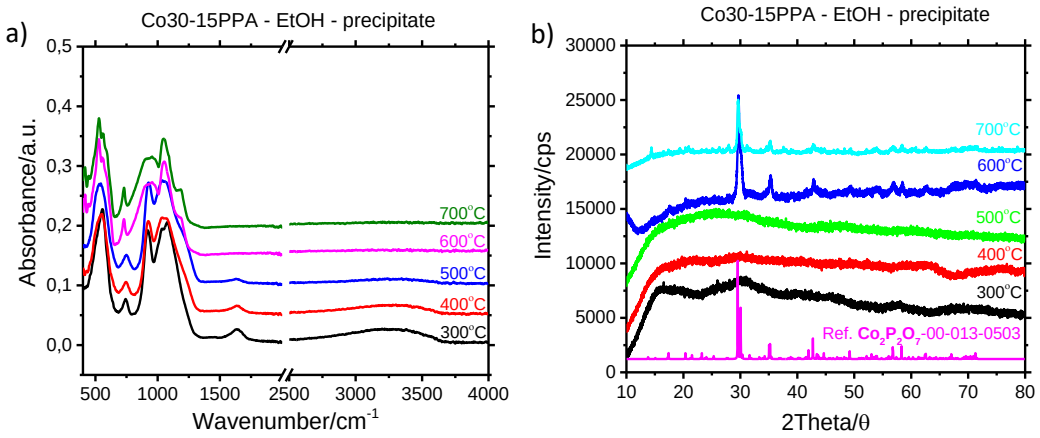


Figure 3.30: a) ATR-FTIR spectra and b) high angle XRD patterns of the mesoporous $Co_2P_2O_7$ powders at different calcination temperatures with reference $Co_2P_2O_7$ (pink, ICDD – 00-013-0503).

N_2 (77 K) adsorption-desorption measurement is also conducted to check the porosity, surface area, pore size, and pore widths of these samples. The isotherms and Barrett-Joyner-Halenda (BJH) pore size distribution plots are shown in Figure 3.31. Brauner-Emmett-Teller (BET) surface area and other surface properties of the calcined samples are tabulated in Table 3.1.

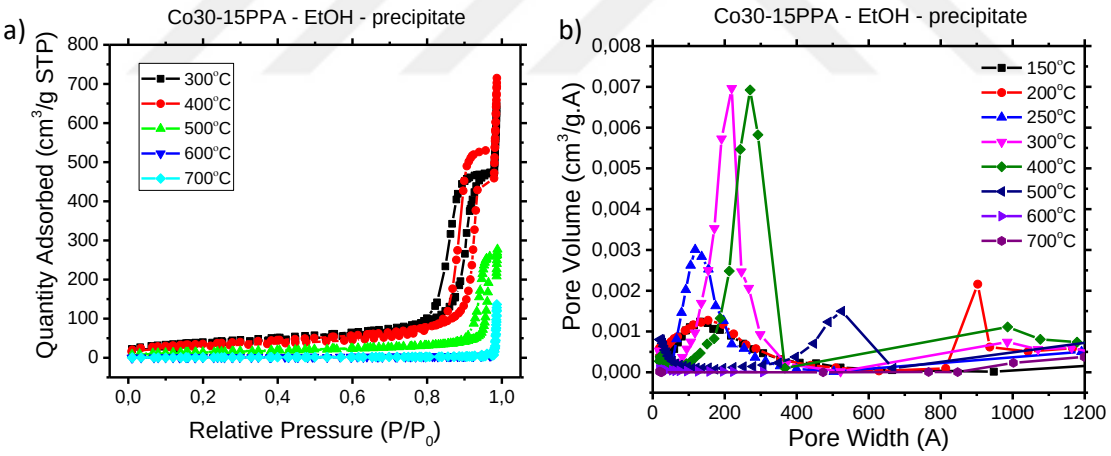


Figure 3.31: a) N_2 (77 K) adsorption and desorption isotherms and b) BJH pore-size distribution plots of the $Co_2P_2O_7$ samples, obtained from the precipitate part of the ethanol solution.

In order to understand the reason for the porosity, whether it is because of the removal of the surfactant or the sample is porous as well, the dried sample at 100ºC is calcined at 150, 200, 250ºC as well. And the pore size distributions and porosity informations are also given in Figure 3.31 and Table 3.1 as well. At 150ºC, the BET surface area of the powder is 67 m^2/g. At this calcination temperature, the P123 surfactant can not be removed from the powder, but yet the $Co_2P_2O_7$ is already have a porous structure. However, above 300ºC, the surfactant is

completely removed from the sample and it results in highly porous, high surface area material. Upon further calcination, the $Co_2P_2O_7$ species start to grow and pores start to collapse. However, because of the pore-wall growth, there are macroporous regions at higher calcination temperatures (see Figure 3.32). Figure 3.33 shows a schematic representation for this process.

Table 3.1: BET surface area, BJH pore width, and pore volume of the $Co_2P_2O_7$ samples, obtained from the precipitate part of the $Co_2P_2O_7$ ethanol solution.

Calcination Temperature (°C)	BET Surface Area (m^2/g)	Pore Width (Å)	Pore Volume (cm^3/g)
150	67	107	0.44
200	94	152	0.66
250	78	117	0.63
300	145	139	0.99
400	127	176	1.10
500	60	525	0.47
600	5	-	-
700	3	-	-

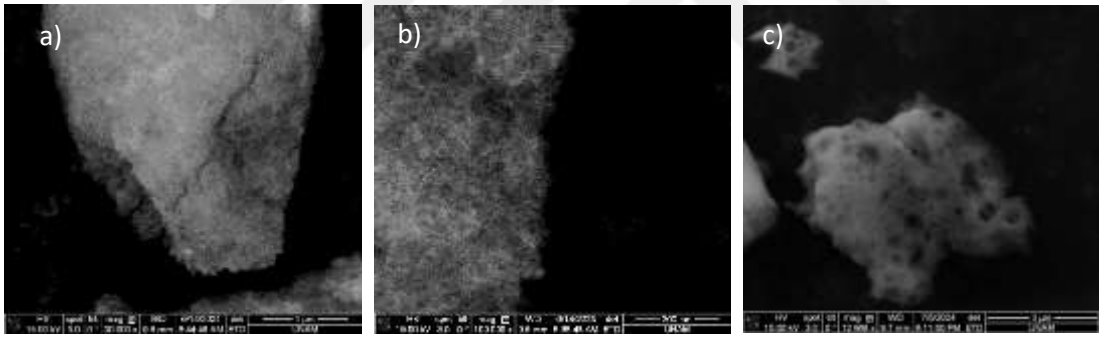


Figure 3.32: a) SEM image of the $Co_2P_2O_7$ samples, calcined at a) 300ºC, b) 500ºC, and c) 700ºC.

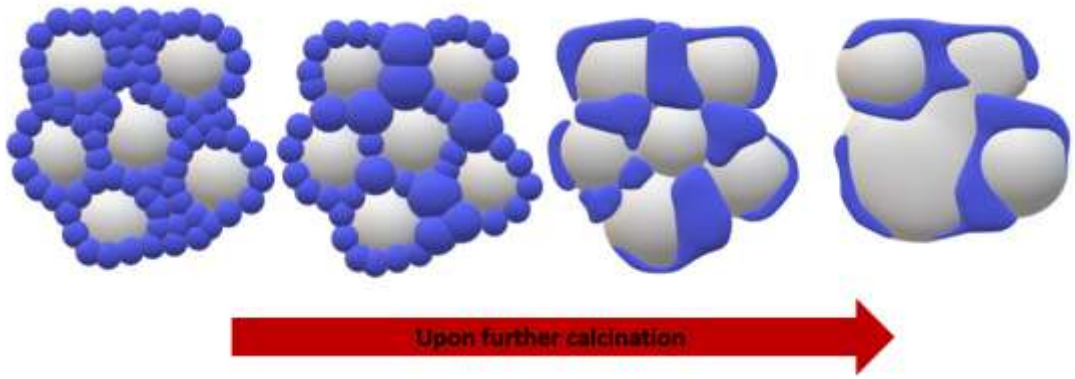


Figure 3.33: The schematic representation of the change in the porosity upon further calcination of the $Co_2P_2O_7$ samples (blue spheres represent $Co_2P_2O_7$ particles/pore-wall and light gray spheres are the pores).

The $Co_2P_2O_7$ powders, obtained from ethanol solution are mesoporous materials. And the porosity is not only coming from the burned out surfactant domains, the sample itself is porous as well. From the calcination of gel-phase and precipitate parts at 600ºC, α-phase $Co_2P_2O_7$ crystals are obtained. However, the supernatant part is phosphate deficient and forms the crystalline $Co_3(PO_4)_2$, not $Co_2P_2O_7$ phase.

3.1.4.2. Butanol System

Butanol 30-15PPA solution quickly forms a gel through sol-gel process. Then, in order not to disturb the gel-phase, it is poured into a pyrex cup and dried at 100ºC for 1 day. The color of the dried sample is purple, see Figure 3.34. Then, this sample was ground in a mortar, and calcined at 300ºC and further annealed. The colors of these samples change from purple to black and at 700ºC it turns back to purple color, indicating presence of some tetrahedral coordinated sides. Note that tetrahedral Co(II) compounds are blue in color and that of the octahedral ones are pink. Moreover, the tetrahedral species are almost 10-100 times stronger in intensity than octahedral ones. Therefore, a small percentage of Co(II) species may be in the tetrahedral side in the crystalline $Co_2P_2O_7$.

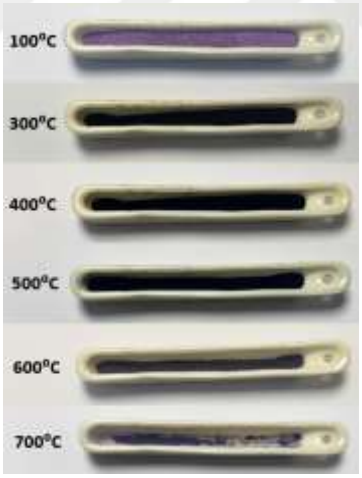


Figure 3.34: Photographs of the $Co_2P_2O_7$ samples, prepared from the Co30-15PPA butanol solution and calcined at different temperatures.

Figure 3.35(a) shows the ATR-FTIR spectra of the calcined samples. The peak around 750 cm^{-1} is characteristic for a bend P-O-P moiety in the cobalt pyrophosphate. Therefore, this peak is a strong evidence for the formation of cobalt pyrophosphate even at 300ºC. However, in one of the phases of metal pyrophosphates, the P-O-P unit is linear and the its symetric stretching mode is IR inactive, not observed. Also, the crystallization starts at 600ºC and yields the α-phase $Co_2P_2O_7$, evidenced from high-angle XRD measurements, see Figure 3.35(b).

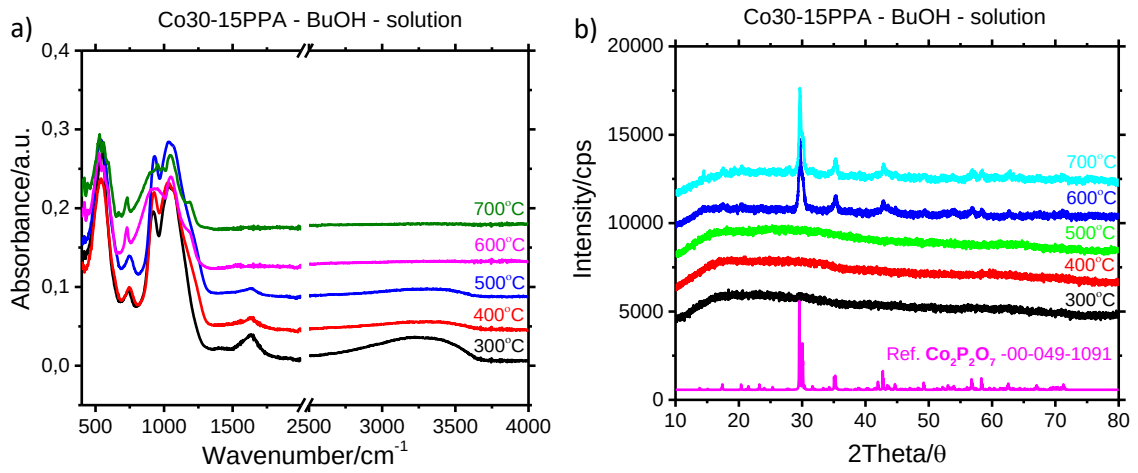


Figure 3.35: a) ATR-FTIR spectra and b) high-angle XRD patterns of the calcined samples of the Co30-15PPA butanol solution part.

ATR-FTIR spectra can also provide some indirect evidence about porosity and surface area. The ATR-FTIR spectra, in the water stretching region of the calcined samples at 300, 400 and 500ºC, show evidence for the presence of water in the samples. The samples with high surface area have large amount of water that gradually decreases with increasing annealing temperature. These water molecules fill the pores in the samples (Figure 3.35(a)) and its amount depends on the surface area and pore-volume. Therefore, it may be used to qualitatively determine the porosity in the samples. The SEM images in Figure 3.36 are recorded from these samples at 300, 400, and 500°C. Presence of flake like particles with porous structure are strong evendiences for the formation of porous film-like morphology. The pores expand and become visible in the images of the samples, annealled at higher temperatures (compare images in Figure 3.36).

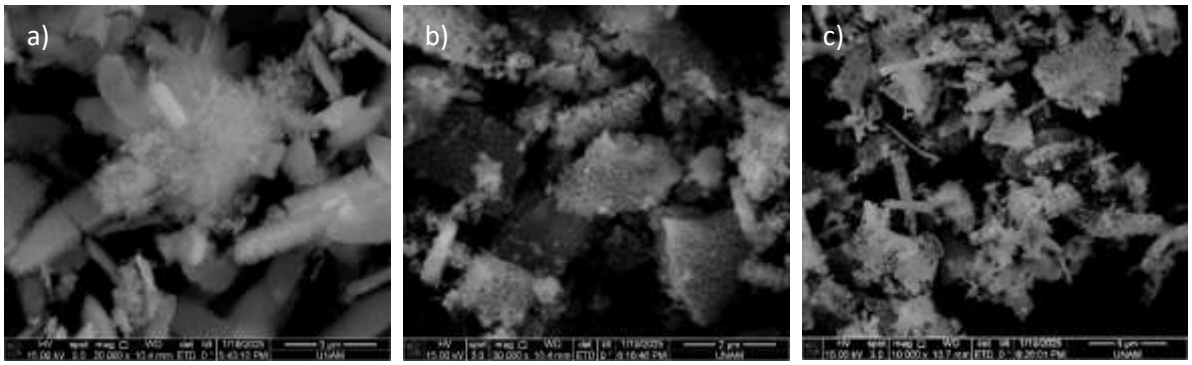


Figure 3.36: SEM images of the samples, prepared from Co30-15PPA butanol supernatant part, calcined at different calcination temperatures; a) 300ºC b) 500ºC, and c) 700ºC.

After removing the supernatant part, the precipitate left in centrifuge tube is dried in 100ºC oven for 1 day. Then, it is ground in a mortar and calcined in a at 300ºC in pre-heated

oven for 1 hour. The ATR-FTIR spectra of the powders and high-angle XRD patterns collectively show that the powders crystallize at around 600ºC into α- $Co_2P_2O_7$, see Figure 3.37.

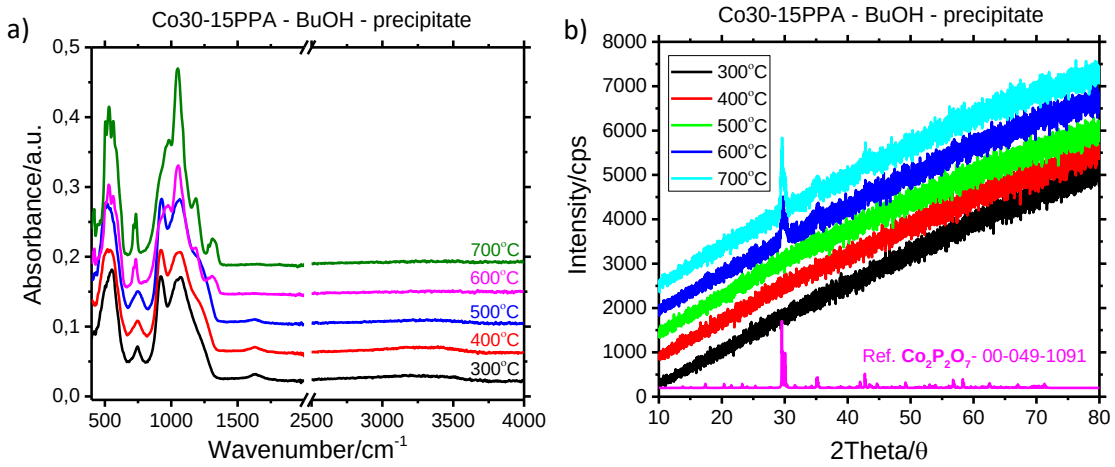


Figure 3.37: a) ATR-FTIR spectra and b) high-angle XRD patterns of the samples from calcined Co30-15PPA butanol precipitate part.

The ATR-FTIR spectra also display water peaks up to 600ºC. It means that the powders have porous structure and hold water in the pores. As the calcination temperature increases, the amount of water decreases as expected. Because as mentioned before and shown in Figure 3.33, as the calcination temperature increases, the smaller pores start to collapse and the pore-wall grow and crystallize. The N_2 adsorption-desorption isotherms are also collected and displayed in Figure 3.38(a). The BET surface area, BJH pore width, and pore volume values are tabulated in Table 3.2. These data also accord well with the ATR-FTIR data.

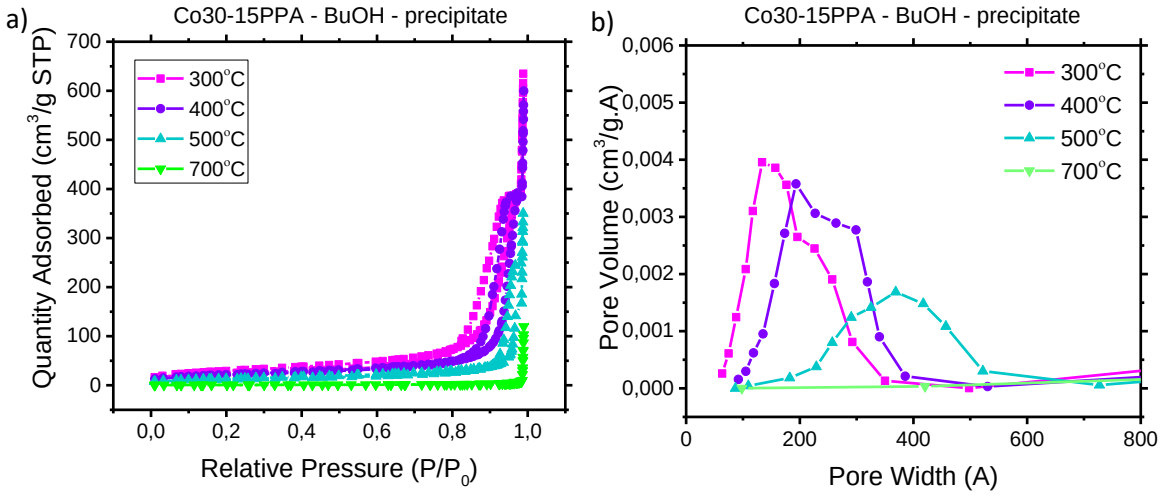


Figure 3.38: a) N_2 (77 K) adsorption-desorption isotherms, and b) BJH pore size distribution plots of the $Co_2P_2O_7$ samples, obtained from the precipitate part of the butanol solution.

Table 3.2: The BET surface area, BJH pore width, and pore volume values of the calcined $Co_2P_2O_7$ samples, obtained from the Co30-15PPA butanol precipitate.

Calcination Temperature (ºC)	BET Surface Area (m^2/g)	Pore Width (Å)	Pore Volume (cm^3/g)
300	124	153	0.93
400	79	248	0.93
500	48	375	0.54
700	3	-	0.16

The $Co_2P_2O_7$ powder (from Co30-15PPA butanol solution precipitate parts) has a relatively high surface area at lower calcination teperatures with an amorphous structure. SEM images (Figure 3.39) display flake-like morphology at 300ºC and it is also an indication of thin-film formation. At higher calcination temperatures, the surface area drops to 48 m^2/g and pores expand even though the sample is still amorphous. When the calcination temperature increases to 700ºC, the sample becomes crystalline and the surface area decreases drastically, The SEM images also display larger macropores.

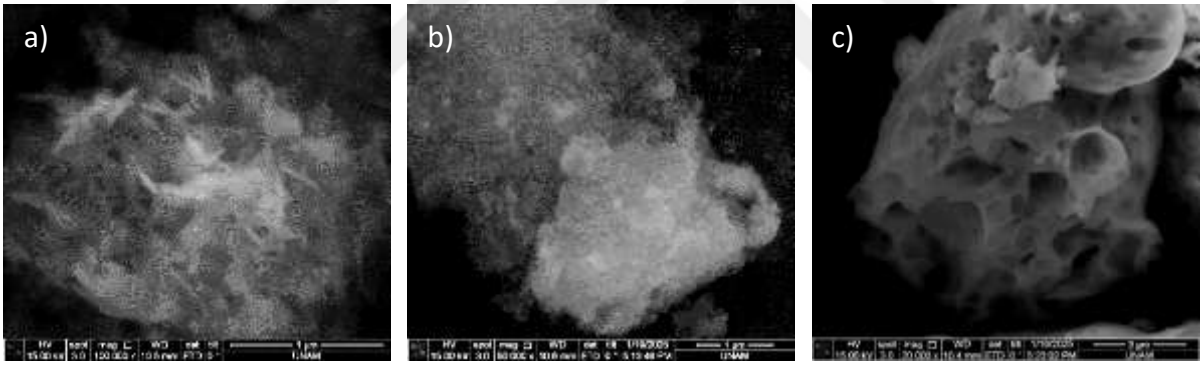


Figure 3.39: SEM images of the Co30-15PPA butanol precipitate, calcined at different temperatures; a) 300ºC b) 500ºC, and c) 700ºC.

3.1.4.3. Methanol System

Remember that the methanol Co30-15PPA solution is cloudy, pale-pink colored solution and does not undergo a sol-gel process. In order to compare these samples with the samples of the other solvent systems, this solution is also poured into a pyrex cup and dried at 100ºC for 24 hours to remove the solvent. The dried powder is then collected and ground in a mortar and then calcined at 300ºC for 1 hour in a pre-heated oven. These powders are also further annealed at higher temperatures, namely 400, 500, 600 and 700ºC, and at each calcination temperature the samples are characterized using the same techniques. Figure 3.40 displays the colors of these powders at various calcination/annealing temperatures. At 300ºC,

the color of the powder is lighter brown than that of the 400, 500 and 600ºC calcined samples. However, it is almost grey at 700ºC.

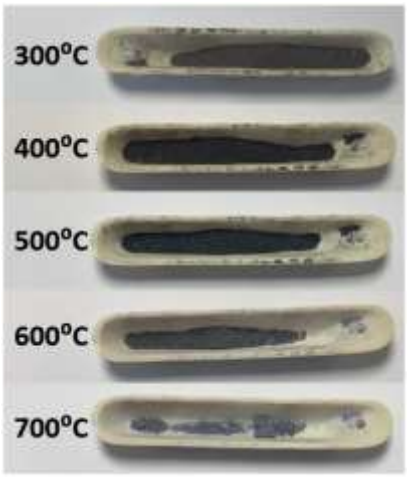


Figure 3.40: Photographs of the $Co_2P_2O_7$ samples, obtained from the Co30-15PPA methanol solution, calcined at different temperatures.

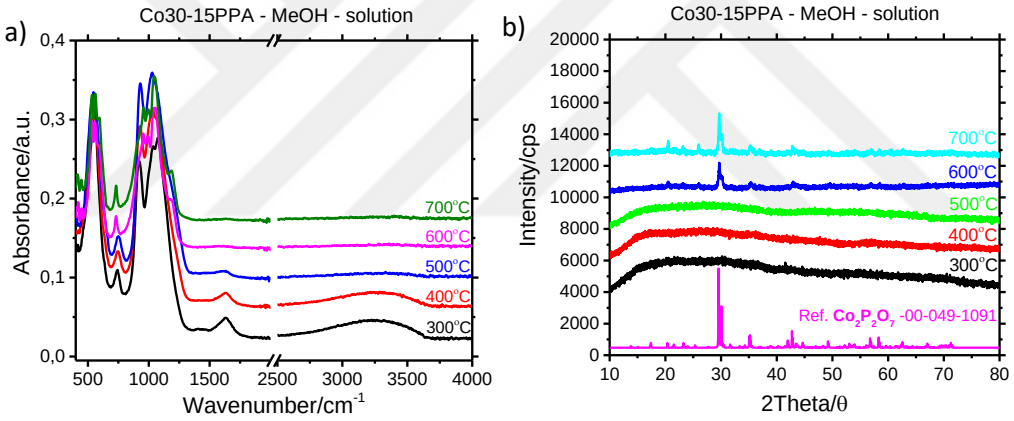


Figure 3.41: a) ATR-FTIR spectra and b) high-angle XRD patterns of calcined samples of the Co30-15PPA methanol solution.

ATR-FTIR spectra of these calcined samples display characteristic pyrophosphate peaks together with intense water peaks that almost disappear over 600ºC, see Figure 3.41(a). The bridging P-O-P asymmetric stretching peak at around 750 cm^{-1} becomes sharper at 600ºC, indicating crystallization of the amorphous $Co_2P_2O_7$. The high-angle XRD pattern of the sample at 600ºC, also correlate the assignment, Figure 3.41(b). Notice that the samples are amorphous below this temperature. The diffraction lines are indexed to the α-phase of $Co_2P_2O_7$.

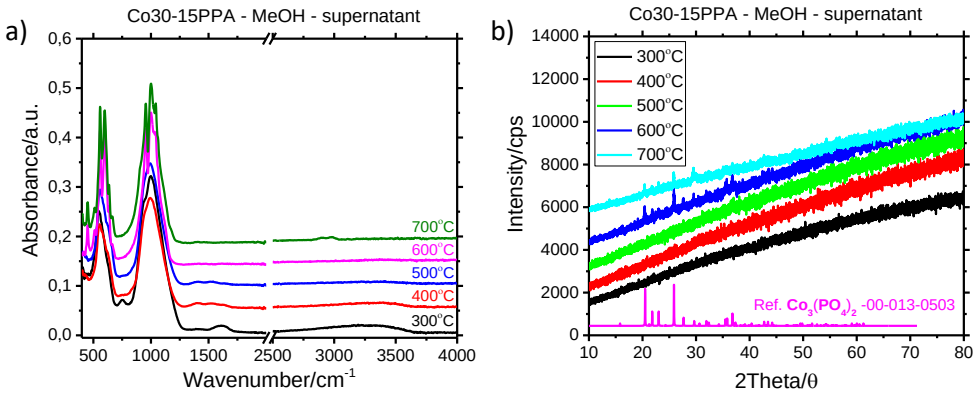


Figure 3.42: a) ATR-FTIR spectra and b) high-angle XRD patterns of calcined samples of the Co30-15PPA methanol solution.

Since the solution is not clear, the supernatant part is separated and characterized upon calcination. Figure 3.42 displays the ATR-FTIR spectra and high-angle XRD patterns of the samples, obtained by calcining the Co30-15PPA methanol supernatant. The pyrophosphate region of the spectra are quite different than the solution part, because the supernatant part forms $Co_3(PO_4)_2$ rather than $Co_2P_2O_7$ as predicted from their XRD patterns. Presence of the water peaks is also indecation for the porosity in the samples. The sample crystallizes at 600ºC at which the ATR-FTIR signals becomes sharper. Also the XRD line can be indexed to the PDF card of $Co_3(PO_4)_2$.

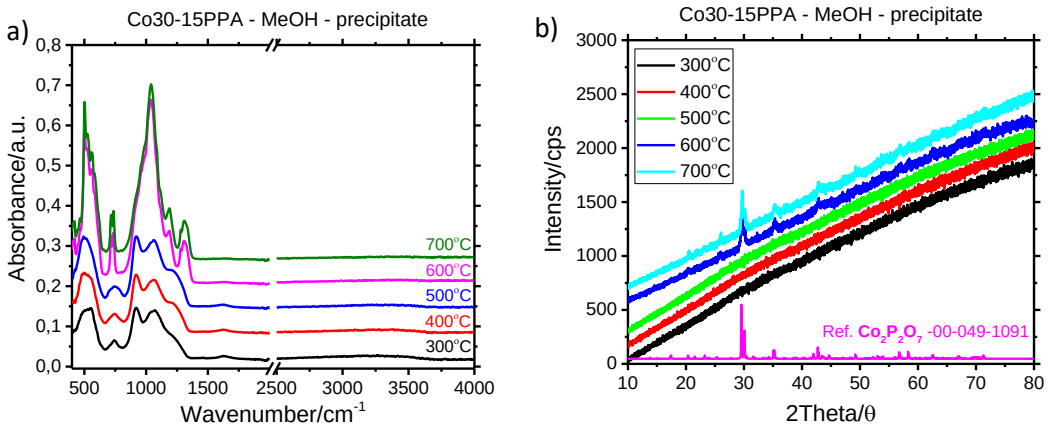


Figure 3.43: a) ATR-FTIR spectra and b) high-angle XRD patterns of the calcined samples of the Co30-15PPA methanol precipitate.

Unlike the supernatant part, the calcination of the precipitate produces mesoporous $Co_2P_2O_7$ powders that crystallize at around 600°C, evidenced in both ATR-FTIR spectra and high-angle XRD patterns (Figure 3.43). The sample is amorphous below 600°C and holds some water molecules that indirectly indicate porosity. However, the surface area in this sample is

low and displays a broad pore-size distribution, which are consistent with the observed weak water peaks in the ATR-FTIR spectra.

Table 3.3: The BET surface area, BJH pore width, and pore volume values of the calcined $Co_2P_2O_7$ samples, obtained from the Co30-15PPA methanol precipitate.

Calcination Temperature (°C)	BET Surface Area (m^2/g)	Pore Width (Å)	Pore Volume (cm^3/g)
300	48	-	-
400	35	219	0.61
500	21	436	0.41

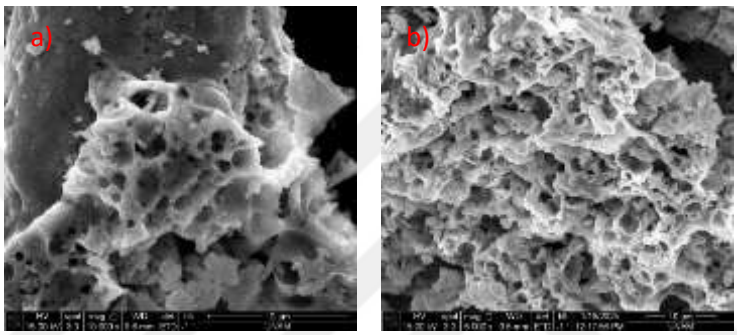


Figure 3.44: SEM images of the Co30-15PPA methanol precipitate, calcined at a) 300ºC and b) 400ºC.

3.1.4.4. Solvent Comparison of Mesoporous $Co_2P_2O_7$

The first difference between these three solvents is the colors before and after the calcination steps, see Figure 3.45. Before the calcination step, the sol-gel formation is observed in ethanol and butanol solvents and the colors of these solutions are darker than that in methanol. After calcination, again, the color of the calcined solution samples in ethanol and butanol are darker than that in methanol. Also, the calcined $Co_2P_2O_7$ from solutions of ethanol and butanol have shiny parts which reflect the light, which is commonly attributed to film formation and interference effects [84].

In each of these solvents, calcination of the solution and precipitate at 600ºC result in α-$Co_2P_2O_7$ crystals. However, the $Co_3(PO_4)_2$ crsytals are obtained when the supernatant part is calcined at 600ºC.

The surface area and porosity is the highest in the samples obtained from ethanol whereas the lowest from methanol precipitate. Moreover, the pore size distribution is uniform

in the powders of ethanol but, it is very broad in the samples of butanol and methanol precipitate.

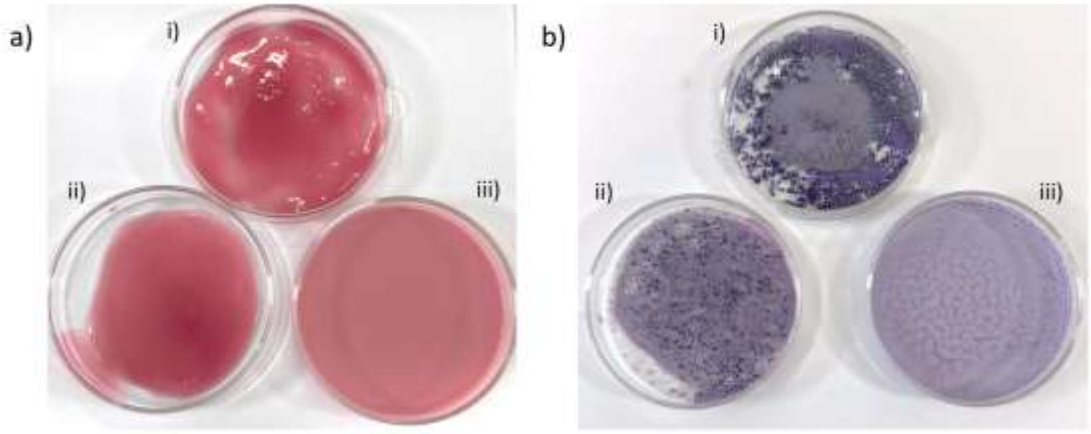


Figure 3.45: The solutions of $Co_2P_2O_7$ in i) ethanol, ii) butanol, iii) methanol solvents, a) poured into pyrex cup, and b) dried at 100ºC for one day.

3.1.4.5. Electrochemical Characterization of Mesoporous $Co_2P_2O_7$ and Its Transformation to β-$Co(OH)_2$

Since the ethanol and butanol solutions of Co30-15PPA form gels, the solutions are 5 times diluted with the alcohol used in the synthesis. These clear solutions are spin-coated over fluorine doped tin oxide (FTO) glasses or dip-coated over graphite rods (GR) and calciend at different temperatures (300-700ºC) to obtain 1 cm^2 FTO, and GR coated electrodes. A three electrode system, shown in Figure 2.5, is used in a 1 M KOH solution for the electrochemical measurements.

Firstly, the FTO coated electrodes are used to collect cyclic voltammograms (CVs) to evalute stability of the electrodes and their oxygen evolution reaction (OER) performance. Figure 3.46 shows the CVs of the FTO coated $Co_2P_2O_7$ electrodes with a scan rate of 50 mV/s in a potential window of -0.5 - 2.0 V versus NHE (normal hydrogen electrode) in a 30 ml of 1 M KOH solution as an electrolyte. The peaks due to oxidation and reduction of cobalt species appear in the first cycles with a high current density but in the second and additional cycles the peak currents display low current density and also the current density at 2.0 V decreases with cycling. This behaviour shows that the coated FTO electrodes are unstable. The degradation of the electrode deminishes with increasing the calcination temperature.

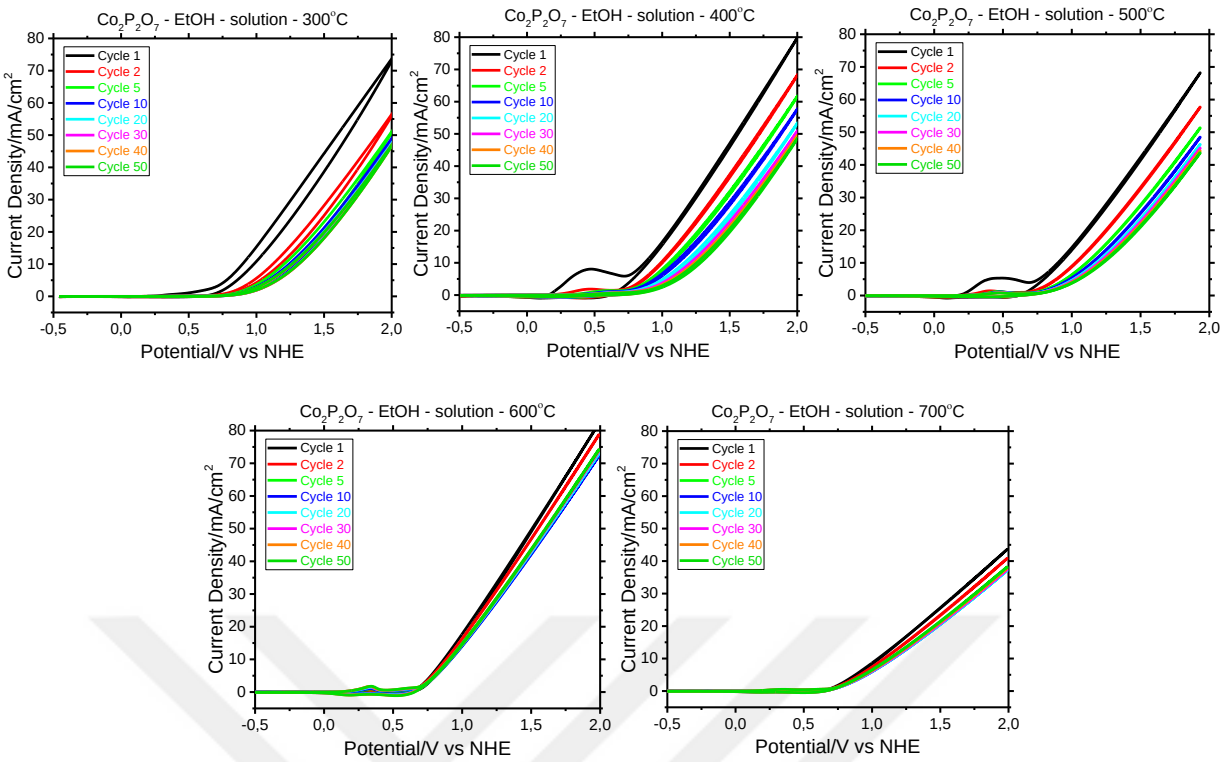


Figure 3.46: A selected group of CVs from 50 cycles in 1 M KOH electrolyte solution with a scan rate of 50 mV/s of the $Co_2P_2O_7$ (ethanol solution coated) FTO electodes.

To increase the conductivity and current density at OER, the electrolyte solution is changed to 3 M KOH solution. However, it didn't affect the electrode stability at lower calcination temperatures but the electrode calcined at 700ºC is much more stable with a significantly increased current density in OER potentials, see Figure 3.47.

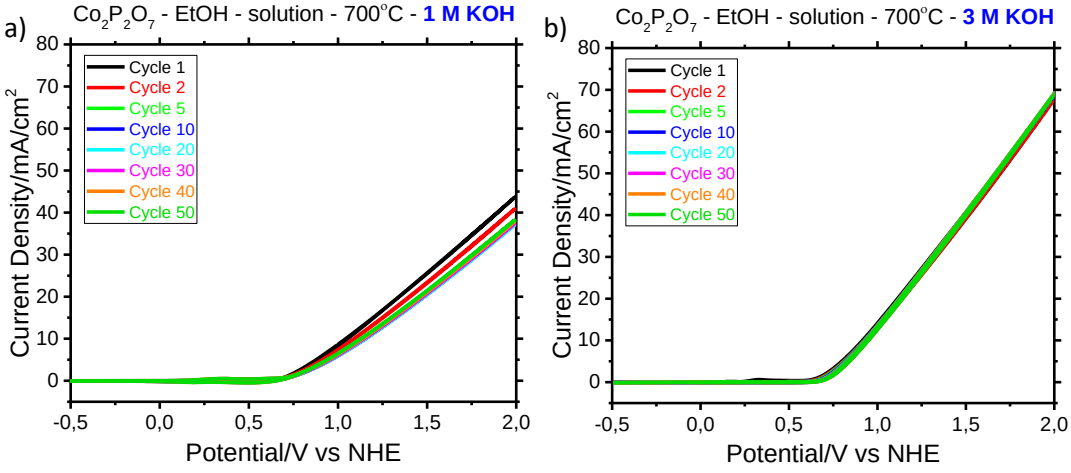


Figure 3.47: A selected group of CVs from 50 cycles of the $Co_2P_2O_7$ (ethanol solution coated) FTO electodes with a scan rate of 50 mV/s in a) 1 M KOH and b) 3 M KOH electrolyte solution.

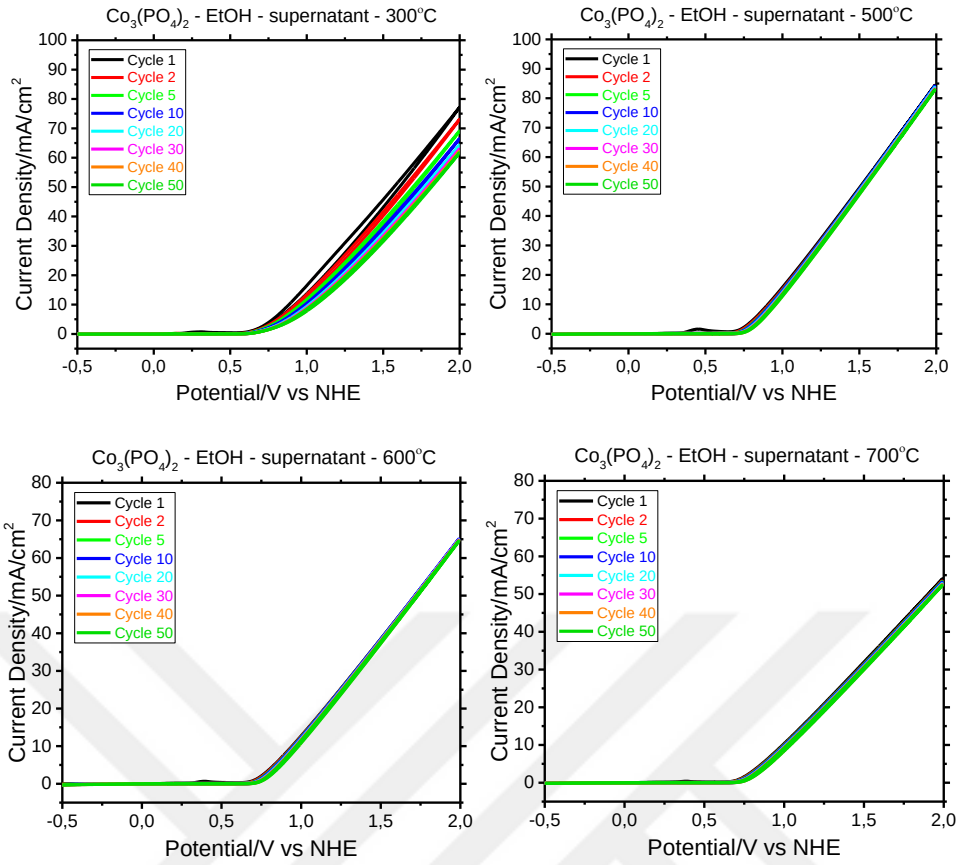


Figure 3.48: A selected group of CVs from 50 cycles in 1 M KOH electrolyte solution with a scan rate of 50 mV/s of the $Co_2P_2O_7$ (ethanol solution supernatant coated) FTO electodes.

The Co30-15PPA ethanol supernatant yields $Co_3(PO_4)_2$ crystals when the sample is calcined above 500ºC. Some of the CVs of these electrodes are given in Figure 3.48. Compared to the solution part, which yields $Co_2P_2O_7$ crystals, the electrodes, coated with the supernatant part, with $Co_3(PO_4)_2$ crystals, are more stable. Figure 3.49(a) shows the 50th CVs before CA and CP experiments and after the MCA experiments (carried at 10 and 50 mA/cm^2 current density for 15 hours at each current density) which indicate the stability of these electrodes. Figure 3.49(b)-(c) show the MCA and MCP plots of the same electrode, showing the Tafel slope (50 mV/dec) and overpotential (250 mV at 1 mA/cm^2 current density). The MCPs (15 hours at 10 and 50 mA/cm^2) are given in Figure 3.49(d); no change in the overpotential is an indication for the electrode stability. Some fluctuation in the 50 mA -15 hours CP experiments is due to fast and intense OER, namely O_2 bubbles, see Figure 3.49(e), that affect the conductivity and overpotential values.

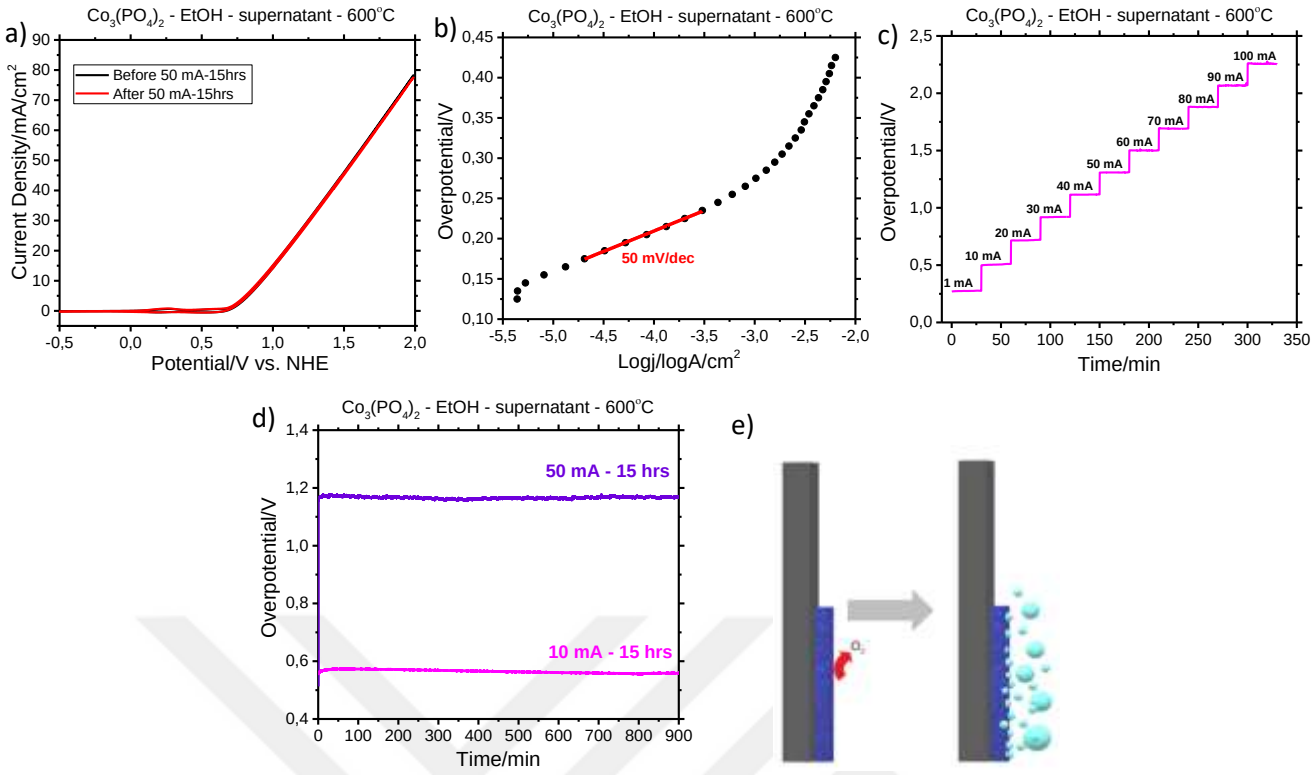


Figure 3.49: a) Three cycle CVs of the electrode coated using Co30-15PPA ethanol supernatant and calcined at 600ºC, b) chronoamperometry experiment and Tafel slope, c) and d) chronopotentiometry experiment, and e) a schematic represention of the electrode during OER.

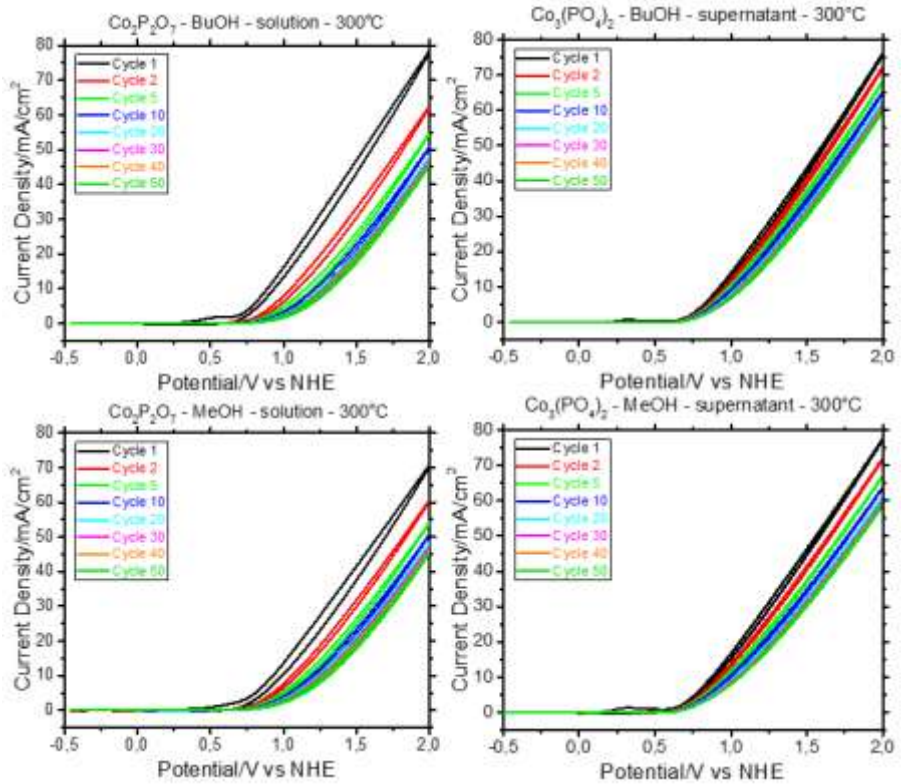


Figure 3.50: A selected group of CVs from 50 cycles in 1 M KOH electrolyte solution with a scan rate of 50 mV/s of the $Co_2P_2O_7$ from a) and b) butanol solution, c) and d) methanol solution and supernatant, coated FTO electodes (calcined at 300ºC).

Figure 3.50 shows CVs from both solution and supernatant coated on FTO electrodes. The CVs show that the electrodes are not stable on FTO substrate. Even the high temperature calcination and crystallization could not help on the electrode stability.

In order to elucidate the changes in the electrode in 1 M KOH electrolyte solution, a 0.1 g of $Co_2P_2O_7$ sample, obtained from Co30-15PPA ethanol solution, is put into 10 ml of 1 M KOH solution. One of them is directly centrifuged after keeping the sample for 5 minutes. The other samples are centrifuged after 15, 30, and 60 minutes. Then, the separated samples are washed with deionized water for 4-5 times to get rid of KOH and other impurities and dried in 80ºC oven for 1 day. As shown in the ATR-FTIR spectra in Figure 3.51(a), amount of the phosphate species decrease while the –OH species increase in these samples. The high-angle XRD patterns accord well with the spectra and shows that the samples are crystalline and the patterns are indexed well with the $Co(OH)_2$ crystals, see Figure 3.51(b). It means that the cobalt pyrophosphate is transforming to $Co(OH)_2$ in 1 M KOH electrolyte solution. Therefore, it is reasonable to suggest the following chemical equilibrium reaction (Eq.3).

$$\mathbf{Co_2P_2O_7(s) + 4OH^-(aq) \leftrightarrow 2Co(OH)_2(s) + P_2O_7{}^{4-}(aq)} \qquad \textbf{Eqn. 3}$$

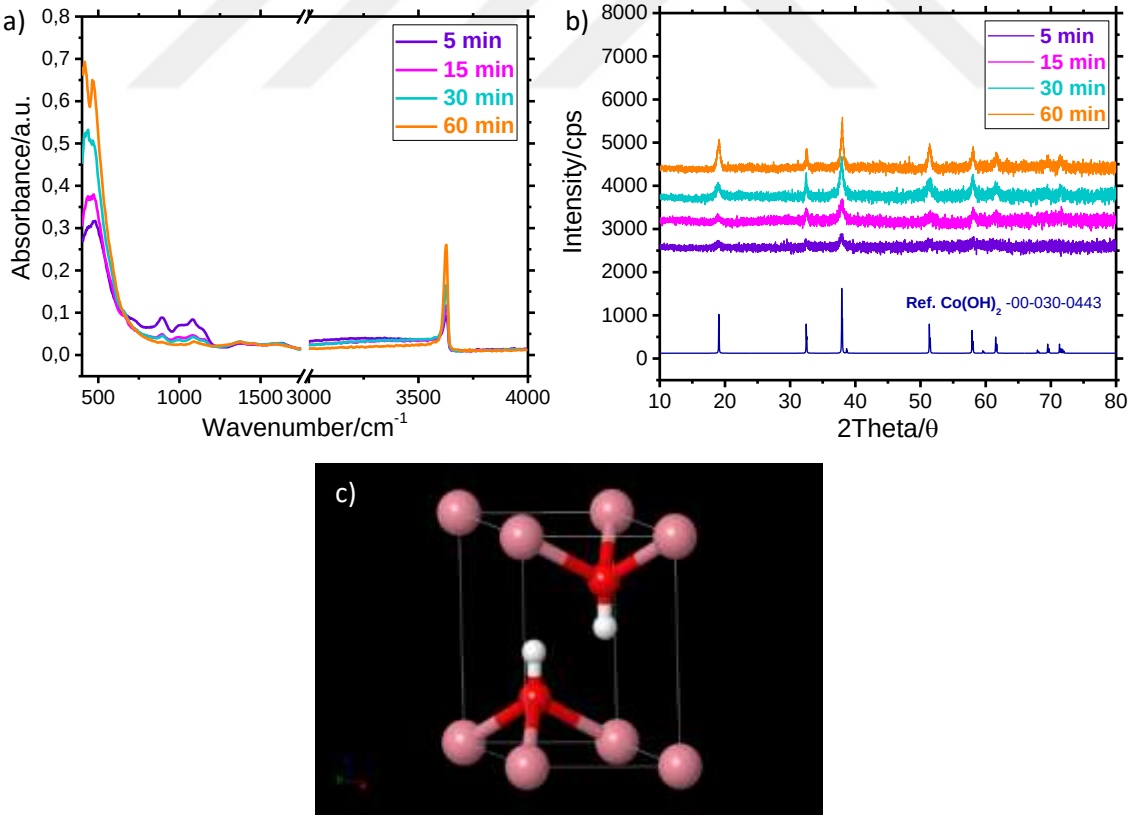


Figure 3.51: a) The ATR-FTIR spectra and b) high-angle XRD patterns of the $Co_2P_2O_7$ samples put into 1 M KOH solution. c) The unit cell structure of $Co(OH)_2$.

The SEM images shown in Figure 3.52 belongs to the $Co_2P_2O_7$ sample, aged in 3 M KOH solution, centrifuged, washed with water four times, and dried at 80ºC for 1 day. The morphology also changes and becomes plate-like under basic conditions.

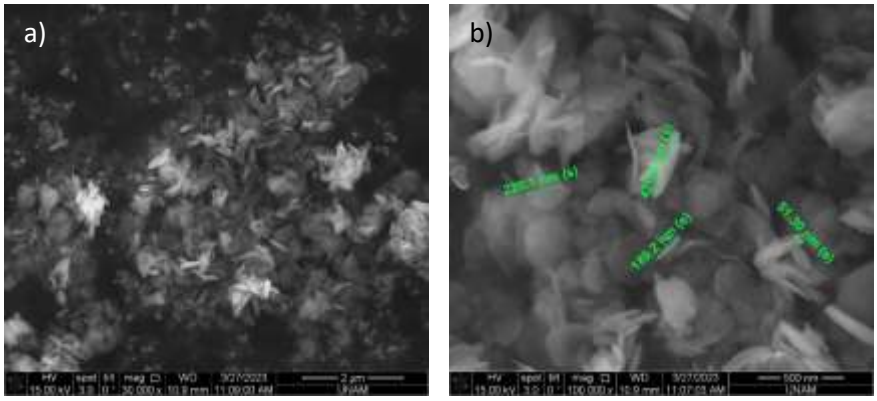


Figure 3.52: The SEM images of $Co(OH)_2$ sample obtained from the transformation of $Co_2P_2O_7$ sample aged in 3 M KOH solution.

Since the transformation of $Co_2P_2O_7$ into $Co(OH)_2$ is very fast, electrochemical methods are employed to follow this transformation in a slower manner. Firstly, 1 M KOH electrolyte solution is changed with 0.05 M KOH solution. The solution resistance increases to 32 ohms and current density at 2.0 V decreases significantly because of the decrease in the ion concentration as well as the conductivity. In Figure 3.53(b), a selected group of CVs from 100 cycles are given in 0 to 1 V potential window. In the first 5 cycles, there are two oxidation peaks at ~ 0.4 V and a broad one at 0.6 V. In the reverse cycle, there is a broad peak at 0.7 V and relatively more intense peak at 0.3 V. At 5^{th} cycle, the two oxidation peaks remain and another peak at 0.5 V appears. The peak at 0.5 V shifts to 0.4 V after 40 cycles. In the further cycles, this peak shifts towards 0.45 V. In the reverse cycles, there are two peaks at 0.3 V and 0.65 V and the peak at 0.3 V shifts to higher potentials while the peak at 0.65 V shifts towards lower potentials during cycling. The current densities of both oxidation and reduction peaks are increasing in each cycle. It is believed that in the first 5 cycles, the redox couples belong to $Co_2P_2O_7$ species. In the 5^{th} cycle, the surface of the electrode is coated with $Co(OH)_2$ species and the redox couples due to hydroxide species that dominates in further cycles as the electrode surface is fully coated with $Co(OH)_2$ species. And the high current density at 2.0 V is showing that the $Co(OH)_2$ species are better OER electrocatalysts than $Co_2P_2O_7$ species.

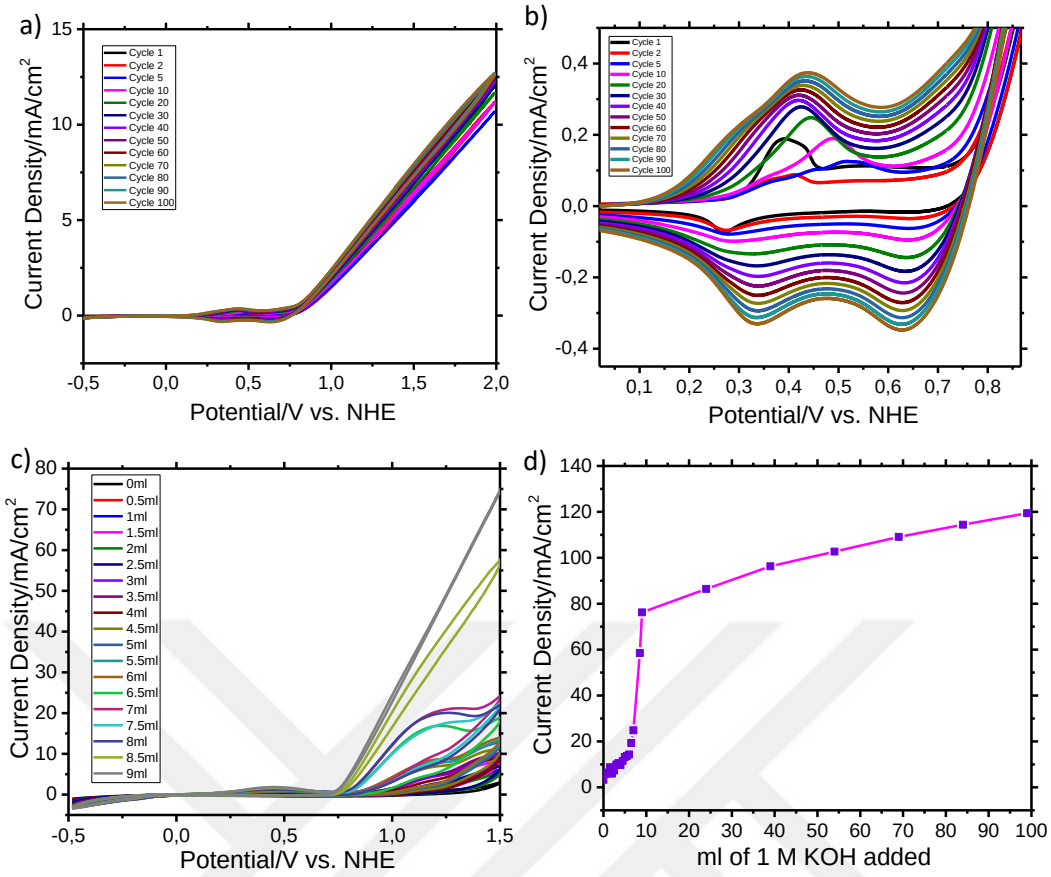


Figure 3.53: a) A selected group of CVs from 100 cycles of the $Co_2P_2O_7$ coated FTO electrode with scan rate of 100 mV/s and in 0.05 M KOH electrolyte solution, b) CVs in the 0-1 V potential window, c) $Co_2P_2O_7$ coated GR electrode 5th cycles of the CVs with consecutive addition of 0.5 ml of 1 M KOH solution, and d) current densities at 1.5 V at 5th CVs each step as a function of volume of 1 M KOH added.

Another experiment is designed to follow the transformation of $Co_2P_2O_7$ into $Co(OH)_2$ using a neutralized solution (equal volumes of 2.4 M KOH and 0.6 M $H_4P_2O_7$) as the electrolyte. A 0.5 ml of 1 M KOH solution is added after each 5 CV cycles to incrementally change the pH of the electrolyte solution. Figure 3.53(c) shows the 5th CVs. Figure 3.53(d) shows the current densities at 1.5 V of these CVs as a function of the amount of 1 M KOH added to the electrolyte solution. Up to 3.5 ml of 1 M KOH addition, the first region, the current densities are very low. After that point till 8 ml 1 M KOH addition, in the second region, there are two peaks around 1.2 V and both of them are having positive current densities. After 8 ml, in the third region, these two peaks disappear and current density at 1.5 V started to increase much more drastically. As it is explained in the nickel system as well, in the first region, the electrode surface is coated with $Co_2P_2O_7$ species. Since hydroxide concentration is still low in this region, the transformation does not happen. In the second region, the electrode surface is getting covered by $Co(OH)_2$ species and the full coverage of the electrode surface with $Co(OH)_2$ species happens in the third region. The changes in the CVs by addition of hydroxide and increasing

pH is a way of following the conversion process to evaluate solubility of $Co_2P_2O_7$ in aqueous media. If we assume 8 ml is the critical and use its hydroxide concentration and known K_{sp} of $Co(OH)_2$, one will find out the K_{sp} of $Co_2P_2O_7$. K_{sp} of $Co(OH)_2$ is taken as $5.92x10^{-15}$ M^3 and $[OH^-]$ and $[P_2O_7^{4-}]$ as 8/38 and 6/38 M, respectively, and $[Co^{2+}]$ is calculated to be $1.34x10^{-13}$ M after 8 ml 1M KOH addition. Therefore the Ksp of $Co_2P_2O_7$ is calculated to be $3.57x10^{-27}$ M^3. This value is very close to estimated value in the literature [80].

3.1.5. Synthesis and Characterization of Mesoporous $Ni_2P_2O_7$

The Ni(II):PPA:P123 (with 30:15:1 Ni(II):PPA:P123 mole ratio) sol-gel solution is directly poured into a pyrex cup in order not to disturb the gel-phase. In order to remove the solvents, the samples are kept in oven at 100ºC for 1 day to ensure complete drying. Then, the powder is collected and ground in a mortar to have fine powders, then it is put into a combustion crucible and calcined at 300ºC to remove the surfactant and obtain the mesoporous $Ni_2P_2O_7$ powders. This sample is then further calcined upto 700ºC and the samples are characterized at each calcination step by several techniques.

3.1.5.1. Mesoporous $Ni_2P_2O_7$ from Ethanol System

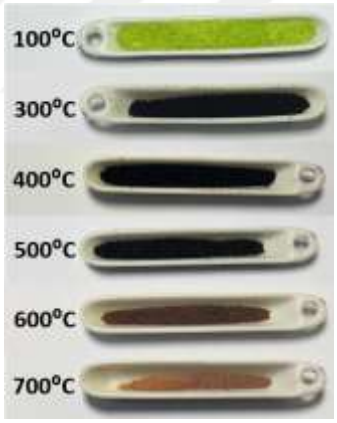


Figure 3.54: Photographs of the $Ni_2P_2O_7$ samples, obtained from Ni30-15PPA ethanol solution, calcined at different temperatures.

In ethanol, the color of the sol-gel solution is blurry green and after keeping in a 100ºC oven for 24 hours, the color of the powder obtained was yellow-green. As the calcination temperature increased to a 300, 400, and 500ºC, the color of the powders are dark brown. However, at 600ºC, the color of the powder is lighter brown and at 700ºC, it turned into orange color.

These samples are characterized using ATR-FTIR spectrocopy and high-angle XRD techniques. In ATR-FTIR spectra, the phosphate peaks almost do not alter through out

annealing, from 300 to 700 ºC (see Figure 3.55(a)). However, high angle XRD pattern shows that the sample is crystalline at 700 ºC (see Figure 3.55(b)). Collectively, these two techniques show that the powders are amorphous up to 700 ºC but, having the same structure of the crystalline phase. High-angle XRD patterns of the crystalline phase indexes to α-phase of $Ni_2P_2O_7$.

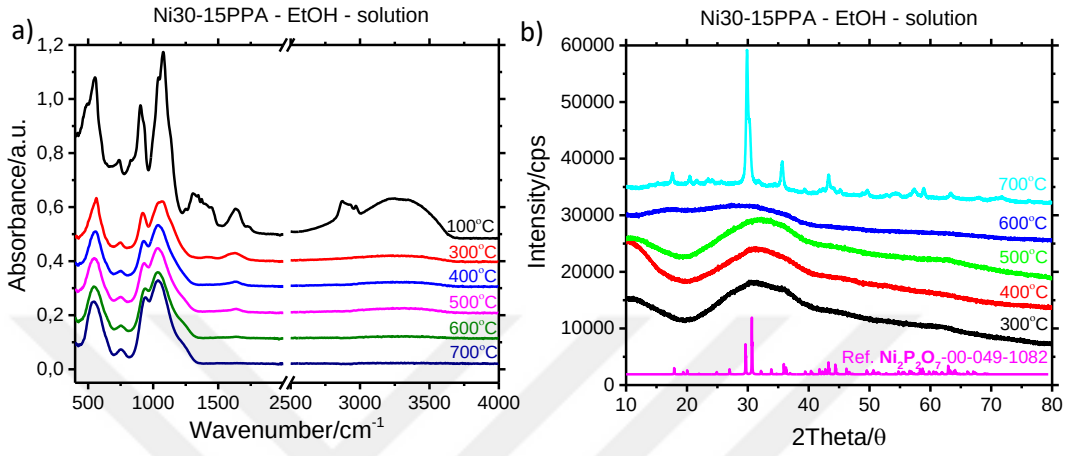


Figure 3.55: a) ATR-FTIR spectra and b) high-angle XRD patterns of the calcined samples of the Ni30-15PPA ethanol solution.

The amount of water in these powders, which is related with the porosity and surface area may also be estimated from the ATR-FTIR spectra. The water peak is very high at lower calcination temperatures but, it drastically decreases as the calcination temperature increases and disappears when the calcination temperature reaches to 700ºC, where the crystallization occurs.

Figure 3.56 shows the SEM images of the same samples, annealed at 300, 400, 500, 600 and 700ºC. The particles are large (monoliths) with some feature in nanoscale in the image of the 700ºC annealed sample. At the other annealing temperature, it is impossible to resolve some features in nanometer-scale. Further imaging is need to elucidate nano-scale structures of these samples.

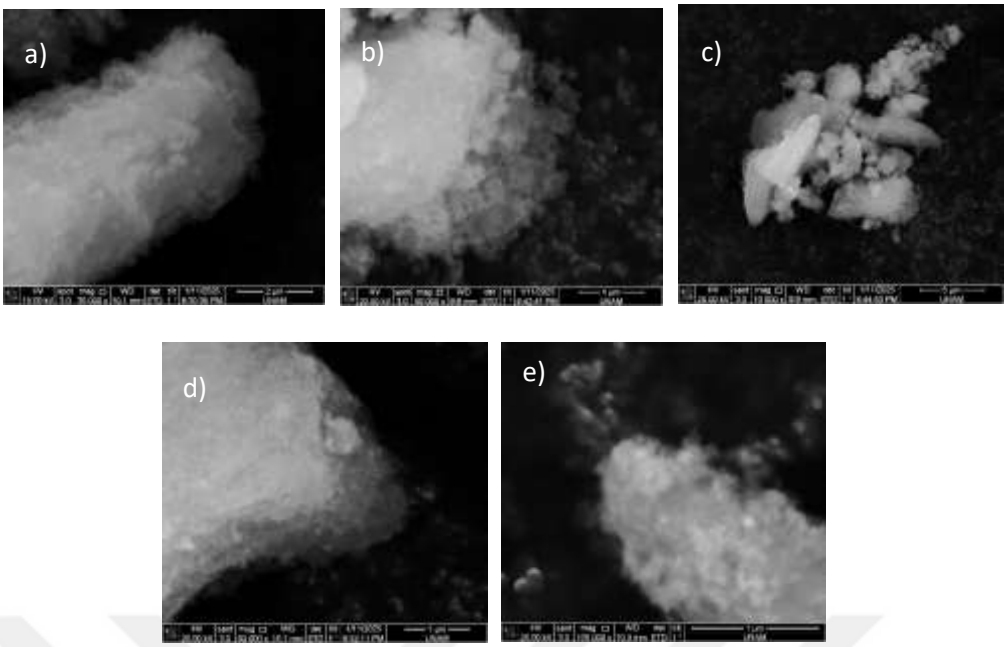


Figure 3.56: SEM images of the Ni30-15PPA ethanol solution, calcined at different calcination temperatures; a) 300ºC, b) 400ºC, c) 500ºC, d) 600ºC, and e) 700ºC.

Even though the SEM images are not providing details of the porous structure, the N_2 adsorption-desorption isotherms display type IV isotherms with an characteristic hysteresis, characteristic of the mesoporous materials. Figure 3.57 displays the N_2 adsorption-desorption isotherm of the $Ni_2P_2O_7$ powder, obtained from the ethanol solution, calcined at 300ºC. It has a 228 m^2/g surface area, 12.2 nm pore size and 1.22 cm^3/g pore-volume. These numbers are quite high compared to the literature values [85][86].

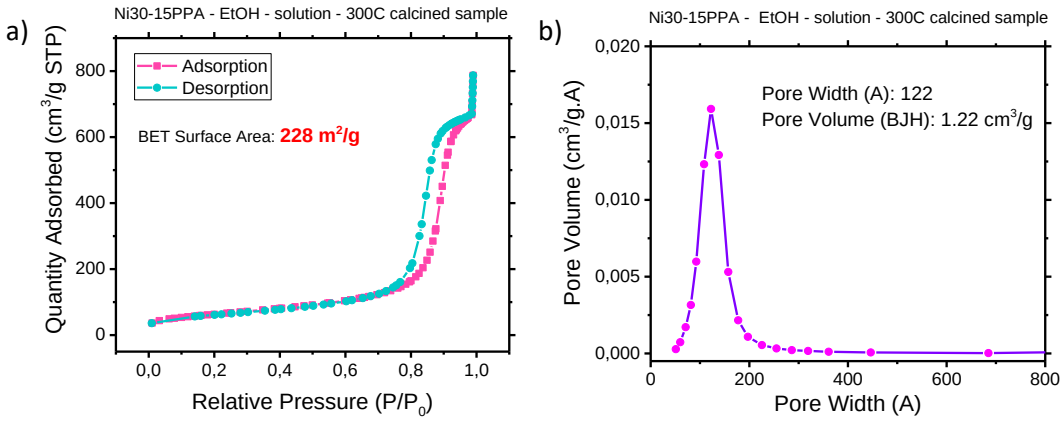


Figure 3.57: a) N_2 (77 K) adsorption-desorption isotherm, and b) BJH pore size distribution plot of $Ni_2P_2O_7$ sample, obtained by calcination of the Ni30-15PPA ethanol solution at 300ºC.

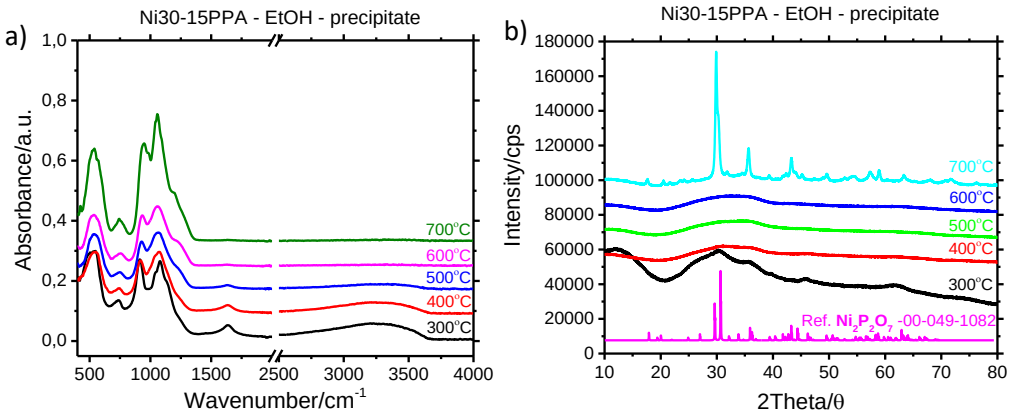


Figure 3.58: a) Powder XRD patterns and b) ATR-FTIR spectra of the calcined/annealed ethanol precipitate.

The calcination of the precipitate also yields α-$Ni_2P_2O_7$ powders at 700ºC. Also note that below 700ºC, the sample is amorphous (Figure 3.58(a)). The ATR-FTIR spectra shows large amounts of water, in the calcined samples, which also indicates the presence of a high porosity and surface area, which is consistant with the N_2 adsorption-desorption (see Figure 3.58(b)) data. The BJH pore size distribution plots are uniform but, the pores gradually expands and gets broader as the calcination temperature increases (see Figure 3.59(b)). The surface and pore parameters, evaluated from BET and BJH analysis, are tabulated in Table 3.4. The SEM images, given in Figure 3.60, are also providing good evidence for the porosity in these samples.

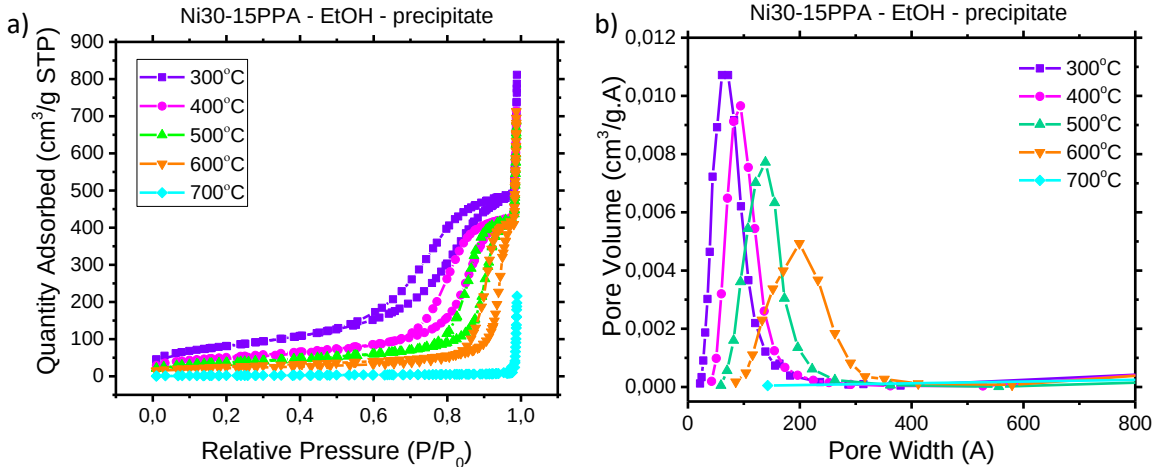


Figure 3.59: a) N_2 (77 K) adsorption-desorption isotherms and b) BJH pore size distribution plots of the precipitate from ethanol system of Ni30-15PPA, calcined at indicated temperatures.

Table 3.4: The BET surface area, BJH pore width, and pore volume values of the calcined $Ni_2P_2O_7$ samples, obtained from the Ni30-15PPA ethanol precipitate.

Calcination Temperature (°C)	BET Surface Area (m^2/g)	Pore Width (Å)	Pore Volume (cm^3/g)
300	297	68	1.26
400	184	94	1.11
500	134	138	1.06
600	91	200	1.10
700	8	-	0.94

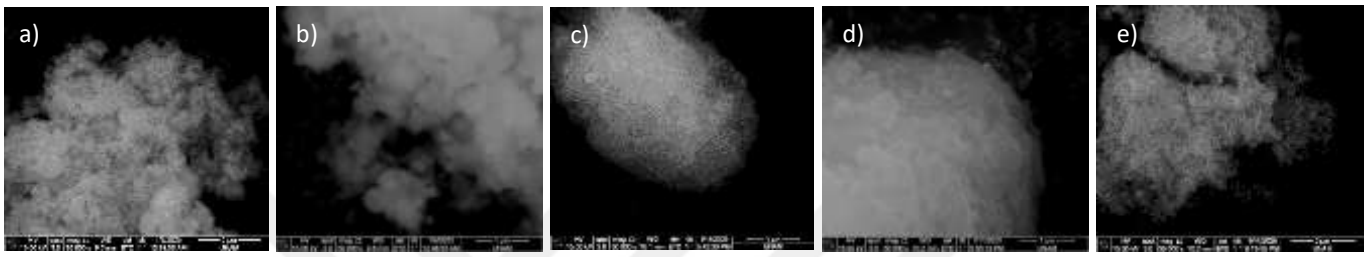


Figure 3.60: SEM images of the Ni30-15PPA ethanol precipitate, calcined at different calcination temperatures; a) 300ºC, b) 400ºC, c) 500ºC, d) 600ºC, and e) 700ºC.

3.1.5.2. Mesoporous $Ni_2P_2O_7$ from Butanol System

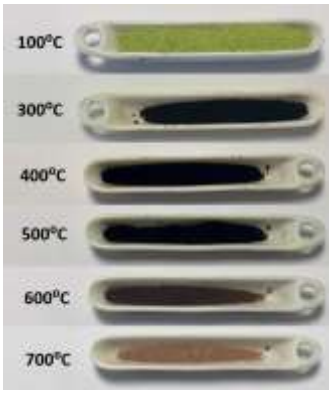


Figure 3.61: Photographs of the $Ni_2P_2O_7$ samples, obtained from the Ni30-15PPA butanol solution, calcined at different temperatures.

Among the $Ni_2P_2O_7$ samples, the fastest and most stable sol-gel process occurs in the butanol solvent. However, when the acid solution is added to the nickel salt solution, a homogeneous solution can be obtained that gradually undergoes gelation. Afterwards, the gel-phase is carefully poured into a pyrex cup and dried at 100ºC to remove the solvent for 1 day. Then, the powder is ground in a mortar for further heat treatment. The color of this sample is bright green, see Figure 3.61. However, as the sample calcined up to 600ºC, the color of the

powders are black. It can be due to carbonization of the surfactant species. However, at 700ºC, the color of the sample becomes orange that is also the color of crystalline α-$Ni_2P_2O_7$.

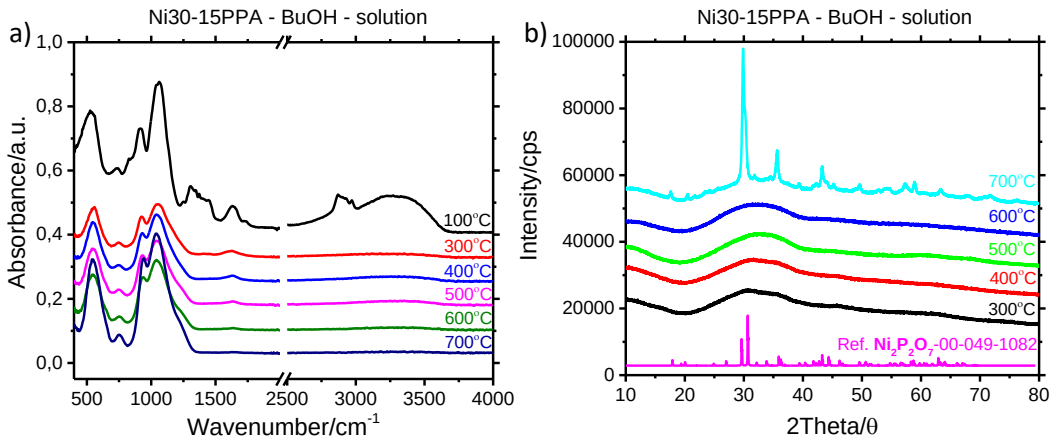


Figure 3.62: a) ATR-FTIR spectra and b) high-angle XRD patterns of the Ni30-15PPA butanol solution, calcined at indicated temperatures.

The ATR-FTIR spectrum of the dried sample displays intense water, and surfactant peaks with some nitrate species (Figure 3.62). However, in the calcined samples, there is no surfactant species and the amount of water is significantly decreased. In all of these calcined samples, the pyrophosphate regions are similar with a characteristic peak at 750 cm^{-1}, indicating the formation of $Ni_2P_2O_7$. However these samples may have different phases of $Ni_2P_2O_7$ in the amorphous phase that may still provide the characteristic 750 cm^{-1} peak. Since the samples are amorphous, it is also difficult to determine by XRD patterns to predict if there is a phase change during high temperature calcination process. Moreover, the sample crystallize at 700ºC to yield α-$Ni_2P_2O_7$ crystals.

The N_2 adsorption-desorption isotherms are also collected from this set of samples. The isotherms display fetures, characteristic for mesoporous naterials, indicating the formation of highly mesoporous samples, especially at lower calcination temperatures. The pore size of the sample at 300ºC is 53 Å. Using surface area and pore-size data, a simple calculation (assuming a cylindrical pores) gives a few unit cell thick pore-walls in these samples. Since the sol-gel process is very quick in butanol, the particles remain very small and have no time to aggregate

and yield large particles. The nucleation is faster than the growth, resulting in stable and very quick gelation in butanol and providing thinner pore-walls and larger surface area.

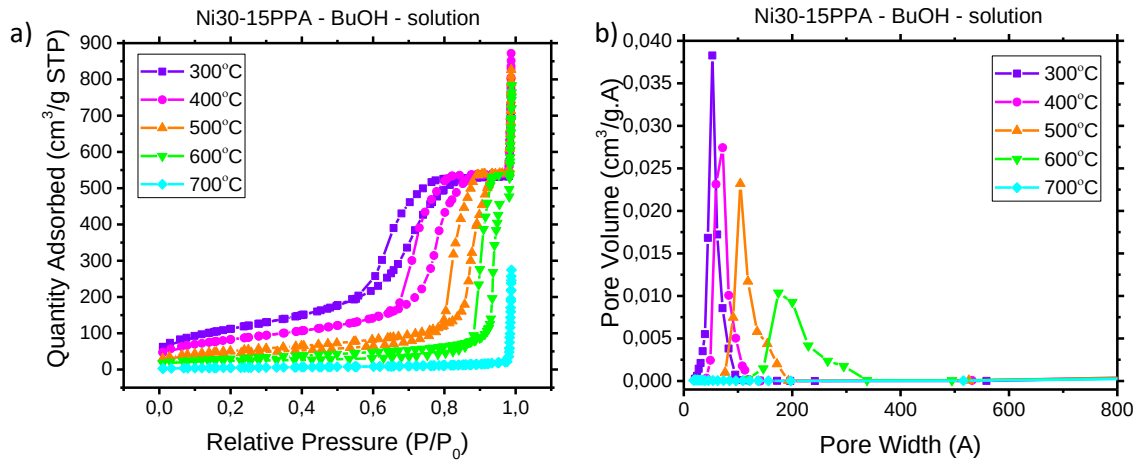


Figure 3.63: a) N_2 (77 K) adsorption-desorption isotherms and b) BJH pore size distribution plots of the gel-phase from butanol system of Ni30-15PPA, calcined at indicated temperatures.

Table 3.5: The BET surface area, BJH pore width, and pore volume values of the calcined $Ni_2P_2O_7$ samples obtained from Ni30-15PPA butanol solution.

Calcination Temperature (°C)	BET Surface Area (m^2/g)	Pore Width (Å)	Pore Volume (cm^3/g)
300	410	53	1.15
400	299	73	1.35
500	184	106	1.28
600	107	174	1.21
700	18	-	0.42

The BET surface area, BJH pore width, and pore volume values are given in Table 3.5. The BET surface area (410 m^2/g) is almost twice of that in the literature for the $Ni_2P_2O_7$ samples. Controling the sol-gel process to reduce the pore-wall thicknes may result in higher surface area materials. In these samples even at 700ºC, where the crystallization occurs, the BET surface area is still 18 m^2/g. The pore size distributions are also very uniform and sharp. At 600ºC, the pore size distribution becomes broader and at 700ºC, the sample becomes mesoporous/macroporous and the pore size distribution becomes even broader.

SEM images of these highly porous and high surface area materials show the pores at higher calcination steps, at which the pores are large enough to resolve. TEM imaging technique may help to observe the porous structure better especially at lower calcination temperatures. However, the samples are beam sensitive and undergo thermal degradation during imaging.

Cryo-imaging may be employed to observe the mesopores of the samples, calcined at lower temperatures.

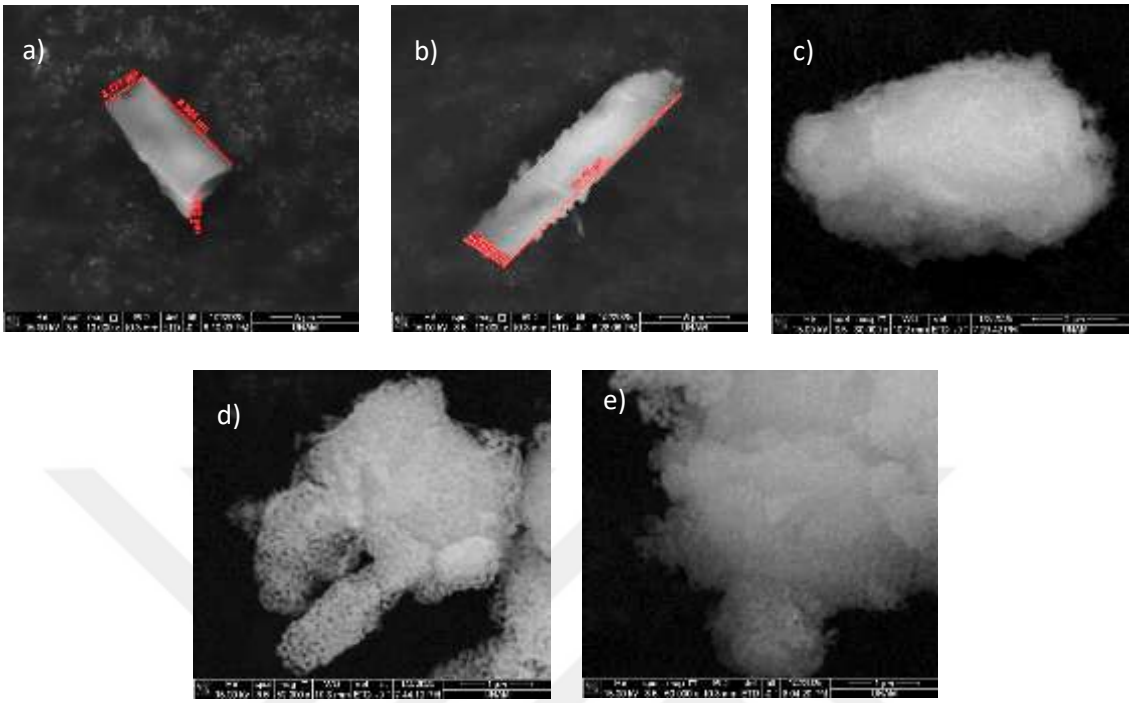


Figure 3.64: SEM images of the Ni30-15PPA samples, from butanol solution part calcined at a) 300ºC, b) 400ºC, c) 500ºC, d) 600ºC, and e) 700ºC.

The supernatant is also coated on a microscope slide by using drop-cast coating technique and calcined at 300ºC. It is also annealed at further temperatures and characterized using the same techniques. The sample, obtained from the supernatant part, is also porous, has high surface area, uniform and sharp pore size distribution at low calcination temperatures. The SEM images of the samples, calcined at 300 and 400ºC, proves a film formation. However, in some parts of the sample, there are flake-like particles as well.

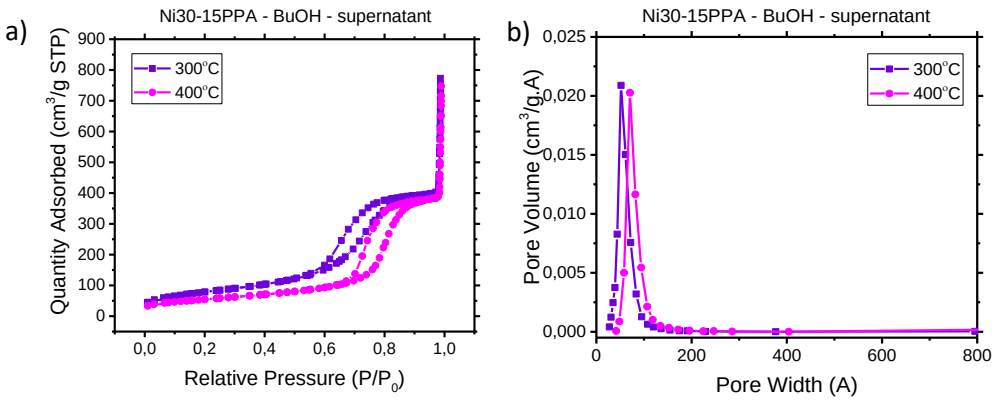


Figure 3.65: a) N_2 (77 K) adsorption-desorption isotherms, and b) BJH pore size distribution plots of the Ni30-15PPA butanol supernatant, calcined at 300ºC and 400ºC samples.

Table 3.6: The BET surface area, BJH pore width, and pore volume values of the $Ni_2P_2O_7$ samples obtained from Ni30-15PPA butanol supernatant calcined at 300ºC and 400ºC.

Calcination Temperature (ºC)	BET Surface Area (m^2/g)	Pore Width (Å)	Pore Volume (cm^3/g)
300	286	53	1.2
400	197	69	1.16

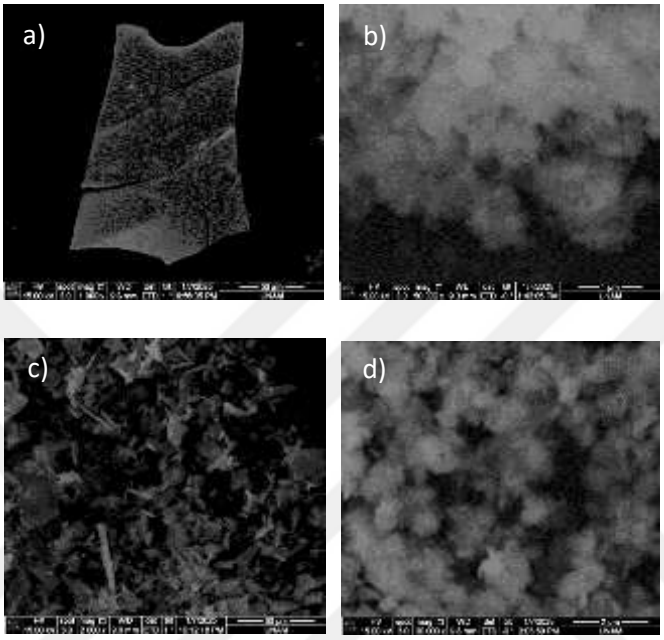


Figure 3.66: SEM images of the Ni30-15PPA samples, obtained from butanol supernatant, calcined at a), b) 300ºC and c),d) 400ºC.

After removing the supernatant, the gel left in the centrifuge tube is inserted in an oven at 100ºC for 1 day. Then, the sample is further calcined at different temperatures as usual. The ATR –FTIR spectra of these samples are given in Figure 3.67. The dried sample has large amount of water and surfactant but almost no nitrate, indicating that polimerization is more extended. The other samples, calcined between 300 and 700ºC, keeps large amount of water, likely in their pores. Even the sample, annealed at 600ºC, displays intense water peaks. Similar to the other samples, the precipitate from Ni30-15PPA butanol is also amorphous up to 600ºC and crsytalize to the α-$Ni_2P_2O_7$ phase at 700 ºC.

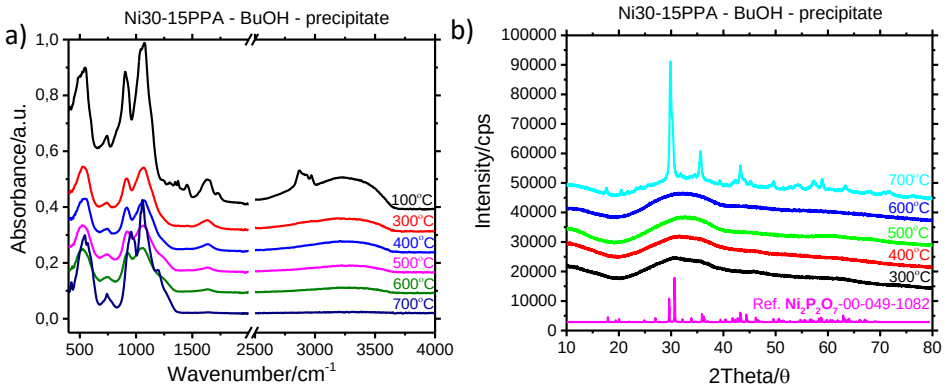


Figure 3.67: a) ATR-FTIR spectra and b) high-angle XRD patterns of the Ni30-15PPA butanol precipitate, calcined samples.

ATR-FTIR spectra display, at lower calcination temperatures, intense water peaks, indirectly indicating a highly porous structure. The spectra are normalized using the peak at 750 cm^{-1} after back ground subtraction (Figure 3.68) to evaluate the trend in water amount in the samples with increasing calcination temperature.

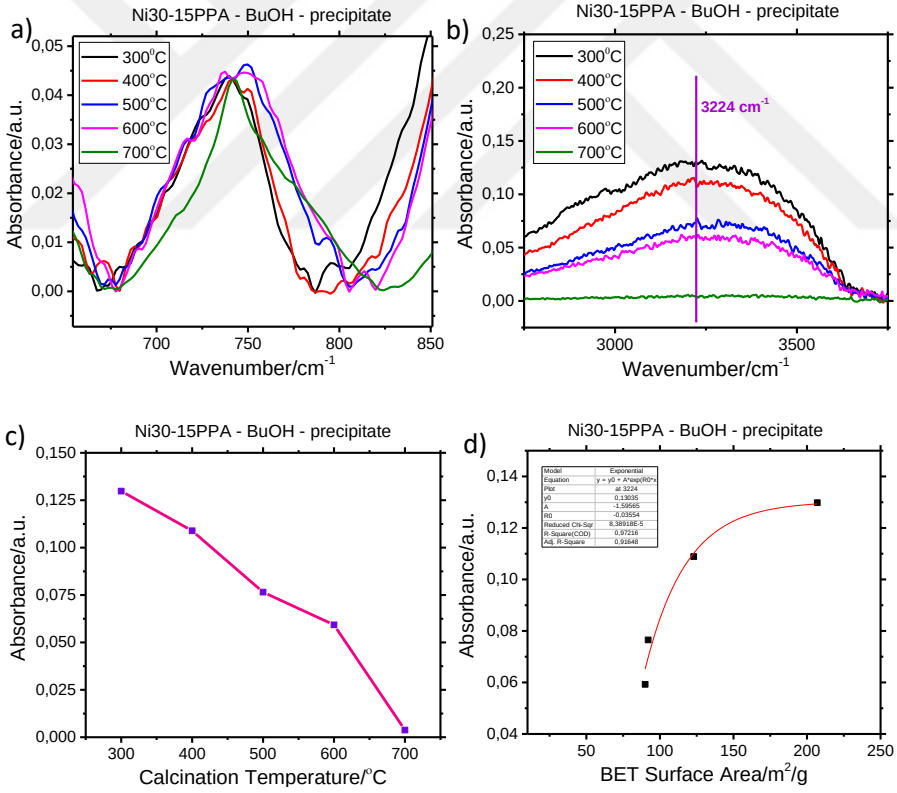


Figure 3.68: a) and b) Normalized ATR-FTIR spectra of the calcined Ni30-15PPA of butanol precipitate and absorbance at 3224 cm^{-1} vs c) calcination temperature and d) BET surface area plots.

In Figure 3.68(c), the absorbance at 3224 cm^{-1} vs calcination temperature is plotted. As the calcination temperature increases, the amount of water in these powders decreases and accords well with the N_2 adsorption-desorption isotherms data (see Figure 3.68(c) and (d)).

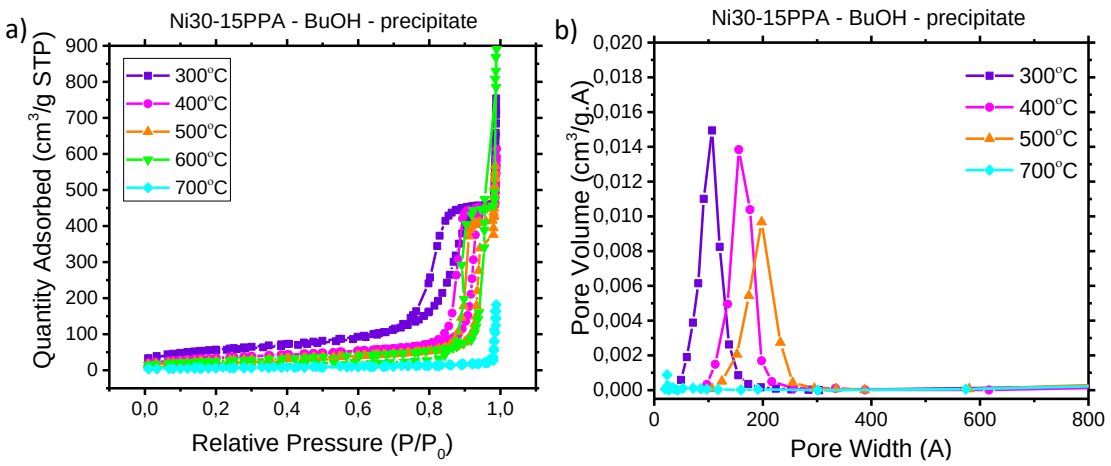


Figure 3.69: a) N_2 (77 K) adsorption-desorption isotherms and b) BJH pore size distribution plots of the calcined Ni30-15PPA of butanol precipitate.

The N_2 adsorption-desorption isotherms of the samples, obtained from butanol precipitate are also type-IV, which is characteristic for mesoporous structures [88]. The BET surface area at 300ºC is 207 m^2/g that is less than the solution and supernatant parts but still very high. The pore size distributions are also uniform and sharp. At 700ºC, where the crystallization starts, the surface area decreases to 19 m^2/g, which is low compared to the lower calcination temperatures but, it is very high for a crystalline sample.

Table 3.7: The BET surface area, BJH pore width, and pore volume values of the calcined $Ni_2P_2O_7$ samples, obtained from Ni30-15PPA butanol precipitate.

Calcination Temperature (ºC)	BET Surface Area (m^2/g)	Pore Width (Å)	Pore Volume (cm^3/g)
300	207	106	1.17
400	123	156	0.95
500	92	197	0.88
600	90	-	-
700	19	-	0.28



Figure 3.70: SEM images of the Ni30-15PPA samples, obtained from butanol precipitate, calcined at a) 300ºC, b) 400ºC, c) 500ºC, d) 600ºC, and e) 700ºC.

SEM images of the $Ni_2P_2O_7$ samples, obtained from Ni30-15PPA butanol precipitate, indicate porous structures at 300ºC (see Figure 3.70). Since the surface area decreases with increasing calcination temperatures, the images of the sample, calcined at 700ºC, does not show any porous structures. The SEM images correlate well with both ATR-FTIR spectra and N_2 adsorption-desorption isotherms.

3.1.5.3. Mesoporous $Ni_2P_2O_7$ from Methanol System

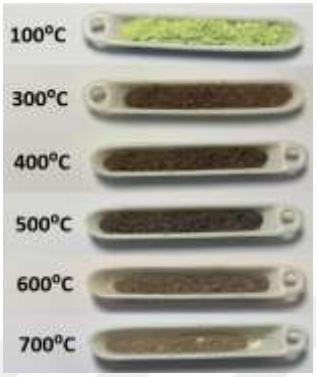


Figure 3.71: Photographs of the $Ni_2P_2O_7$ samples, obtained from Ni30-15PPA methanol solution, calcined at different temperatures.

In methanol solvent, the sol-gel formation in not observed in the Ni30-15PPA solution. The solution is clear and turns into a cloudy solution within a minute and the color of the solution becomes brighter green. Even though the gelation does not occur in the solution phase, the process of drying and calcination has been carried similarly. The solution is poured into a pyrex cup and dried at 100ºC oven for 1 day to remove the solvent. The color of the powder at this stage is bright green, see Figure 3.71. However, the color is different shades of brown at higher temperatures but, it becomes gray-yellow at 700ºC.

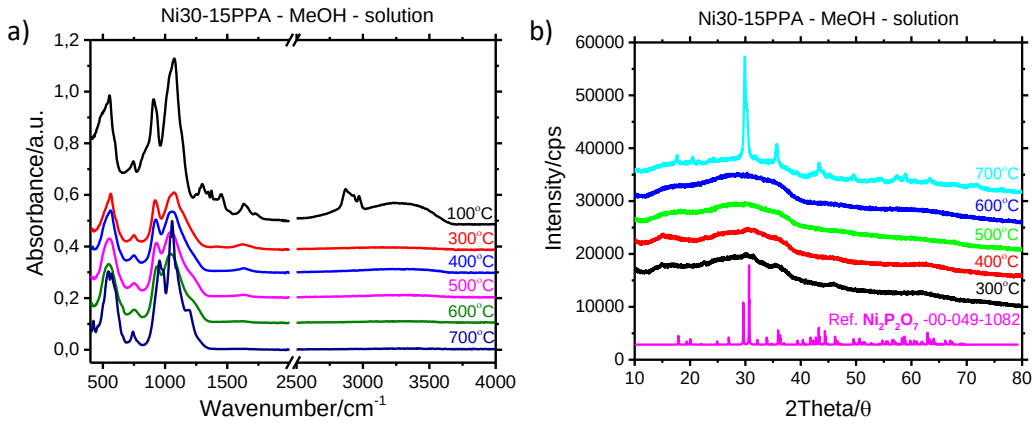


Figure 3.72: a) ATR-FTIR spectra and b) high-angle XRD patterns of the Ni30-15PPA methanol solution, calcined at indicated temperatures.

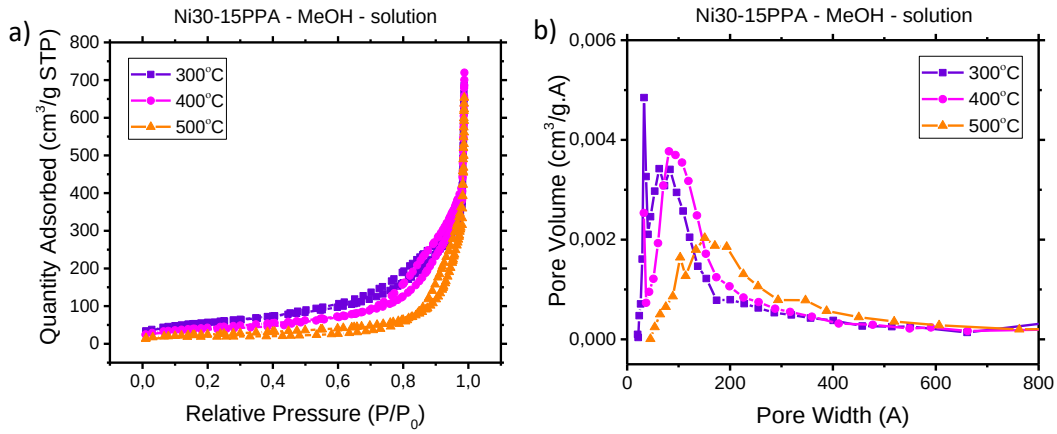


Figure 3.73: a) N_2 (77 K) adsorption-desorption isotherms and b) BJH pore size distribution plots of $Ni_2P_2O_7$, obtained from Ni30-15PPA methanol solution and calcined at different temperatures.

Figure 3.73 displays the N_2 adsorption-desorption isotherms and pore size distribution plots at 300, 400 and 500ºC. The isotherms are type-IV and characteristic for mesoporous materials. However, pore size distribution is less uniform compared to the samples, obtained from other solvents. Nevertheless they are porous and display decent surface area and pore volumes (see Table 3.8).

Table 3.8: The surface area, BJH pore width, and pore volume values of the calcined $Ni_2P_2O_7$ samples, obtained from Ni30-15PPA methanol supernatant.

Calcination Temperature (°C)	BET Surface Area (m^2/g)	Pore Width (Å)	Pore Volume (cm^3/g)
300	207	-	1.07
400	154	94	1.11
500	90	-	1.01

Figure 3.74 displays a set of SEM images of these samples that have flake-like morphologies. Also, in addition to flake-like particles, a spherical particles are also observed in the images. Even at 700ºC, this morphology is preserved.

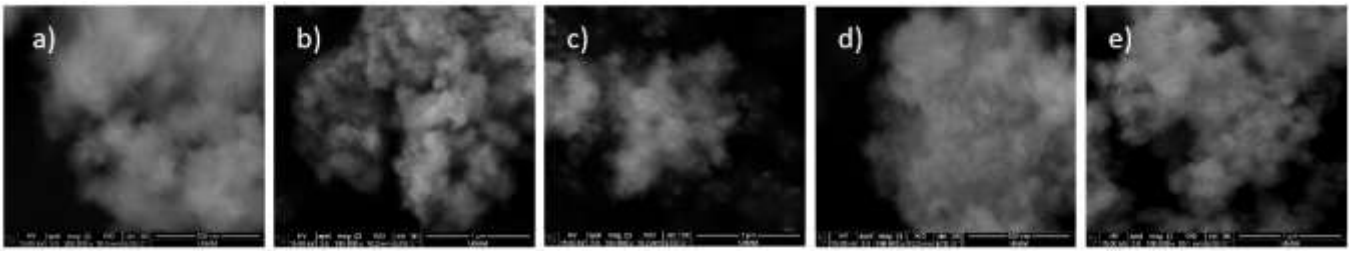


Figure 3.74: SEM images of the $Ni_2P_2O_7$ powders, prepared from the methanol solution and calcined at a),b) 300ºC, c),d) 400ºC, e) ,f) 500ºC, g),h) 600ºC, and i),j) 700ºC.

Methanol solvent behaves different than the other two solvents (butanol and ethanol). The solution is clear immediately after mixing the metal salt and acid solutions but, becomes cloudy within a minute. When the precipitate is separated, the supernatant parts is also a clear solution, see Figure 3.75(a). However, after 1 day aging the supernatant, a white precipitate settles down in very small amount with a cloudy solution, Figure 3.75(b). The precipitate is collected and calcined at different temperatures; Figure 3.75(c) display the XRD pattern of these samples. Similar to the other samples, the precipitate also crystalize at 700ºC and pattern is indexed to the pure α- $Ni_2P_2O_7$ phase.

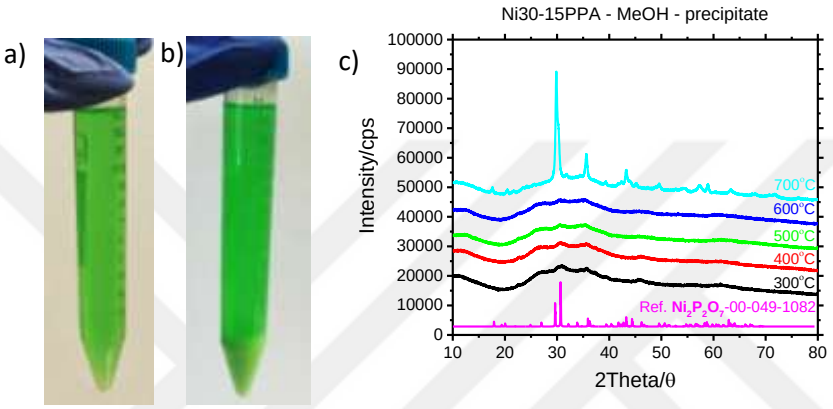


Figure 3.75: a) Photographs of the Ni30-15PPA methanol solution a) after centrifugation, and b) after 1 day aging, and c) high-angle XRD patterns of the precipitate, calcined at different temperatures.

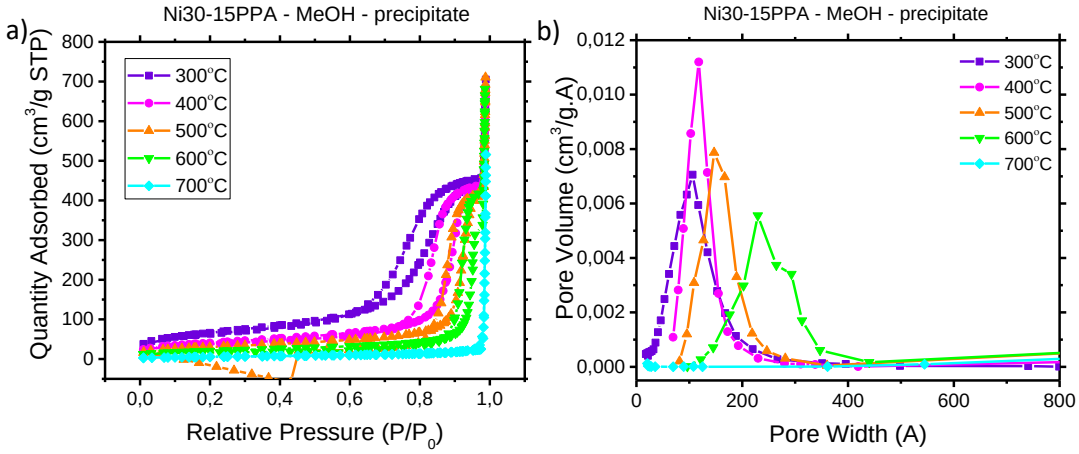


Figure 3.76: a) N_2 (77 K) adsorption-desorption isotherm, and b) BJH pore size distribution plot of $Ni_2P_2O_7$ calcined at different temperatures obtained from Ni30-15PPA in methanol solution precipitate part.

The N_2 adsorption-desorption isotherms and BET surface area values prove that these samples are also mesoporous and have high surface areas (see Figure 3.76 and Table 3.9). As the calcination temperature increases the surface area and porosity decreases but, even at 700ºC, the surface area is about 20 m^2/g, which is a quite high for a crystalline material.

Table 3.9: The BET surface area, BJH pore width, and pore volume values of the calcined $Ni_2P_2O_7$ samples, obtained from Ni30-15PPA methanol precipitate.

Calcination Temperature (°C)	BET Surface Area (m^2/g)	Pore Width (Å)	Pore Volume (cm^3/g)
300	240	106	1.09
400	147	118	1.06
500	108	146	1.1
600	73	230	1.05
700	20	-	-

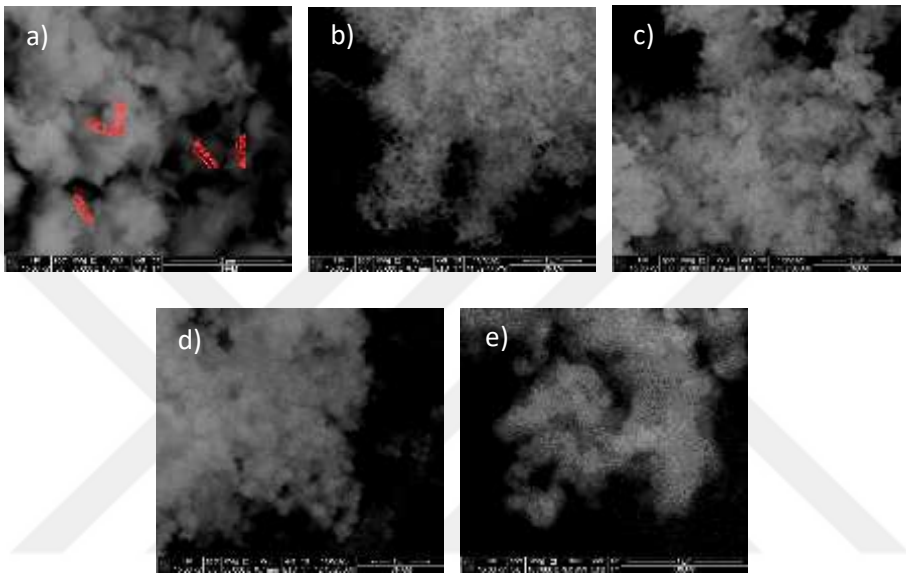


Figure 3.77: SEM images of the samples, obtained from the Ni30-15PPA methanol precipitate after calcination at different temperatures; a) 300ºC, b) 400ºC, c) 500ºC, d) 600ºC, and e) 700ºC.

And SEM images correlate well with the N_2 adsorption-desorption data. At 300ºC, the morphology is very similar to that of the powders obtained from the solution part. The flake-like structures with spherical particles are also observed in the images (see Figure 3.77). Only spherical particles are observed at higher calcination temperatures. At 700ºC, the particles are larger and still spherical and accords well with the reduced surface area.

3.1.5.4. Solvent Comparison of Mesoporous $Ni_2P_2O_7$

Remember that Ni30-15PPA solutions in ethanol and butanol are forming sol-gels, while in methanol there is a cloudy solution formation. The effect of the sol-gel formation is observed as a significant increase in the surface area of the powders, obtained from the gels. In butanol, the BET surface area is 410 m^2/g while the typical surface area recorded for mesoporous $Ni_2P_2O_7$ is in the range of 6-216 m^2/g in the literature [27][81][82][85][86].

In each solvent, both the solutions and precipitates, calcined samples at 700ºC, yield $Ni_2P_2O_7$ crystals. The precipitates also have high surface area, the highest, 297 m^2/g, is recorded from the ethanol and the lowest (207 m^2/g) from the butanol system.

3.1.5.5. Electrochemical Characterization of Mesoporous $Ni_2P_2O_7$ and Its Transformation to β-$Ni(OH)_2$

As the solutions of the Ni30-15PPA in ethanol and butanol are forming sol-gels, the solutions are 5 times diluted with the alcohol used in the synthesis. These clear solutions are spin-coated over FTO glasses or dip-coated over graphite rods (GR) and calciend at different temperatures (300 to 600ºC) to obtain 1 cm^2 FTO, and GR coated electrodes and used in a three electrode system in a 1 M KOH solution to evaluate electrochemical properties.

First, the FTO-coated electrodes were prepared, and cyclic voltammetry (CV) measurements were conducted to assess their stability and oxygen evolution reaction (OER) performance. Figures 3.78, 3.79, and 3.80 presents the CV curves of $Ni_2P_2O_7$ synthesized using ethanol, butanol and methanol, respectively, of FTO coated electrodes. The CVs are recorded at a scan rate of 50 mV/s within a potential range of -0.5 to 2.0 V versus the normal hydrogen electrode (NHE) in 1 M KOH electrolyte solution. In the initial cycles, prominent redox peaks corresponding to the oxidation and reduction of nickel species are observed with high current densities. However, in subsequent cycles, these peaks display reduced current densities, and the current at 2.0 V declines progressively with cycling. This behavior is attributed to instability of the coated material on the FTO substrate. Notably, the electrodes, calcined at 500 and 600ºC, exhibit improved stability with a reduced degradation.

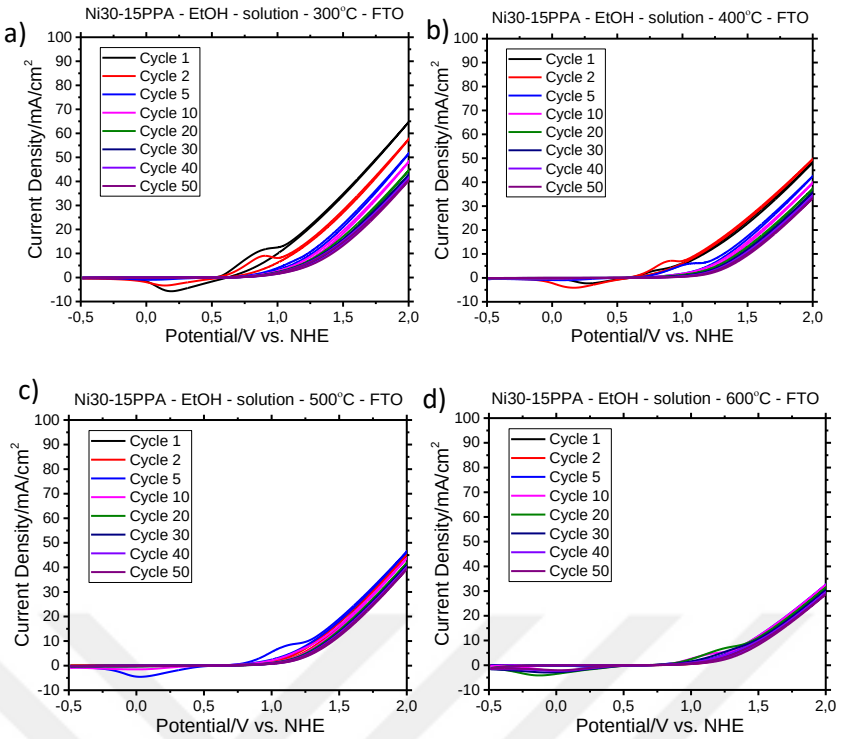


Figure 3.78: A selected group of CVs from 50 cycles in 1 M KOH electrolyte solution with a scan rate of 50 mV/s of the FTO $Ni_2P_2O_7$ electrodes, coated from ethanol solution and calcined at a) 300, b) 400, c) 500, and d) 600ºC.

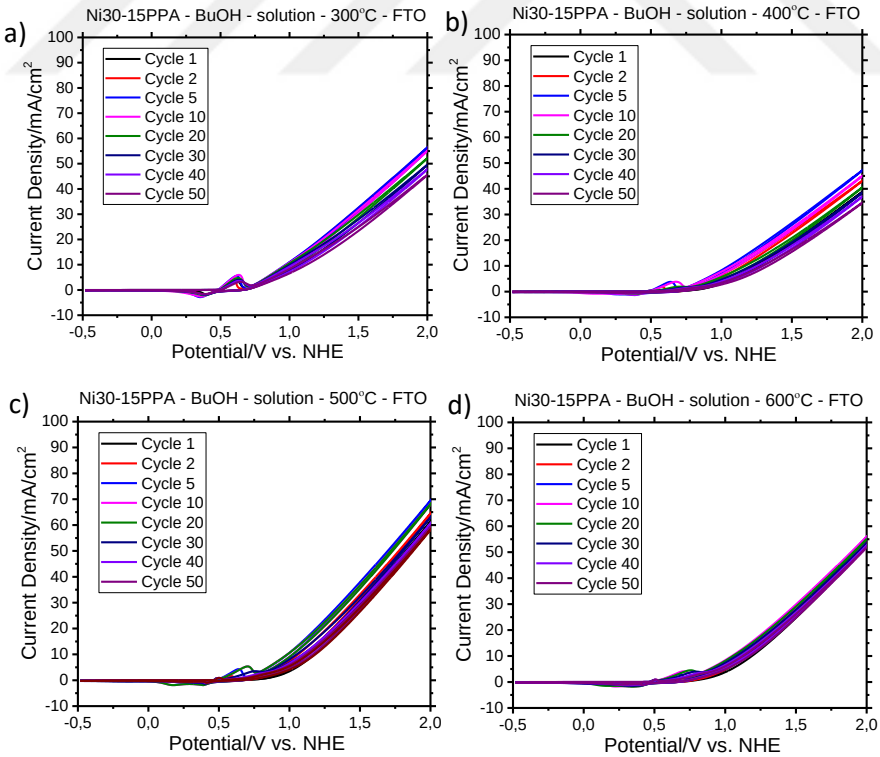


Figure 3.79: A selected group of CVs from 50 cycles in 1 M KOH electrolyte solution with a scan rate of 50 mV/s of the FTO $Ni_2P_2O_7$ electrodes, coated from butanol and calcined at a) 300, b) 400, c) 500, and d) 600ºC.

The change in the solvent from ethanol to butanol or methanol didn't affect the electrode stability on FTO substrate in these potential windows. However, the electrodes coated with $Ni_2P_2O_7$ samples prepared in methanol have slighlty less current density at each calcination temperature.

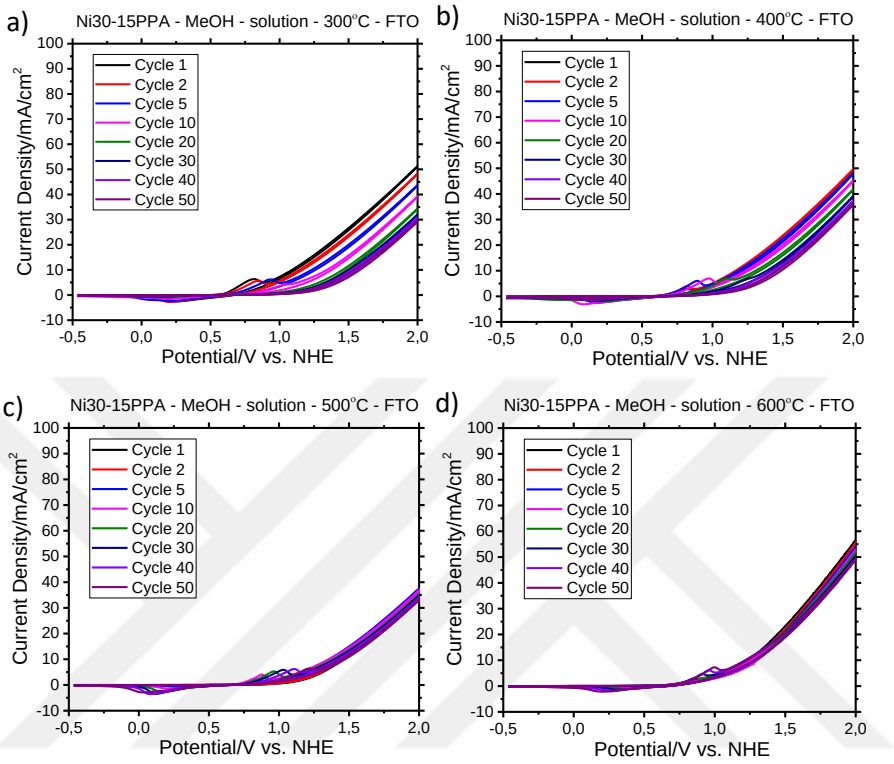


Figure 3.80: A selected group of CVs from 50 cycles in 1 M KOH electrolyte solution with a scan rate of 50 mV/s of the FTO $Ni_2P_2O_7$ electrodes, coated from methanol and calcined at a) 300, b) 400, c) 500, and d) 600ºC.

Since the samples are not stable on FTO substrate during CV, the substrate is changed to GR and to coat it homogeneously as a thin layer, the Ni30-15PPA solutions are 5 times diluted with the solvent used in the synthesis. Then, these coated GR electrodes are calcined at different calcination temperatures. Even tough, the $Ni_2P_2O_7$ samples crystallize at 700ºC, the GR electrodes begin to degrade and disintegrate over 600ºC. That's why the electrodes are calcined betwent 300 and 600ºC.

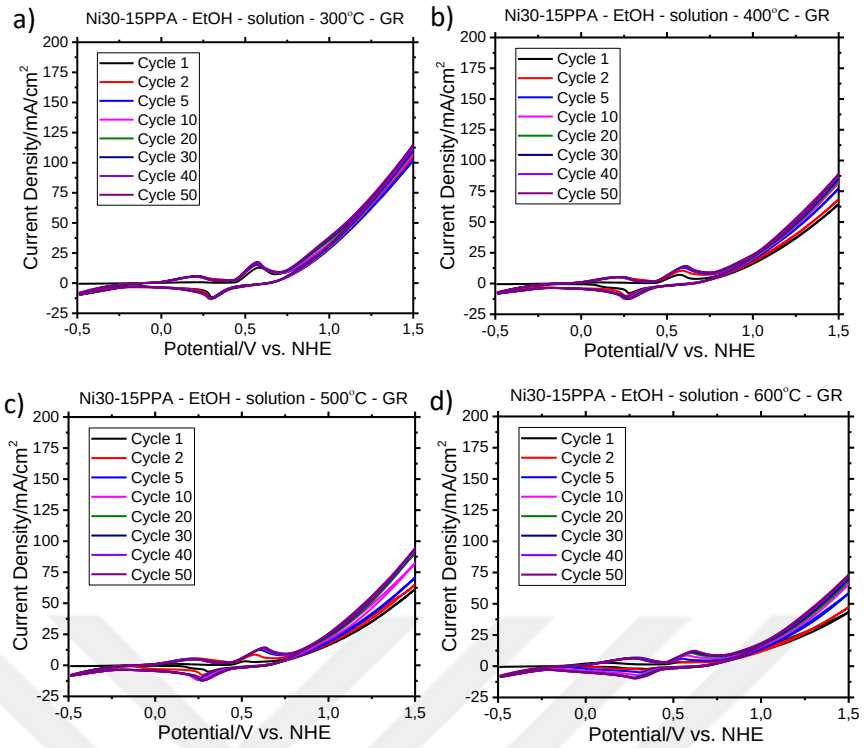


Figure 3.81: A selected group of CVs from 50 cycles in 1 M KOH electrolyte solution with a scan rate of 50 mV/s of the GR $Ni_2P_2O_7$ electrodes, coated from ethanol and calcined at a) 300, b) 400, c) 500, and d) 600ºC.

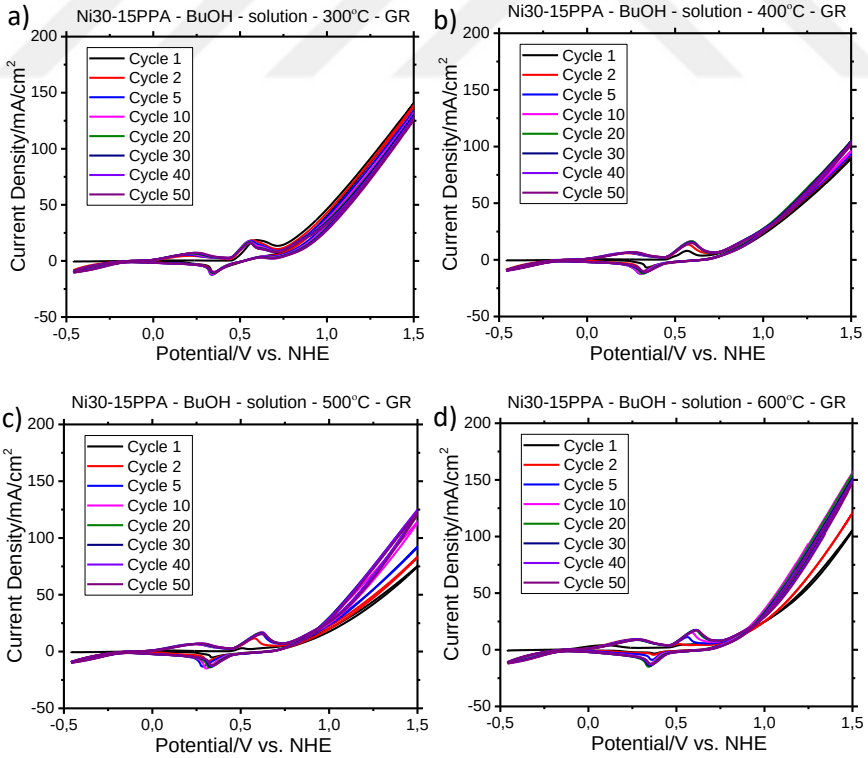


Figure 3.82: A selected group of CVs from 50 cycles in 1 M KOH electrolyte solution with a scan rate of 50 mV/s of the GR $Ni_2P_2O_7$ electrodes, coated from butanol and calcined at a) 300, b) 400, c) 500, and d) 600ºC.

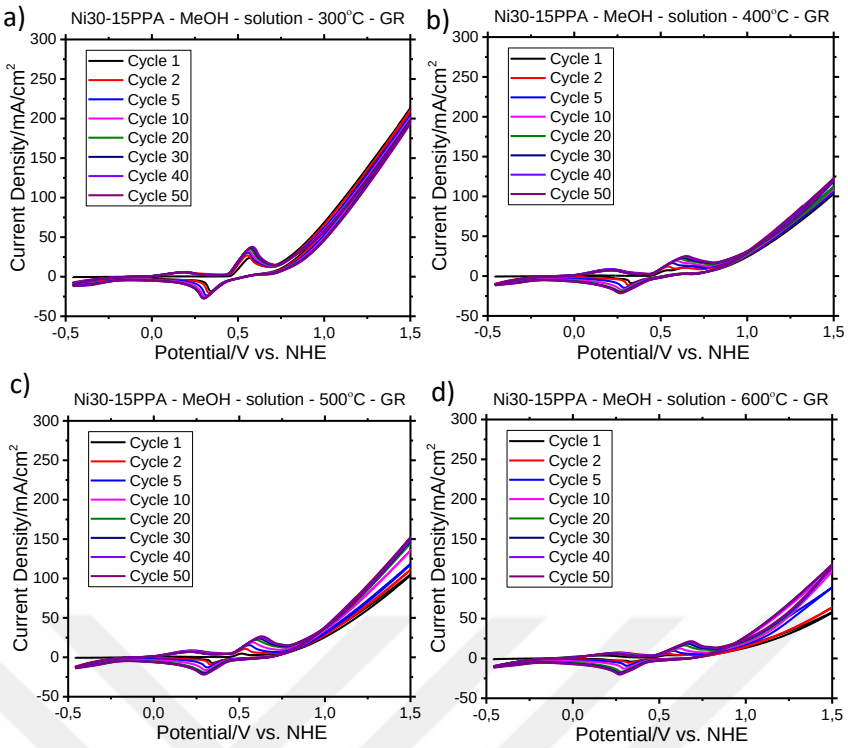


Figure 3.83: A selected group of CVs from 50 cycles in 1 M KOH electrolyte solution with a scan rate of 50 mV/s of the GR $Ni_2P_2O_7$ electrodes, coated from methanol and calcined at a) 300, b) 400, c) 500, and d) 600ºC.

To conduct the electrode's OER performance, the chronoamperometry and chronopotentiometry experiments are done, see Figure 3.84. From the chronoamperometry experiments, the Tafel slopes can be obtained, which shows the Tafel slope value as 44 mv/dec, it is a low value indicating fast OER kinetics and a low overpotential. And the chronopotentiometry plots give overpotentials of 276 and 857 mV at 1 and 100 mA/cm^2 current densities, respectively. Also, the electrode is stable during these measurements.

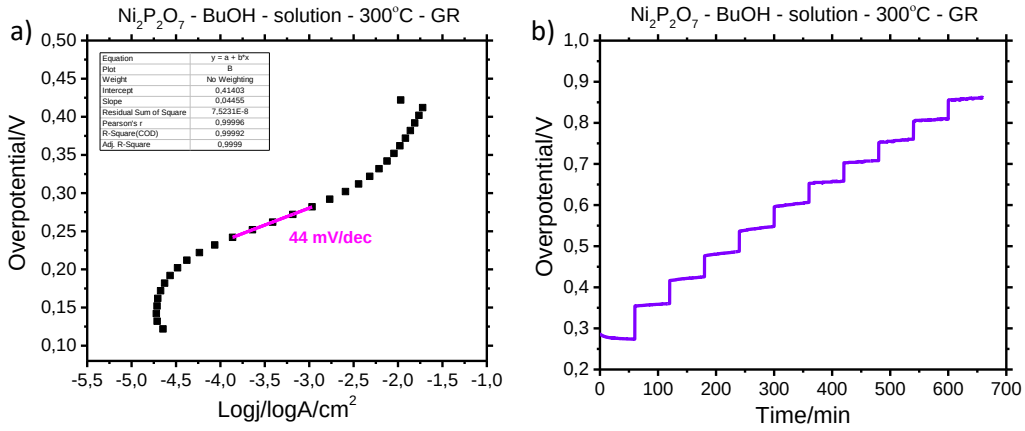


Figure 3.84: a) The chronoamperometry plot, indicating 44 mV/dec Tafel slope and b) chronopotentiometry plot of GR-$Ni_2P_2O_7$ electrode, prepared from butanol and calcined at 300ºC.

To show effect of the electrolyte, 0.1 g of $Ni_2P_2O_7$ sample (Ni30-15PPA butanol solution) is put into 10 ml of 1 M KOH solution. Then, one sample is directly centrifuged at 6000 rpm for 15 minutes. In the other samples, $Ni_2P_2O_7$ powder, aged in 1 M KOH solution for 15, 30, and 60 minutes and removed by centrifuging as above. Then, each sample is washed with deionized water 4-5 times to get rid of any contamination from the KOH solution. The powder is then dried at 80ºC oven for 1 day. ATR-FTIR spectra of these powders display a decrease in intensity of the phosphate peaks, while there is an increase in the hydroxide and carbonate peaks, Figure 3.85(a). Note that the carbonate species are observed because of inefficient washing of KOH that react with atmospheric CO_2 to from carbonates. The disappearance of phosphorus in the sample in 1 M KOH solution is also confirmed by EDX analysis, see Figure 3.85 (d). The phosphorous peak completely disappears. High-angle XRD patterns also matchwith the XRD pattern of the β-$Ni(OH)_2$, however the diffraction lines are very broad, indicating the formation ultra-small particles, Figure 3.85(b). To evaluate the change in the surface area, N_2 adsorption-desorption isotherms are collected using the $Ni_2P_2O_7$ sample, kept in 1 M KOH for 60 minutes. As shown in Figure 3.85(c)-(d), the porosity and surface area significantly decrease after this transformation and the resulting $Ni(OH)_2$ is not mesoporous.

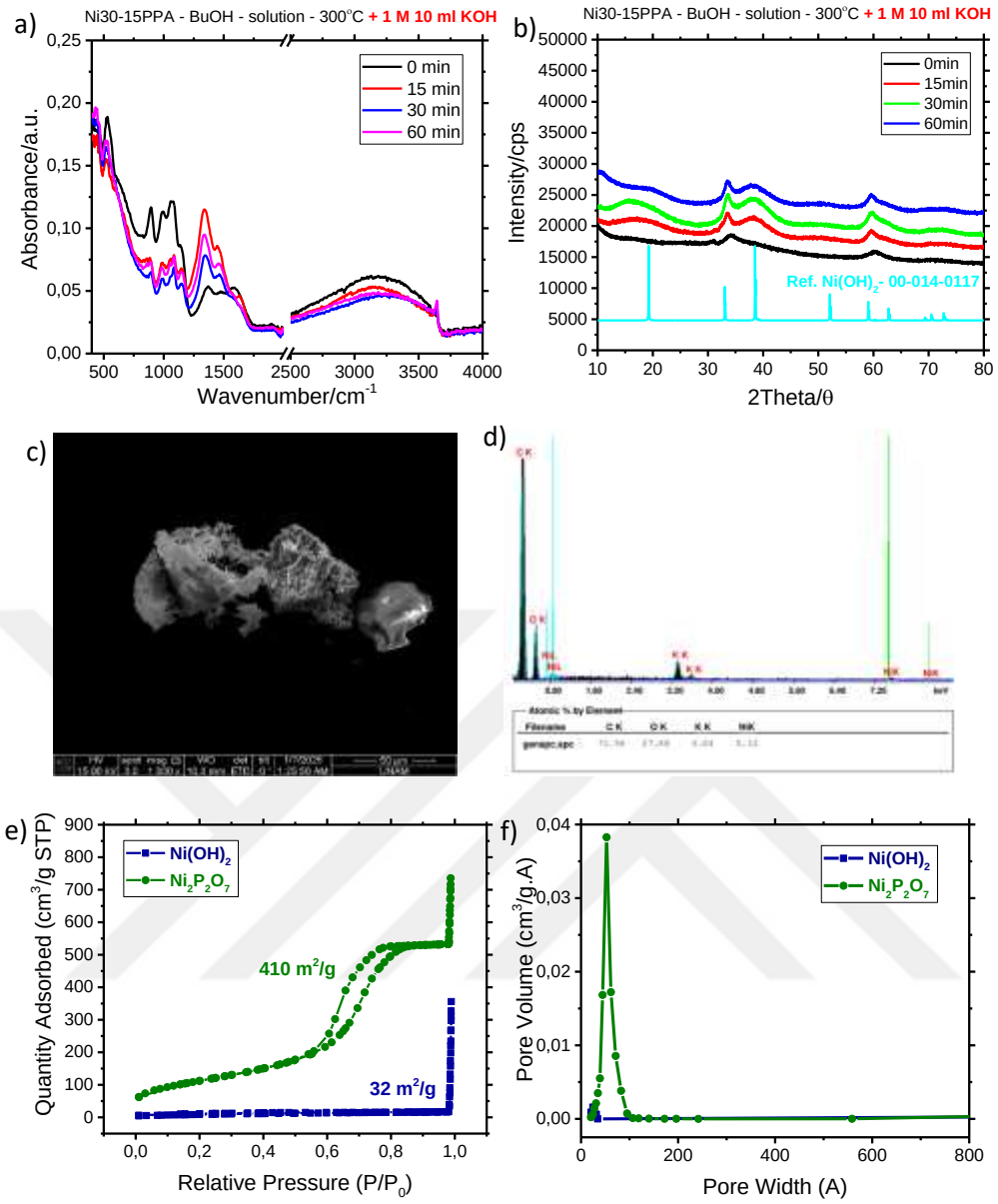


Figure 3.85: a) The ATR-FTIR spectra and b) high-angle XRD patterns of the $Ni_2P_2O_7$ samples, kept in 1 M KOH solution for various durations, c)-d) SEM image and EDX spectrum of the $Ni_2P_2O_7$ samples, kept in 1 M KOH solution for 60 minutes and washed and dried, e)-f) N_2 adsorption-desorption isotherms and BJH pore-size distribution plots of $Ni_2P_2O_7$ and $Ni(OH)_2$ powders.

As this transformation proceeds rapidly in 1 M KOH solution but, does not ocur in a neutralized solution. 30 ml of the neutralized solution is used as the electrolyte solution while the electrode is $Ni_2P_2O_7$-coated GR electrode. After each consecutive 5 cycles, 0.5 ml of 1 M KOH solution is added to the electrolyte solution until complete transformation is achieved.

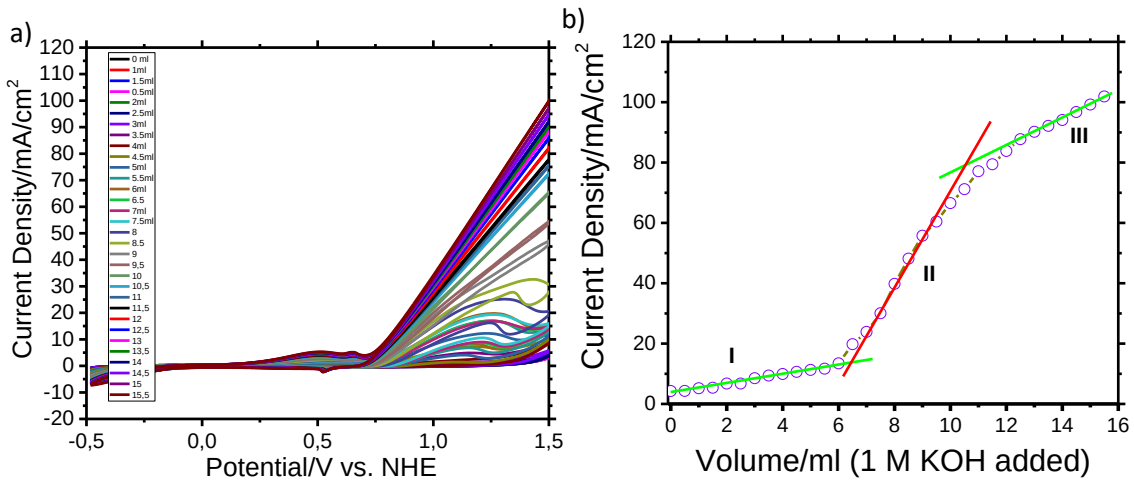


Figure 3.86: a) 5th CVs after addition of 0-15.5 ml of 1M KOH to neuralized (2.4 M KOH + 0.6 M $H_4P_2O_7$ solution) electrolite solution and (b) plot of current density versus added KOH at 1.5 V.

Figure 3.86(a) presents the 5th CVs from each step, as well as a plot of the current density at 1.5 V as a function of the total volume of KOH added to the neutalized electrolyte solution. These results show the transformation of $Ni_2P_2O_7$ into $Ni(OH)_2$ with increasing alkalinity. Figure 3.86(b) shows OER current versus volume of KOH added. The OER is highly dependent on hydroxide ion concentration. In Region I, upto 3.5 ml of 1 M KOH addition, a high concentration of $P_2O_7^{4-}$ ions in the medium suppresses this transformation. After this point, a new oxidation peak appears at around 1.2 V and its current density decreases with further KOH additions up to 8.5 ml. In the reverse scan, this peak reappears at a similar potential with a smaller, yet still positive, current density. This newly observed peak at 1.2 V is attributed to the newly formed $Ni(OH)_2$ species on the electrode surface. When the surface becomes fully covered wih $Ni(OH)_2$, after addition of 10 ml of 1 M KOH, the current density increases linearly with potential in the OER region, confirming its catalytic role and the $Ni(OH)_2$ being more efficient OER electrocatalyst than $Ni_2P_2O_7$. The change in the electrode surface during consecutive additions of 1 M KOH is shown in Figure 3.87.

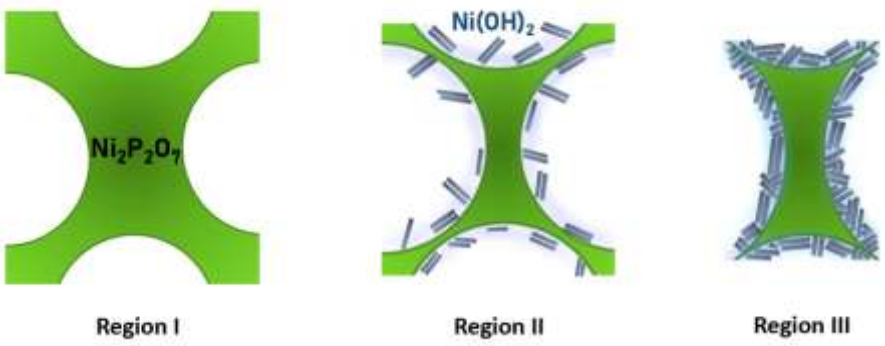


Figure 3.87: The schematic representation of the surface of the electrode (Region I) 0-3.5 ml, (Region II) 4-7.5 ml, and (Region III) 8-15.5 ml addition of 1 M KOH to a neuralized (2.4 M KOH + 0.6 M $H_4P_2O_7$) solution.

3.1.6. Synthesis and Characterization of Mesoporous $Mn_2P_2O_7$

The Mn30-15PPA solutions also undergo sol-gel process in ethanol and butanol but, not in methanol. The solutions are colorless immediately after the two solutions are mixed. However, as time passes, the colors of these solutions became pale-pink and then goes to brown after almost 1 day aging. The mixtures from sol-gels and solutions are poured in pyrex cup and dried at 100ºC and ground in a mortar and then placed in combustion crucibles and calcined at different temperatures. The powder, obtained from supernatant, is almost colorless and the amount of precipitate is large, therefore, the supernatant part is not further characterized in these solutions.

3.1.6.1. Mesoporous $Mn_2P_2O_7$ from Ethanol System

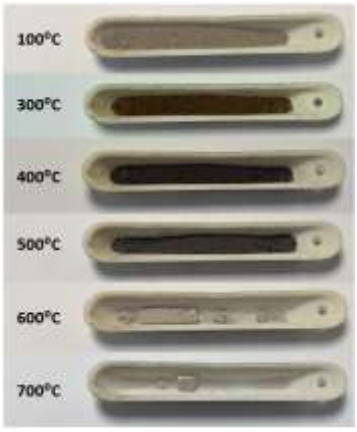


Figure 3.88: Photographs of the $Mn_2P_2O_7$ samples, obtained from the Mn30-15PPA ethanol solution, calcined at different temperatures.

The ethanol solutions undergo a sol-gel process after adding the acid solution to the metal salt solutions in one or two minutes. The color of the dried samples at 100ºC from this

gel is lighter brown but, it becomes dark brown at higher calcination temperatures till 600ºC. At 600 and 700ºC, the color is lighter, almost white. It becomes very hard that makes it hard to get it out from the combustion crucible at 600ºC and it becomes even harder at 700ºC.

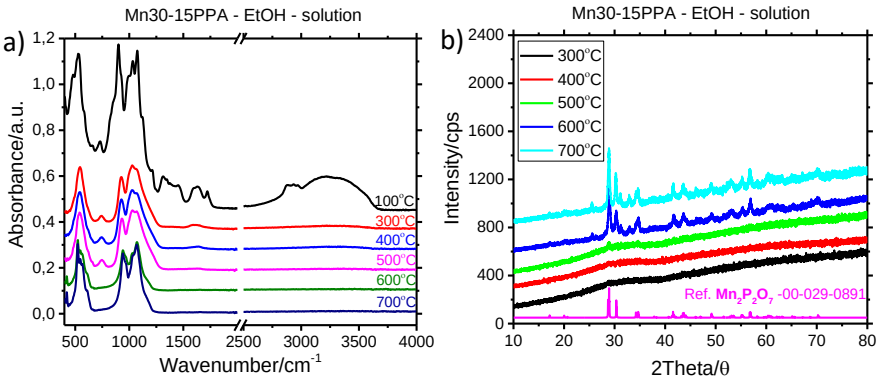


Figure 3.89: a) ATR-FTIR spectra and b) high-angle XRD patterns of the Mn30-15PPA ethanol solution after calcination.

The ATR-FTIR spectrum of the dried sample displays the surfactant peaks that disappear after calcining at 300ºC (see Figure 3.89(a)). And the spectra of the calcined samples up to 600ºC, has a peak at 750 cm^{-1} but above 600ºC, this peak disappears in the spectrum. It means that the amorphous phase, up to 600ºC, has a different $Mn_2P_2O_7$ phase than the crystalline $Mn_2P_2O_7$. The crytalline phase has a linear P-O-P bonds and its symetric stretching mode is IR inactive. However, major peaks of $Mn_2P_2O_7$ are unaltered in the spectra at 600 and 700ºC. The XRD patterns also correlate the IR data. The pattern display lines that can be indexed to α-$Mn_2P_2O_7$ with an additional unkown phase (see Figure 3.89(b)).

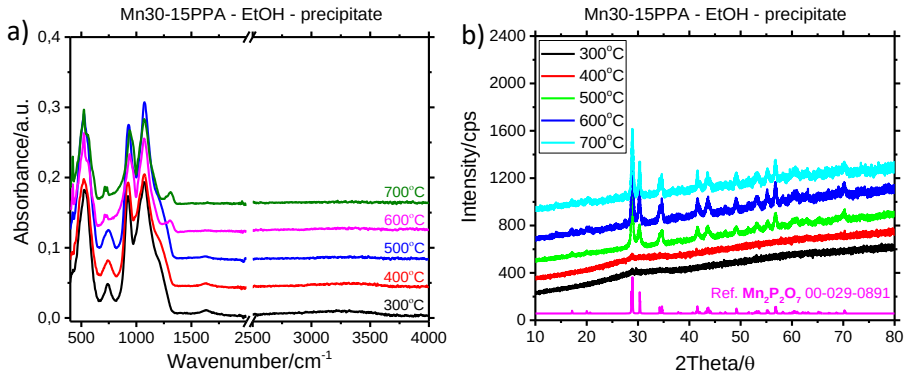


Figure 3.90: a) ATR-FTIR spectra and b) high-angle XRD patterns of the calcined Mn30-15PPA ethanol precipitates.

The precipitate is separated, dried at 100ºC, and calcined at different temperatures. Unlike the solution and/or gel-phase, the ATR-FTIR spectra of the calcined precipitate keep

the peak at 750 cm^{-1} even at 700ºC (see Figure 3.90(a)). Moreover, the sample at 600 and 700ºC are crystalline and all the lines can be indexed to only phase of $Mn_2P_2O_7$ (see Figure 3.90(b)).

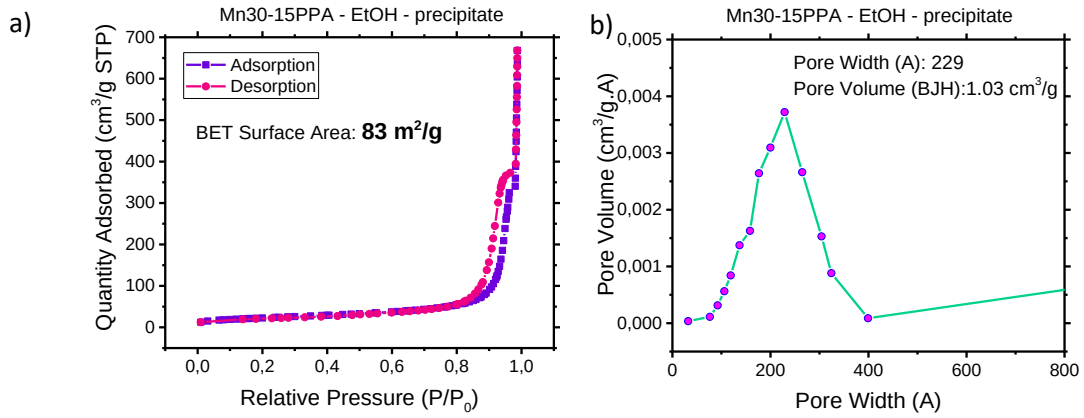


Figure 3.91: a) N_2 (77 K) adsorption-desorption isotherm and b) BJH pore size distribution plot of the calcined (at 300ºC) Mn30-15PPA ethanol precipitate.

N_2 adsorption-desorption isotherm proves that the powder, calcined at 300ºC, is mesoporous and have a surface area of 83 m^2/g. However, the pore size is around 229 Å and the pore-size distribution is very broad (see Figure 3.91). SEM images of the samples, calcined at 300 and 400ºC (Figure 3.92) show that the particles have a spherical morphology. However, as shown in Figure 3.92(b), there are also non-spherical and porous particles in these samples.

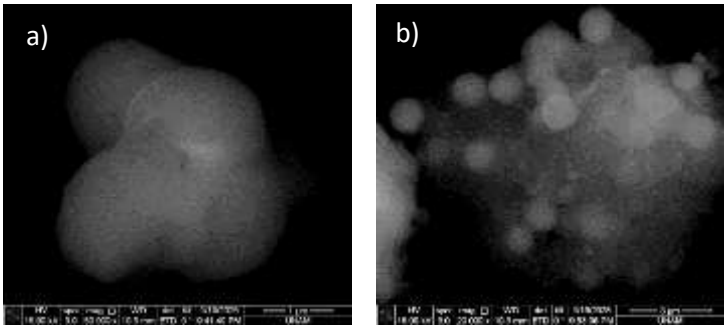


Figure 3.92: SEM images of the Mn30-15PPA of ethanol precipitate after calcination at a) 300ºC and b) 400ºC.

Thus, the calcined ethanol solution does not produce a pure $Mn_2P_2O_7$ phase. The sample is amorphous with a different phase of $Mn_2P_2O_7$ than its usual crystalline phase. However, the precipitate yields only $Mn_2P_2O_7$ crystals. And the precipitate part (calcined at 300ºC) is porous with a spherical morphology.

3.1.6.2. Mesoporous $Mn_2P_2O_7$ from Butanol System

In butanol system, the $Mn_2P_2O_7$ solution undergoes a very fast gelation (sol-gel process). However, very slow addition of the acid solution to the metal salt solution yield a homogeneous solution. Same steps for the calcination of gels are followed. The colors of the calcined samples are shown in Figure 3.93. Color of the powder is light-brown at 100ºC, and darker up to 600ºC, but becomes colorless at 600ºC.

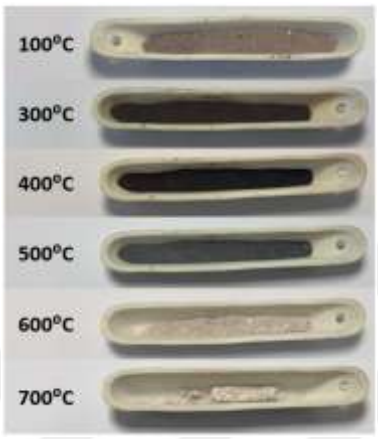


Figure 3.93: Photographs of the $Mn_2P_2O_7$ powders, obtained from the Mn30-15PPA butanol solution after calcination at indicated temperatures.

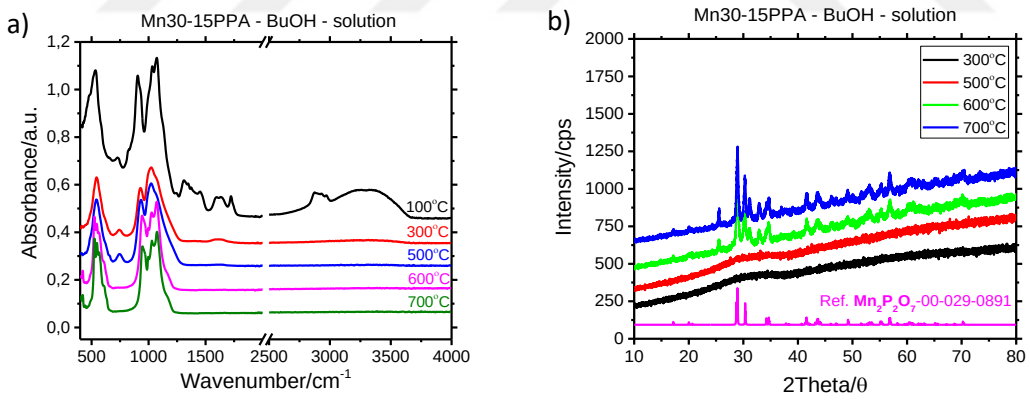


Figure 3.94: a) ATR-FTIR spectra and b) high-angle XRD patterns of the calcined Mn30-15PPA butanol solution.

The ATR-FTIR spectra of the calcined samples display no surfactant peaks, indicating an effective removal from the sample at 300ºC. The crystallization starts at 600ºC and the sample contains $Mn_2P_2O_7$ crystals along with at least one more unknown crystalline phase. As in the ethanol solution part, the ATR-FTIR spectra of the amorphous phase of the calcined samples, up to 600ºC, has a peak at 750 cm^{-1} that is an good indicator of the pyrophosphate species and also means that the amorphous phase has another phase of $Mn_2P_2O_7$.

Unlike the solution part, the calcined samples of the precipitate part display high-angle XRD patterns that can be indexed to only one phase of $Mn_2P_2O_7$. The crystallization occurs at a lower calcination temperatures, the most intense diffraction line around 30º, 2θ, appears even at 400ºC (see Figure 3.95(a)). In the ATR-FTIR spectra, the phosphate region indicates the formation pyrophosphate species and the amount of water in these samples are very low indicating low porosity and surface area (Figure 3.95(b)). However, the N_2 adsorption-desorption isotherms indicate a porous structure with a low surface area and very broad pore size distribution (see Figure 3.95(c)-(d)).

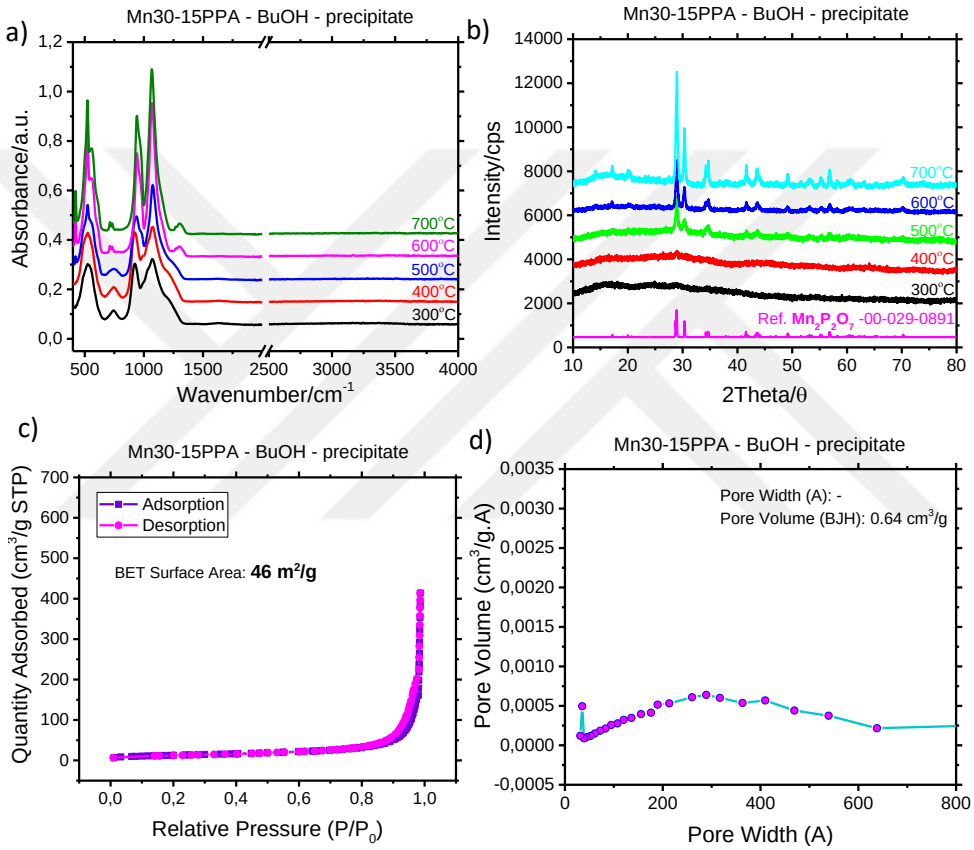


Figure 3.95: a) ATR-FTIR spectra and b) high-angle XRD patterns of Mn30-15PPA butanol precipitate part calcined samples, c) N_2 (77 K) adsorption-desorption isotherm, and d) BJH pore-size distribution plot of $Mn_2P_2O_7$ calcined at 300ºC obtained from Mn30-15PPA butanol precipitate part.

3.1.6.3. Mesoporous $Mn_2P_2O_7$ from Methanol System

In methanol system, the solution does not undergo a sol-gel process. The calcination process is kept the same and the calcined samples have different shades of grey color up to 700ºC, Figure 3.96. At 700ºC, the color became closer to white. ATR-FTIR spectra show that there is a phase change at 600ºC. The peak at 750 cm^{-1} disappears above this temperature. Also,

high-angle XRD patterns show that there is at least one more diffraction lines due to another unkn0wn phase of $Mn_2P_2O_7$.

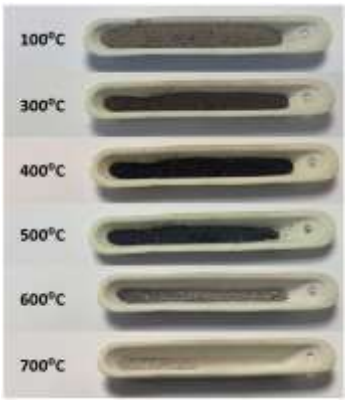


Figure 3.96: Photographs of the $Mn_2P_2O_7$ samples, obtained from the calcined Mn30-15PPA methanol solution.

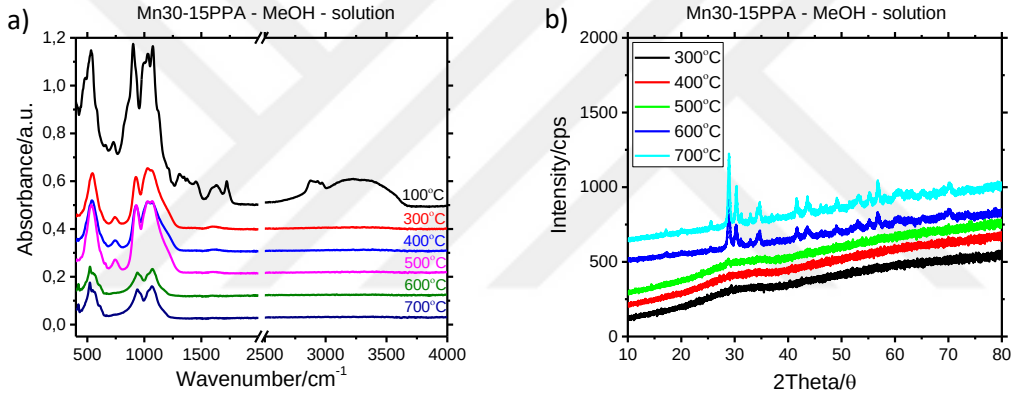


Figure 3.97: a) ATR-FTIR spectra and b) high-angle XRD patterns of the calcined Mn30-15PPA methanol solution.

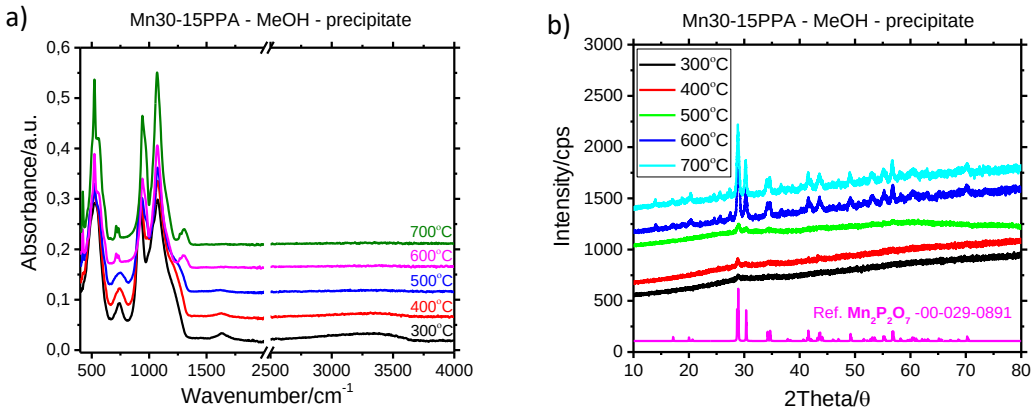


Figure 3.98: a) ATR-FTIR spectra and b) high-angle XRD patterns of the samples from calcined Mn30-15PPA methanol precipitate.

As in the other solvents, the precipitate part also yields $Mn_2P_2O_7$ crystals above 600ºC and the amount of water in ATR-FTIR spectra show low porosity and surface area, which is also correlated by N_2 (77 K) adsorption-desorption isotherms. The BJH pore size distribution is also very broad (see Figure 3.99(b)).

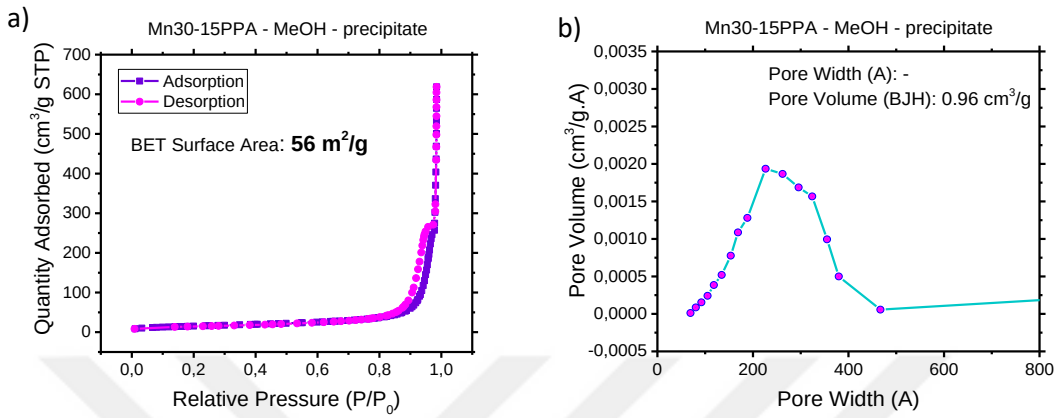


Figure 3.99: a) N_2 (77 K) adsorption-desorption isotherm, and b) BJH pore size distribution plot of the calcined Mn30-15PPA methanol solution (calcined at 300ºC) powder.

3.1.6.4. Solvent Comparison of Mesoporous $Mn_2P_2O_7$

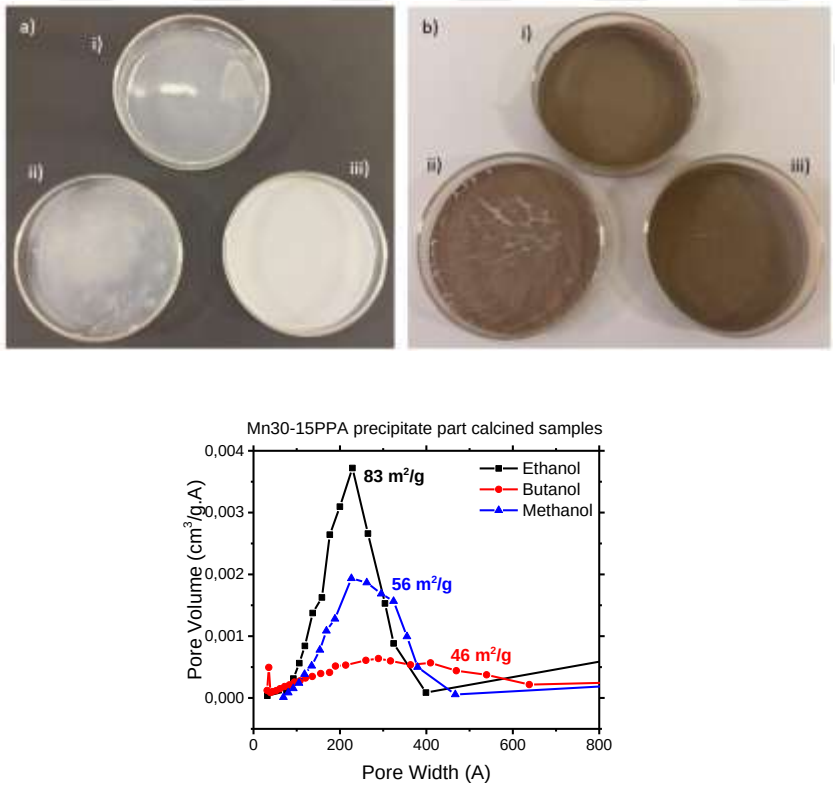


Figure 3.100: The solutions of $Mn_2P_2O_7$ in i) ethanol, ii) butanol, iii) methanol a) poured into pyrex cup, and b) dried at 100ºC for one day, c) the pore-size distributions of the Mn30-15PPA precipitate, calcined at 300ºC.

In ethanol and butanol solvents, as in the other metals, there is a sol-gel formation. However, in methanol, a cloudy solution forms. Both the gels and solution are clear immediately after the acid and metal salt solutions are mixed. However, the color changes to pink and brown as time passes in each of these solvents. The solution part (calcined samples) has at least two crystal phase above 600ºC but, the precipitate yields a pure $Mn_2P_2O_7$ phase. And the precipitate crystallizes at 400 or 500ºC but, the solution crystallizes at 600ºC. The porosity and surface area in these $Mn_2P_2O_7$ samples are low in butanol and metanol systems, 56 and 46 m^2/g, respectively, but, in the ethanol system, the surface area almost doubles, 83 m^2/g and pores are more uniform (see Figure 3.100).

3.1.6.5. Electrochemical Characterization of Mesoporous $Mn_2P_2O_7$ and Its Transformation to β-$Mn(OH)_2$

The Mn30-15PPA forms sol-gel in ethanol and butanol solvents and cloudy solution in methanol solvent. These samples are spin-coated over FTO glasses or dip-coated over GR and calcined at a desired temperature (300 to 600ºC) and tested in a three-electrode system in 1 M KOH solution.

Firstly, 50 CVs are recorded to check their electrochemical behaviours. Figures 3.101, 3.102, and 3.103 shows a selected group of CVs from each electrodes, prepared from ethanol, butanol and methanol systems, respectively. The CVs are recorded with a scan rate of 50 mV/s in a potential window of -0.5 - 2.0 V versus NHE. In the first cycle of the electrodes, calcined at 300, 400ºC, and 500ºC, there is a very broad peak. In the second and the further cycles, the current density of this broad peak gradually decreases and disappears in third cycle. This shows that the oxidized species is used irreversibly in the OER region or in the electrolyte solution. In almost all the CVs, there is a decline in the current density in the OER region as the cycle number increases. This is attributed to electrode degradation during cycling. Also, in these electrodes during the first oxidation scan, a pink color is observed around the surface of the electrode but, it disappears very quickly. In 2024, Karakaya et al. suggested a degredation mechanism for the manganese disproportionation reaction to produce pink colored MnO_4^- species at the surface of the electrode in alkaline media [87]. As the color indicates, this reaction can be the reason of the decrease in the current density at 1.5 V.

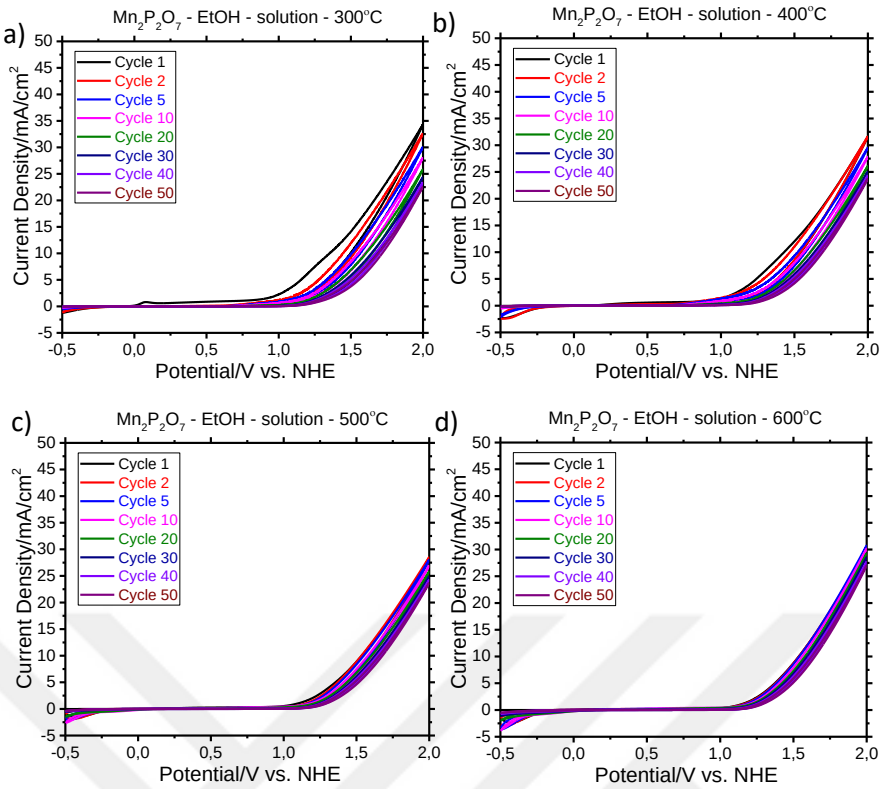


Figure 3.101: A selected group of CVs from 50 cycles in 1 M KOH electrolyte solution with a scan rate of 50 mV/s of the FTO $Mn_2P_2O_7$ electrodes, coated from ethanol and calcined at a) 300, b) 400, c) 500, and d) 600ºC.

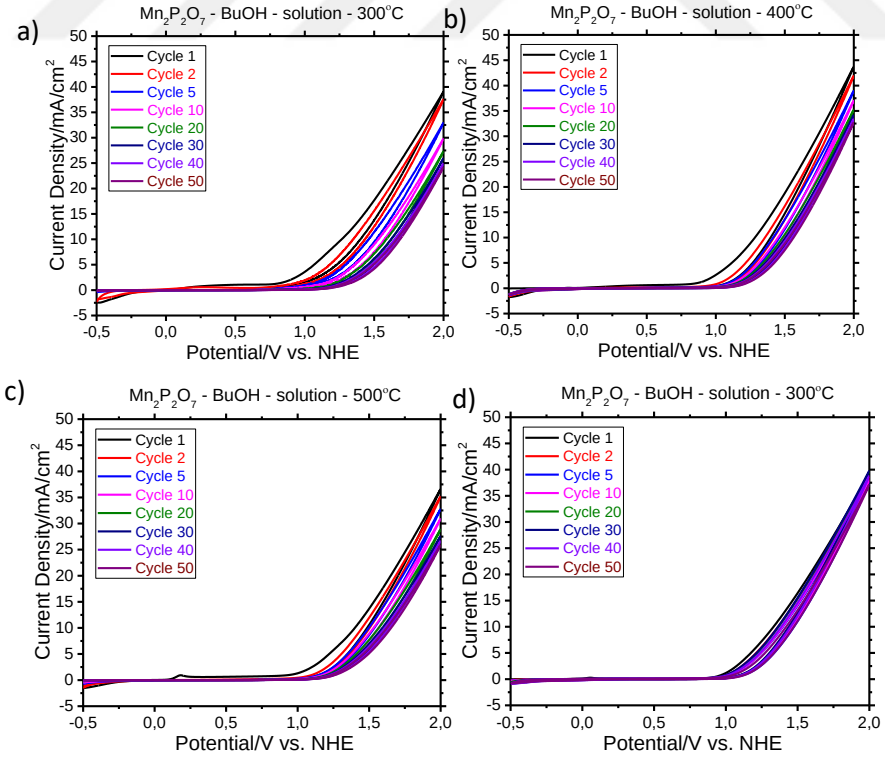


Figure 3.102: A selected group of CVs from 50 cycles in 1 M KOH electrolyte solution with a scan rate of 50 mV/s of the FTO $Mn_2P_2O_7$ electrodes, coated from butanol and calcined at a) 300, b) 400, c) 500, and d) 600ºC.

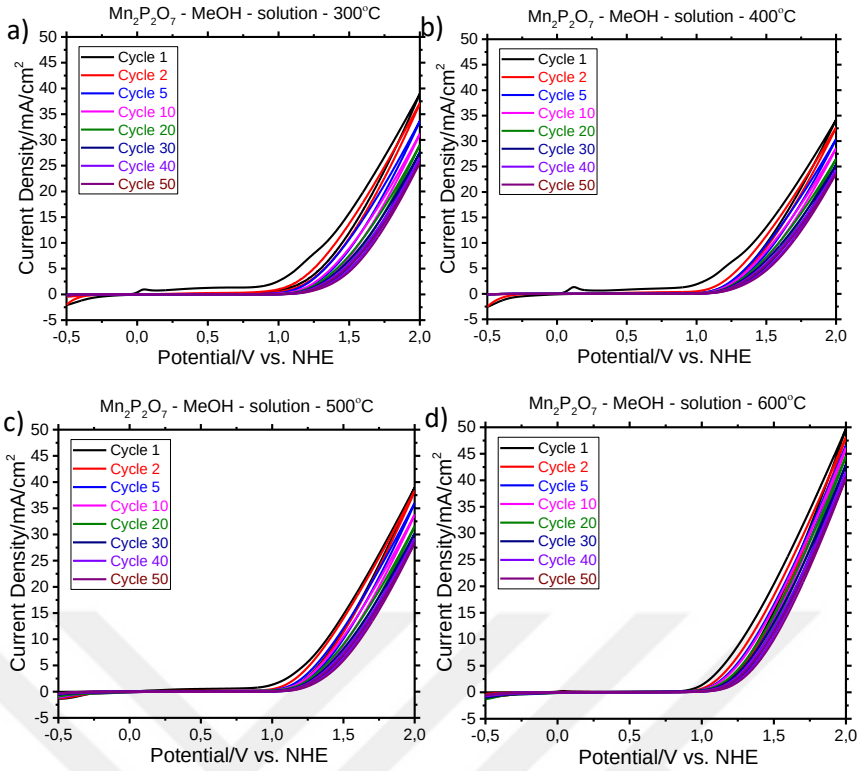


Figure 3.103: A selected group of CVs from 50 cycles in 1 M KOH electrolyte solution with a scan rate of 50 mV/s of the FTO $Mn_2P_2O_7$ electrodes, coated from methanol and calcined at a) 300, b) 400, c) 500, and d) 600ºC.

As in cobalt and nickel systems, 0.1 g of $Mn_2P_2O_7$ powder is put in 10 ml of 1 M KOH solution. Exact same procedure is employed to collect the samples after removing at 0, 15, 30, and 60 minutes from KOH solution. The ATR-FTIR spectra given in Figure 3.104(a) show that even tough there is a decrease in the amount of phosphate species, not all the phosphate disappears from the samples. High-angle XRD patterns, shown in Figure 3.104(b), show that the $Mn_2P_2O_7$ crystals remain in the samples, even tough there is a transformation of $Mn_2P_2O_7$ to $Mn(OH)_2$ crystals.

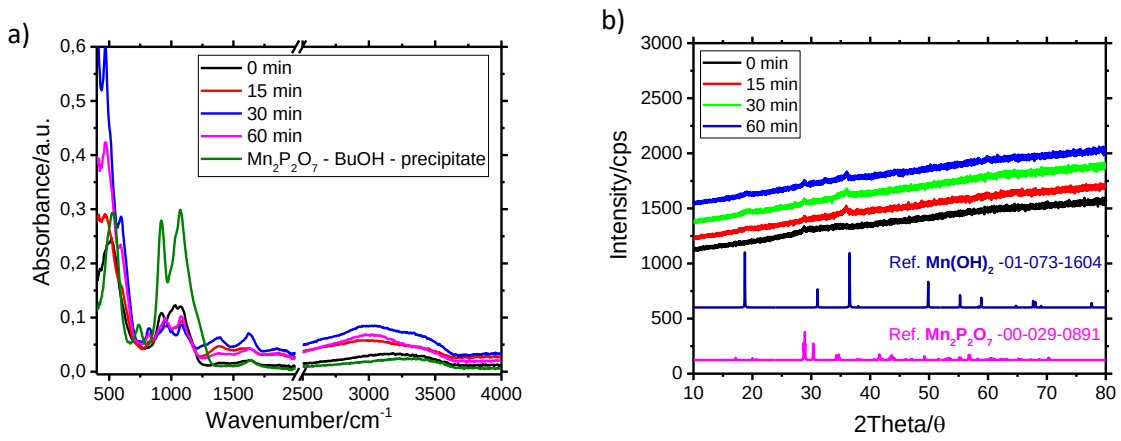


Figure 3.104: a) The ATR-FTIR spectra and b) high-angle XRD patterns of the $Mn_2P_2O_7$ samples, kept in 1 M KOH solution for durations, given in the spectra and patterns.

Again, to follow above transformation, CVs are recorded after addition of 1M KOH to the neuralized solution as decribed in the nickel and cobalt sections, The 5th cycles of the CVs at each step is shown in Figure 3.105(a). The current density increases at each step since the conductivity of the electrolyte solution increases as well as the $Mn(OH)_2$ species at the surface of the electrode increases. A similar changes occur as in the cobalt and nickel systems. Figure 3.105(c) also shows the change in the oxidation peaks. Up to 10.5 ml of KOH addition only the peak at ~0.4 V appears and increases gradually, which is due to the oxidation of –OH species forming at the surface of the electrode. After 10.5 ml, another peak at ~0.6 V appears that may have an origin of oxidation of bulk hydroxide species. These changes in the oxidation peaks may also confirm the transformation of $Mn_2P_2O_7$ to $Mn(OH)_2$ species. The origin of these peaks need to be find out to fully elucidate the process.

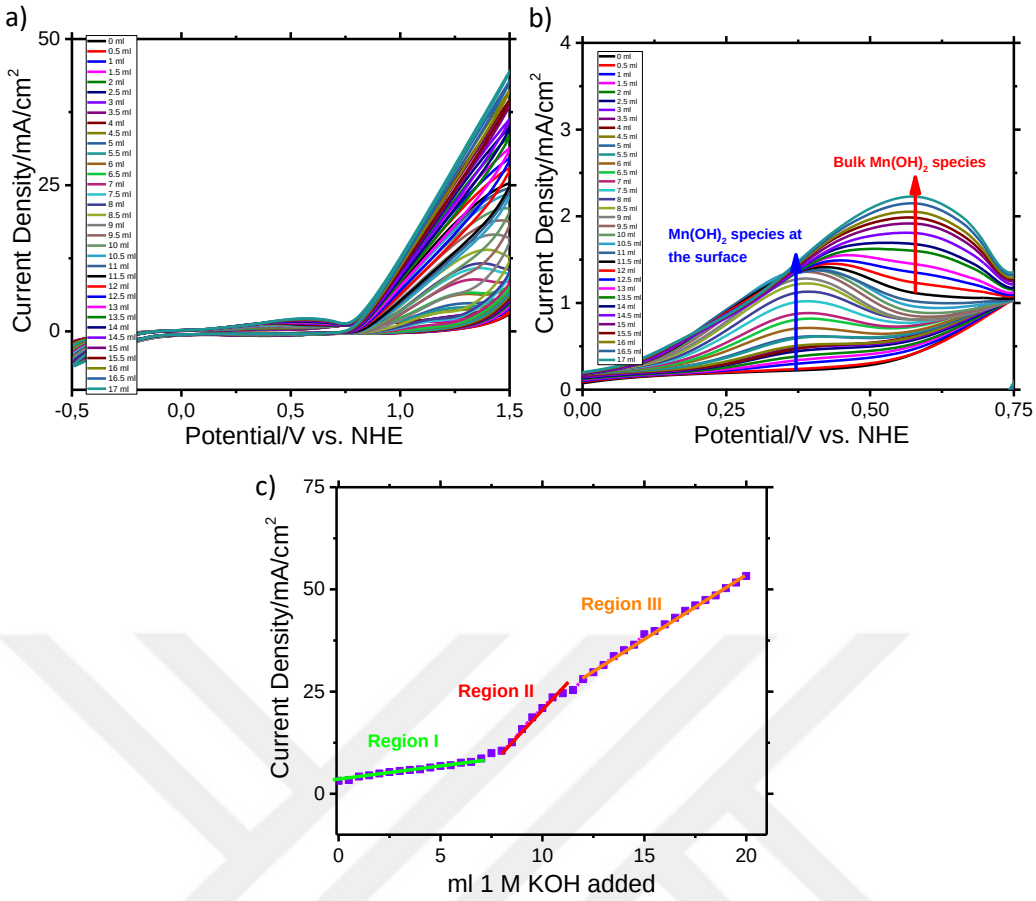


Figure 3.105: a) $Mn_2P_2O_7$ coated GR electrode, 5th CVs with consecutive addition of 0.5 ml of 1 M KOH solution, b) same CVs, zoomed in, and c) current densities at 1.5 V at 5th CVs at each step as a function of volume of 1 M KOH added.

3.2. Synthesis and Characterization of Binary Metal Pyrophosphates ($M_{2-x}M'_xP_2O_7$, M= Mn, and M'= Ni(II) and Co(II))

Solutions of binary metal mixtures of Mn(II) with Co(II) and Ni(II) are also prepared to be able to increase the stability of the manganese pyrophosphate, change the morphology, and increase the surface area. The mole ratio of metal salt:PPA:P123 (30:15:1) is kept constant but 5, 10, and 25% of Co(II) and Ni(II) salts are added to the Mn(II) solutions while the amount of Mn(II) is 95, 90, and 75%, respectively, in these solutions. Therefore, three solutions are prepared from each nickel and cobalt salts and the samples are labeled as MnM5%, MnM10%, and MnM25%, where the M is Ni and Co, respectively.

3.2.1. Ethanol Systems

3.2.1.1. Mesophases of the MnNi5-10-25% from Ethanol Systems

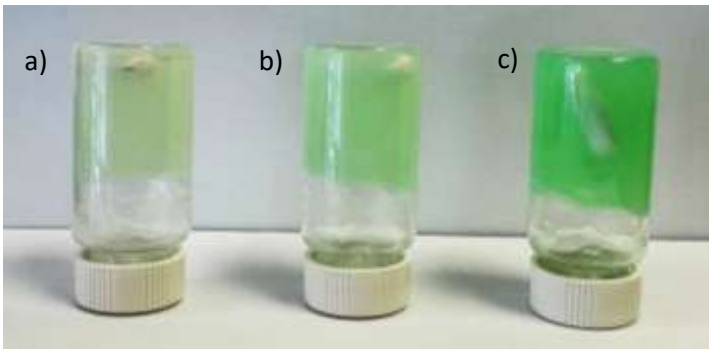


Figure 3.106: Photographs of the a) MnNi5%, b) MnNi10%, and c) MnNi25% ethanol mixtures.

The ethanol solutions of the MnNi5%, MnNi10% and MnNi25% (5, 10, and 25% Ni(II)) undergo quick sol-gel formation that the entire solution becomes a gel in a short-time after mixing the acid to salt solutions. The color of these solutions changes from a pale to darker green with increasing Ni(II), see Figure 3.106. Due to sol-gel formation, the solution part (gel), coated on the microscope slide is very thick. The same applies to the precipitate part, it was also hard to coat it on a microscope slide as a thin film. Both gel- and precipitate-coatings do not display any small-angle diffraction line, indicating a disordered phase. However, the supernatant part is a clear and stable solution for a long time and can be coated as smooth thin-film that displays diffraction lines at small anngles, indicating an ordered mesophase formation.

The color of this solution is a pale green but with aging for more than one or two hours, its color becomes brownish. Even though, the color of the solution is changed, the gel is still stable. As shown in the small-angle XRD patterns of the supernatant part, in Figure 3.107, there are diffraction lines that appear after 40 minutes at 1.97 and 3.03º, 2θ. However, after 5 hours, the first diffraction line shiftes to 1.77º, 2θ, and the second one disappears.

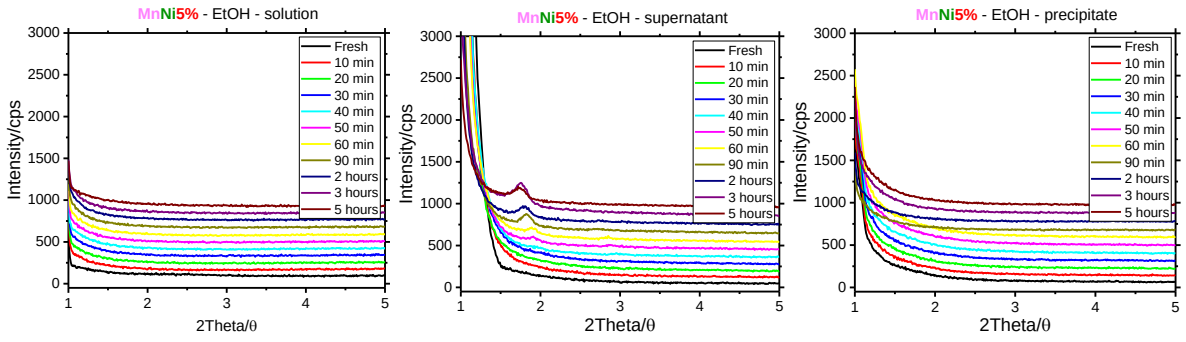


Figure 3.107: Small-angle XRD patterns of the (left to right) MnNi5% ethanol solution, supernatant, and precipitate.

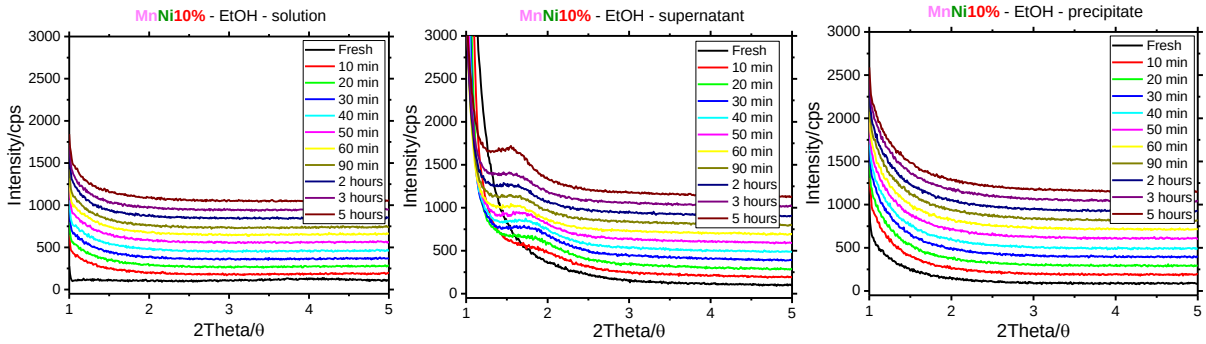


Figure 3.108: Small-angle XRD patterns of the (left to right) MnNi10% ethanol solution, supernatant, and precipitate during aging.

In MnNi10% ethanol sytem, again, there are diffraction lines in small-angle region only in the supernatant part. A broad diffraction line at 1.97º appears after 10 minute and it shifts to 1.58º after 5 hours, Figure 3.108. In MnNi25% ethanol supernatant, there is also a very broad diffraction line at 1.97º and it shifts to 1.60º after 5 hours, see Figure 3.109. As the amount of nickel in these mixtures increases, the diffraction line appear earlier during aging but, it becomes more broad.

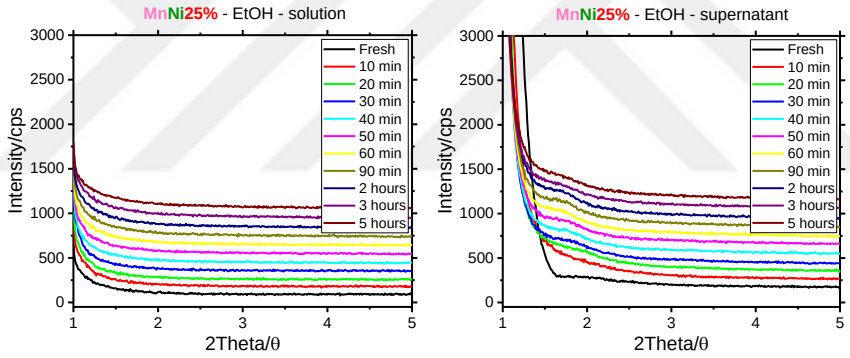


Figure 3.109: Small-angle XRD patterns of the MnNi25% ethanol solution and supernatant parts.

3.2.1.2. Mesoporous $Mn_{2-x}Ni_xP_2O_7$ from Ethanol MnNi5-10-25% Mixtures

The calcination step is the same as in the single metal pyrophosphates. The gels and solutions are put into pyrex cup and dried at 100ºC for one day and calcined at 300, 400, 500, 600, and 700ºC. The powders are characterized by ATR-FTIR, XRD, N_2 adsorption-desorption, and SEM techniques.

In the ATR-FTIR spectra of the powders, obtained from the calcination of MnNi5%, MnNi10%, and MnNi25% ethanol solutions, the phosphate region shows the formation of pyrophosphate species (see Figure 3.110(a)-(c)-(e)). Remember in the pure $Mn_2P_2O_7$ samples, the peak at 750 cm^{-1} disappears after calcining the samples at 600ºC. However, it reappears with low intensity in the spectra of the calcined samples of the binary metal solution. By

increasing the Ni(II) in the mixture, it becomes more dominant, likely because of Ni(II) disturbing the linear P-O-P bond making it bend and becomes IR active. Moreover, the water region displays peaks due to presence of high amount of water and also an indicator of high surface area and porosity.

The high-angle XRD patterns of these samples show that the crystallization of $Mn_2P_2O_7$ starts above 600ºC, like in the single metal system (see Figure 3.110(b)-(d)-(f)). And also, as in the calcined single metal solution, the binary metals yield at least one more unkown phase.

The supernatant gives metal phosphates (not metal pyrophosphates) as in the single metal sytems, therefore, binary metal mixtures of the supernatant is not further characterized. However, the precipitate is calcined at each calcination temperatures and characterized by several techniques (see Figure 3.112).

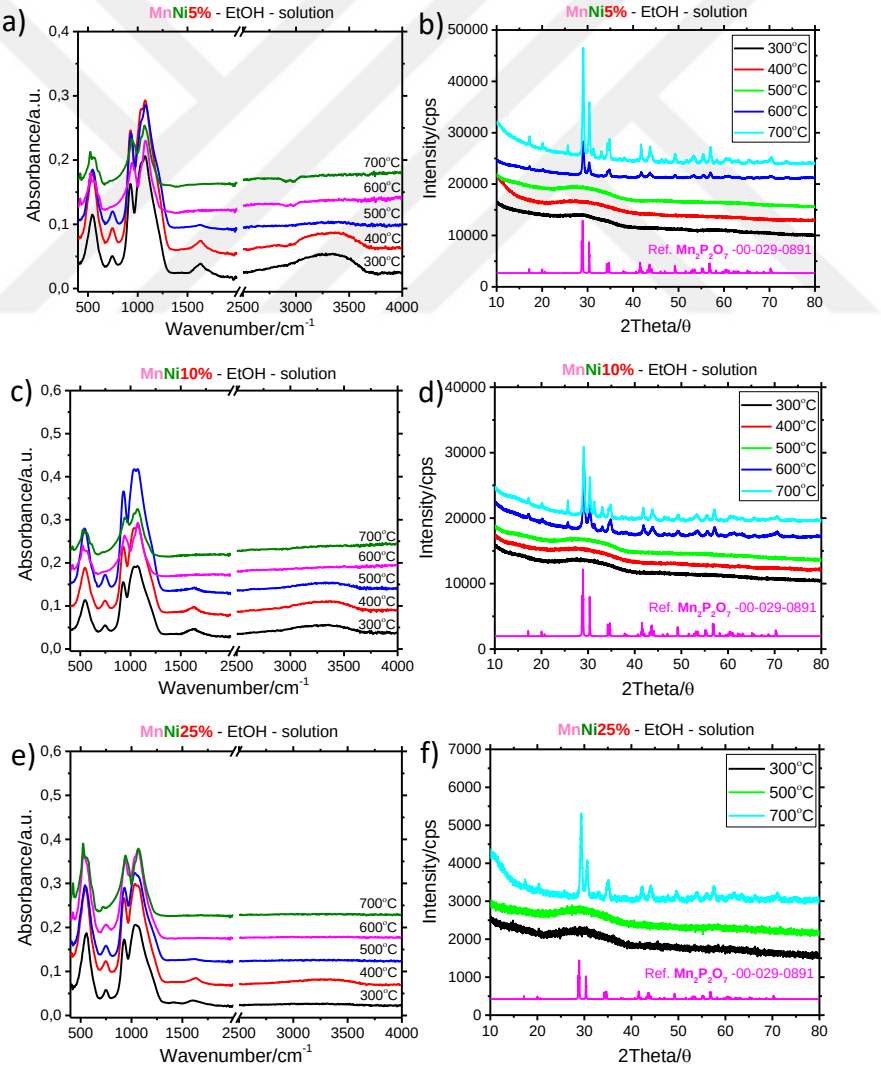


Figure 3.110: a), c), and d) ATR-FTIR spectra and b), d), and f) high-angle XRD patterns of the calcined MnNi5%, MnNi10%, and MnNi25% ethanol solutions.

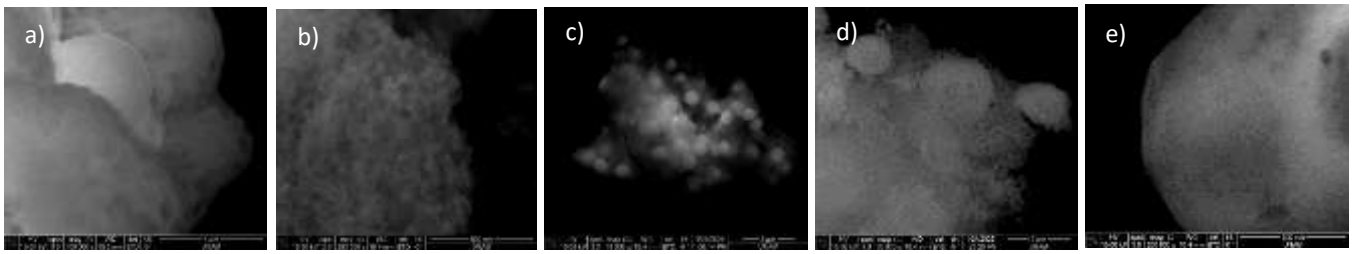


Figure 3.111: SEM images of the MnNi25% ethanol solution, calcined at a) 300, b) 400, c) 500, d) 600, and e) 700ºC.

The SEM images of the calcined MnNi5% and MnNi25% samples show pores samples, Figure 3.111. In the calcined MnNi25% samples, there are spherical particles with porous structures. At lower temperatures, the porosity is not that obvious. However, at higher calcination temperatures, the particles grow, crystallize and the morphologies and porosity become more obvious.

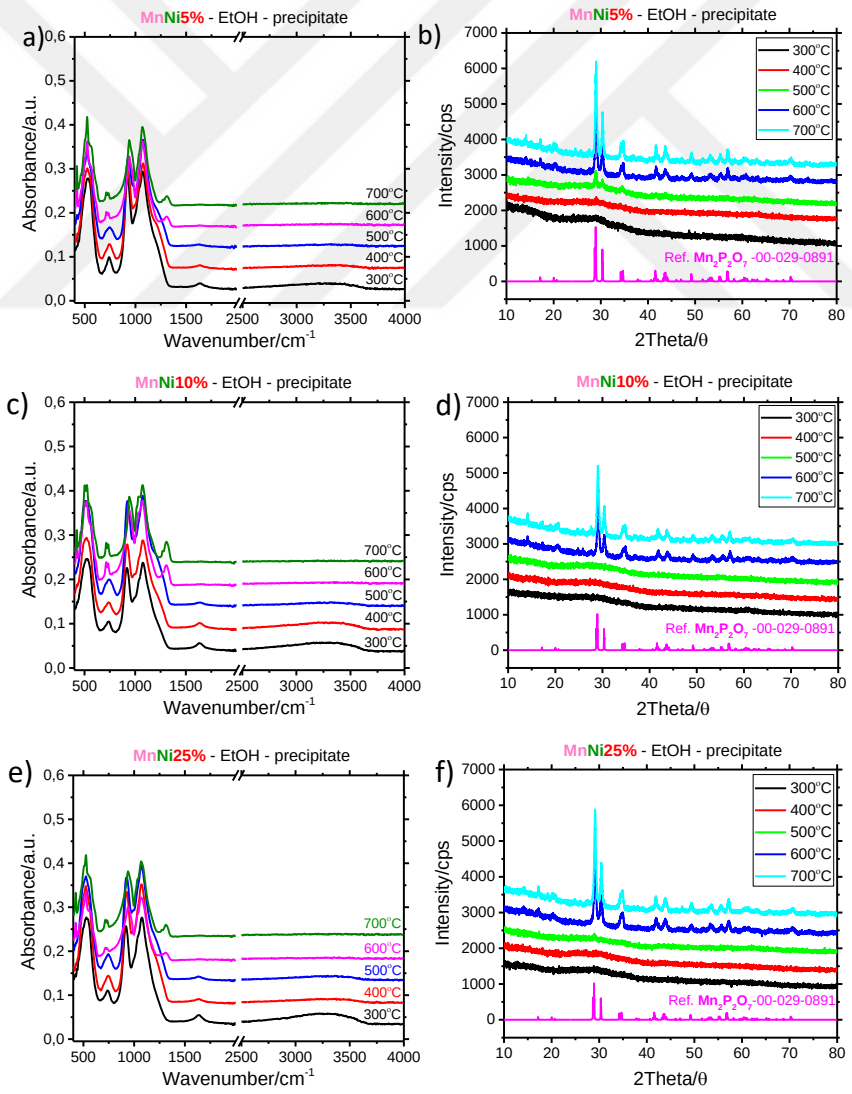


Figure 3.112: a), c), and d) ATR-FTIR spectra and b),d, and f) high-angle XRD patterns of calcined samples of the MnNi5%, MnNi10%, and MnNi25% ethanol precipitates.

The ATR-FTIR spectra of the calcined samples of the MnNi5%, MnNi10%, and MnNi25% (ethanol precipitate) display peaks related to the pyrophosphate species. The peak at 750 cm^{-1} is observed at each of the calcination temperature as in the pure calcined Mn(II): PPA:P123 precipitates. The water peaks are also intense at low calcination temperatures, indicating high porosity and surface area in these samples. The high-angle XRD patterns display diffraction lines at relatively lower temperatures in these binary metal samples. The crystallization starts at as low as 400, 500, and 600ºC in the MnNi5%, MnNi25%, and MnNi10% precipitates, respectively. Since there is no trend in the crystallization temperature, it may be said that Ni(II) may not be homogeneously distributed in the structure.

N_2 adsorption-desorption isotherms with BJH pore-size distribution plots of the MnNi5%, MnNi10%, and MnNi25% mixtures (ethanol precipitate) are shown in Figures 3.113(a) and (b), respectively. The isotherms are type-IV, characteristic for the mesoporous material (see Figure 3.113(a)). The BJH pore-size distributions are relatively more uniform and sharper than pure $Mn_2P_2O_7$ sample. As the amount of Ni(II) increases, the pores get smaller and become more uniform (see Figure 3.113(b)). Also, Table 3.10 tabulates the details of the data. The surface area increases with increasing Ni(II) amount in the samples. Even in the MnNi5% sample, the surface area doubles, compared to the $Mn_2P_2O_7$ sample.

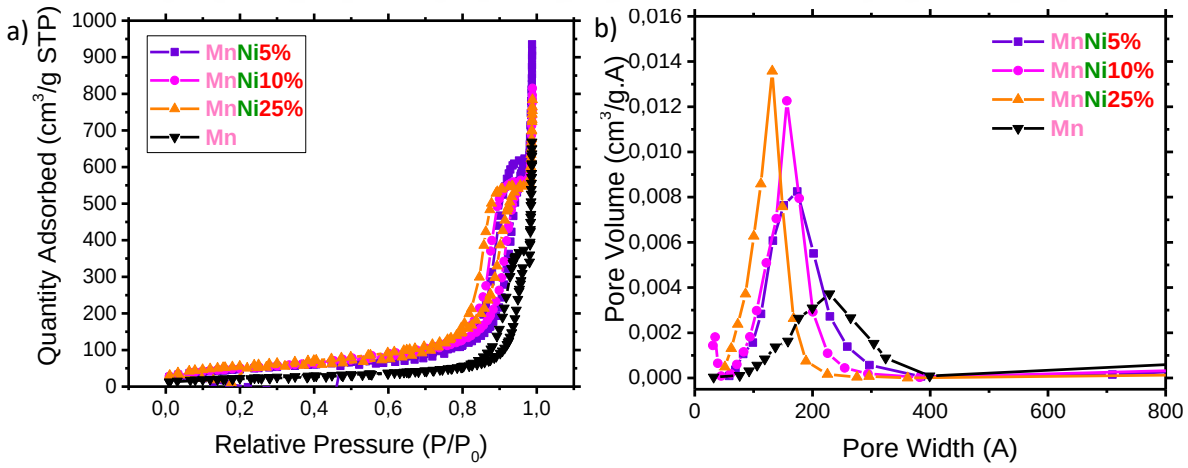


Figure 3.113: a) N_2 (77 K) adsorption-desorption isotherms, and b) BJH pore size distribution plots of the calcined MnNi5%, MnNi10%, MnNi25%, and pure $Mn_2P_2O_7$ samples, from ethanol precipitate, calcined at 300ºC.

Table 3.10: The BET surface area, BJH pore width and pore volume values of the MnNi5%, MnNi10%, MnNi25%, and pure $Mn_2P_2O_7$ ethanol precipitates, calcined at 300ºC.

Samples	BET Surface Area (m^2/g)	Pore Width (Å)	Pore Volume (cm^3/g)
MnNi5%	172	172	1.37
MnNi10%	182	157	1.26
MnNi25%	202	134	1.15
Mn	83	230	1.03

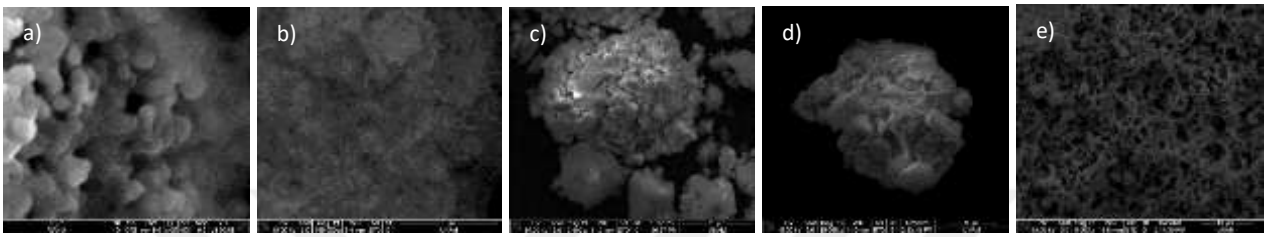


Figure 3.114: SEM images of the MnNi5% ethanol precipitate, calcined at a) 300, b) 400, c) 500, d) 600, and e) 700ºC.

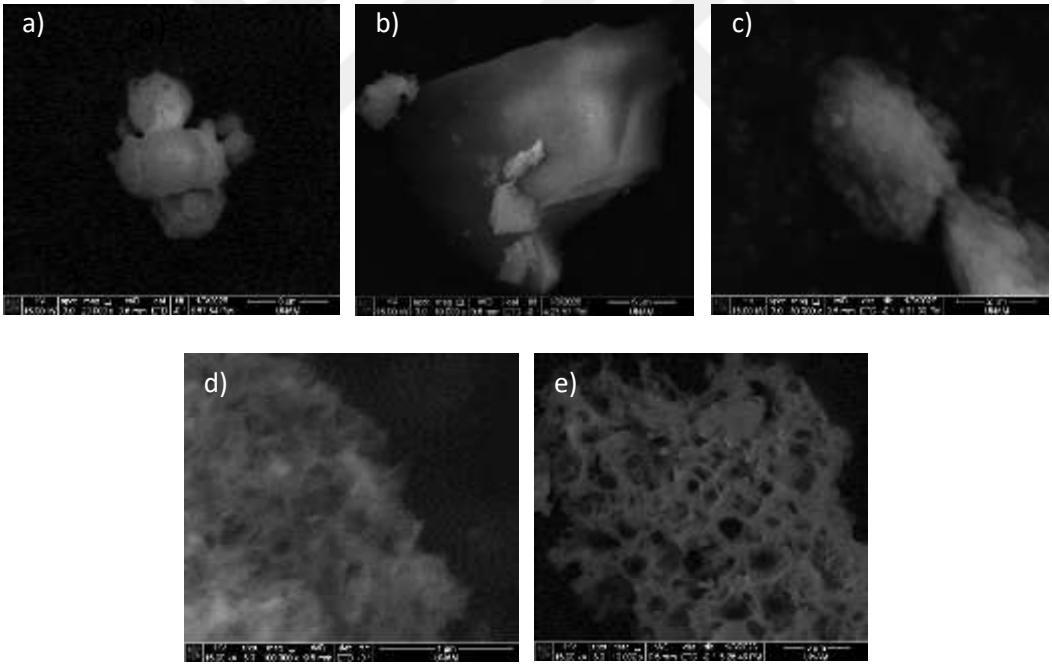


Figure 3.115: SEM images of the MnNi10% precipitate (from ethanol solvent), calcined at a) 300, b) 400, c) 500, d) 600, and e) 700ºC.

The SEM images of the precipitate parts of these binary metal mixtures (ethanol solvent) have both spherical and flake-like morphologies, which anneal to form macroporous crystals at high calcination temperatures, 600 and 700ºC, see Figures 3.114-115-116.

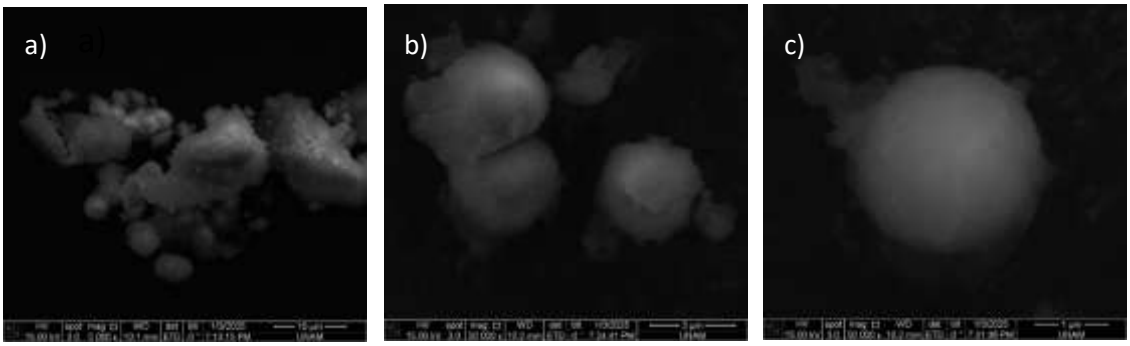


Figure 3.116: SEM images of the calcined MnNi25% precipitate (from ethanol solvent) after calcination at a) 300, b) 400, and c) 500.

3.2.1.3. Mesophases of the MnCo5-10-25% from Ethanol Systems

In ethanol, the MnCo5%, MnCo10%, and MnCo25% solutions undergo sol-gel formation, see in Figure 3.117. The colors of these solutions changes from pale pink to darker pink with increasing Co(II).

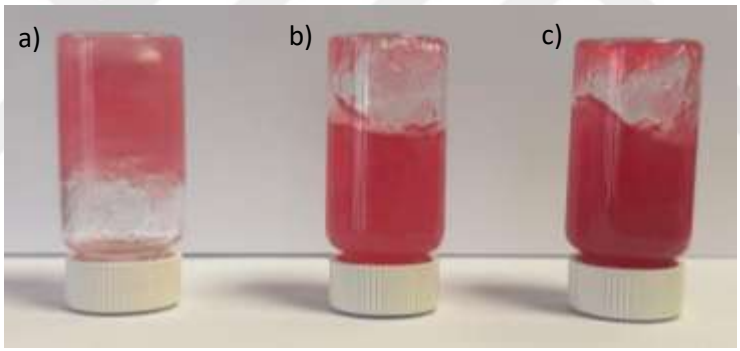


Figure 3.117: Photographs of the a) MnCo5%, b) MnCo10%, and c) MnCo25% ethanol mixtures.

3.2.1.4. Mesoporous $Mn_{2-x}Co_xP_2O_7$ from Ethanol MnCo5-10-25% Mixtures

After the calcination of these samples at different temperatures, 300 to 700ºC, several characterization techniques have been employed for their characterization. ATR-FTIR spectra display $Mn_2P_2O_7$ related peaks in the MnCo5% and MnCo10% samples, Figure 3.118(a)-(c)-(e). However, in MnCo25% sample, the peak at 750 cm^{-1}, which is assigned to the bend P-O-P bond in pyrophosphate species disappears after calcining the sample at 600ºC. High-angle XRD patterns, given in Figure 3.118(b)-(d)-(e), display diffraction lines of the $Mn_2P_2O_7$ crystal in the MnCo5% and MnCo10% samples, whereas the $Co_3(PO_4)_2$ crystals and another unknown crystal formation occurs in the MnCo25% sample.

ATR-FTIR spectra also display the peaks of water, which is an indication of a high-surface-area material. In order to check the porosity and surface area of these samples, the N_2 adsorption-desorption experiments were also conducted. The isotherm, given in Figure 3.119(a), is collected from calcined (300ºC) MnCo25% ethanol mixture. The isotherm is type IV. The BET surface area is 114 m^2/g. It means that addition of Co(II) species to the manganese system increases the surface area of these samples. The pore size distribution plot is given in Figure 3.119(b), also indicating this high-surface-area material having a relatively uniform pore-size, ~80 Å, as well.

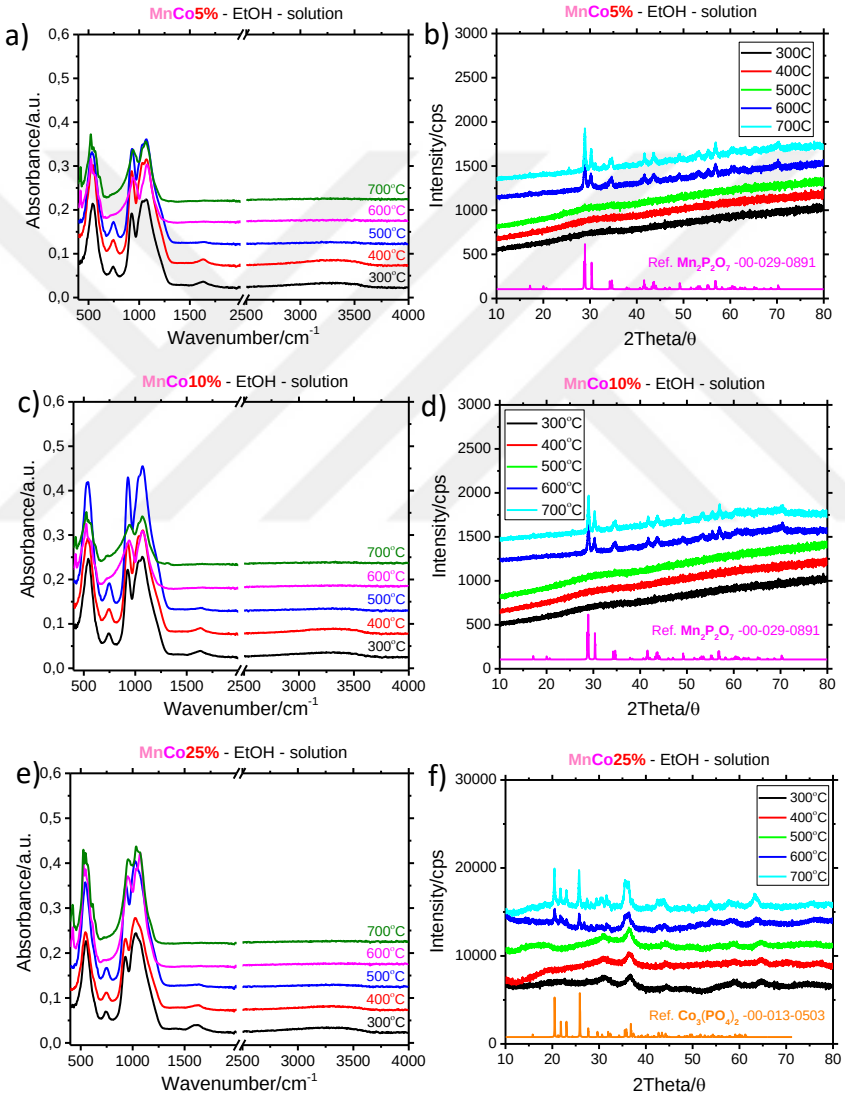


Figure 3.118: a), c), and d) ATR-FTIR spectra and b), d), and f) high-angle XRD patterns of the calcined MnCo5%, MnCo10%, and MnCo25% ethanol solutions.

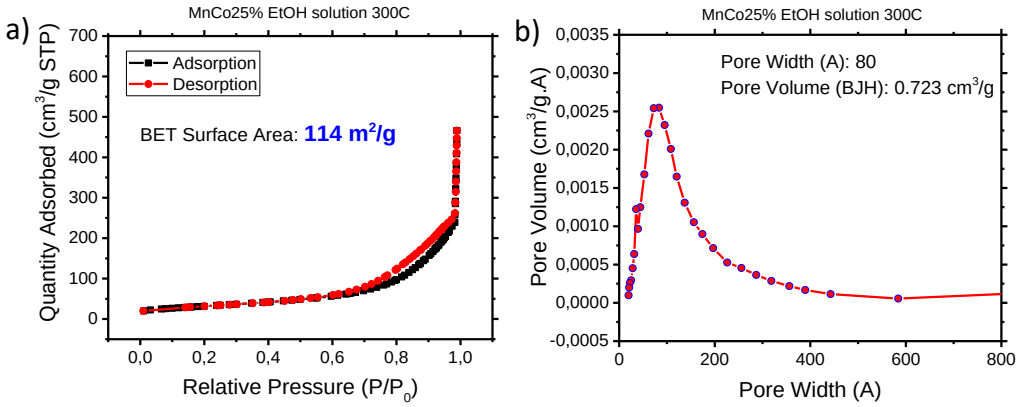


Figure 3.119: a) N_2 (77 K) adsorption-desorption isotherms, and b) BJH pore size distribution plot of the MnCo25% from ethanol solution, calcined at 300ºC.

Unlike the solution part, the calcined precipitate samples yield $Mn_2P_2O_7$ crystals. As the amount of cobalt is increased in these samples, the crystallization temperature also increases. The ATR-FTIR spectra of the calcined MnCo25% samples proves that these samples also hold water; an indicator of high surface area. The SEM images of these samples display both flake-like and spherical particles.

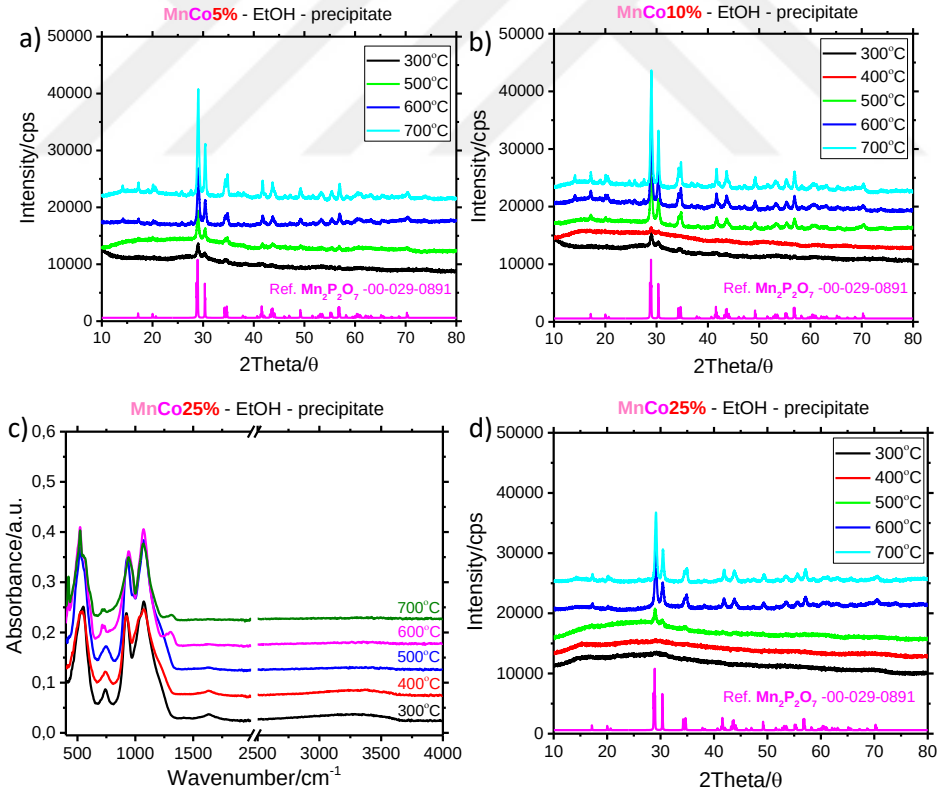


Figure 3.120: a), b), and d) high-angle XRD patterns of the MnCo5%, MnCo10%, and MnCo25% samples and c) ATR-FTIR spectra of the MnCo25% samples, obtained from ethanol solution and calcined at various temperatures.

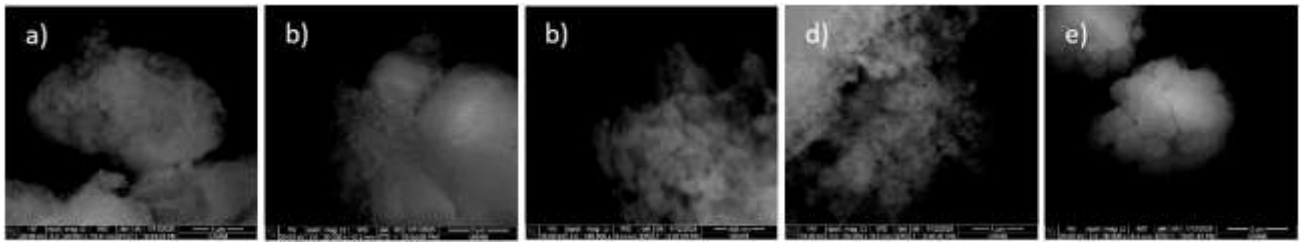


Figure 3.121: SEM images of the calcined MnCo25% precipitate (from ethanol solvent) after calcination at a) 300, b) 400, c) 500, d) 600, and e) 700ºC.

3.2.2. Butanol Systems

3.2.2.1. Mesophases of the MnNi5-10-25% from Butanol Systems

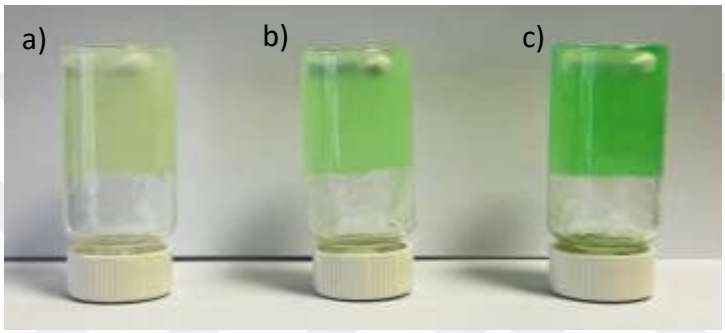


Figure 3.122: Photographs of the a) MnNi5%, b) MnNi10%, and c) MnNi25% butanol mixtures.

The MnNi5%, MnNi10%, and MnNi25% butanol solutions undergo a sol-gel process, see Figure 3.122. The clear solution immediately turns into a gel. Change in the colors of these solutions are due to the amount of Ni(II) in these solutions; as the amount of Ni(II) increases, the solution becomes darker green. To check the stability and order in the mesophases, small-angle XRD measurements are also conducted. These measurements prove that there is an ordered mesophase/mesostructure in the MnNi5% supernatant part. Two diffraction lines are observed at 2.30 and 2.97º, 2θ, which shifts to 1.78 and 2.6º, 2θ, after 5 hours aging. There is also a very broad diffraction line in the MnNi25% supernatant part at 1.67º, 2θ. However, in the other samples (solution and precipitate) there are no diffraction lines, observed in small-angle XRD patterns, see Figure 3.123, Figure 3.124, and Figure 3.125.

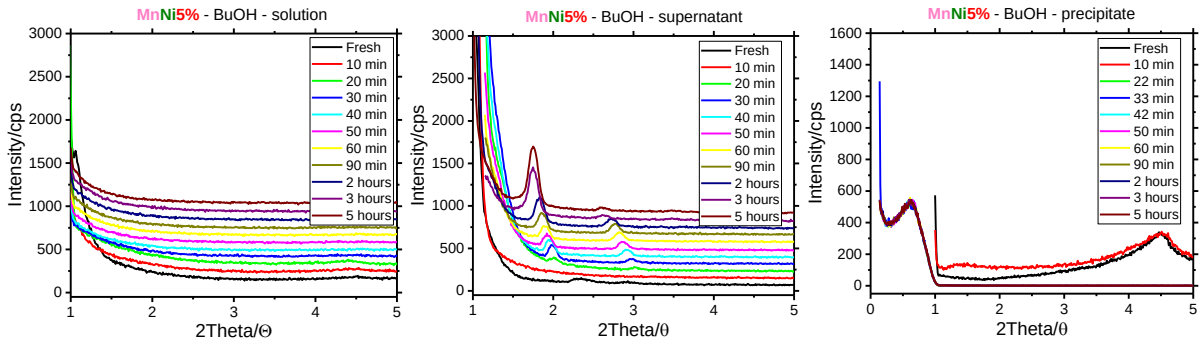


Figure 3.123: Small-angle XRD patterns of the (from left to right) MnNi5% butanol solution, supernatant and precipitate parts.

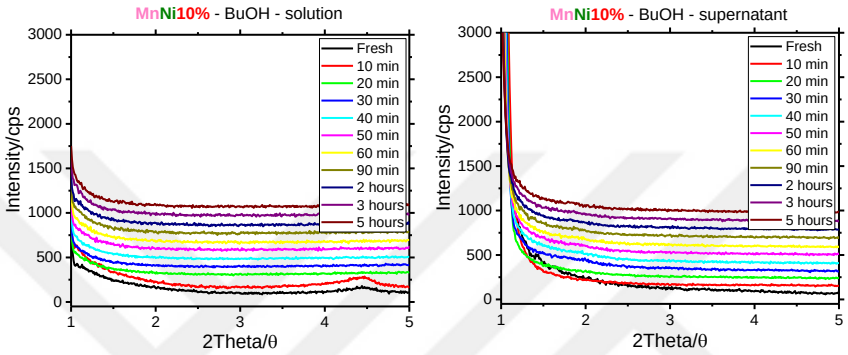


Figure 3.124: Small-angle XRD patterns of the MnNi10% butanol solution and supernatant parts.

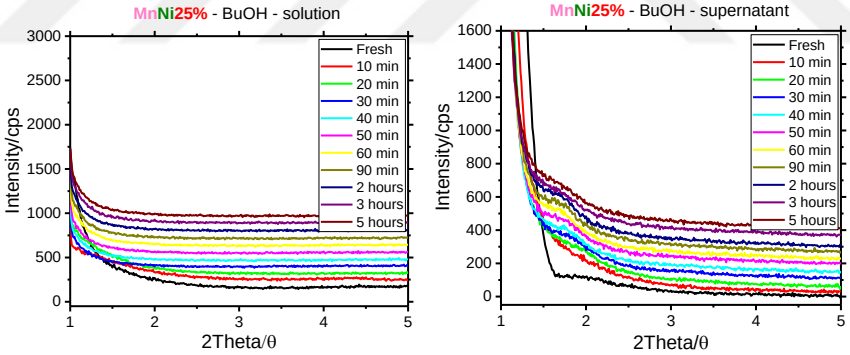


Figure 3.125: Small-angle XRD patterns of the MnNi25% butanol solution and supernatant parts.

3.2.2.2. Mesoporous $Mn_{2-x}Ni_xP_2O_7$ from Butanol MnNi5-10-25% Mixtures

The gel-phase is dried at 100ºC and calcined at different temperatures and the ATR-FTIR spectra and high-angle XRD patterns are collected, see Figure 3.126(b)-(d)-(f). The spectra and patterns collectively show the formation of $Mn_2P_2O_7$ crystals at 600ºC in these samples.

The calcined precipitate yields $Mn_2P_2O_7$ crystals even at 300ºC. However, there is at least one more unknown crystal phase at higher calcination temperatures, see Figure 3.127. This

phase is more visible in the high-angle XRD patterns of the calcined MnNi10% precipitate, see Figure 3.127(d).

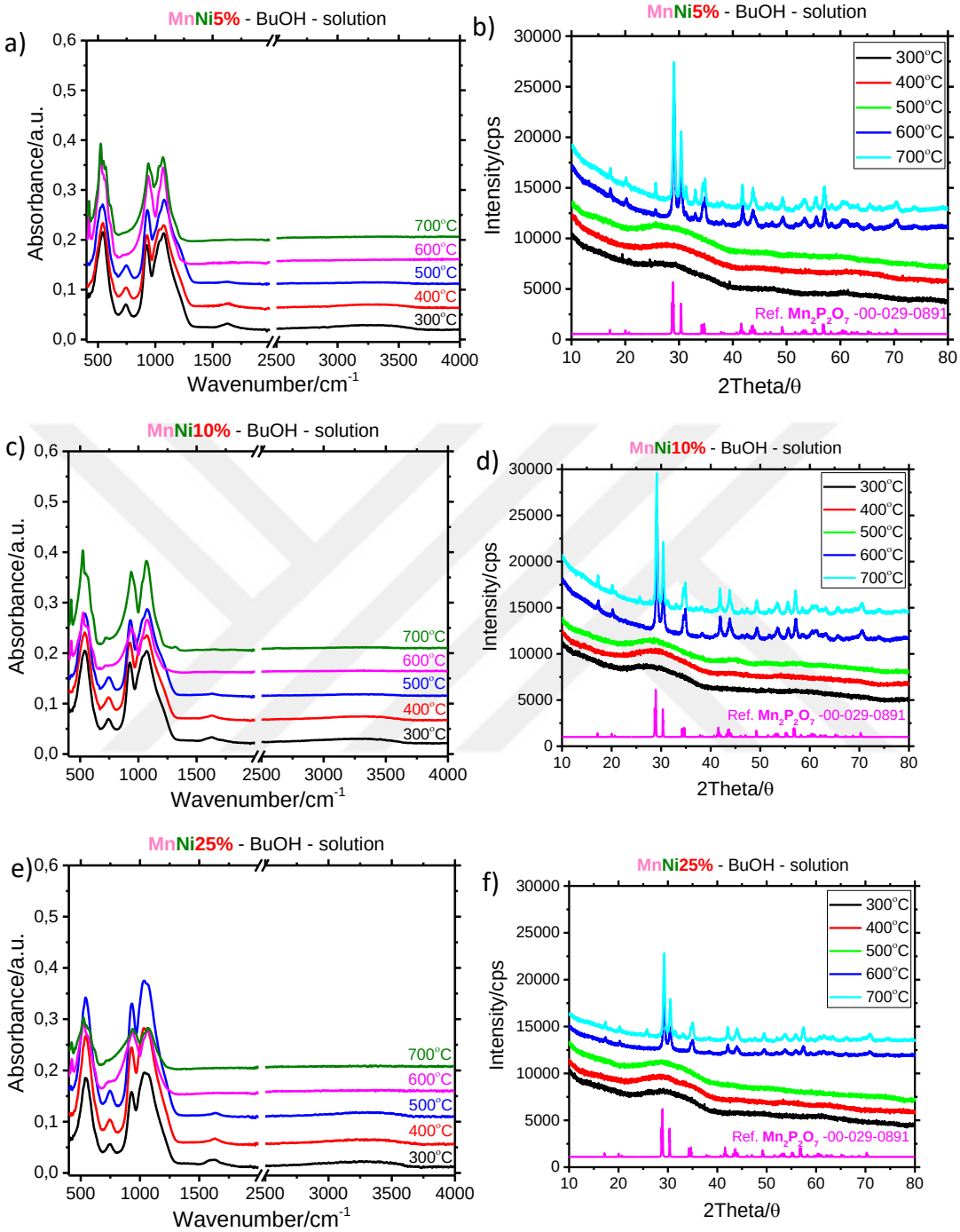


Figure 3.126: a), c), and d) ATR-FTIR spectra and b), d), and f) high-angle XRD patterns of the calcined MnNi5%, MnNi10%, and MnNi25% butanol solutions.

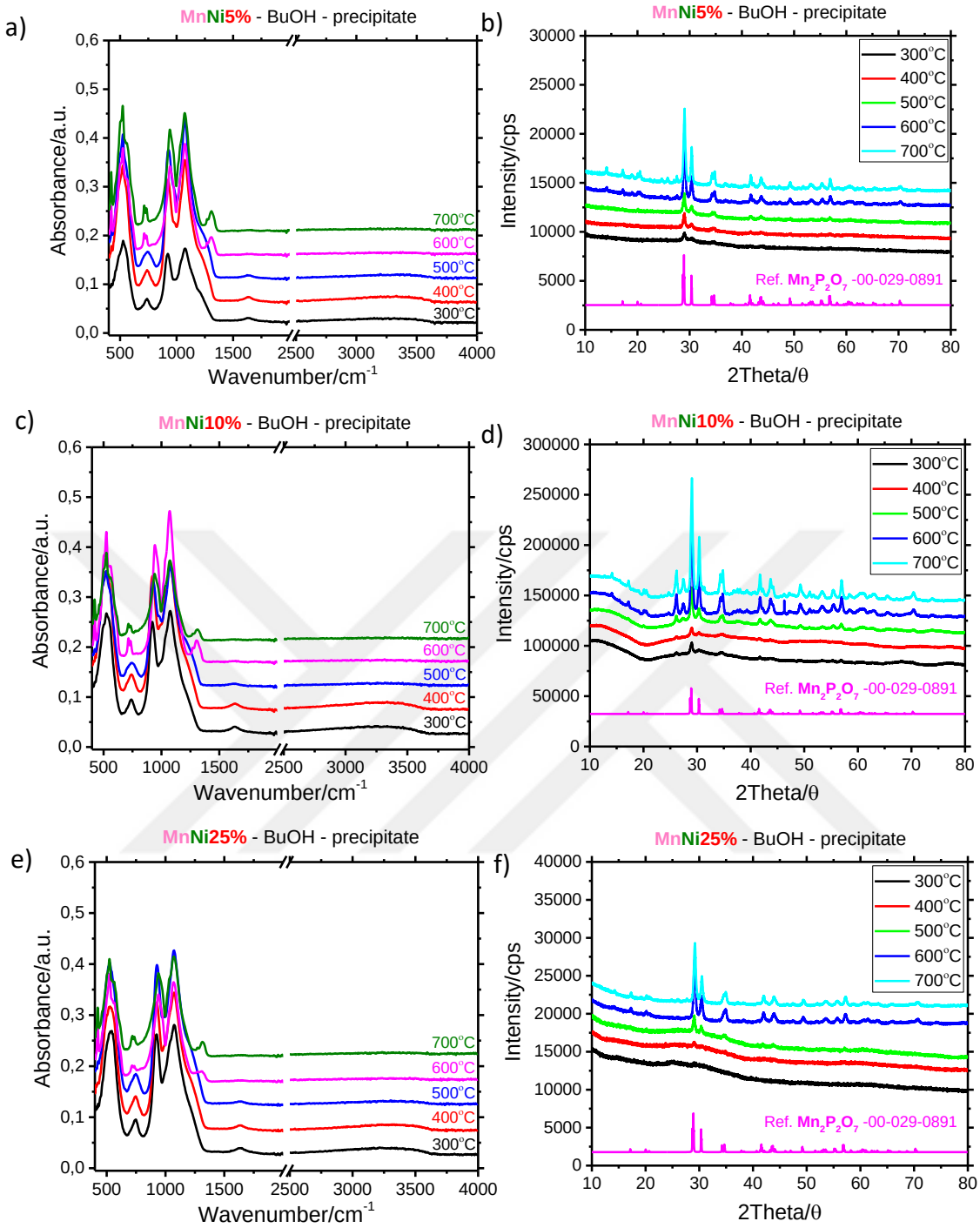


Figure 3.127: a), c), and d) ATR-FTIR spectra and b),d, and f) high-angle XRD patterns of the calcined MnNi5%, MnNi10%, and MnNi25% butanol precipitate.

The SEM images of the samples of calcined MnNi5% and MnNi10% ethanol precipitate are given in Figures 3.128 and 3.129. The images presents that the morphology of the samples, calcined up to 500ºC, is also flake-like, indicating a posibility for film formation in this system.

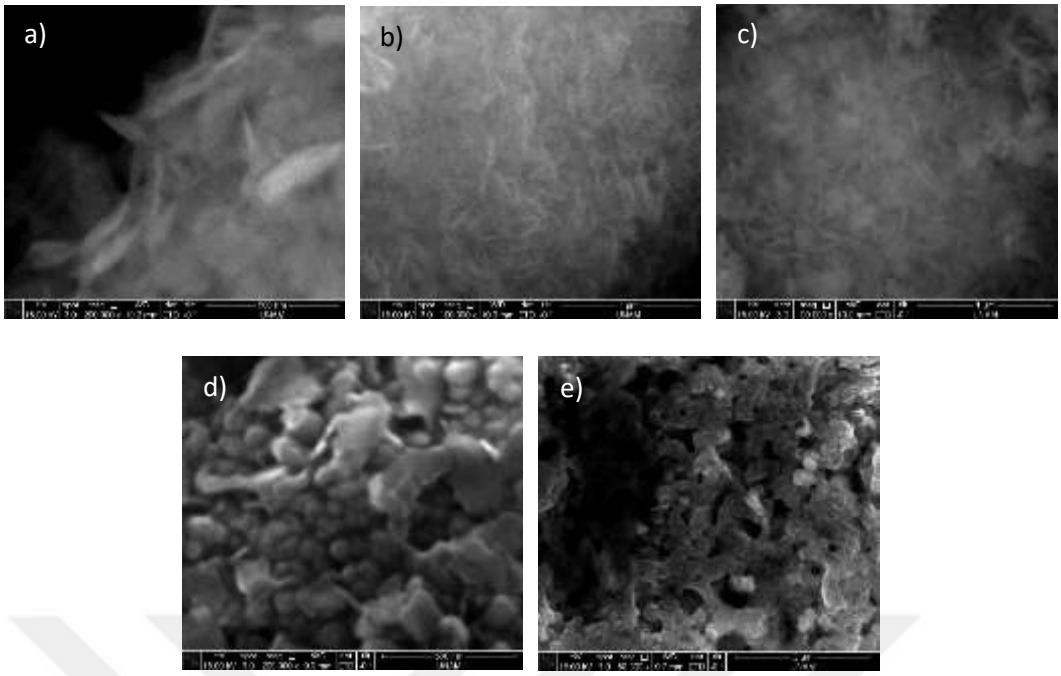


Figure 3.128: SEM images of the MnNi5% precipitate (from butanol) after calcination at a) 300, b) 400, c) 500, d) 600, and e) 700ºC.

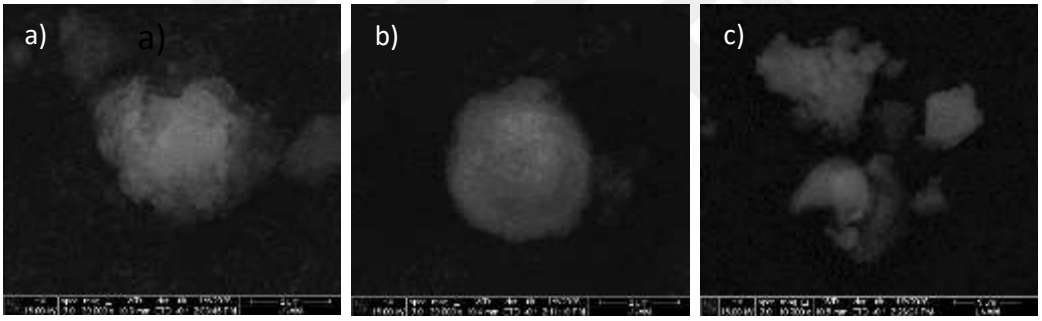


Figure 3.129: SEM images of the MnNi10% precipitate (from butanol) after calcination at a) 300, b) 400, c) 500ºC.

3.2.2.3. Mesophases of the MnCo5-10-25% Mixtures

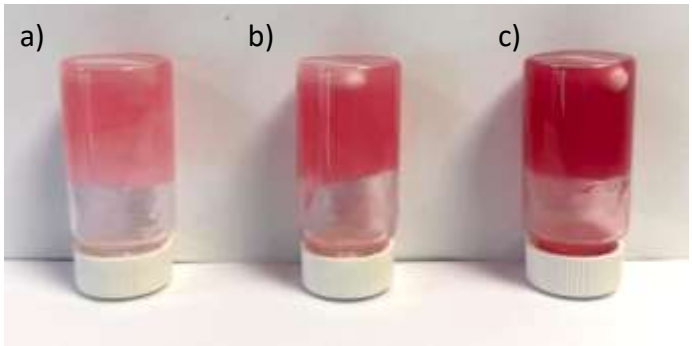


Figure 3.130: Photographs of the a) MnCo5%, b) MnCo10%, and c) MnCo25% butanol mixtures.

As shown in Figure 3.130, the MnCo5%-10%-25% mixtures also undergo a sol-gel process in butanol. The gel-phase is very rigid and forms very fast upon mixing acid solution with the binary metal salt solution. The colors of the solutions are pale pink to dark pink, corresponding to 5%, 10%, and 25% of Co(II) in the mixture solutions. The small-angle XRD patterns of the solution, supernatant, and precipitate of these binary metal mixtures from butanol system prove that there is no ordered mesophase formation in these samples during 5 hours of aging at RT.

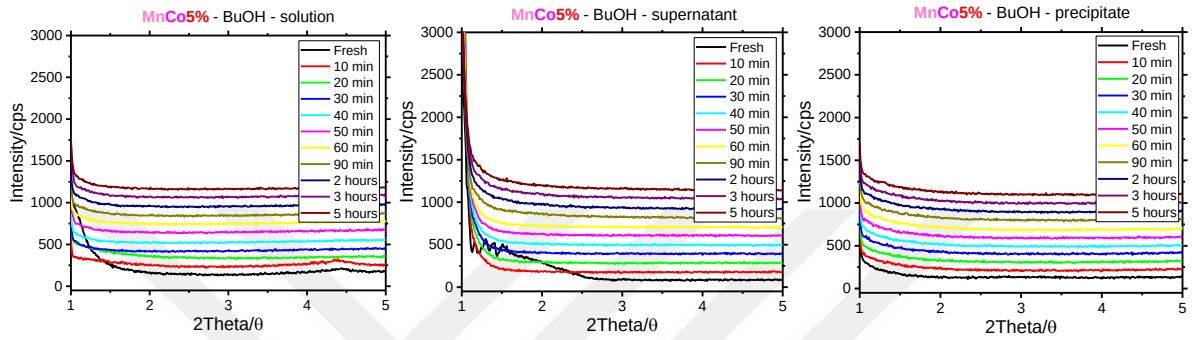


Figure 3.131: Small-angle XRD patterns of the (from left to right) MnCo5% butanol solution, supernatant and precipitate.

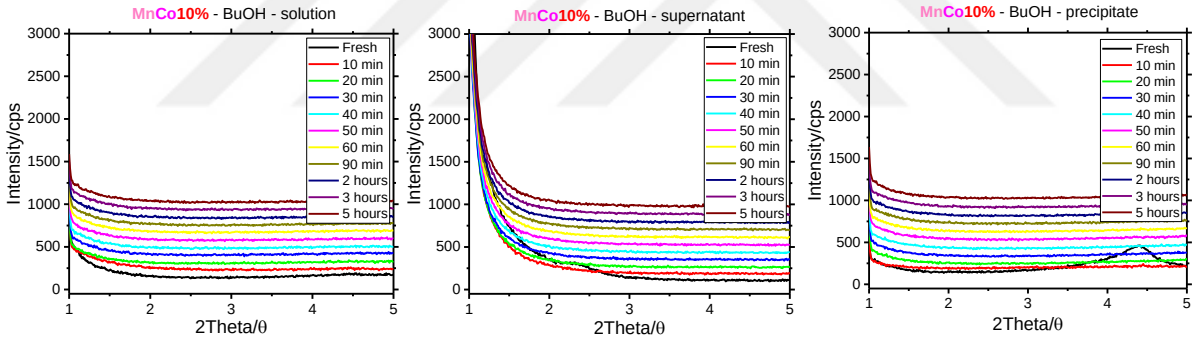


Figure 3.132: Small-angle XRD patterns of the (from left to right) MnCo10% butanol solution, supernatant and precipitate.

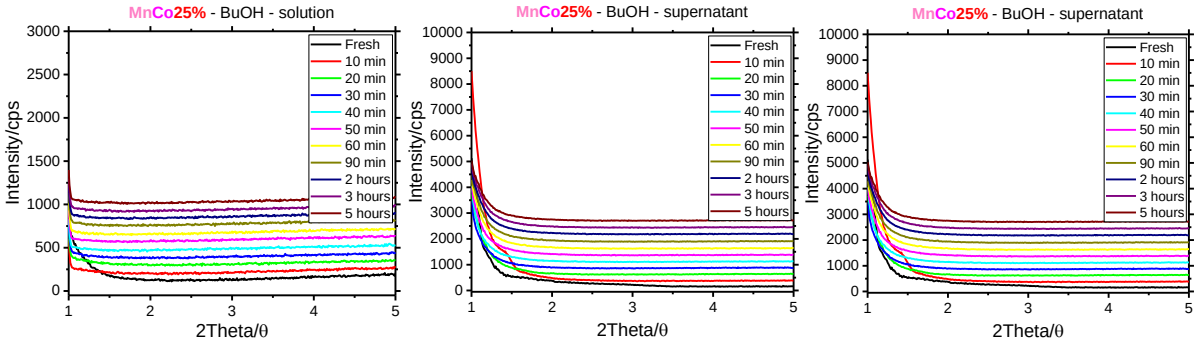


Figure 3.133: Small-angle XRD patterns of the (from left to right) MnCo25% butanol solution, supernatant and precipitate during aging.

3.2.2.4. Mesoporous $Mn_{2-x}Co_xP_2O_7$ from Butanol MnCo5-10-25% Mixtures

Unlike the calcined samples from single metal solution, the binary metal solutions do not yield $Mn_2P_2O_7$ crystals at high calcination temperatures. ATR-FTIR spectra display phosphate related peaks in the calcined samples, see Figure 3.13,(a)-(c)-(e). The spectra also display water peaks. It means these samples are holding water species at low calcination temperatures and indicatinh porosity and high surface area.

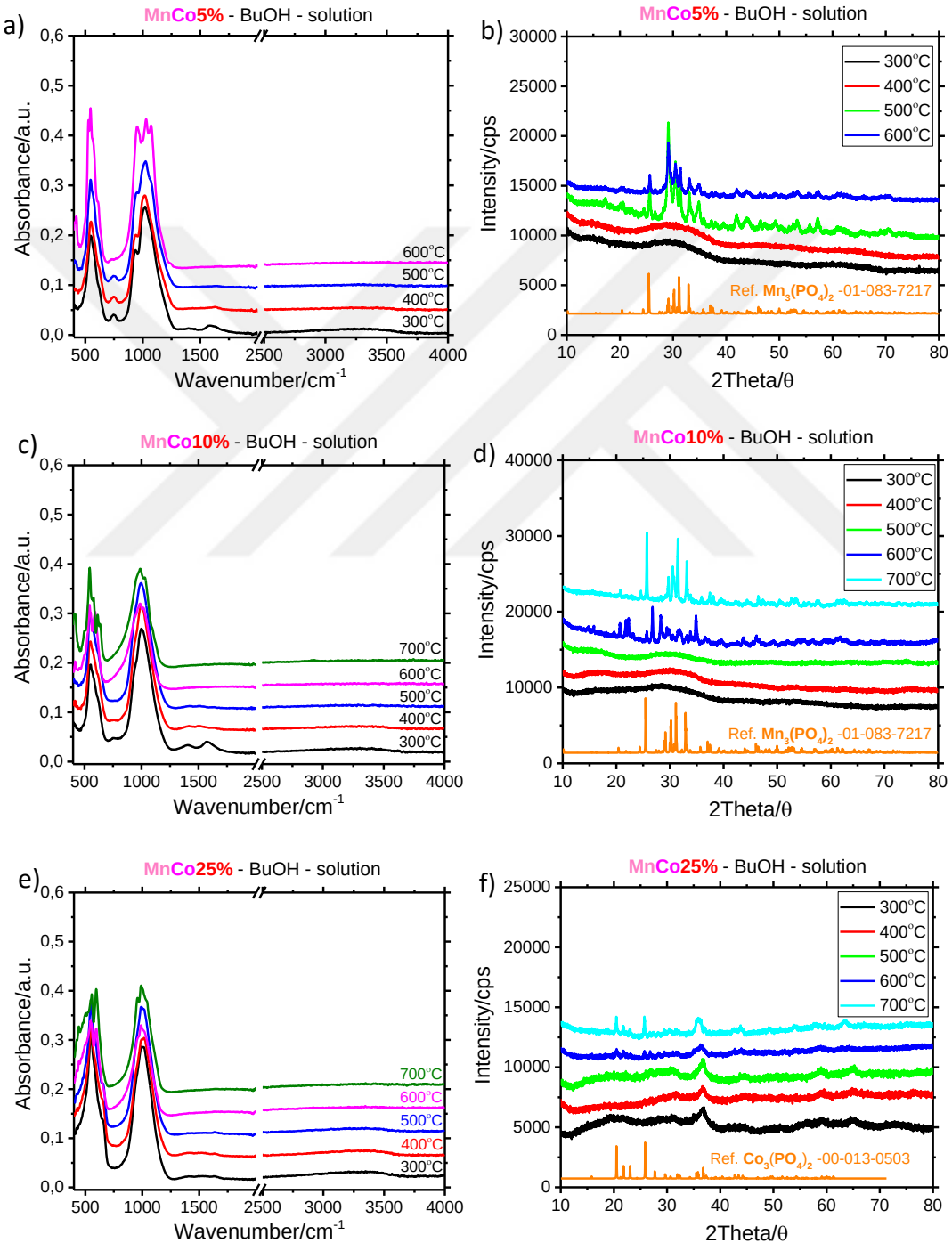


Figure 3.134: a), c), and d) ATR-FTIR spectra and b), d), and f) high-angle XRD patterns of the calcined MnCo5%, MnCo10%, and MnCo25% samples from butanol solutions.

High-angle XRD patterns of the calcined MnCo5% solution, samples are given in Figure 3.134(b). The sample crytallize at around 500ºC. The pattern can be indexed to $Mn_3(PO_4)_2$ phase. The calcined MnCo10%, solution crystallizes at around 600ºC but, the crystal phase is unknown. At 700ºC, these crystals transform to $Mn_3(PO_4)_2$ phase. However, the calcined MnCo25%, solution has a crystal phase at 300ºC but, at 600ºC it converts to $Co_3(PO_4)_2$ phase. Interestingly, thermal behaviours are highly dependent on the solution composition event in such as small cobalt concentration range and needs to be explored further.

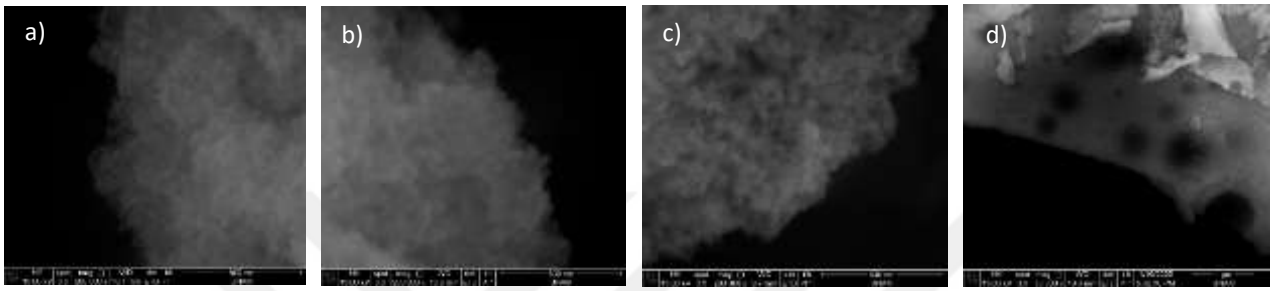


Figure 3.135: SEM images of the MnCo5% from butanol solution, calcined at a) 300, b) 400, c) 600, and d) 700ºC.

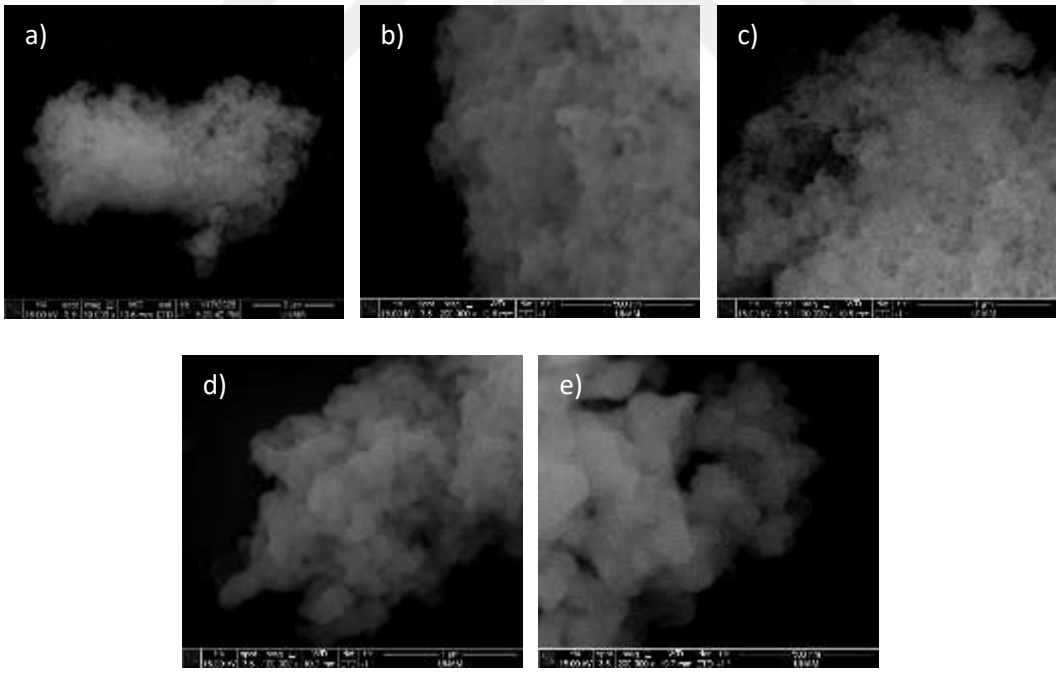


Figure 3.136: SEM images of the MnCo25% from butanol solution, calcined at a) 300, b) 400, c) 500, d) 600 and e) 700ºC.

The SEM images of the MnCo5% mixture (in butanol solvent) are shown in Figure 3.135. The images display particle like and film like morphologies. Intense water peaks in the ATR-FTIR spectra are indication of porosity. However, at 700ºC, the pores become larger, the sample crystallizes and the mesopores collapse. This results in a significant decrease in the

surface area. The particles from solution of MnCo25% mixture are also spherical, see Figure 3.136. At 300ºC, the flake-like and spherical particles are observed in the SEM images. At 400 and 500ºC, these spherical particles anneal to each other to form bigger spherical particles. At 600 and 700ºC, the sample crystallizes and pores collapse.

Unlike the solution part, the calcined precipitate samples of the mixtures, MnCo5% and MnCo10%, crystallize at 300ºC and yield $Mn_2P_2O_7$ crystals. However, the MnCo25% samples are amorphous up to 600ºC but, yield crystalline $Co_3(PO_4)_2$ phase at 600ºC.

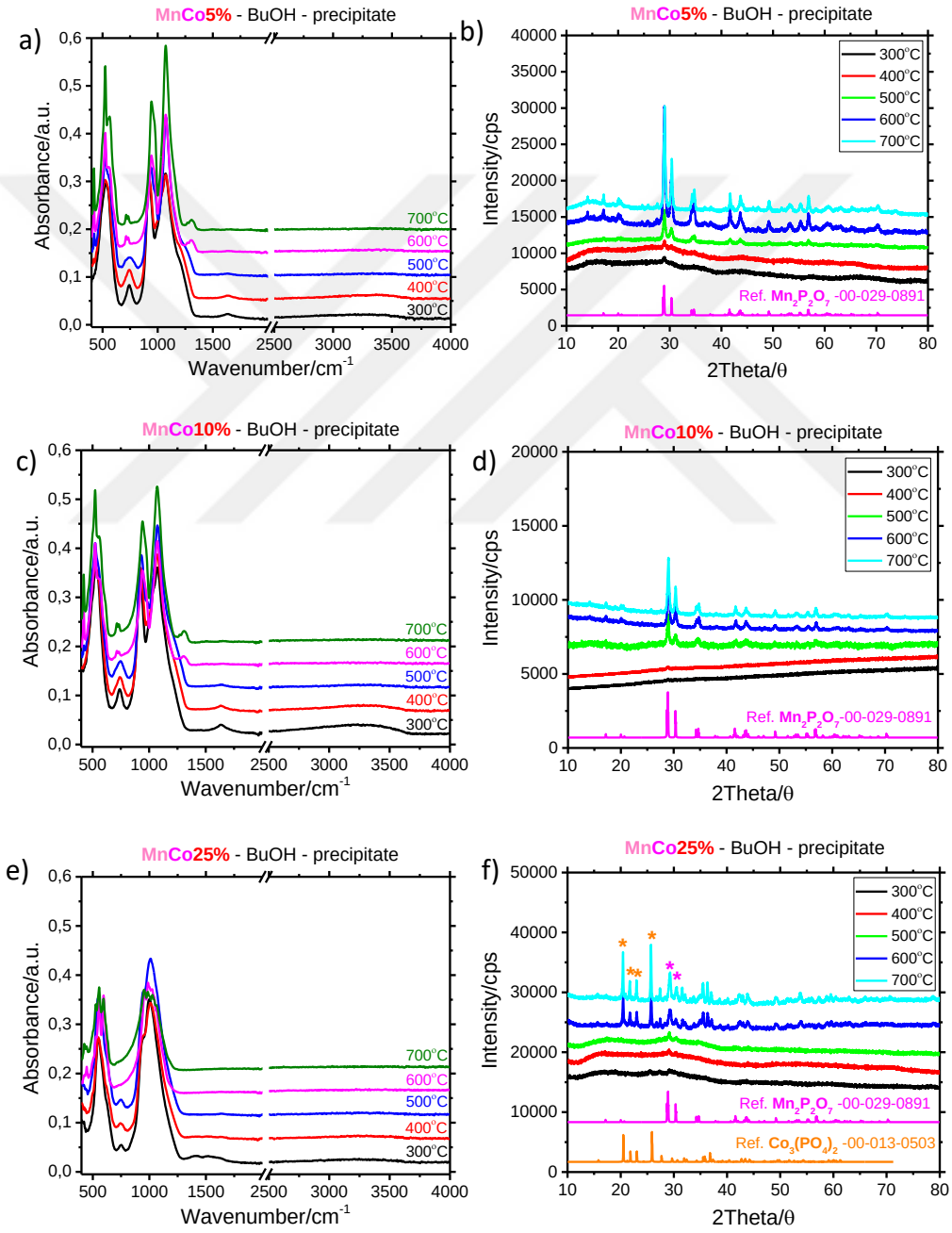


Figure 3.137: a), c), and d) ATR-FTIR spectra and b),d, and f) high-angle XRD patterns of the calcined MnCo5%, MnCo10%, and MnCo25% samples, from butanol precipitate.

N_2 adsorption-desorption isotherms of the MnCo5%, MnCo10%, MnCo25% samples (butanol precipitate part 300ºC calcined samples) are also type-IV, see Figure 3.138. Comparing these samples with pure $Mn_2P_2O_7$ butanol precipitate, the surface area is increased significantly and the pore size distributions become sharper and shifted to lower size, see Table 3.11.

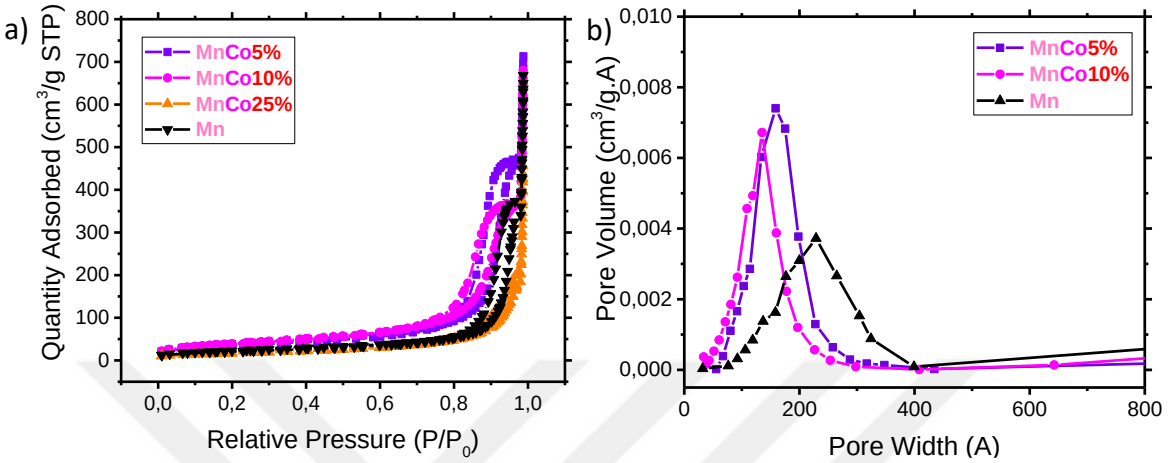


Figure 3.138: a) N_2 (77 K) adsorption-desorption isotherms, and b) BJH pore size distribution plot of MnCo5%, MnCo10%, and pure $Mn_2P_2O_7$ butanol precipitate, calcined at 300ºC.

Table 3.11: The BET surface area, BJH pore width and pore volume values of MnCo5%, MnCo10%, and pure $Mn_2P_2O_7$ butanol precipitates, calcined at 300ºC.

Samples	BET Surface Area (m^2/g)	Pore Width (Å)	Pore Volume (cm^3/g)
MnCo5%	140	160	1.10
MnCo10%	144	136	1.05
Mn	46	~300	0.64

In Figure 3.139, SEM images of the MnCo10% mixture precipitate part, calcined samples, are given. The morphology of these samples are consisting of both flake-like and spherical particles. The flake-like formations can result in an increase in the surface area of these samples. In higher calcination temperatures, the number of the spherical particles increases.

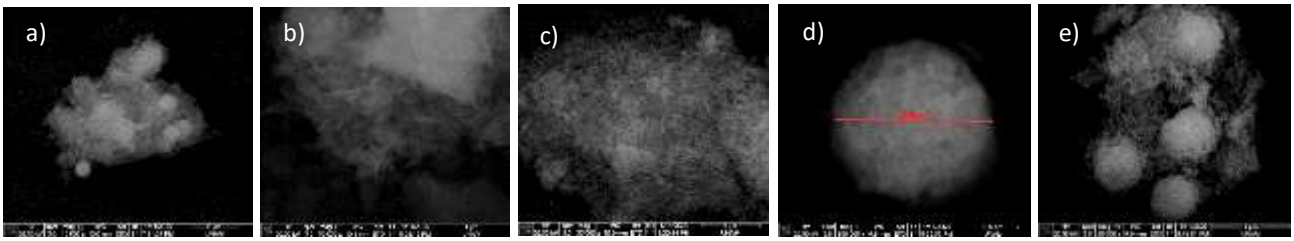


Figure 3.139: SEM images of the MnCo10% butanol precipitate, calcined at a) 300, b) 400, c) 500, d) 600, and e) 700ºC.

3.2.3. Methanol Systems

3.2.3.1. Mesophases of the Methanol MnNi5-10-25% from Methanol Systems

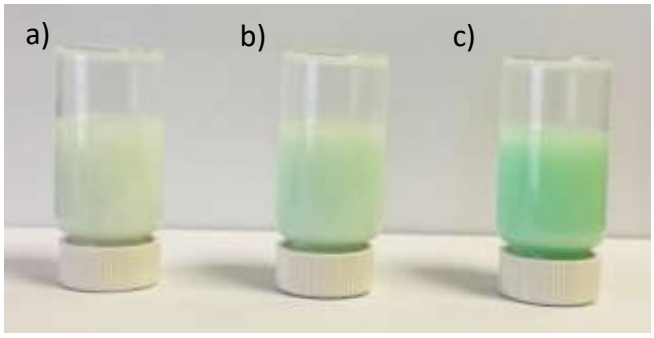


Figure 3.140: Photographs of the a) MnNi5%, b) MnNi10%, and c) MnNi25% mixtures in methanol.

Figure 3.140 shows the photographs of the methanol solutions. There is no sol-gel formation in Mn(II)/Ni(II) binary metal mixtures in methanol. The colors of these solutions are reflecting the amount of Ni(II) in these systems as in the other binary metal systems. Again, to check the stability and order in the mesophases, small-angle XRD measurements are conducted. However, there are diffraction lines only in the MnNi10% and MnNi25% supernatants, indicating an order mesostructure. The diffraction line in the MnNi10% is at 1.80º, 2θ, and in MnNi25% it is at 1.65º, 2θ, indicating that the particle size is larger in the MnNi25% supernatant.

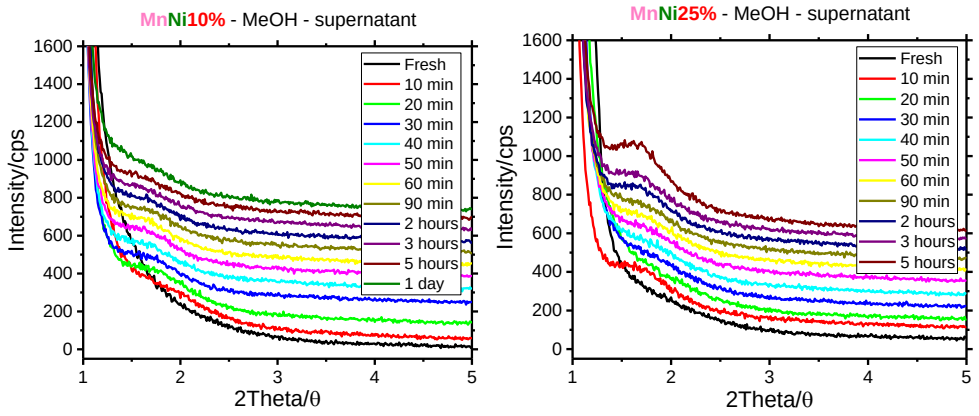


Figure 3.141: Small-angle XRD patterns of the a) MnNi10% and b) MnNi25% butanol supernatants.

3.2.3.2. Mesoporous $Mn_{2-x}Ni_xP_2O_7$ from Methanol MnNi5-10-25% Mixtures

Even tough there is no sol-gel formation, the same procedure for the calcination of the solution parts is followed in these solutions as well. ATR-FTIR spectra and high-angle XRD patterns are shown in Figure 3.142. Both techniques show the formation of the $Mn_2P_2O_7$ crystals at high calcination temperatures.

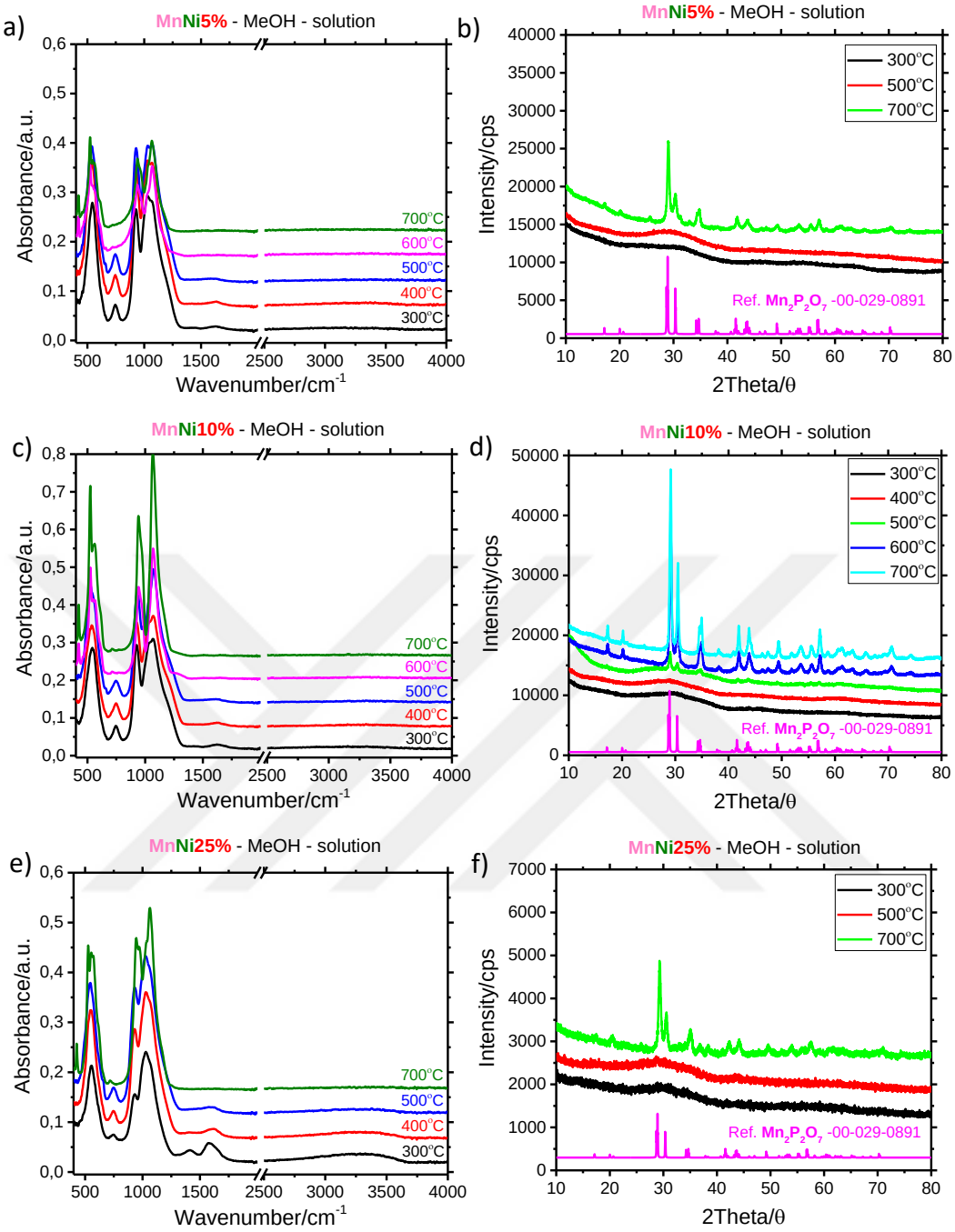


Figure 3.142: a), c), and d) ATR-FTIR spectra and b),d, and f) high-angle XRD patterns of the MnNi5%, MnNi10%, and MnNi25% methanol solution calcined samples.

N_2 adsorption-desorption isotherms and pore size distribution plots are given in Figure 3.143. The calcined MnNi10% and MnNi25% solution samples, are mesoporous. Table 3.12 tabulates the BET surface area and BJH pore size, and pore volume values of these samples, together with the pure $Mn_2P_2O_7$. Compared to pure $Mn_2P_2O_7$, the surface area increases with the addition of Ni(II) and pore width becomes smaller and uniform.

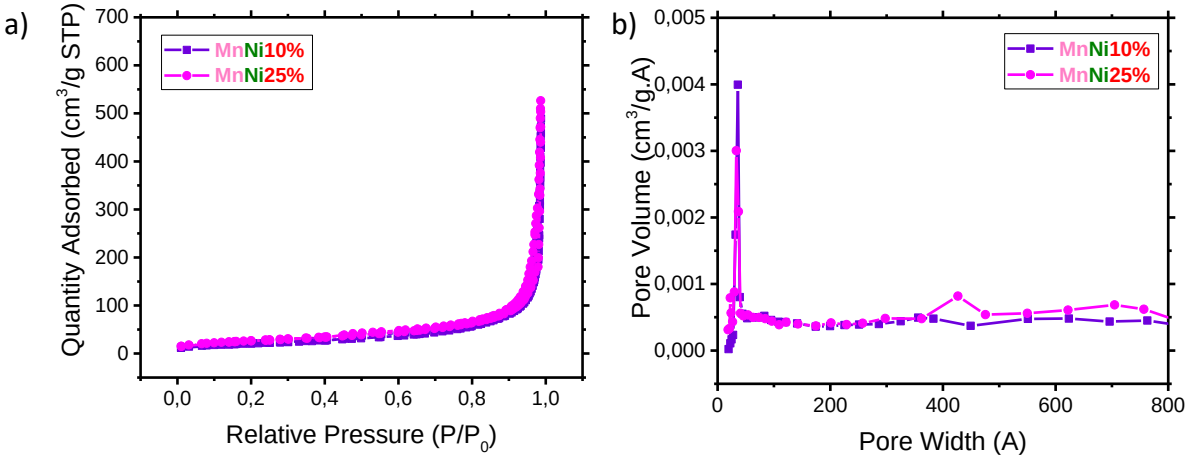


Figure 3.143: a) N_2 (77 K) adsorption-desorption isotherms, and b) BJH pore size distribution plots of the MnNi10%, MnNi25% methanol solution, calcined at 300ºC.

Table 3.12: The BET surface area, BJH pore width and pore volume values of the MnCo5%, MnCo10%, and pure $Mn_2P_2O_7$ butanol precipitates, calcined at 300ºC.

Samples	BET Surface Area (m^2/g)	Pore Width (Å)	Pore Volume (cm^3/g)
MnNi10%	77	32	0.76
MnNi25%	97	33	0.82
Mn	55	277	0.96

SEM images (Figure 3.144) display both flake-like and spherical particle morphology at 300, 400 and 500ºC, and indication of thin-film formation. At higher calcination temperatures, the surface area drops and pores expand, and at 600ºC, the sample becomes crystalline.

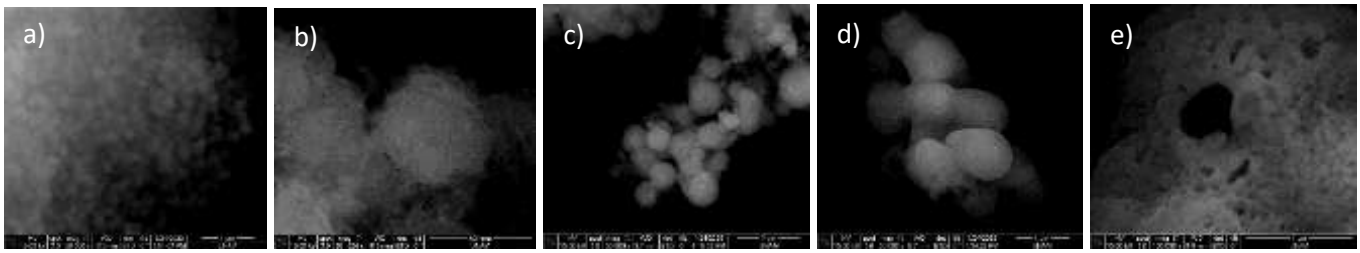


Figure 3.144: SEM images of the MnNi5% methanol solution, calcined at a) 300, b) 400, c) 500, d) 600, and e) 700ºC.

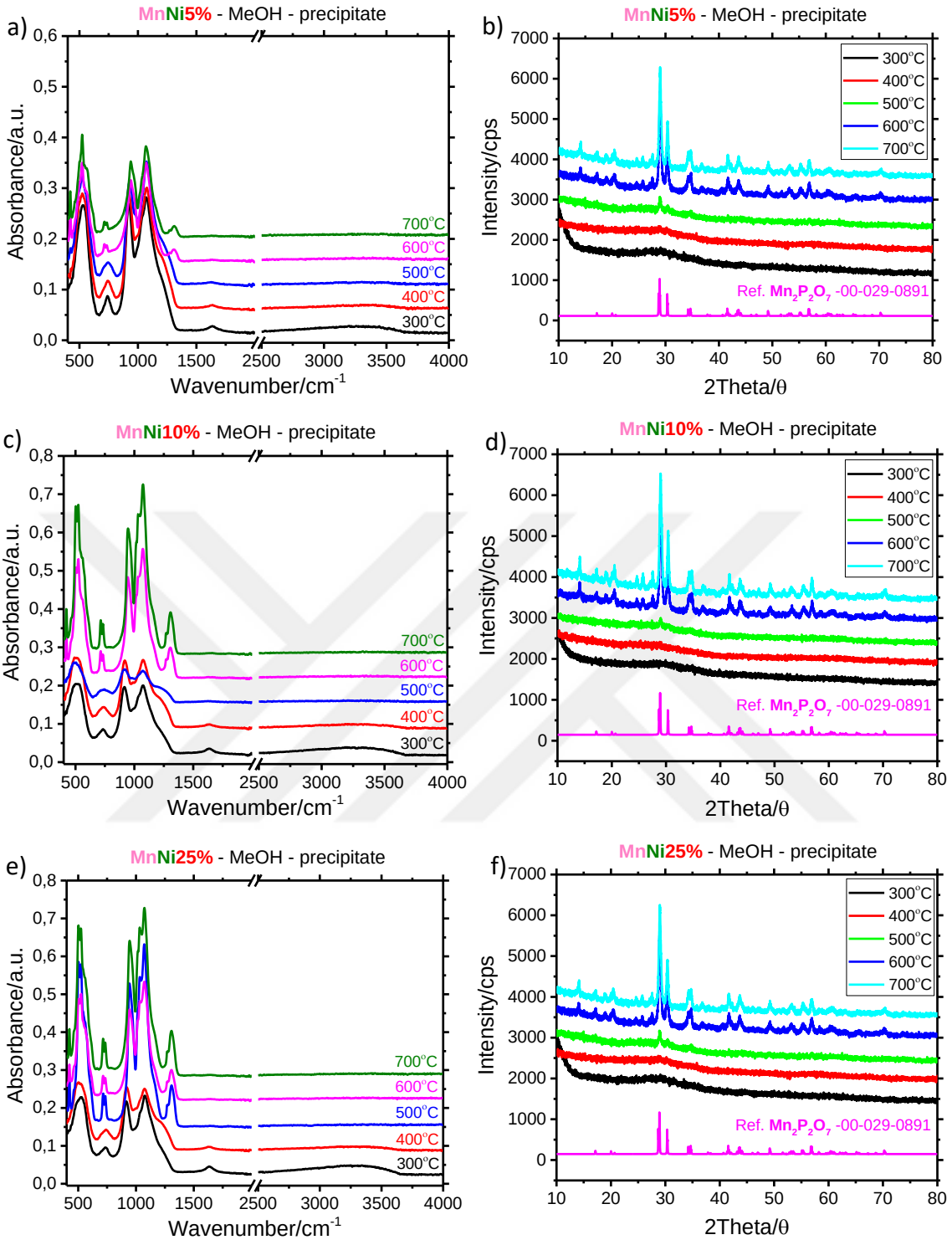


Figure 3.145: a), c), and d) ATR-FTIR spectra and b),d, and f) high-angle XRD patterns of the MnNi5%, MnNi10%, and MnNi25% methanol precipitate, calcined samples.

Figure 3.145 displays the ATR-FTIR spectra and high-angle XRD patterns of the methanol-precipitate-derived MnNiX% samples. Even though, the ATR-FTIR spectra display metal pyrophosphate related peaks, XRD patterns show that the $Mn_2P_2O_7$ phase forms with at least another undefined crystalline phase.

Figures 3.146, 3.147, and 3.148 present the SEM images of the MnNi5%, MnNi10%, and MnNi25% methanol precipitate parts, respectively. The morphology of these samples consists of spherical particles at low calcination temperatues but, as calcination temperature increases, the particles annealed to each other and pores expand resulting in decrease in the surface area.

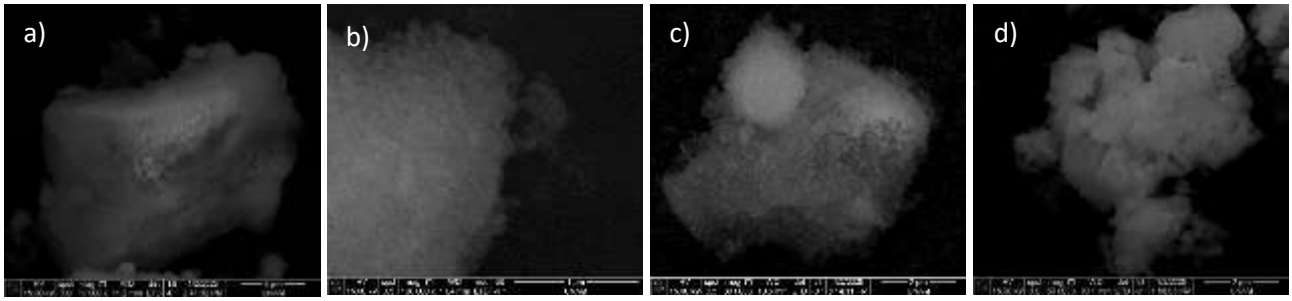


Figure 3.146: SEM images of the MnNi5% precipitate (from methanol solvent), calcined at a) 400, b) 500, c) 600, and d) 700ºC.

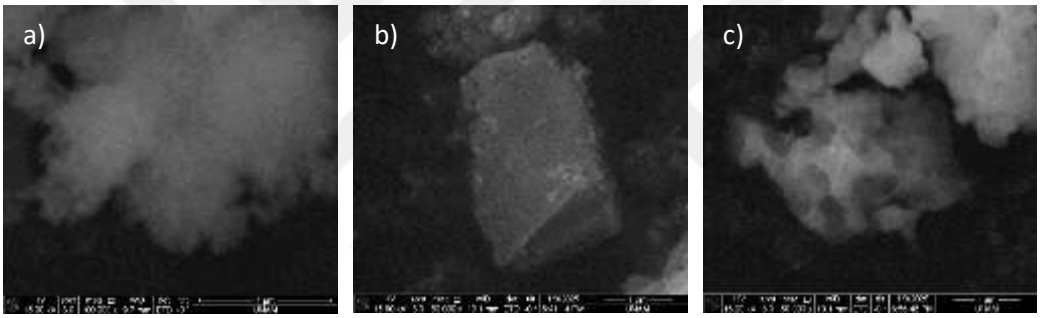


Figure 3.147: SEM images of the MnNi10% % precipitate (from methanol solvent), calcined at a) 300, b) 500, and c) 700ºC.

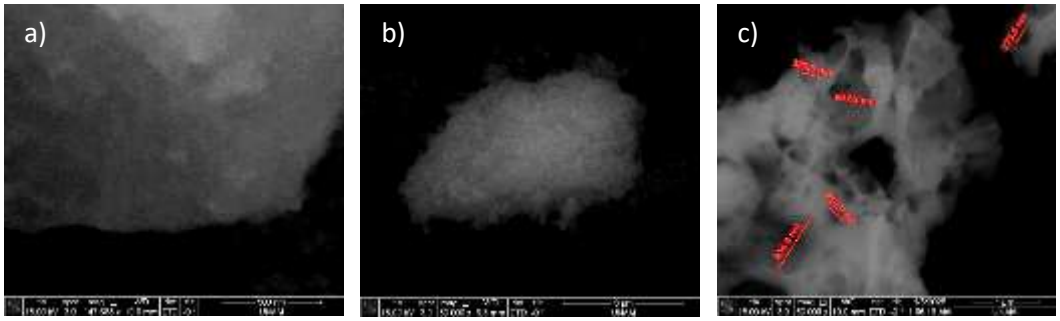


Figure 3.148: SEM images of the MnNi25% % precipitate (from methanol solvent), calcined at a) 300, b) 500, and c) 700ºC.

3.2.3.3. Mesophases of the MnCo5-10-25% from Methanol Systems

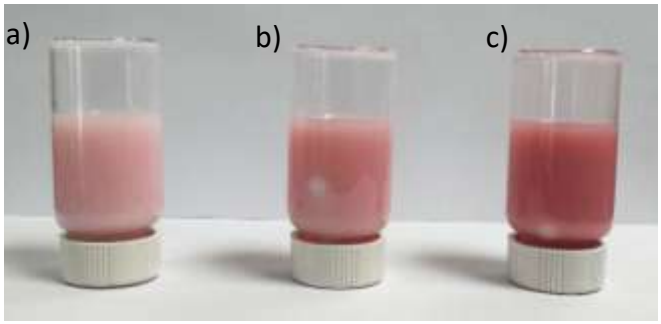


Figure 3.149: Photographs of the a) MnCo5%, b) MnCo10%, and c) MnCo25% mixtures in methanol.

Figure 3.149 shows photographs of the methanol solutions. No sol-gel formation is observed in the Mn(II)/Co(II) binary metal mixtures in methanol. The colors of these solutions are reflecting the amount of Co(II) in these solutions. Again, to check the stability and order in the mesophases, small-angle XRD measurements have been conducted. However, there is a diffraction line only in the MnNi10% and MnNi25% supernatant parts indicating order in the mesostructure. A diffraction line is observed at 1.80º, 2θ, in the pattern of MnNi10% and at 1.65º, 2θ, in the MnNi25%, indicating that the particle size is larger in the MnNi25%.

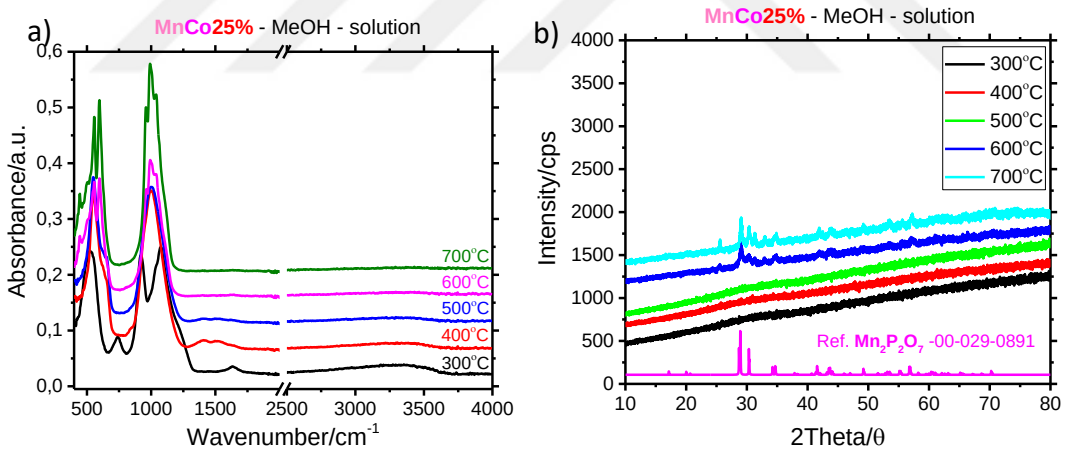


Figure 3.150: a) ATR-FTIR spectra and b) high-angle XRD patterns of the MnCo25% from methanol solution, calcined samples.

3.2.3.4. Mesoporous $Mn_{2-x}Co_xP_2O_7$ from Methanol MnCo5-10-25% Mixtures

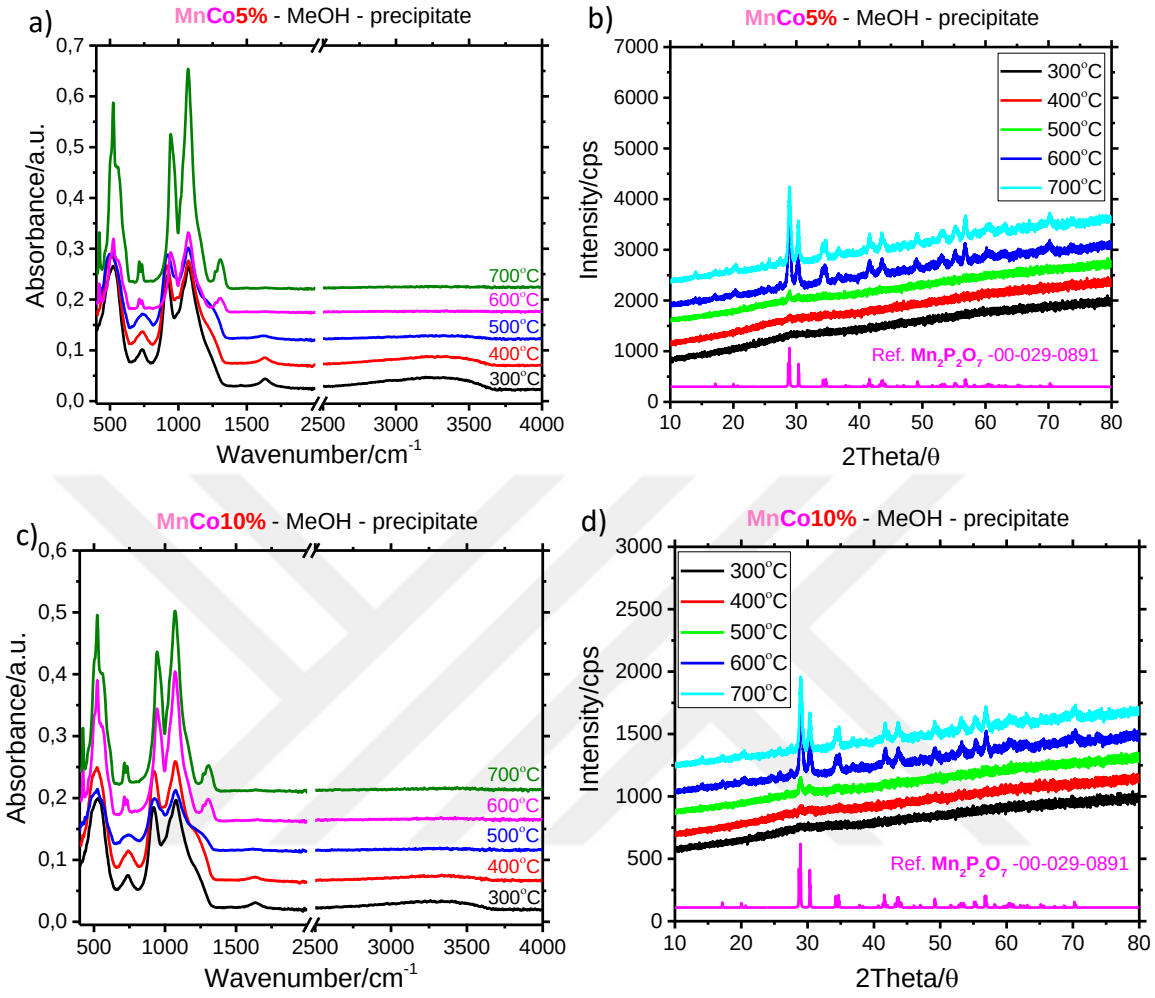


Figure 3.151: a) and c) ATR-FTIR spectra, and b) and d) high-angle XRD patterns of MnCo5% and MnCo10% methanol precipitate, calcined samples.

The ATR-FTIR spectra and high-angle XRD patterns of the calcined samples (from methanol precipitate) are shown in Figure 3.151. Both data prove that $Mn_2P_2O_7$ crystals form at 400ºC. However, again, there is at least one more unkown phase in these samples.

The SEM images of the MnNi10% (Figure 3.152) and MnNi25% (Figure 3.153) from precipitate part (calcined samples) display the morphologies in these samples. Particles are, again, flake-like and spherical particles at low calcination temperatures and become macroporous spherical at high calcination temperatures.

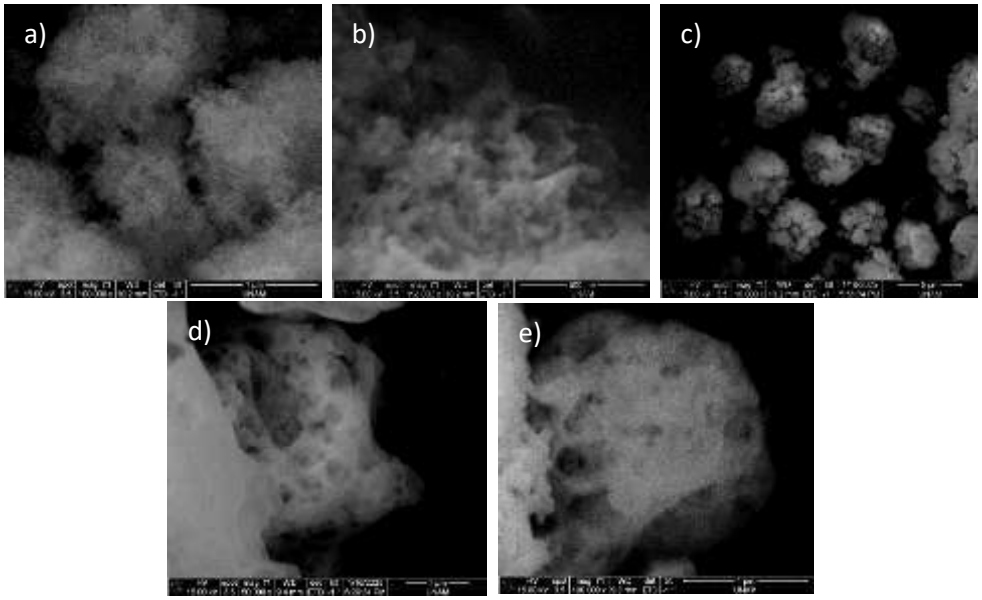


Figure 3.152: SEM images of the MnCo10% precipitate (from methanol solvent), calcined at a) 300, b) 400, c) 500, d) 600, and e) 700ºC.

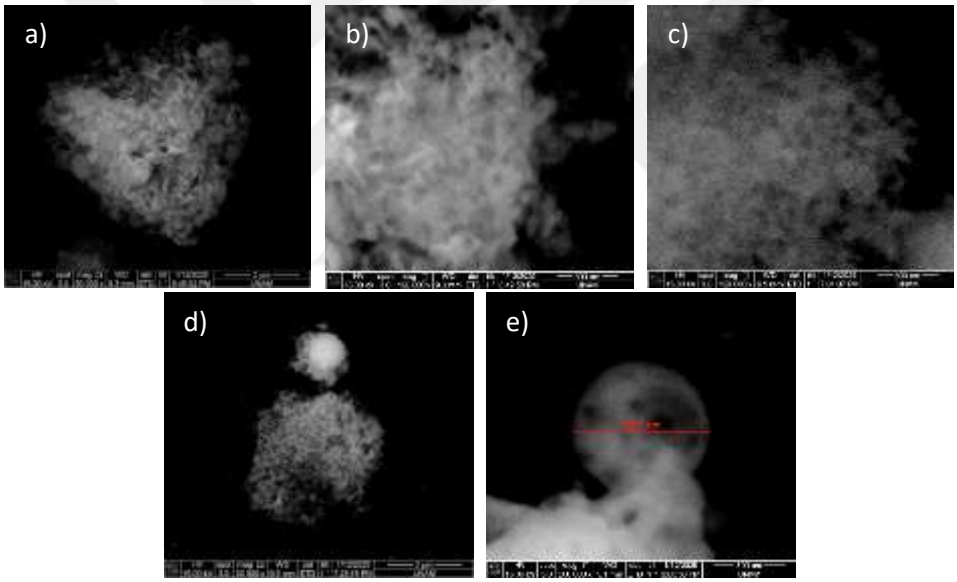


Figure 3.153: SEM images of the MnCo10% methanol precipitate, calcined at a) 300, b) 400, c) 500, d) 600, and e) 700ºC.

3.3. Electrochemical Characterization of Mesoporous Binary Metal Pyrophosphates

3.3.1. Ethanol System

The gels, obtained in binary metal pyrophosphate solutions, are dispersed and diluted 5 times in ethanol and dip-coated over GR electrodes, followed by calcination at various temperatures, 300 to 600ºC to obtain the electrodes of MnMX%-YºC (M = Ni and Co, X = 5,10, and 25, and Y = 300 - 600ºC). The electrochemical measurements are performed in the same three electrode system and in 1 M KOH electrolyte solution as in the single metal pyrophosphate system otherwise mentioned in the text. The multi-step chronoamperometry

analysis is performed to determine the electrodes' Tafel slopes. The measurement is carried within 0.5-0.8 V potential window, for 300 seconds at each step. Multi-step chronopotentiometry experiments are also performed to evaluate the overpotentials, at current densities of 1, 10, 20, 30, 40, 50, 60, 70, 80, 90, and 100 mA/cm^2 for 1 hour at each step.

Figure 3.154 shows both cyclic voltammograms and multi-step chronoamperometry plots with Tafel slopes. Comparing the CVs, the current density close to 1.5 V is higher in the MnNi25% coated electrode but, its stability is worse than the other compositions. Tafel slopes of the MnNi5%-300ºC and MnNi25%-300ºC electrodes are closer to each other but that of the MnNi10% is lower, which indicates the overpotential required is less with this electrode.

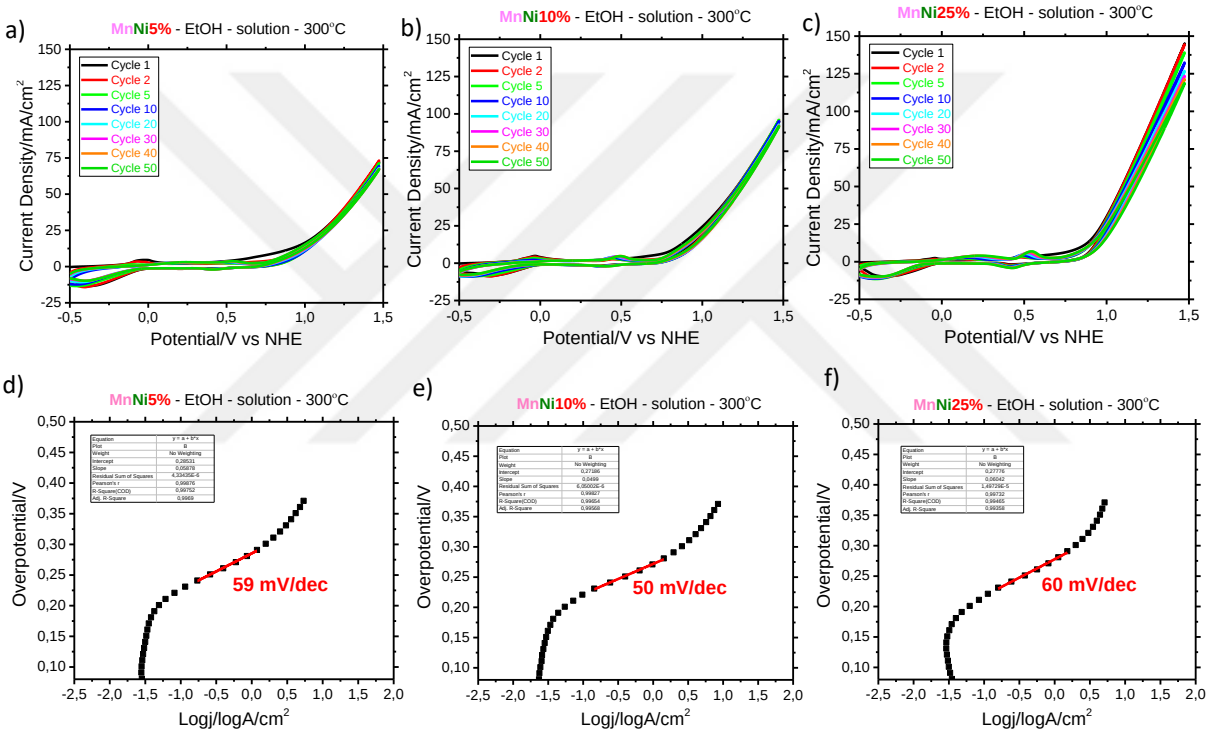


Figure 3.154: a), b), c) 50 CV cycles and d), e), f) multistep chronoamperometry plots with Tafel slopes of the MnNi5%-300ºC, MnNi10%-300ºC, and MnNi25%-300ºC coated GR electrodes.

Figure 3.155 shows the multi-step chronopotentiometry plots of the MnNi5%, MnNi10% and MnNi25% electrodes combined. It is clear that in each of these electrodes there is a point where the GR electrode degradates. The color of the electrolyte solution also changes and becomes grey during the measurements. However, comparing these electrodes, one can say that the overpotential required is the least in the MnNi10% and highest in the MnNi5% electrodes in ethanol system.

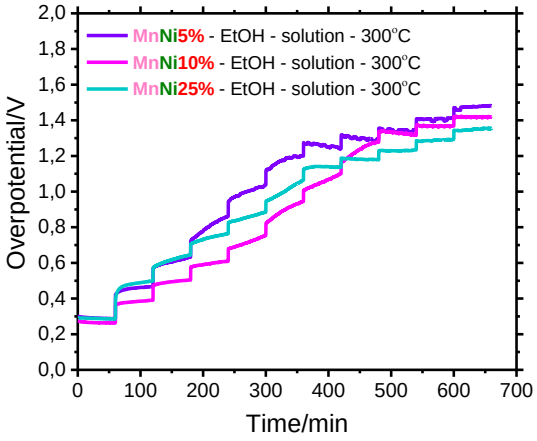


Figure 3.155: Multi-step chronopotentiometry plots of the MnNi5%-300ºC, MnNi10%-300ºC, and MnNi25%-300ºC electrodes, from ethanol system.

The same measurements are conducted using the MnCo5%, MnCo10%, and MnCo25% electrodes. The CVs of the MnCo5% electrode, calcined at different temperatures, are shown in Figure 3.156. Among these electrodes, the most stable one is MnCo5%-300ºC but, its current density at 1.5 V is less than the other electrodes. The least current density is obtained from the MnCo5%-600ºC electrode at 1.5 V and it is also not stable.

Figure 3.157(a) shows the multistep chronoamperometry plots of these electrodes. They also correlate well with the CVs. The least Tafel slope is obtained from the MnCo5%-400ºC electrode, which also has the highest current density at 1.5 V, whereas the highest Tafel slope is obtained from the MnCo5%-600ºC electrode, which has the least current density. However, the multistep chronopotentiometry plots, shown in Figure 3.157(b), indicate that these electrodes degregade at 30 mA/cm^2 current density during measurement and at low currents, the overpotentials are almost the same but, the MnCo5%-600ºC electrode has slightly less overpotential than the others.

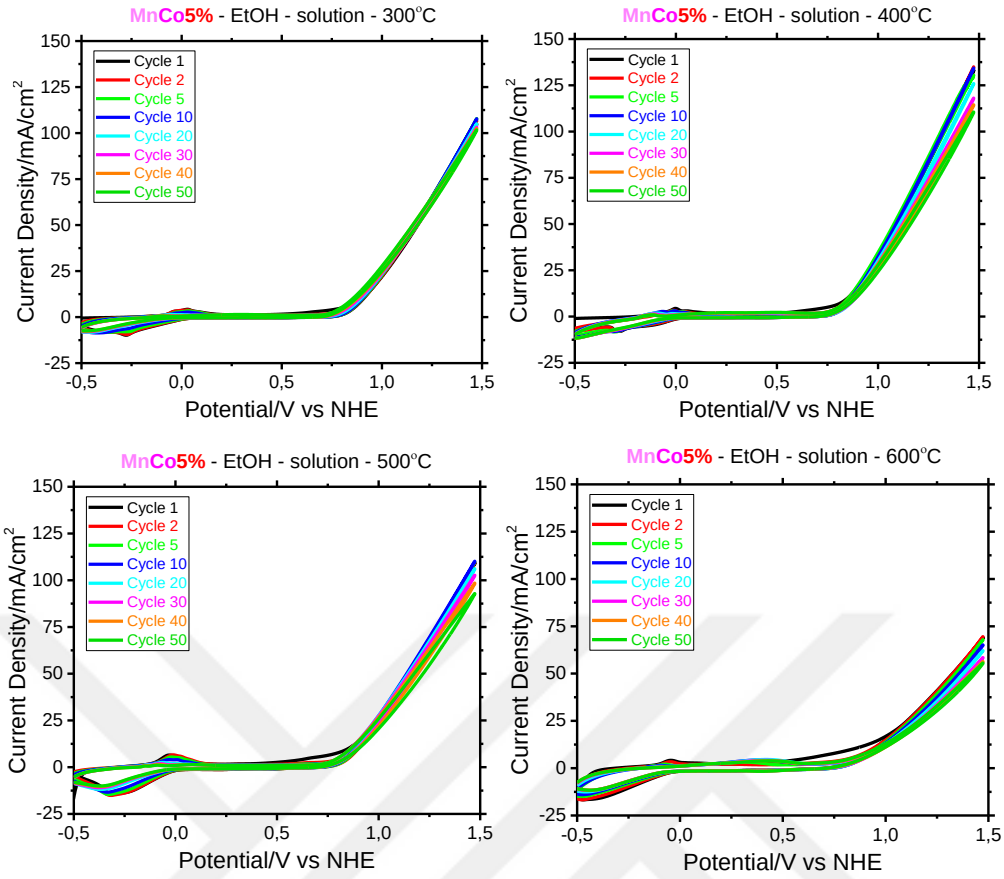


Figure 3.156: A selected group of CVs from 50 cycles in 1 M KOH electrolyte solution with a scan rate of 50 mV/s of the MnCo5% electrode, calcined at different temperatures.

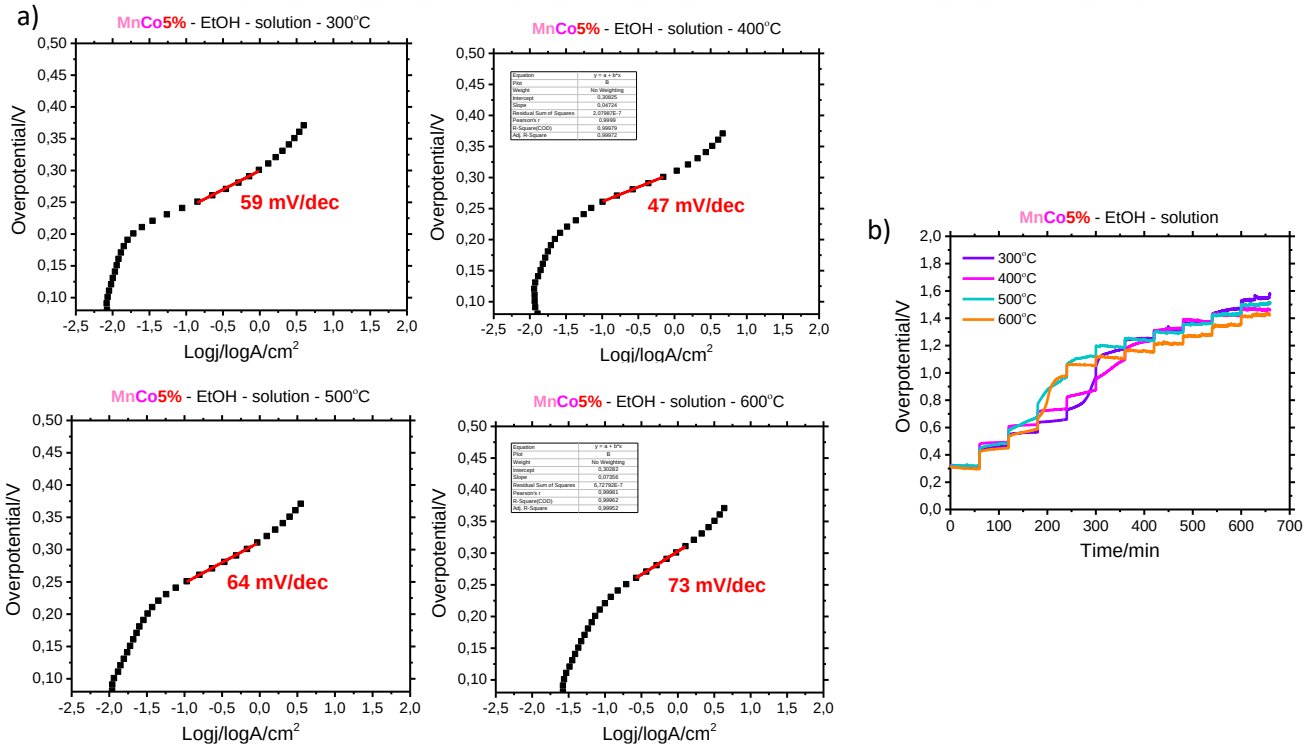


Figure 3.157: a) Multistep chronoamperometry plots with their Tafel slopes and b) Multi-step chronopotentiometry plots of the MnCo5%-300ºC, MnCo5%-400ºC, MnCo5%-500ºC, and MnCo5%-600ºC electrodes, from ethanol system.

In the case of the MnCo10% electrode, the CVs (Figure 3.158) show that the MnCo10%-300ºC electrode is stable and display high current density, around 125 mA/cm^2, at 1.5V. With the other electrodes, the current density at 1.5 V is low, around 75 mA/cm^2, but these electrodes are also stable during 50 CV cycles.

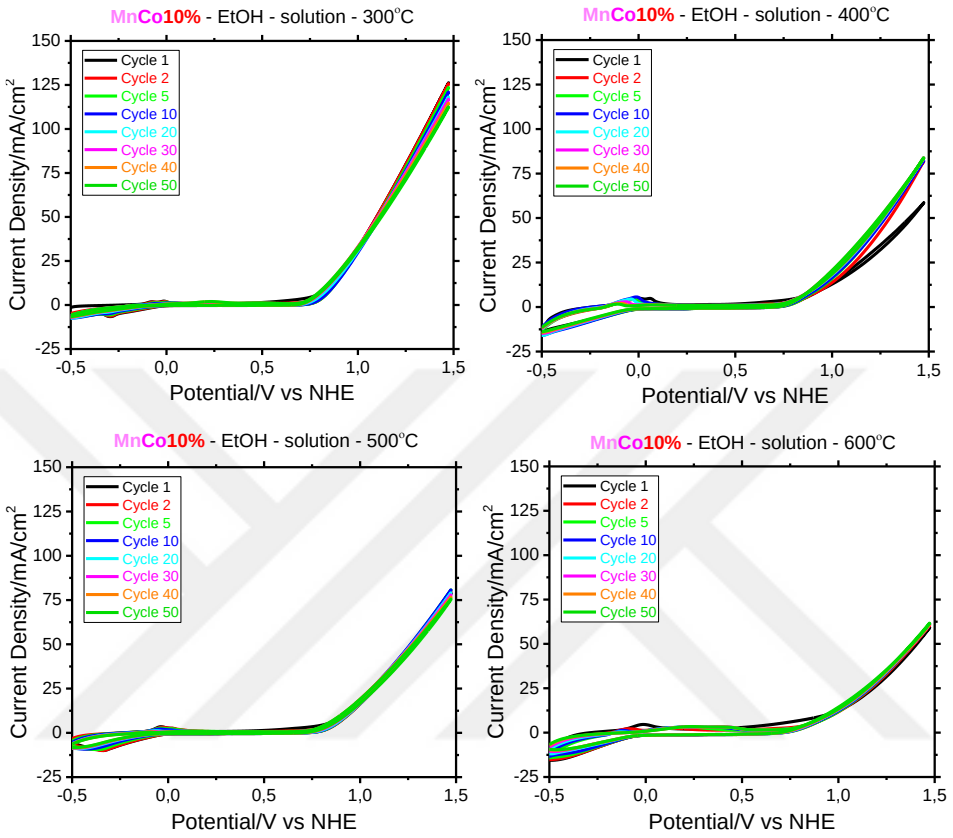


Figure 3.158: A selected group of CVs from 50 cycles in 1 M KOH electrolyte solution with a scan rate of 50 mV/s of the MnCo10% electrode, calcined at different temperatures.

The multi-step chronoamperometry plots along with the Tafel slopes of these electrodes are given in Figure 3.159(a). The lowest Tafel slope is obtained from the MnCo10%-300ºC electrode (43 mV/dec) and the highest from the MnCo10%-400ºC electrode (71 mV/dec). The other electrodes have almost the same Tafel slopes, 56 and 58 mV/dec.

The multi-step chronopotentiometry plots of these electrodes indicate the least overpotential is required for the MnCo10%-300ºC electrode and the highest for the MnCo10%-500ºC before the degradation. This shows that there is not a clear trend in the overpotentials and calcination temperatures. It may be because of the inhomogeneous distribution of Mn(II) and Co(II) sites on the electrode surface.

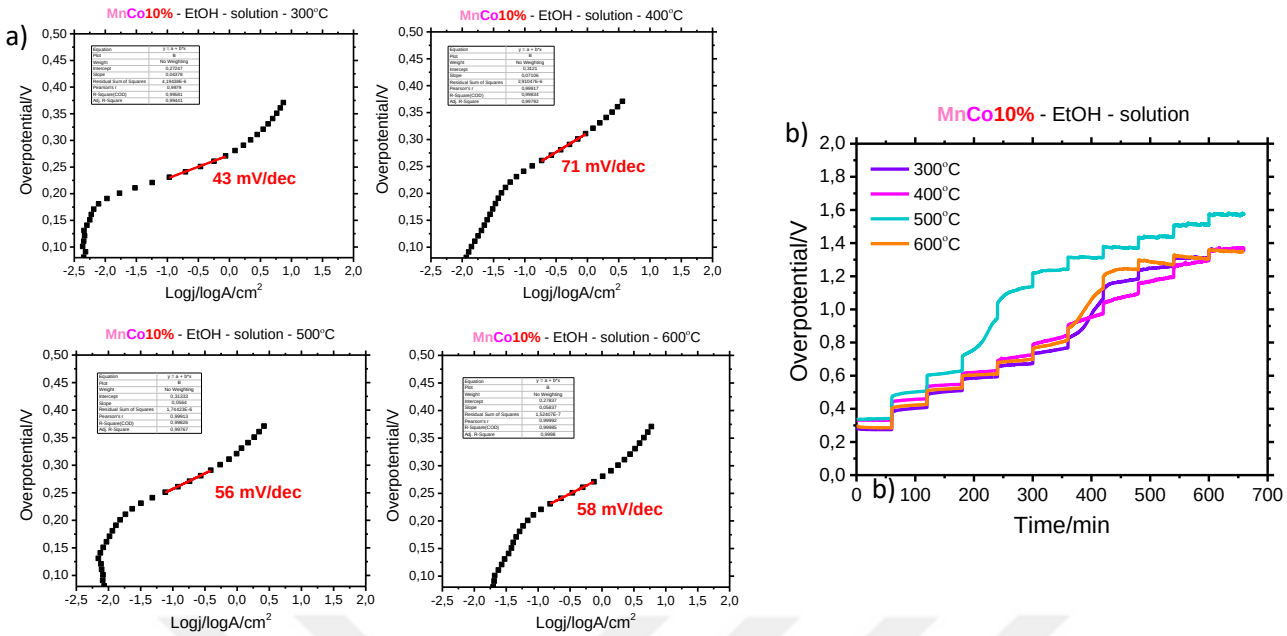


Figure 3.159: a) Multi-step chronoamperometry plots with Tafel slopes, b) multi-step chronopotentiometry plots of the MnCo10%-300ºC, MnCo10%-400ºC, MnCo10%-500ºC, and MnCo10%-600ºC electrodes, from ethanol system.

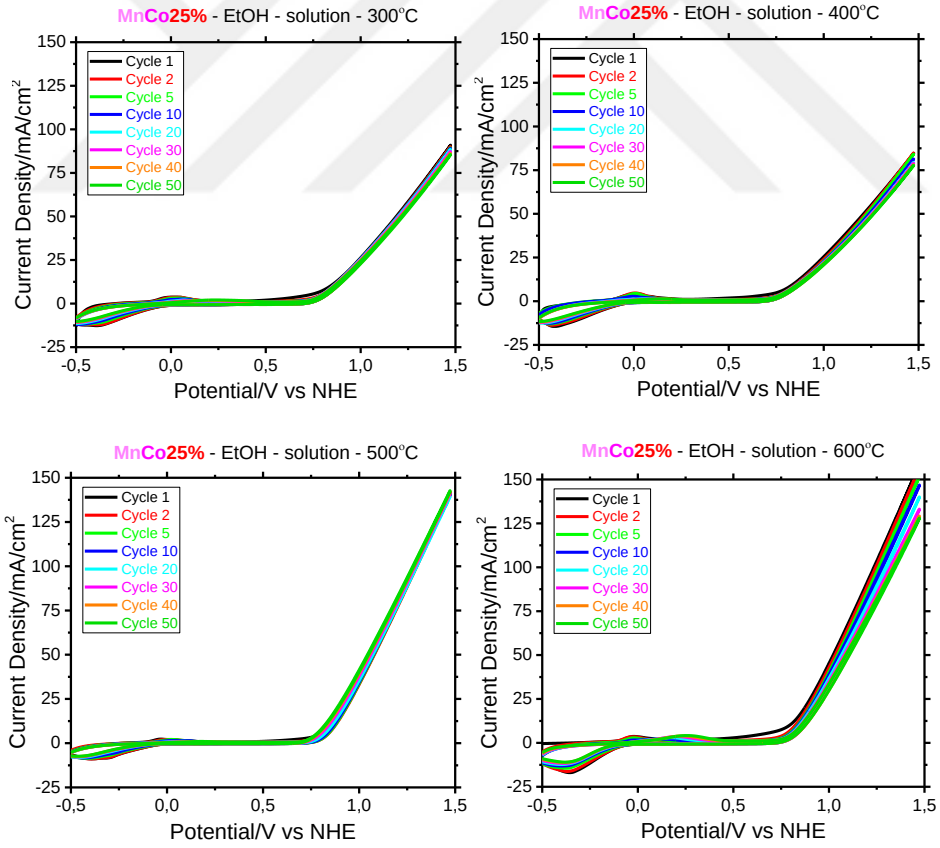


Figure 3.160: A selected group of CVs from 50 cycles in 1 M KOH electrolyte solution with a scan rate of 50 mV/s of the MnCo25%, calcined at different temperatures.

Figure 3.160 presents CVs of the MnCo25%-300ºC, MnCo25%-400ºC, MnCo25%-500ºC, and MnCo25%-600ºC electrodes. Even tough the highest current density is observed in

the MnCo25%-600ºC electrode, it is unstable during these cycles. However, the MnCo25%-500ºC electrode has also high current density, around 150 mA/cm^2, and stable during these cycles. The current density, obtained from the other electrodes at 1.5 V is close to 100 mA/cm^2.

The small Tafel slope, shown in Figure 3.161(a), indicates that the least overpotential is required for the MnCo25%-500ºC electrode. The other electrodes have almost the same Tafel slope, around 55-60 mV/dec.

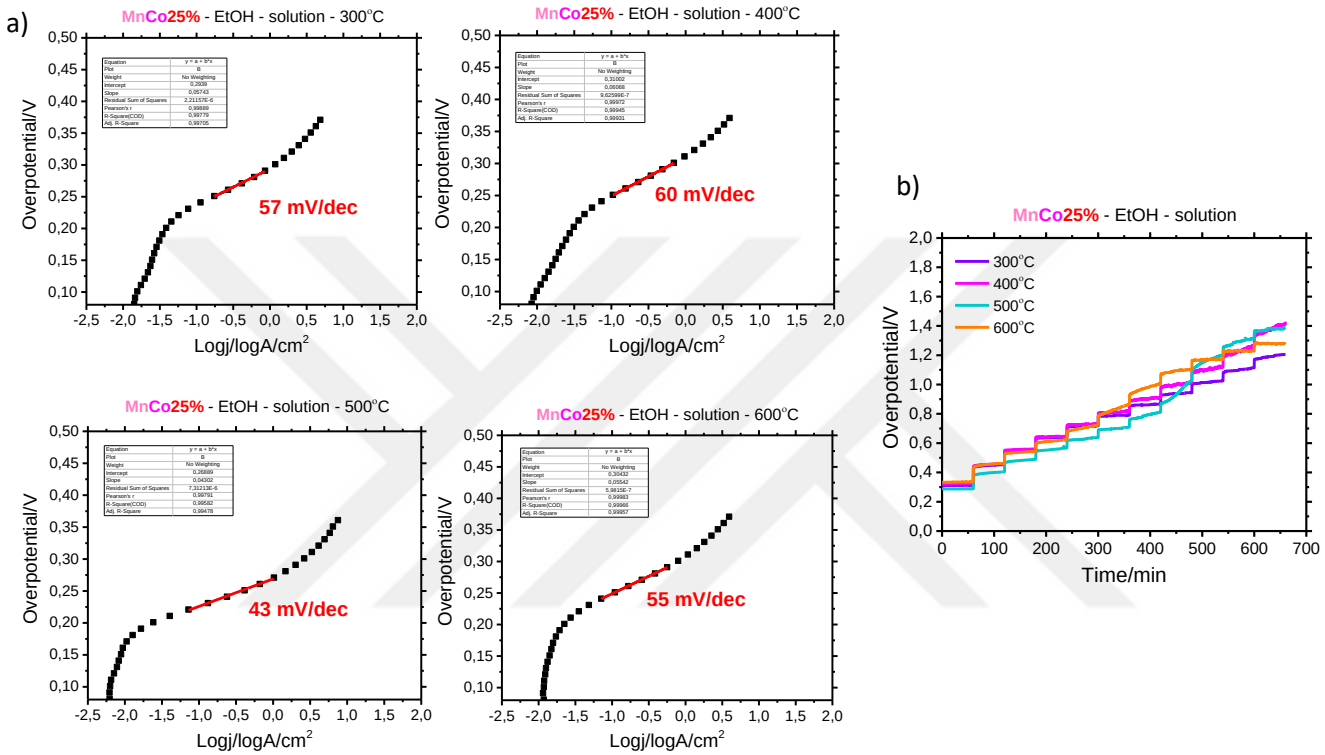


Figure 3.161: a) Multistep chronoamperometry plots with Tafel slopes, b) multi-step chronopotentiometry plots of the MnCo25%-300ºC, MnCo25%-400ºC, MnCo25%-500ºC, and MnCo25%-600ºC electrodes, from ethanol system.

To make a comparison of the electrodes in ethanol system, the chronopotentiometry plots of the electrodes with the least overpotentials are given in Figure 3.162. Even though all of these electrodes are degragading, the MnCo25%-500ºC electrode starts degragading at a higher current density, 70 mA/cm^2, than the other electrodes. And even tough the MnNi10%-300ºC electrode requires the least overpotential at low current densities and MnCo25%-500ºC requires the least overpotential at higher currents.

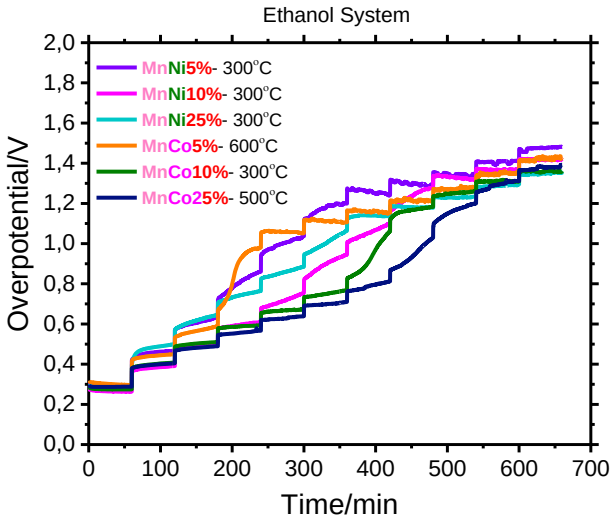


Figure 3.162: Multi-step chronopotentiometry plots of the MnCoX% and MnNiX% electrodes with the least overpotentials, from the ethanol system.

3.3.2. Butanol Systems

The same electrochemical measurements are carried using the electrodes, derived from butanol system. Figure 3.163 shows the CVs of the MnNi5% electrodes. Even tough the current density at 1.5 V from the MnNi25%-300ºC is low, 50 mA/cm^2, the others have high current densities, around 125-175 mA/cm^2.

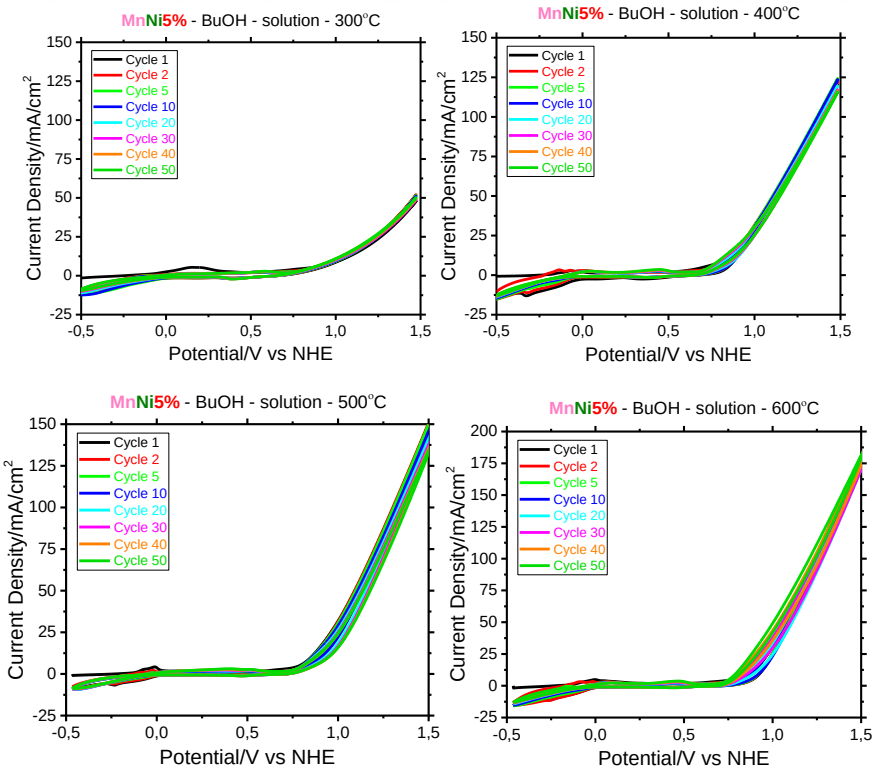


Figure 3.163: A selected group of CVs from 50 cycles in 1 M KOH electrolyte solution with a scan rate of 50 mV/s of the MnNi5% electrodes, calcined at different temperatures.

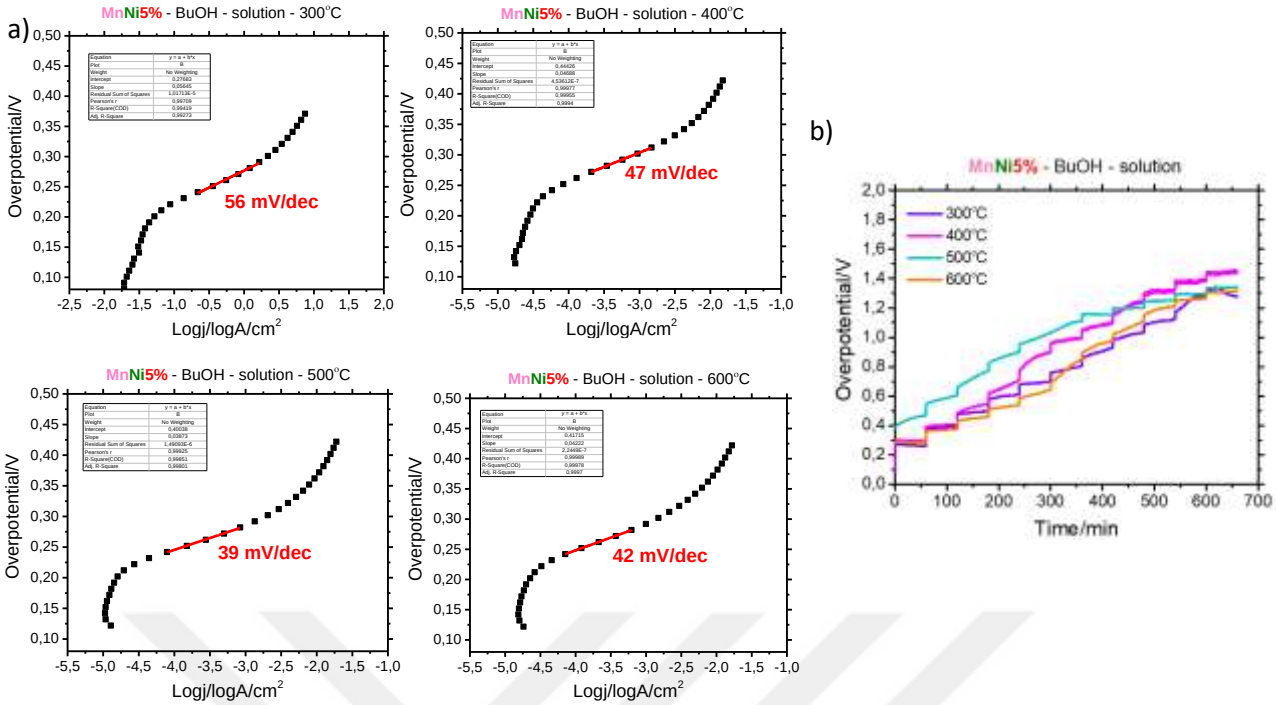


Figure 3.164: a) Multistep chronoamperometry plots with Tafel slopes, b) multi-step chronopotentiometry plots of the MnNi5%-300ºC, MnNi5%-400ºC, MnNi5%-500ºC, and MnNi5%-600ºC electrodes in butanol system.

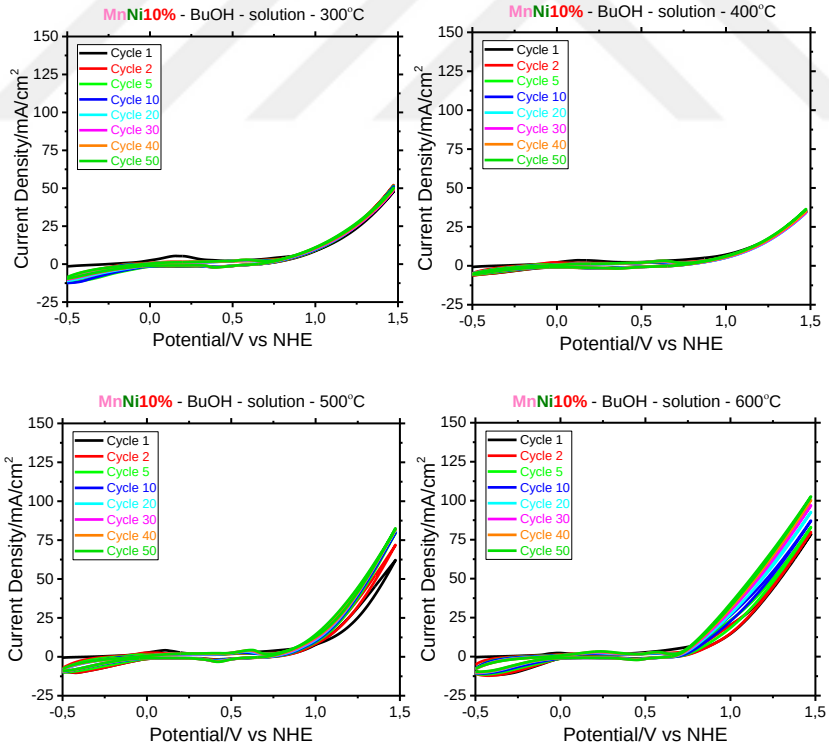
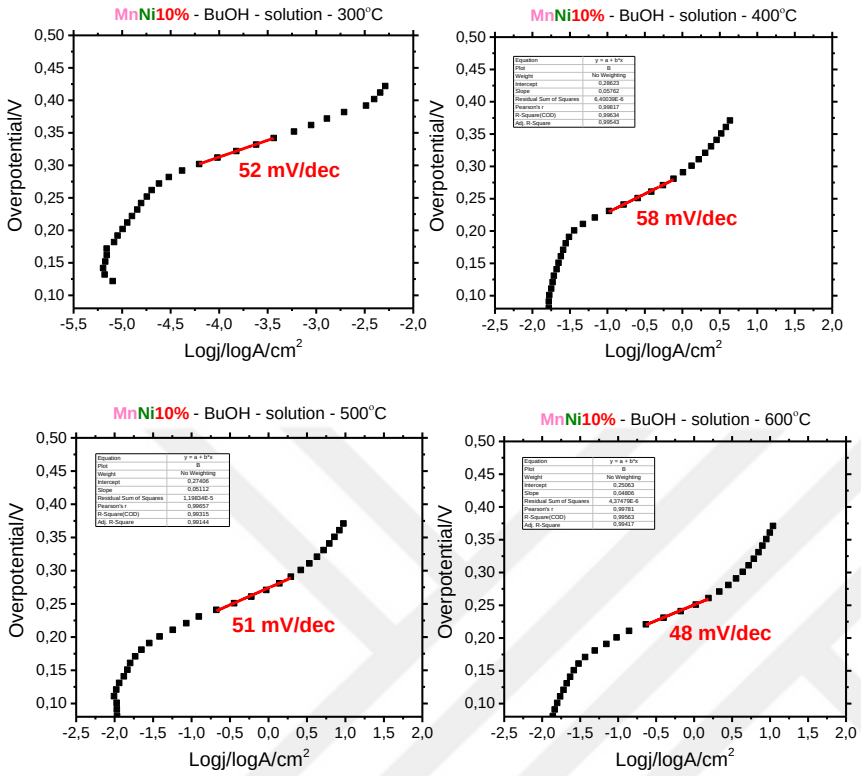


Figure 3.165: A selected group of CVs from 50 cycles in 1 M KOH electrolyte solution with a scan rate of 50 mV/s of the MnNi10% electrodes, calcined at different temperatures.

Figure 3.165 shows the CVs of the MnNi10% electrodes. The current density at 1.5 V is less in the MnNi10%-300ºC and MnNi10%-400ºC electrodes. However, in the other

electrodes, current density at 1.5 V increases during cycling in each step. It can be because of the removal of Mn(II) species and increase in the amount of Ni(II) species on the surface of the electrodes.

a)



b)

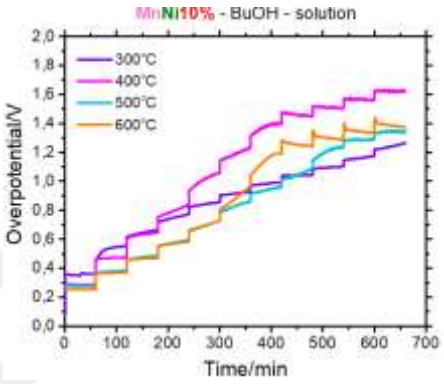


Figure 3.166: a) Multistep chronoamperometry plots with Tafel slopes, b) multi-step chronopotentiometry plots of the MnNi10%-300ºC, MnNi10%-400ºC, MnNi10%-500ºC, and MnNi10%-600ºC electrodes, from butanol system.

The multi-step chronoamperometry plots and Tafel slopes of these electrodes are given in Figure 3.166(a). The highest Tafel slope is obtained from the MnNi10%-400ºC electrode and least from the MnNi10%-600ºC electrode. The chronopotentiometry plots, given in Figure 3.166(b), show that the overpotential is the least in the MnNi10%-600ºC before these electrodes degregade.

Figure 3.167 shows the CVs of the MnNi25% electrodes. The current density at 1.5 V is the highest in MnNi25%-400ºC electrode, almost 150 mA/cm^2 and this electrode is stable during cycling. The least current density is observed from the MnNi25%-500ºC electrode, 50 mA/cm^2. The other electrodes have almost 100 mA/cm^2 current denisty at around 1.5 V.

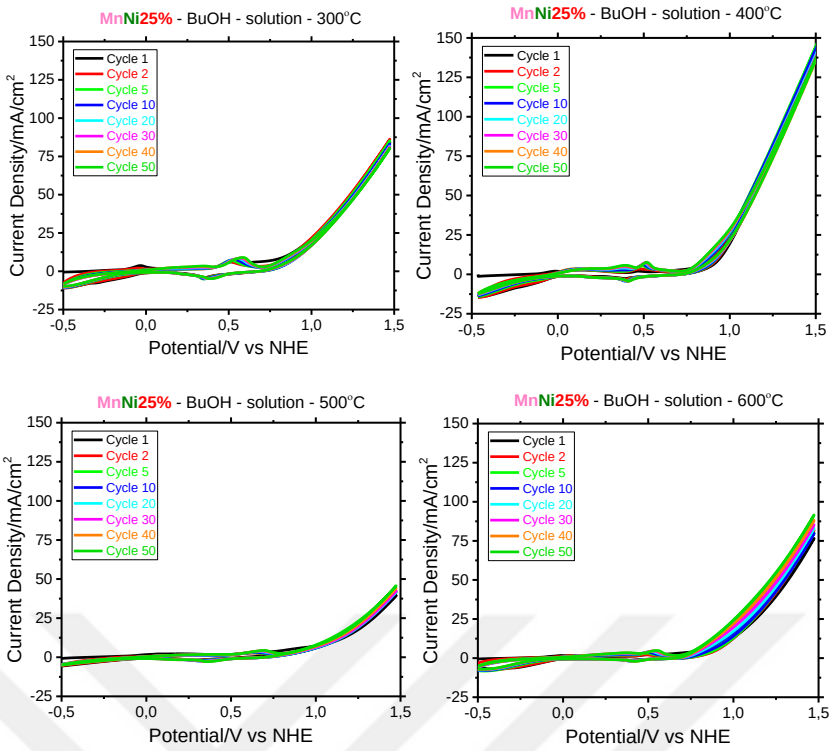


Figure 3.167: A selected group of CVs from 50 cycles in 1 M KOH electrolyte solution with a scan rate of 50 mV/s of the MnNi25% electrodes, calcined at different temperatures.

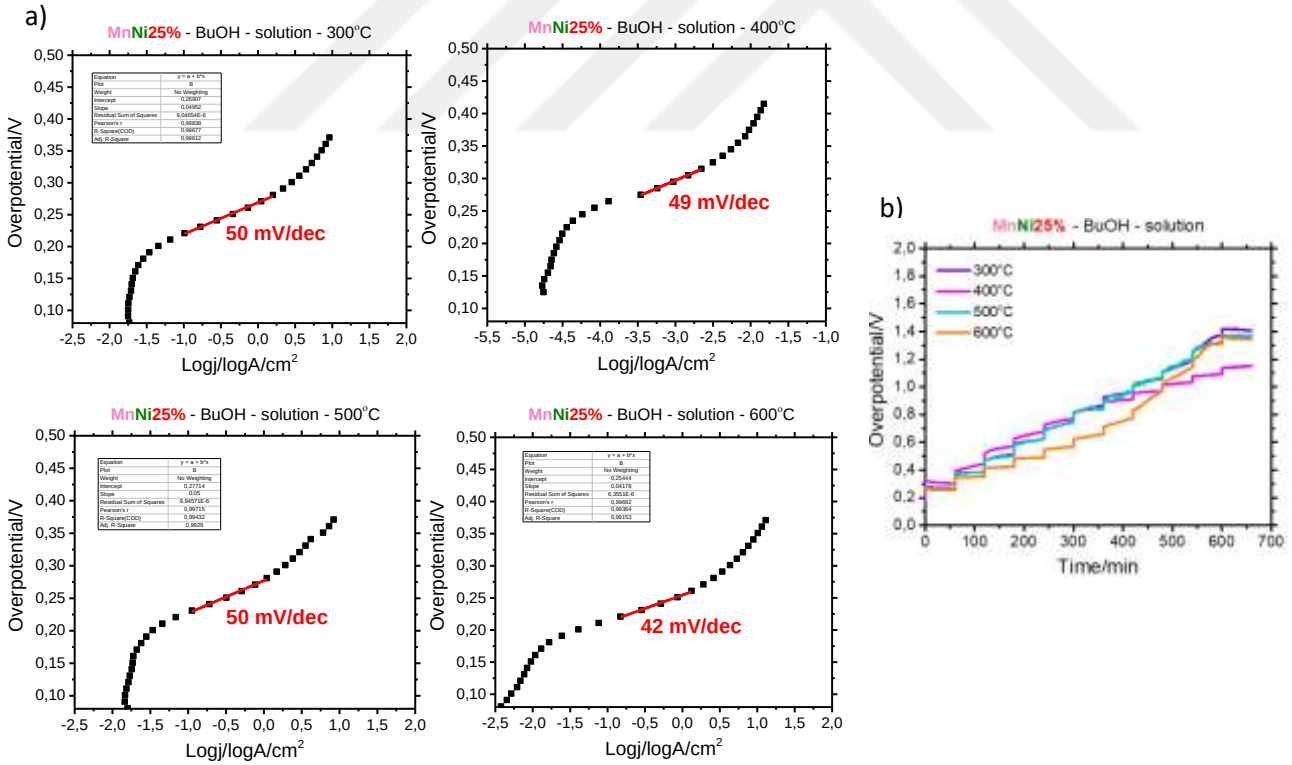


Figure 3.168: a) Multistep chronoamperometry plots with Tafel slopes, b) multi-step chronopotentiometry plots of the MnNi25%-300ºC, MnNi25%-400ºC, MnNi25%-500ºC, and MnNi25%-600ºC electrodes, from butanol system.

Figure 3.168(a) shows the multi-step CA plots and Tafel slopes of these electrodes. Tafel slope of the MnNi25%-600ºC electrode, 42 mV/dec, is less than the other electrodes but the others also have low Tafel slopes, 49-50 mV/dec. Figure 3.168(b) also shows that the least overpotential is observed from the MnNi25%-600ºC electrode.

Figure 3.169 shows the CVs of the MnCo5%-300ºC, MnCo5%-400ºC, MnCo5%-500ºC, and MnCo5%-600ºC electrodes. The highest current density at 1.5 V is obtained from the MnCo5%-600ºC but, this electrode along with the MnCo5%-500ºC electrode is not stable. The other electrodes display slightly less current density at 1.5 V, around 100 mA/cm^2 but, they are stable.

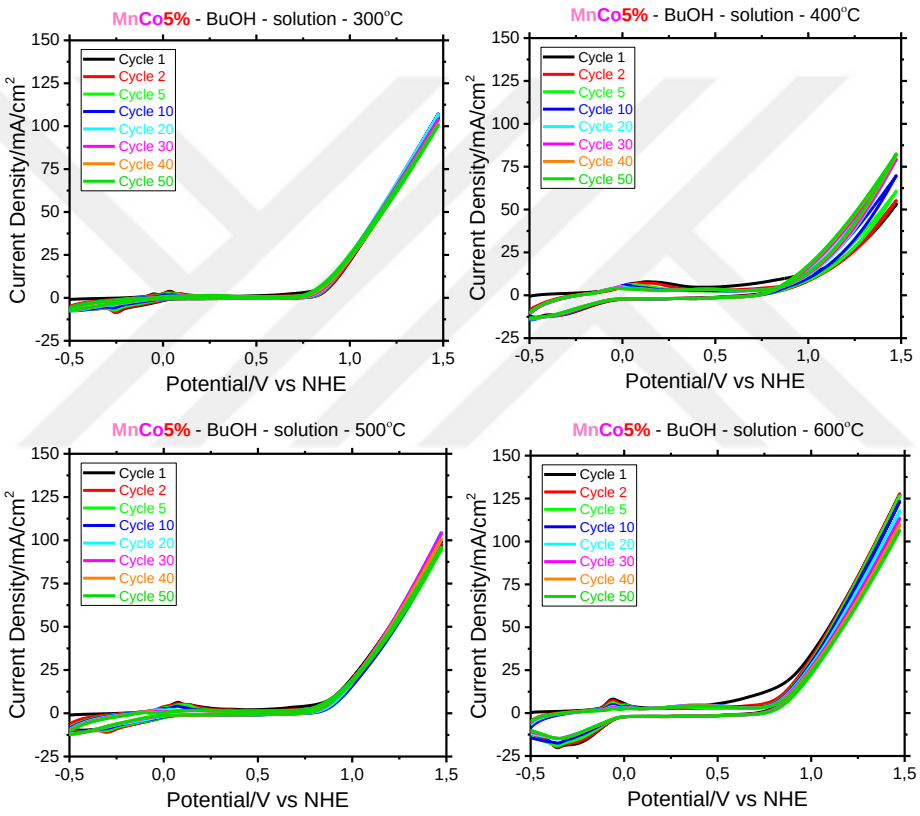


Figure 3.169: A selected group of CVs from 50 cycles in 1 M KOH electrolyte solution with a scan rate of 50 mV/s of the MnCo5% electrodes, calcined at different temperatures.

Tafel slope of the MnCo5%-300ºC electrode, 40 mV/dec, is the least among these electrodes and the highest Tafel slope is observed in the MnCo5%-600ºC electrode, 66 mV/dec, see Figure 3.170(a) . The other electrodes have almost the same Tafel slopes of 60, 57 mV/dec. The CPs show that the least overpotential is required for the MnCo5%-600ºC electrode before it degregates, see Figure 3.170(b).

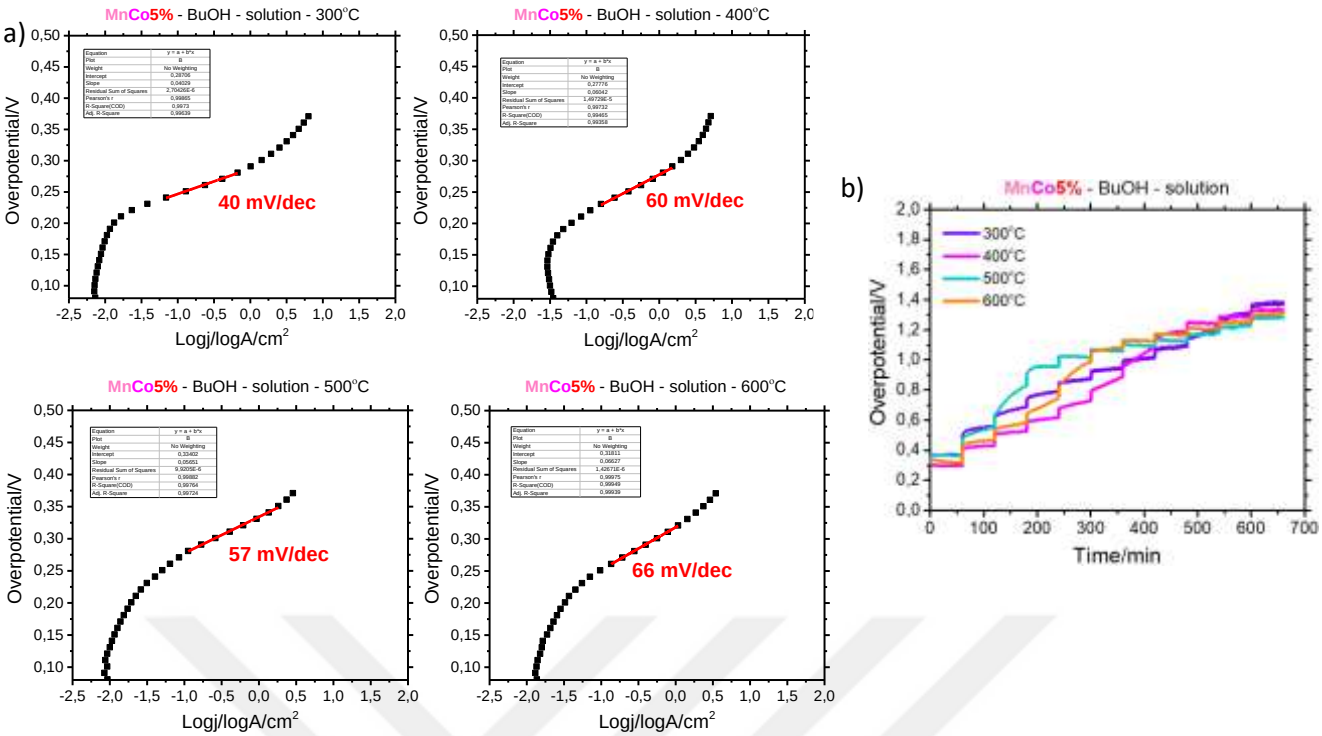


Figure 3.170: a) Multistep chronoamperometry plots with Tafel slopes and b) multi-step chronopotentiometry plots of the MnCo5%-300ºC, MnCo5%-400ºC, MnCo5%-500ºC, and MnCo5%-600ºC electrodes, from butanol system.

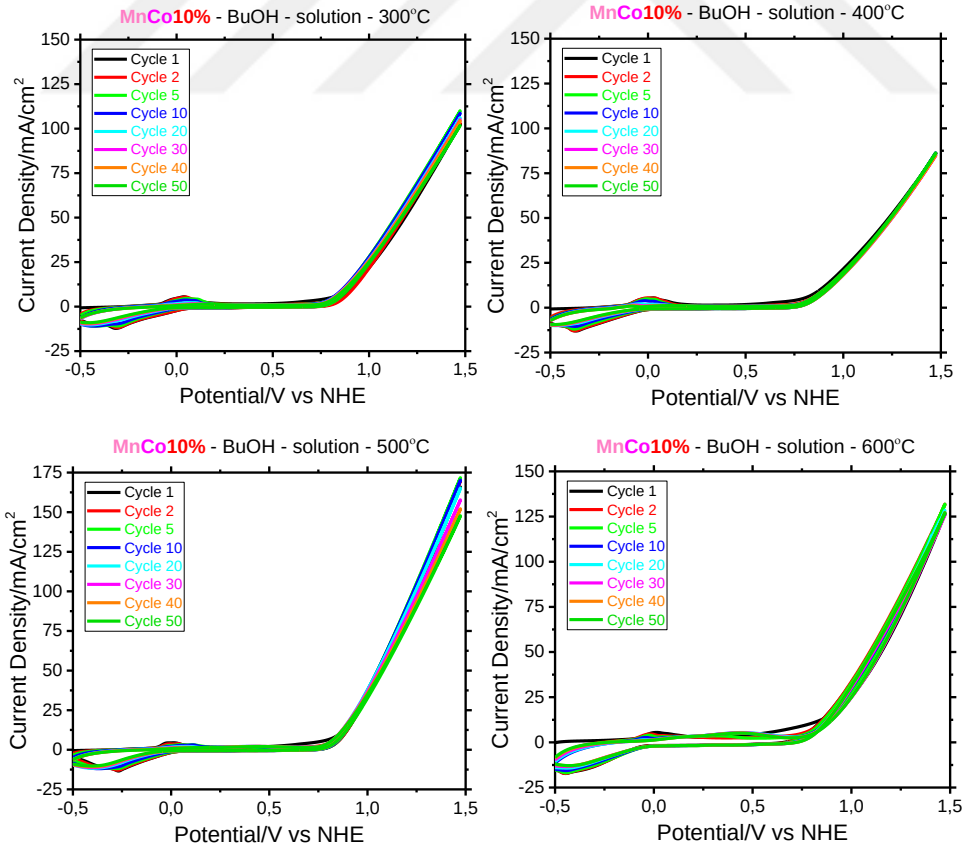


Figure 3.171: A selected group of CVs from 50 cycles in 1 M KOH electrolyte solution with a scan rate of 50 mV/s of the MnCo10% electrodes, calcined at different temperatures.

The CVs of the MnCo10% electrodes are given in Figure 3.171. The highest current density at 1.5 V is obtained from the MnCo10%-500ºC electrode but, it is also unstable. The other electrodes are stable during the cycles and the current density is around 90-125 mA/cm^2 range.

Figure 3.172(a) shows the multi-step chronoamperometry plots and Tafel slopes of these electrodes. Even tough, the MnCo10%-600ºC electrode has a high Tafel slope, 62 mV/dec, the other electrodes have relatively lower Tafel slopes of 46-47 mV/dec. And their chronopotentiometry plots, given in Figure 3.172(b), also show that these electrodes have low overpotentials even at high currents. While the MnCo10%-600ºC electrode degregades and has high overpotentials at each current density.

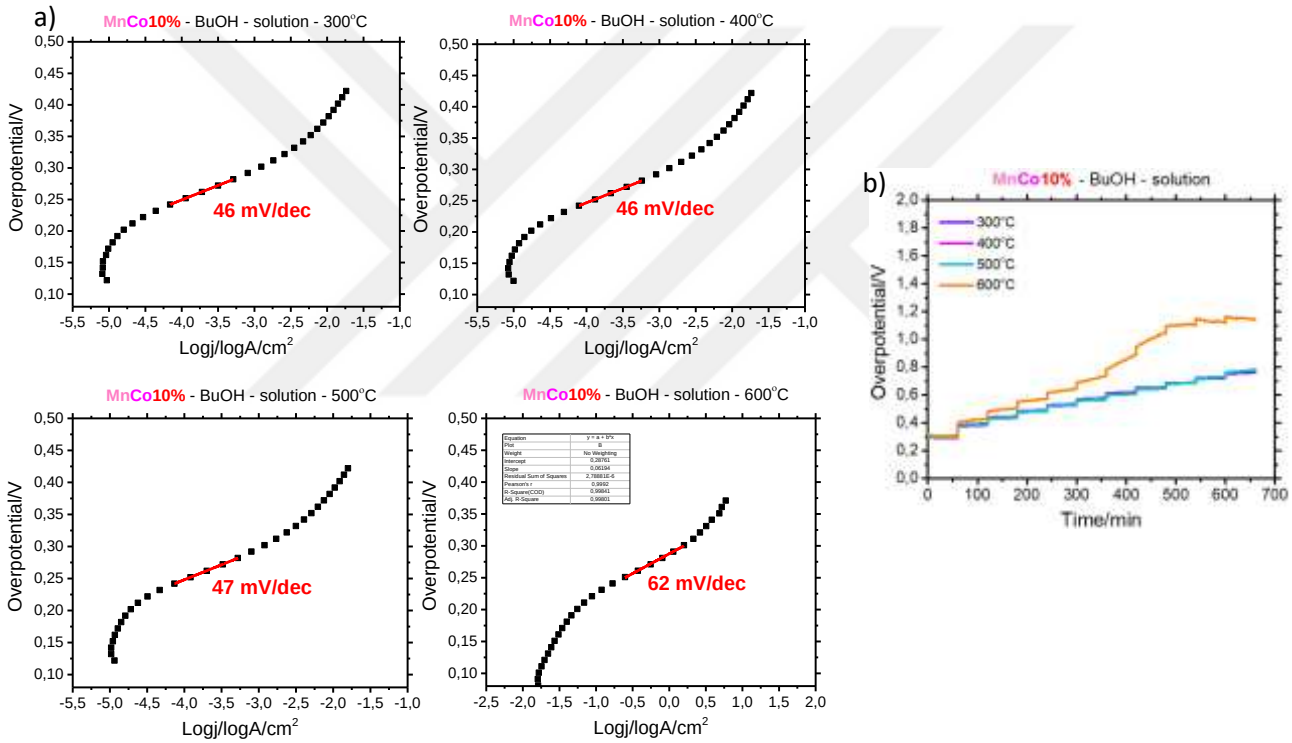


Figure 3.172: a) Multistep chronoamperometry plots with Tafel slopes and b) multi-step chronopotentiometry plots of MnCo10%-300ºC, MnCo10%-400ºC, MnCo10%-500ºC, and MnCo10%-600ºC electrodes.

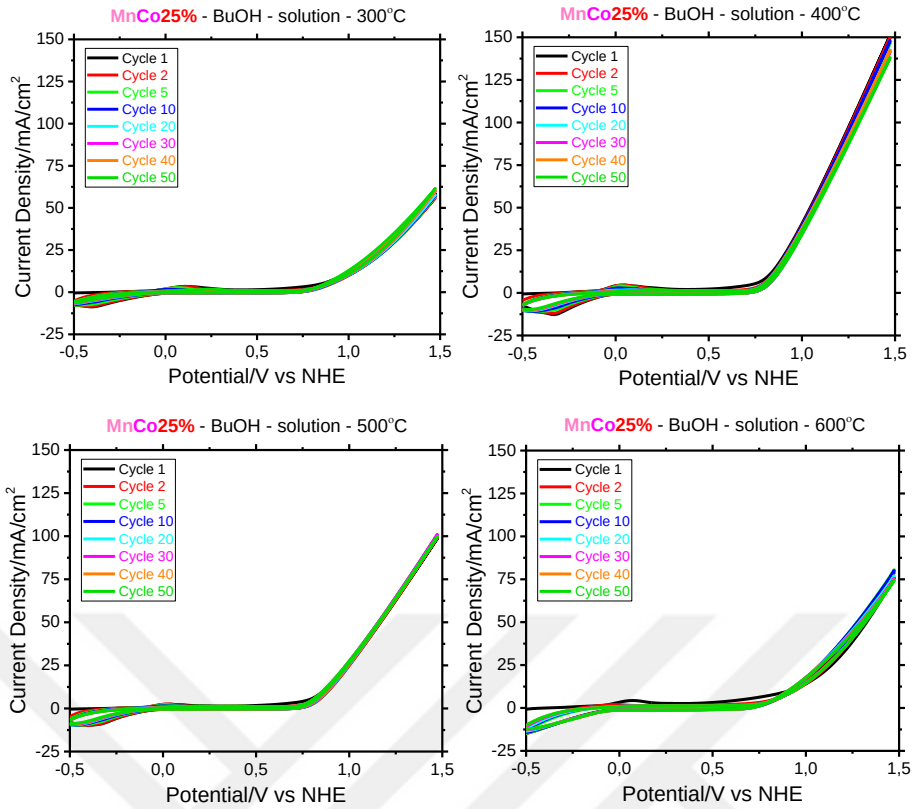


Figure 3.173: A selected group of CVs from 50 cycles in 1 M KOH electrolyte solution with a scan rate of 50 mV/s of the MnCo25% electrodes, calcined at different temperatures.

CVs of the MnCo25% electrodes are given in Figure 3.173. The highest current density at 1.5 V is obtained from the MnCo25%-400ºC electrode, 151 mA/cm^2 and it is followed with 100 mA/cm^2, from the MnCo25%-500ºC electrode. However, in the other electrodes, it is around 75 mA/cm^2.

The least Tafel slope is obtained from the MnCo25%-500ºC, 39 mV/dec and the highest with MnCo25%-600ºC, 63 mV/dec, see Figure 3.174(a). The other electrodes have 51 and 54 mV/dec Tafel slopes. Even tough, the overpotential is the smallest in the MnCo25%-500ºC electrode, the MnCo25%-400ºC electrode has the least overpotential at higher currents, see Figure 3.174(b).

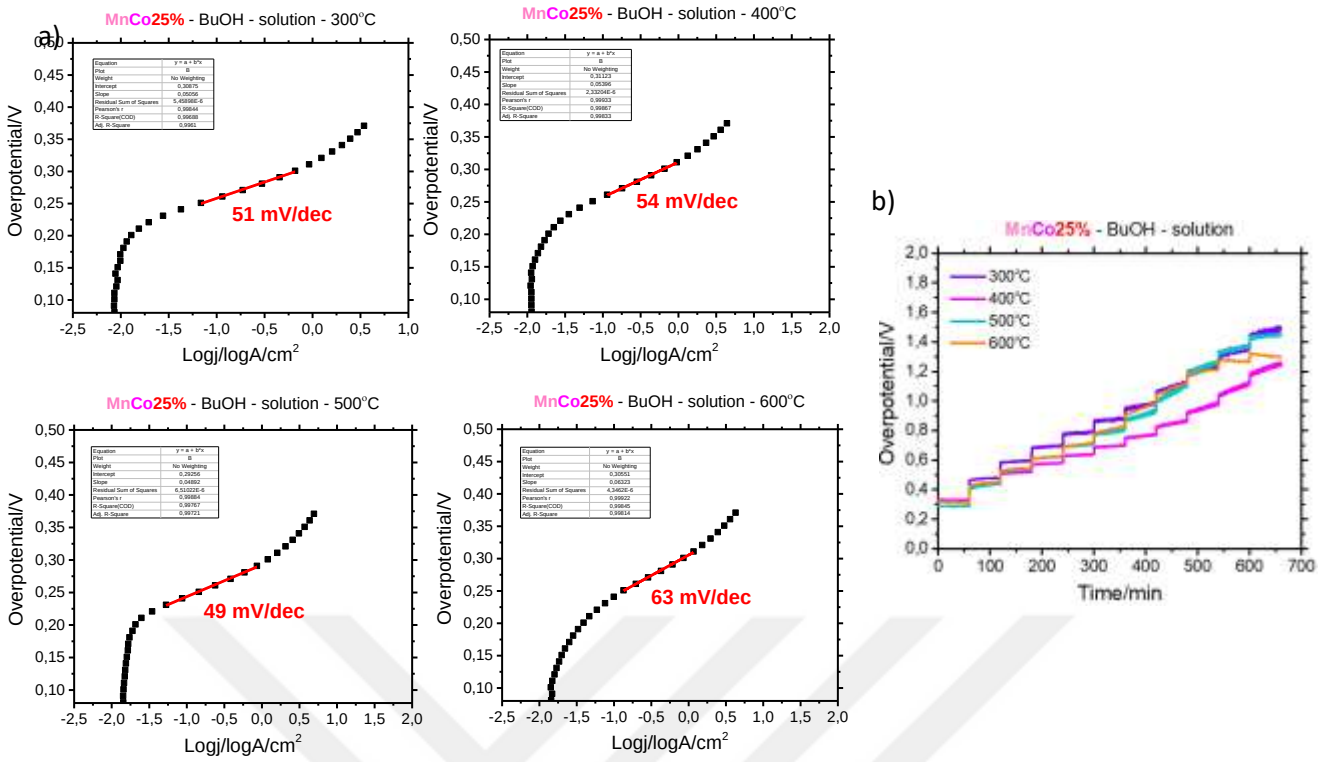


Figure 3.174: a) Multistep chronoamperometry plot with Tafel slopes and b) multi-step chronopotentiometry plots of MnCo10%-300ºC, MnCo10%-400ºC, MnCo10%-500ºC, and MnCo10%-600ºC electrodes.

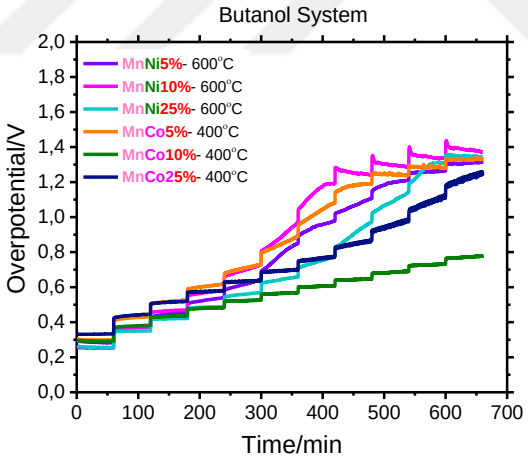


Figure 3.175: Multi-step chronopotentiometry plots of the MnCoX% and MnNiX% electrodes with the least overpotentials.

To make a comparison of the both MnCoX%-Y and MnNiX%-Y electrodes of the butanol system, the electrodes with the least overpotentials are shown in Figure 3.175. The MnNi% electrodes are the most stable ones with least overpotentials at 600ºC but, the MnCo% electrodes are stable at 400ºC. And the MnCo10%-400ºC electrode is the most stable electrode and especially at high current densities, it has the least overpotential among the electrodes.

3.3.3. Methanol Systems

Below in Figure 3.176, the CVs and multi-step chronoamperometry plots with Tafel slopes are given. The current density at 1.5 V is highest in the MnNi10%-300ºC electrode, 110 mA/cm^2 and 100 and 75 mA/cm^2 in the MnNi5% and MnNi25% electrodes, respectively. The lowest Tafel slope of 46 mV/dec is obtained from the MnNi25%-300ºC electrode while the highest is obtained from the MnNi5%-300ºC electrode (77 mV/dec).

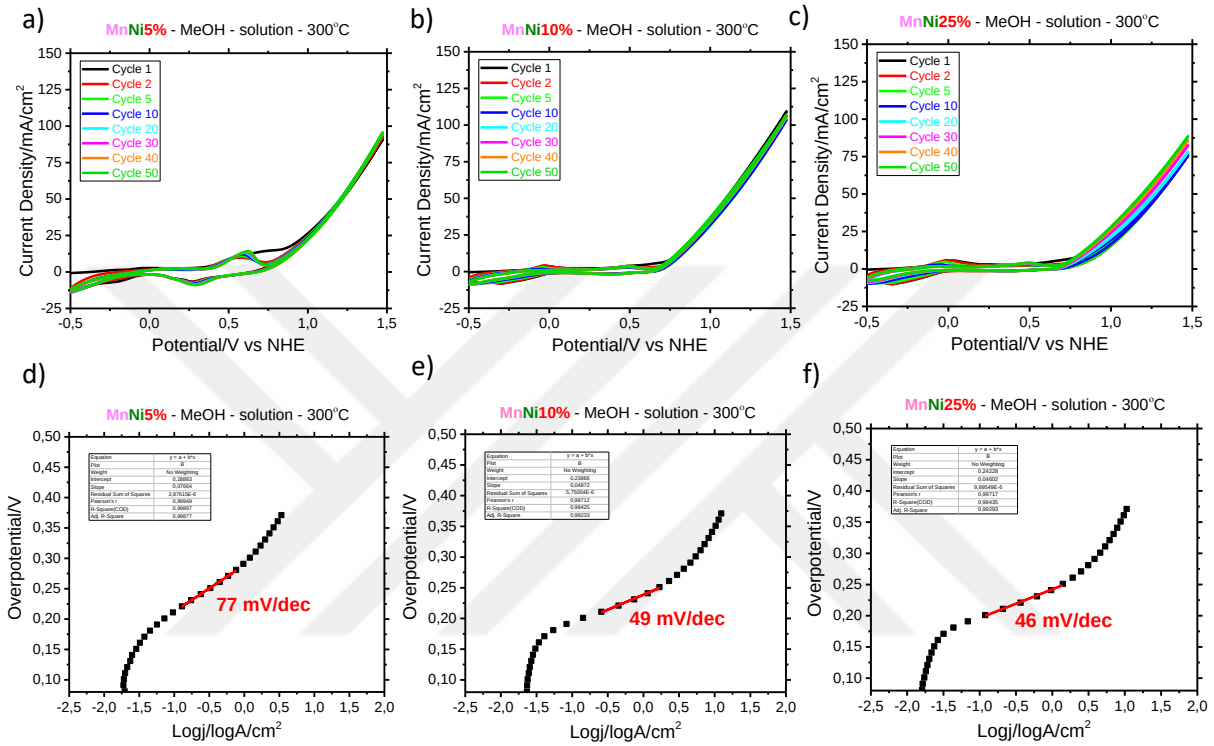


Figure 3.176: a), b) ,c) A selected group of CVs from 50 cycles in 1 M KOH electrolyte solution with a scan rate of 50 mV/s and d), e), f) multi-step chronoamperometry plots with Tafel slopes of the MnNi5%-300ºC, MnNi10%-300ºC, and MnNi25%-300ºC GR coated electrodes.

The chronopotentiometry plots, given in Figure 3.177, provide the overpotentials, required for the MnNi10%-300ºC and MnNi25%-300ºC electrodes are almost similar and around 250 mV at 1 mA/cm^2 current density. However, these electrodes degregade at 50 mA current density, while only the MnNi5%-300ºC electrode is stable. The overpotential value obtained from the MnNi5%-300ºC electrode is higher, around 310 V at 1 mA/cm^2 current density and stable throughout the experiment.

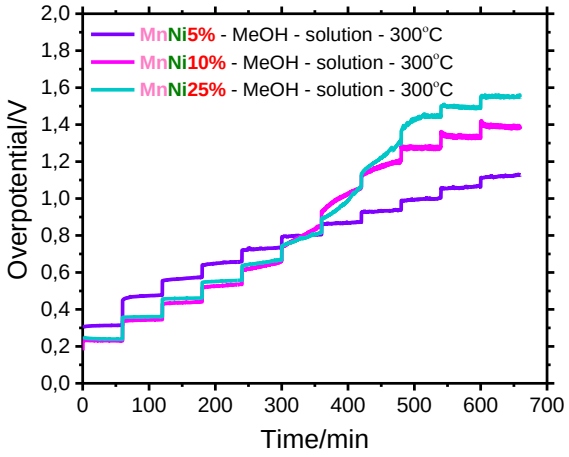


Figure 3.177: Multi-step chronopotentiometry plots of the MnNi5%-300ºC, MnNi10%-300ºC, and MnNi25%-300ºC electrodes.

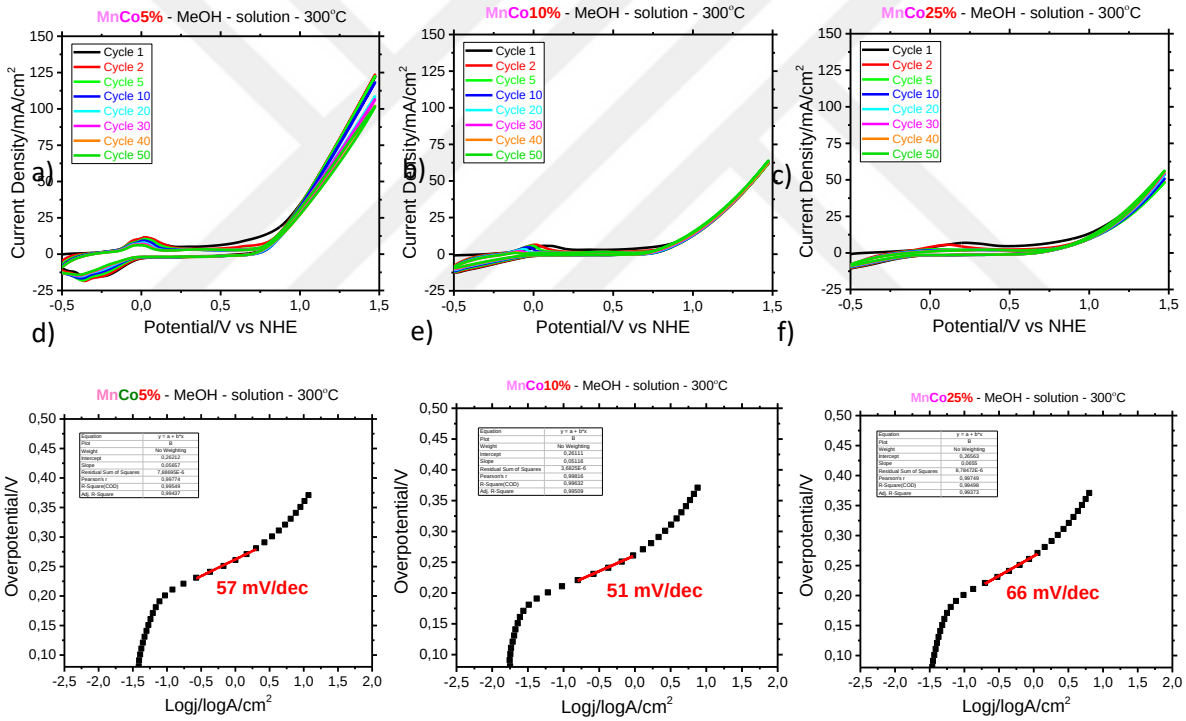


Figure 3.178: a), b) ,c) A selected group of CVs from 50 cycles in 1 M KOH electrolyte solution with a scan rate of 50 mV/s and d), e), f) multi-step chronoamperometry plots with Tafel slopes of the MnCo5%-300ºC, MnCo10%-300ºC, and MnCo25%-300ºC coated GR electrodes.

Figure 3.178 shows the CVs of the MnCo5%-300ºC, MnCo10%-300ºC, and MnCo25%-300ºC electrodes as well as their multi-step chronoamperometry plots and Tafel slope values. The highest current density at 1.5 V is obtained from the MnCo5%-300ºC electrode as 125

mA/cm^2 but it degregades during cycling. The current density at around 1.5 V is less in the other electrodes, 50-75 mA/cm^2. The Tafel slopes of these electrodes are around 50-66 mV/dec.

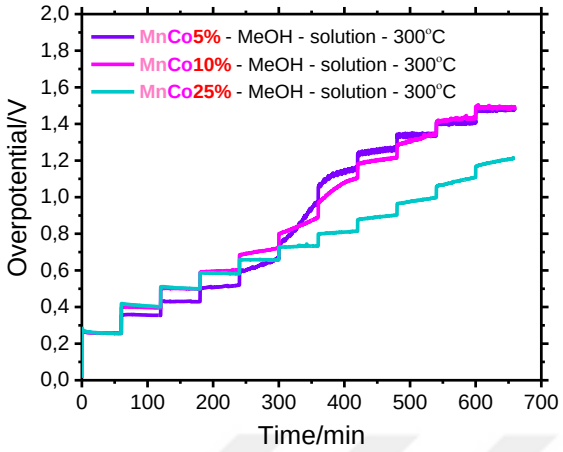


Figure 3.179: Multi-step chronopotentiometry plots of the MnCo5%-300ºC, MnCo10%-300ºC, and MnCo25%-300ºC electrodes.

Figure 3.179 presents the chronopotentiometry plots of these electrodes. The overpotentials required for these electrodes are almost the same at 1 mA/cm^2 current density but, at higher currents, the MnCo25% electrode is much more stable and has lower overpotentials than the others. Figure 3.180 shows the comparison of the electrodes from the methanol system. The least overpotential at high current densities is obtained from the MnCo25%-300ºC electrode.

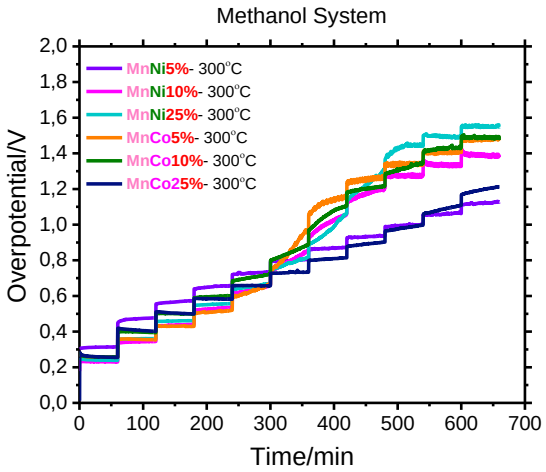


Figure 3.180: Multi-step chronopotentiometry plots of the MnCoX% and MnNiX% electrodes with the least overpotentials, from the methanol system.

To make a comparison of the ethanol, butanol, and methanol systems, the overpotential plots of all the electrodes in these systems are compared and the ones with least overpotentials are shown in Figure 3.181. In these systems the most stable electrodes with least overpotentials are obtained from the MnCo10% or MnCo25% electrodes, especially the MnCo10%-400ºC electrode derived from butanol system.

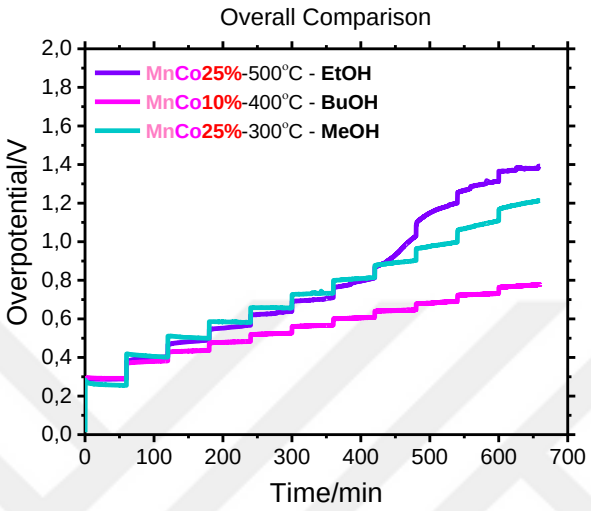


Figure 3.181: Multi-step chronopotentiometry plots of the electrodes with the least overpotentials, from the ethanol, butanol, and methanol systems.

Chapter 4

4. Conclusion

Solutions of the metal salts ($[Mn(H_2O)_4](NO_3)_2$, $[Co(H_2O)_6](NO_3)_2$, and $[Ni(H_2O)_6](NO_3)_2$) and phosphoric acid in the presence of P123 are prepared in ethanol, butanol and methanol solvents. There is a sol-gel formation in the ethanol and butanol solutions but, the methanol always form cloudy solutions. As the solutions are not homogeneous, centrifugation process is used and solution, supernatant, and precipitate parts of these solutions are separately characterized. Gelation and/or precipitation occurs through a reaction among the metal ion and PPA species and assembly by the surfactant species.

During the polymerization reaction, the nitrate species decompose as nitric acid and/or its decomposition products and leave the media. As a result, ordered and uniform mesophases are observed in the aged samples of the supernatants in all compositions and solvent systems. However, in solution and precipitate parts, the ordered mesophases are not observed in their gel-phases.

The calcination of the solution, supernatant and precipitate parts produce mesoporous metal pyrophosphates. The highest surface area is observed by the calcination of Ni30-15PPA butanol solution at 300ºC, as 410 m^2/g. The highest surface areas, obtained for the $Co_2P_2O_7$ and $Mn_2P_2O_7$ samples, from the ethanol precipitate are 145 and 83 m^2/g, respectively. The $Co_2P_2O_7$ and $Mn_2P_2O_7$ crystallize at around 500-600ºC but $Ni_2P_2O_7$ requires higher temperature and crystallizes at 700ºC with a decent surface area of 18-20 m^2/g.

The solutions and supernatants can be spin-coated and dip-coated on FTO and GR electrodes to obtain their electrodes. The coated FTO electrodes are not stable during long term electrochemical measurements in 1M KOH solution. Also, in 1 M KOH electroyte, these electrodes undergo a transformation reaction and are converted to their metal hydroxides. The process occurs chemically, it is not an electrochemical process. However the electrodes can be kept chemically stable in a 2.4 M KOH and 0.6 M $H_4P_2O_7$ solutions. The transformation can be electrochemically monitored by adding small portions of 1M KOH solution to the above neutralized solution. Moreover, the electrochemical measurements prove that the metal hydroxide electrodes are better electrocatalysts than metal pyrophosphates.

$Co_2P_2O_7$ and $Ni_2P_2O_7$ samples are not stable on FTO substrate but GR coated electrodes are stable during electrochemical measurements and allow OER performance analysis. From the chronoamperometry experiments, Tafel slopes of the $Co_2P_2O_7$ and $Ni_2P_2O_7$ coated GR electrodes are determined to be around 50 and 40 mV/dec, respectively. And chronopotentiometry experiments demonsrate low overpotentials, around 0.25-0.30 V at 1 mA/cm^2 current density.

The $Mn_2P_2O_7$ samples are unstable on both FTO and GR substrates. In addition to metal hydroxide chemical transformation, they also undergo degradation through Mn(VI) distroportionation reaction. This process can be monitored through CV measurements because these electrodes release pink colored MnO_4^- species to the electrolyte media during the high potential OER.

In order to keep the manganese species on the surface of the electrode, to check the synergistic effect of mixing two metals on the mesophase formation and electrochemical performances, the binary metal pyrophosphates are also prepared. The mesophases of the binary metal pyrophosphates show similar behaviors as the single metal pyrophosphates. The crystal, obtained from these systems, is also $Mn_2P_2O_7$ but, with almost twice the surface area. In the ethanol system, the MnNi25% precipitate, calcined at 300ºC, has a 202 m^2/g surface area. Similarly the MnCo10% butanol precipitate, calcined at 300ºC, has a significantly large surface area of 144 m^2/g. As the amount of Co(II) and Ni(II) species increases, the surface area increases as well.

The 5x diluted sol-gels and cloudy solutions can be coated on GR by dip-coating and calcined at various temperatures to obtain graphite coated electrodes. The Tafel slopes of these electrodes are in the range of 40-70 mV/dec. And the MnCo10%-400ºC electrode displays the

least overpotential. The binary metal pyrophosphates are better than pure $Mn_2P_2O_7$ in terms of porosity, surface area as well as OER performance and stability during electrochemical tests.

Chapter 5

5. Future Recommendations

This study demonstrates an effective sol-gel process that occurs in alcohol solutions for the synthesis of high surface area and highly porous metal pyrophosphates. Moreover, the type of alcohol is also important. For instance, in butanol, the surface area can be significantly higher than the other alcohols investigated in this work. To find the best solvent for the synthesis of high surface area mesoporous $Ni_2P_2O_7$ samples, other solvents, such as propanol and hexanol are also tested. However, the BET surface areas are 134 and 220 m^2/g from propanol and hexanol, respectively. And the pore size distributions are very broad, unlike the butanol system, see Figure 5.1. However, pentanol is not tested yet. It should also be used and the surface area and pore size distribution should be evaluated to complete the role of the solvent.

The solvent is not the only factor to be considered in the sol-gel synthesis. Temperature, pH, and humidity (amount of water in the system) are the other factors. Even small change in humidity affects the stability of the gel-phase during investigation. Especially, PPA is very sensitive to humidity and using it in its dried form is not easy. That's why the amount of the water added to these solutions could not be controlled.

In 1-butanol solvent, the sol-gel process takes place very quickly. However, if the two solutions are mixed quickly, the sol-gel formation does not occur immediately in a homogeneous ethanol solution. It takes longer time to form a gel-phase in the ethanol media and occurs through a homogeneous solution. The gelation time can be controlled by changing

the pH of the solution and monitored to evalute kinetic details of the process. PPA is a tetraprotic weak acid that is also matter in the reaction between Ni(II) species and PPA. Because at some occations, a precipitation reaction also occurs. It is important to sort out the gelation mechanism and slow down the process by controlling the degree of PPA dissociation to hinder as well as to control the kinetics of the sol-gel process to monitor the process. The time-dependent UV-vis can be used to detect the gelation process.

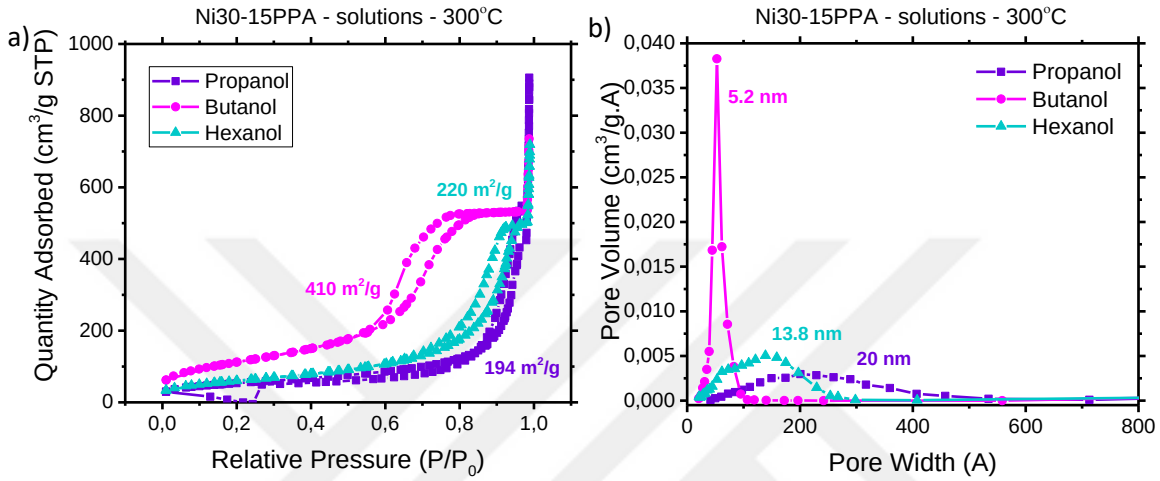


Figure 5.1: a) N_2 (77 K) adsorption and desorption isotherms and b) BJH pore-size distribution plots of the $Ni_2P_2O_7$ samples, obtained from three different alcohols.

Understanding the formation mechanism and the factors affecting its formation, a sol-gel synthesis may be also possible in methanol, water and even in other transition metal pyrophosphate systems or other systems and can result in the formation of high surface area materials.

Another topic worth studying, in much more detail, is the binary metal pyrophosphates. Mn-rich binary metal pyrophosphates MnCo5%-10%-25% and MnNi5%-10%-25% are studied in this thesis. However, Ni-rich or Co-rich systems haven't investigated yet. The preliminary experiments, given in Figure 5.2, with MnNi33% and MnNi50% indicate that in these systems, the calcined samples from solution part also yields $Mn_2P_2O_7$ crystals. And these samples are also porous with 96 and 109 m^2/g BET surface areas, see Figure 5.2(c)-(d).

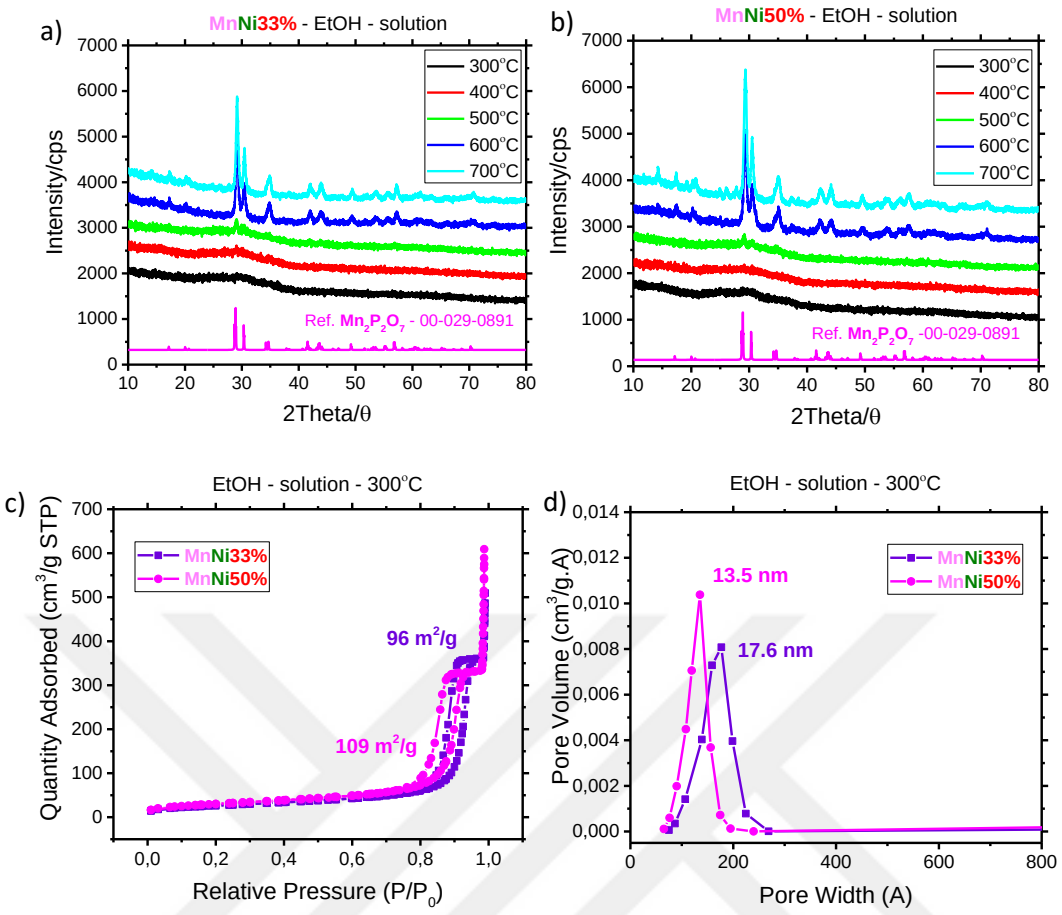


Figure 5.2: High-angle XRD patterns of a) MnNi33%, b) MnNi50% ethanol solution calcined samples and c) N_2 (77 K) adsorption and desorption isotherms and b) pore-size distribution plots of the MnNi33% and MnNi50% ethanol solution, 300ºC calcined samples.

Lastly, as the scope of this thesis is the mesoporous metal pyrophosphates not phosphates, the supernatant parts usually yield $M_3(PO_4)_2$ that haven't been studied yet in detail. Moreover, the $Co_3(PO_4)_2$ sample, coated on FTO displays high stability during electrochemical measurements, see Figure 3.48 and Figure 3.49. Also, remember that calcination of Ni30-15PPA from butanol supernatant at 300 and 400ºC produces highly porous and high-surface-area samples, see Figure 3.65 and Figure 3.66. All above suggested studies should be carried towards understanding the roles underlying for the sol-gel process that may lead to obtain much higher surface area. For instance, a simple calculation shows that the surface area can be as large as 6000 m^2/g if the pore-wall thickness is reduced to a single unit cell for metal pyrophosphates.

Bibliography

[1]- L. B. McCusker, F. Liebau, and G. Engelhardt, “Commossion on colloid and surface chemistry including catalysis nomenclature of structural and compositional characteristics of ordered microporous and mesoporous materials with inorganic hosts,” *Pure Appl. Chem.*, vol. 73, no. 2, pp. 381– 394, 2001.

[2]- G. Q. Lu and X. S. Zhao, Nanoporous Materials: Science and Engineering, London, UK: Imperial College Press, 2004.

[3]- W. Li, J. Liu, and D. Zhao, “Mesoporous materials for energy conversion and storage devices,” *Nature Reviews Materials*, vol. 1, no. 6. Nature Publishing Group, May 04, 2016. doi: 10.1038/natrevmats.2016.23.

[4]- M. S. Park, J. Kim, K. J. Kim, J. W. Lee, J. H. Kim, and Y. Yamauchi, “Porous nanoarchitectures of spinel-type transition metal oxides for electrochemical energy storage systems,” *Physical Chemistry Chemical Physics*, vol. 17, no. 46, pp. 30963–30977, 2015, doi: 10.1039/c5cp05936d.

[5]- A. Walcarius, “Mesoporous materials and electrochemistry,” *Chemical Society Reviews*, vol. 42, no. 9, pp. 4098–4140, Apr. 2013, doi: 10.1039/c2cs35322a.

[6]- T. Yanagisawa, T. Shimizu, K. Kuroda, and C. Kato, “The preparation of alkyltrimethylammonium–kanemite complexes and their conversion to microporous materials,” *Bulletin of the Chemical Society of Japan*, vol. 63, no. 4, pp. 988–992, Apr. 1990, doi: 10.1246/bcsj.63.988.

[7]- T. J. Pinnavaia, “Intercalated clay catalysts,” *Science*, vol. 220, pp. 365-371, 1983.

[8]- C. T. Kresge, M. E. Leonowicz, W. J. Roth, J. C. Vartuli, and J. S. Beck, “Ordered mesoporous molecular sieves synthesized by a liquid-crystal template mechanism,” *Nature*, vol. 359, no. 6397, pp. 710–712, 1992, doi: 10.1038/359710a0.

[9]- A. Monnier *et al.*, “Cooperative formation of inorganic-organic interfaces in the synthesis of silicate mesostructures” [Online]. Available: https://www.science.org

[10]- K. Zhu, K. Egeblad, and C. H. Christensen, “Mesoporous carbon prepared from carbohydrate as hard template for hierarchical zeolites,” *European Journal of Inorganic Chemistry*, no. 25, pp. 3955–3960, 2007, doi: 10.1002/ejic.200700218.

[11]- H. Kim and J. Cho, “Hard templating synthesis of mesoporous and nanowire SnO_2 lithium battery anode materials,” *Journal of Materials Chemistry*, vol. 18, no. 7, pp. 771–775, 2008, doi: 10.1039/b714904b.

[12]- R. Ryoo, S. H. Joo, and S. Jun, “Synthesis of highly ordered carbon molecular sieves via template-mediated structural transformation,” *The Journal of Physical Chemistry B*, vol. 103, no. 37, pp. 7743–7746, Sep. 1999, doi: 10.1021/jp991673a.

[13]- Y. Ren, Z. Ma, and P. G. Bruce, “Ordered mesoporous metal oxides: Synthesis and applications,” *Chemical Society Reviews*, vol. 41, no. 14, pp. 4909–4927, Jun. 2012, doi: 10.1039/c2cs35086f.

[14]- C. Avcı *et al.*, “Molten salt assisted self assembly (MASA): Synthesis of mesoporous metal titanate ($CoTiO_3$, $MnTiO_3$, and $Li_4Ti_5O_{12}$) Thin Films and Monoliths,” *Chemistry of Materials*, vol. 26, no. 20, pp. 6050–6057, Oct. 2014, doi: 10.1021/cm503020y.

[15]- J. Jang and J. Bae, “Fabrication of mesoporous polymer using soft template method,” *Chemical Communications*, no. 9, pp. 1200–1202, Mar. 2005, doi: 10.1039/b416518g.

[16]- R. Li, X. Wen, Y. Zhao, S. Fan, Q. Wei, and K. Lan, “Metal-based mesoporous frameworks as high-performance platforms in energy storage and conversion,” *Energy Reviews*, vol. 4, no. 1. Elsevier B.V., Mar. 01, 2025. doi: 10.1016/j.enrev.2024.100108.

[17]- R. R. Poolakkandy and M. M. Menamparambath, “Soft-template-assisted synthesis: A promising approach for the fabrication of transition metal oxides,” *Nanoscale Advances*, vol. 2, no. 11. Royal Society of Chemistry, pp. 5015–5045, Nov. 01, 2020. doi: 10.1039/d0na00599a.

[18]- C. J. Brinker, Y. Lu, A. Sellinger, and H. Fan, “Evaporation-induced self-assembly: Nanostructures made easy,” *Advanced Materials*, vol. 11, no. 7, pp. 579–585, 1999, doi: 10.1002/(SICI)1521-4095(199905)11:7<579::AID-ADMA579>3.0.CO;2-R.

[19]- H. Yang, N. Coombs, I. Sokolov, and G. A. Ozin, “Free-standing and oriented mesoporous silica films grown at the air–water interface,” *Nature*, vol. 381, no. 6583, pp. 589–592, 1996, doi: 10.1038/381589a0.

[20]- A. Kashyap, N. K. Singh, M. Soni, and A. Soni, “Deposition of thin films by chemical solution-assisted techniques,” in *Chemical Solution Synthesis for Materials Design and Thin Film Device Applications*, Elsevier, 2021, pp. 79–117. doi: 10.1016/B978-0-12-819718-9.00014-5.

[21]- R. Lin and Y. Ding, “A review on the synthesis and applications of mesostructured transition metal phosphates,” *Materials*, vol. 6, no. 1. pp. 217–243, 2013. doi: 10.3390/ma6010217.

[22]- C. Karakaya, Y. Türker, C. Albayrak, and Ö. Dag, "Assembly of molten transition metal salt–surfactant in a confined space for the synthesis of mesoporous metal oxide rich metal oxide–silica thin films," *Chemistry of Materials*, vol. 23, no. 12, pp. 3062–3071, Jun. 2011, doi: 10.1021/cm200932k.

[23]- F. M. Balcı, Ö. U. Kudu, E. Yılmaz, and Ö. Dag, "Synthesis of mesoporous lithium titanate thin films and monoliths as an anode material for high-rate lithium-ion batteries," *Chemistry - A European Journal*, vol. 22, no. 52, pp. 18873–18880, Dec. 2016, doi: 10.1002/chem.201604253.

[24]- C. Karakaya, Y. Türker, and Ö. Dag, "Molten-salt-assisted self-assembly (MASA)-synthesis of mesoporous metal titanate-titania, metal sulfide-titania, and metal selenide-titania thin films," *Advanced Functional Materials*, vol. 23, no. 32, pp. 4002–4010, Aug. 2013, doi: 10.1002/adfm.201202716.

[25]- A. Amirzhanova, N. Akmanşen, I. Karakaya, and Ö. Dag, "Mesoporous $MnCo_2O_4$, $NiCo_2O_4$, and $ZnCo_2O_4$ Thin-Film Electrodes as Electrocatalysts for the Oxygen Evolution Reaction in Alkaline Solutions," *ACS Applied Energy Materials*, vol. 4, no. 3, pp. 2769–2785, Mar. 2021, doi: 10.1021/acsaem.1c00064.

[26]- A. Amirzhanova *et al.*, "Synthesis and water oxidation electrocatalytic and electrochromic behaviours of mesoporous nickel oxide thin film electrodes," *Journal of Materials Chemistry A*, vol. 7, no. 38, pp. 22012–22020, 2019, doi: 10.1039/c9ta07693j.

[27]- I. Uzunok *et al.*, "Lyotropic liquid crystalline mesophases made of salt-acid-surfactant systems for the synthesis of novel mesoporous lithium metal phosphates," *ChemPlusChem*, vol. 84, no. 10, pp. 1544–1553, Oct. 2019, doi: 10.1002/cplu.201900435.

[28]- J. W. Goodby, "Microscopy Applications | Liquid crystals," in Encyclopedia of Analytical Science, vol. 6, pp. V6-75-V6-84, 2005 [Online]. Available: https://doi.org/10.1016/B0-12-369397-7/00393-9.

[29]- F. Reinitzer, "Beitr ge zur Kenntniss des Gholesterins," *Monatshefte für Chemie*, vol. 9, no. 1, pp. 421–441, 1888.

[30]- F. C. Frank, "I. Liquid crystals. On the theory of liquid crystals," *Discussions of the Faraday Society*, vol. 25, no. 0, pp. 19–28, 1958, doi: 10.1039/DF9582500019.

[31]- Ö. Çelik and Ö. Dag, "A new lyotropic liquid crystalline system: Oligo(ethylene oxide) surfactants with $[M(H_2O)_n]X_m$ transition metal complexes," *Angewandte Chemie* -

International Edition, vol. 40, no. 20, pp. 3800–3803, Oct. 2001, doi: 10.1002/1521-3773(20011015)40:20<3799::aid-anie3799>3.0.co;2-i.

[32]- Ö. Dag, S. Alayoğlu, and İ. Uysal, "Effects of ions on the liquid crystalline mesophase of transition-metal salt:surfactant (C_nEO_m)," *The Journal of Physical Chemistry B*, vol. 108, no. 24, pp. 8439–8446, Jun. 2004, doi: 10.1021/jp049716x.

[33]- A. F. Demirörs, B. E. Eser, and Ö. Dag, "Liquid crystalline mesophases of pluronics (L64, P65, and P123) and transition metal nitrate salts ($[M(H_2O)_6](NO_3)_2$)," *Langmuir*, vol. 21, no. 9, pp. 4156–4162, Apr. 2005, doi: 10.1021/la047136l.

[34]- C. Albayrak, G. Gülten, and Ö. Dag, "Phase separation in liquid crystalline mesophases of $[Co(H_2O)_6]X_2$:P65 Systems (X = NO_3^-, Cl^-, or ClO_4^-)," *Langmuir*, vol. 23, no. 2, pp. 855–860, Jan. 2007, doi: 10.1021/la0622119.

[35]- A. E. Danks, S. R. Hall, and Z. Schnepp, "The evolution of 'sol-gel' chemistry as a technique for materials synthesis," *Materials Horizons*, vol. 3, no. 2, pp. 91–112, Mar. 2016, doi: 10.1039/c5mh00260e.

[36]- B. L. Cushing, V. L. Kolesnichenko, and C. J. O'Connor, "Recent advances in the liquid-phase syntheses of inorganic nanoparticles," *Chemical Reviews*, vol. 104, no. 9, pp. 3893–3946, Sep. 2004, doi: 10.1021/cr030027b.

[37]- M. Ebelmen, *Annales de Chimie et de Physique*, vol.16, pp.129,1846.

[38]- M. Ebelmen, *Comptes Rendus de l'Academie des Sciences*, vol. 25, pp. 854, 1847.

[39]- T. Graham, "XXXV. - On the properties of silicic acid and other analogous colloidal substances," *Journal of the Chemical Society*, vol. 17, no. 0, pp. 318–327, 1864, doi: 10.1039/JS8641700318.

[40]- L. L. Hench' and J. K. West, "The sol-gel process," *Chemical Reviews*, vol. 90, no. 1, pp. 33-72, 1990.

[41]- W. Ostwald, "Studien über die Bildung and Umwandlung fester Körper. 1. Abdhandlung: Übersattigung and Überkaltung," *Zeitschrift für Physikalische Chemie*, vol. 27, p. 365, 1897.

[42]- L. Rayleigh, *The London, Edinburgh, and Dublin Philosophical Magazine and Journal of Science*, vol. 38, pp. 738, 1919.

[43]- D. M. Roy and R. Roy, "Synthesis and stability of minerals in the system MgO-Al_2O_3-SiO_2-H_2O," *American Mineralogist*, vol. 39, pp. 957, 1954.

[44]- R. Roy, “Aids in hydrothermal experimentation. II. Methods of making mixtures for both dry and wet phase equilibrium studies,” *Journal of the American Ceramic Society*, vol.39, no. 2, pp. 145, 1956.

[45]- R. Roy, “Synthesis and properties of dense, polycrystalline alumina,” *Journal of the American Ceramic Society*, vol. 52, pp. 344-350, 1969.

[46]- R. K. Iler, The Chemistry of Silica. New York, NY, USA: Wiley, 1955.

[47]- W. Stober, A. Fink, and D. Ernst Bohn, “Controlled growth of monodisperse silica spheres in the micron size range 1,” *Journal of Colloid and Interface Science*, vol. 26, pp. 62-69,1968.

[48]- J. Th. G. Overbeek, *Adv. Colloid Interface Sci.,* vol. 16, pp. 17, 1982.

[49]- J. Th. G. Overbeek, “Monodisperse colloidal systems, fascinating and useful,” *Adv. Colloid Interface Sci.,* vol. 15, pp. 251-277,1982.

[50]- T. Sugimoto, “Preparation of monodispersed colloidal particles,” *Adv. Colloid Interface Sci.,* vol. 28, pp.65, 1987.

[51]- E. Matijevic, M. Bundnick, and L. Meites, “Preparation and mechanism of formation of titanium dioxide hydrosols of narrow size distribution,” *J. Colloid Interface Sci.,* vol. 61, pp. 302, 1977.

[52]- E. Matijevic, *Ultrastructure Processing of Ceramics, Glasses and Composites*, L. L. Hench and D. R. Ulrich, Eds. New York, NY, USA: Wiley, 1984, p. 334.

[53]- E. Matijevic, *Science of Ceramic Chemical Processing*, L.L. Hench, D. R. Ulrich, Eds, New York, NY, USA: Wiley, 1986, p. 463.

[54]- E. Matijevic, *Ultrastructure Processing of Ceramics Glasses and Composites*, J. D. Mackenzie and D. R. Ulrich, Eds. New York, NY, USA: Wiley, 1988, p. 429.

[55]- M. E. A. Hermans, *Sci. Ceram.*, vol. 5, pp. 523, 1970.

[56]- K. Kamiya, S. Sakka, and Y. Tatemichi, *J. Mater. Sci.*, vol. 15, pp. 1765, 1980.

[57]- C. Z. Carroll-Porczynski, *Advanced Materials.* New York, NY, USA: Chemical Publishing Co., 1962.

[58]- S. Choudhury, “A review of the sol-gel process and its application,” Int. Educ. Res. J., vol. 10, no. 7, pp. 122-125, Jul. 2024.

[59]- M. G. Shange, N. L. Khumalo, S. M. Mohomane, and T. E. Motaung, “Factors affecting silica/cellulose nanocomposite prepared via the sol-gel technique: A review,” *Materials*, vol. 17, no. 9, 2024, doi: 10.3390/10.3390/ma17091937.

[60]- G.V. Aguilar, “Introductory chapter: A brief semblance of the sol-gel method in research,” in *Sol-Gel Method - Design and Synthesis of New Materials with Interesting*

Physical, Chemical and Biological Properties. London, U.K.: IntechOpen, Feb. 13, 2019. doi: 10.5772/intechopen.82487.

[61]- Z. Yue, W. Guo, J. Zhou, Z. Gui, and L. Li, "Synthesis of nanocrystilline ferrites by sol-gel combustion process: The influence of pH value of solution," *Journal of Magnetism and Magnetic Materials*, vol. 270, no. 1–2, pp. 216–223, Mar. 2004, doi: 10.1016/j.jmmm.2003.08.025.

[62]- P. Badanayak, J. V. Vastrad, "Sol-gel process for synthesis of nanoparticles and applications thereof," *The Pharma Innovation Journal*, no. 8, 2021, [Online]. Available: http://www.thepharmajournal.com

[63]- L. P. Singh *et al.*, "Sol-Gel processing of silica nanoparticles and their applications," *Advances in Colloid and Interface Science*, vol. 214. Elsevier B.V., pp. 17–37, 2014. doi: 10.1016/j.cis.2014.10.007.

[64]- E. M. Modan and A. G. Plăiașu, "Advantages and disadvantages of chemical methods in the elaboration of nanomaterials," *The Annals of "Dunarea de Jos" University of Galati. Fascicle IX, Metallurgy and Materials Science*, vol. 43, no. 1, pp. 53–60, Mar. 2020, doi: 10.35219/mms.2020.1.08.

[65]- A. A. Kulkarni, V. A. Savekar, T. S. Bhat, and P. S. Patil, "Recent advances in metal pyrophosphates for electrochemical supercapacitors: A review," *Journal of Energy Storage*, vol. 52. Elsevier Ltd, Aug. 15, 2022. doi: 10.1016/j.est.2022.104986.

[66]- C. Wei, C. Cheng, S. Wang, Y. Xu, J. Wang, and H. Pang, "Sodium-doped mesoporous $Ni_2P_2O_7$ hexagonal tablets for high-performance flexible all-solid-state hybrid supercapacitors," *Chemistry - An Asian Journal*, vol. 10, no. 8, pp. 1731–1737, Aug. 2015, doi: 10.1002/asia.201500335.

[67]- K. V. Sankar, Y. Seo, S. C. Lee, and S. Chan Jun, "Redox additive-improved electrochemically and structurally robust binder-free nickel pyrophosphate nanorods as superior cathode for hybrid supercapacitors," *ACS Applied Materials & Interfaces*, vol. 10, no. 9, pp. 8045–8056, Mar. 2018, doi: 10.1021/acsami.7b19357.

[68]- Y. Zhou *et al.*, "Chemical precipitation synthesis of porous $Ni_2P_2O_7$ nanowires for supercapacitor," *Journal of Alloys and Compounds*, vol. 790, pp. 36–41, Jun. 2019, doi: 10.1016/J.JALLCOM.2019.03.192.

[69]- P. Matheswaran, P. Karuppiah, S. M. Chen, and P. Thangavelu, "A binder-free $Ni_2P_2O_7/Co_2P_2O_7$ nanograss array as an efficient cathode for supercapacitors," *New Journal of Chemistry*, vol. 44, no. 30, pp. 13131–13140, Aug. 2020, doi: 10.1039/d0nj00890g.

[70]- J. Zhang *et al.*, "In situ fabrication of a rose-shaped $Co_2P_2O_7$/C nanohybrid via a coordination polymer template for supercapacitor application," *New Journal of Chemistry*, vol. 44, no. 29, pp. 12514–12521, Aug. 2020, doi: 10.1039/d0nj02414g.

[71]- H. Liu *et al.*, "An enhanced capacitive storage of hybrid supercapacitor based on interconnected nitrogen-doped graphene encapsulated honeycomb cobalt manganese pyrophosphate," *Chemical Engineering Science*, vol. 238, p. 116613, Jul. 2021, doi: 10.1016/J.CES.2021.116613.

[72]- A. Padhy, A. K. Samantara, and J. N. Behera, "Cobalt pyrophosphate ($Co_2P_2O_7$) derived from an open-framework cobalt phosphite: a durable electroactive material for electrochemical energy conversion and storage application," *Sustainable Energy and Fuels*, vol. 5, no. 14, pp. 3729–3736, Jul. 2021, doi: 10.1039/d1se00714a.

[73]- R. BoopathiRaja, S. Vadivel, M. Parthibavarman, S. Prabhu, and R. Ramesh, "Effect of polypyrrole incorporated sun flower like $Mn_2P_2O_7$ with lab waste tissue paper derived activated carbon for asymmetric supercapacitor applications," *Surfaces and Interfaces*, vol. 26, p. 101409, Oct. 2021, doi: 10.1016/J.SURFIN.2021.101409.

D. S. Hall, D. J. Lockwood, C. Bock, and B. R. MacDougall, "Nickel hydroxides and related materials: A review of their structures, synthesis and properties," *Proceedings of the Royal Society A: Mathematical, Physical and Engineering Sciences*, vol. 471, no. 2174. Royal Society of London, Feb. 08, 2015. doi: 10.1098/rspa.2014.0792.

[74]- D. S. Hall, D. J. Lockwood, C. Bock, and B. R. MacDougall, "Nickel hydroxides and related materials: A review of their structures, synthesis and properties," *Proceedings of the Royal Society A: Mathematical, Physical and Engineering Sciences*, vol. 471, no. 2174. Royal Society of London, Feb. 08, 2015. doi: 10.1098/rspa.2014.0792.

[75]- R. S. McEwen, "Crystallographic studies on nickel hydroxide and the higher nickel oxides," *The Journal of Physical Chemistry*, vol. 75, no. 12, pp. 1782–1789, Jun. 1971, doi: 10.1021/j100681a004.

[76]- J. P. Cheng, J. Zhang, and F. Liu, "Recent development of metal hydroxides as electrode material of electrochemical capacitors," *RSC Advances*, vol. 4, no. 73, pp. 38893–38917, 2014, doi: 10.1039/C4RA06738J.

[77]- D. Shao, Q. Wang, X. Yao, Y. Zhou, and X.-Y. Yu, "Phase-engineering of nickel hydroxide in the Ni/$Ni(OH)_2$ interface for efficient hydrogen evolution and hydrazine-assisted water splitting in seawater," *Journal of Materials Chemistry A*, vol. 10, no. 41, pp. 21848–21855, 2022, doi: 10.1039/D2TA06481B.

[78]- A. A. S. Rovetta, M. P. Browne, A. Harvey, I. J. Godwin, J. N. Coleman, and M. E. G. Lyons, “Cobalt hydroxide nanoflakes and their application as supercapacitors and oxygen evolution catalysts,” *Nanotechnology*, vol. 28, no. 37, p. 375401, 2017, doi: 10.1088/1361-6528/aa7f1b.

[79]- O. van der Heijden, S. Park, R. E. Vos, J. J. J. Eggebeen, and M. T. M. Koper, “Tafel slope plot as a tool to analyze electrocatalytic reactions,” *ACS Energy Letters*, vol. 9, no. 4, pp. 1871–1879, Apr. 2024, doi: 10.1021/acsenergylett.4c00266.

[80]- I. Ulu, B. Ulgut, and Ö. Dag, “Nanoarchitectonics of mesoporous $M_2P_2O_7$ (M = Mn(II), Co(II), and Ni(II)) and $M_{2-x}Co_xP_2O_7$ and transformation to their metal hydroxides with decent charge capacity in alkali media,” *Inorganic Chemistry*, vol. 62, no. 41, pp. 16994–17011, Oct. 2023, doi: 10.1021/acs.inorgchem.3c02808.

[81]- I. Ulu, B. Ulgut, and Ö. Dag, “Fabrication of mesoporous nickel pyrophosphate electrodes and their transformation to nickel hydroxide with decent capacitance in alkaline media,” *Journal of Materials Chemistry A*, vol. 11, no. 41, pp. 22384–22395, 2023, doi: 10.1039/D3TA05578G.

[82]- R. G. Alargova, I. I. Kochijashky, M. L. Sierra, and R. Zana, “Micelle aggregation numbers of surfactants in aqueous solutions: A comparison between the results from steady-state and time-resolved fluorescence quenching,” *Langmuir*, vol. 14, no. 19, pp. 5412–5418, Sep. 1998, doi: 10.1021/la980565x.

[83]- A. Hezel and S. D. Ross, “The vibrational spectra of some divalent metal pyrophosphates,” Spectrochim. Acta Part A Mol. Spectrosc., vol. 23, no. 5, pp. 1583-1589, 1967, doi:10.1016/0584-8539(67)80381-7.

[84]- H. Cong and W. Cao, “Thin film interference of colloidal thin films,” *Langmuir*, vol. 20, no. 19, pp. 8049–8053, Sep. 2004, doi: 10.1021/la049118.

[85]- H. Pang, Y. Z. Zhang, Z. Run, W. Y. Lai, and W. Huang, “Amorphous nickel pyrophosphate microstructures for high-performance flexible solid-state electrochemical energy storage devices,” *Nano Energy*, vol. 17, pp. 339–347, Oct. 2015, doi: 10.1016/j.nanoen.2015.07.030.

[86]- S. S. Patil and P. S. Patil, “Transition metal pyrophosphate ($M_xP_2O_7$): A new arrival in hybrid supercapacitors,” *Chemical Engineering Journal*, vol. 455. Elsevier B.V., Jan. 01, 2023. doi: 10.1016/j.cej.2022.140639.

[87]- I. K. Durukan, I. Ulu, and Ö. Dag, “Manganese oxide-based mesoporous thin-film electrodes: manganese disproportionation reaction in alkaline media,” *Journal of Materials Chemistry A*, vol. 12, no. 11, pp. 6359–6375, Feb. 2024, doi: 10.1039/d3ta07973b.

[88]- F. Ambroz, T. J. Macdonald, V. Martis, and I. P. Parkin, “Evaluation of the BET theory for the characterization of meso and microporous MOFs,” *Small Methods*, vol. 2, no. 11. John Wiley and Sons Inc, 2018. doi: 10.1002/smtd.201800173.

[89]- Z. Teng, W. Li, Y. Tang, A. Elzatahry, G. Lu, and D. Zhao, “Mesoporous organosilica hollow nanoparticles: Synthesis and applications,” *Advanced Materials*, vol. 31, no. 38, Sep. 2019, doi: 10.1002/adma.201707612.

[90]- I. Artaki, T. W. Zerda, and J. Jonas, “Solvent effects on the condensatıon stage of the sol-gel process,” *Journal of Non-Crystalline Solids*, vol. 81, pp.381-395, 1986. doi.org/10.1016/0022-3093(86)90504-1.

[91]- A. Shokuhfar, E. Eghdam, and M. Alzamani, “Effect of solvent content on the properties of nanostructure silica thin film by sol-gel,” *Nanoscience and Nanotechnology*, vol. 2, no. 1, pp. 22–25, Feb. 2012, doi: 10.5923/j.nn.20120201.05.

[92]- G. Mitran, T. L. P. Nguyen, and D. K. Seo, “Effect of solvent, in the sol-gel synthesis of $CoAl_2O_4$, on the structure and catalytic properties in 1,4-butanediol dehydrocyclization,” *Reaction Chemistry and Engineering*, vol. 8, no. 8, pp. 1901–1913, Apr. 2023, doi: 10.1039/d3re00095h.

[93]- A. Khadir, G. Roux-Desgranges, and A. H. Roux, “Comparison of the cosurfactant character of 1-butanol and phenol in sodium dodecylsulfate aqueous solutions from relative enthalpies of dilution at 298.15 K,” *Thermochimica acta*, vol. 292, pp. 59-69, May 1997, https://doi.org/10.1016/S0040-6031(96)03124-3.